UNIVERSITAT DE BARCELONA

Heterogeneous Integration of RF and Microwave Systems

Using Multi-layer Low-Temperature Co-fired Ceramics Technology

Saiyd Ahyoune

Heterogeneous Integration of RF and Microwave Systems

Using Multi-layer Low-Temperature Co-fired Ceramics Technology

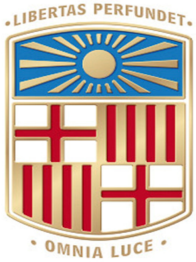

UNIVERSITAT *DE* BARCELONA

Saiyd Ahyoune

Supervisors: Dr. **Javier José Sieiro Córdoba**
Dra. **María Nieves Vidal Martínez**

Tutor: Dr. **José María López Villegas**

Departament d'Enginyeries: Secció d'Electrònica
Universitat de Barcelona

This dissertation is submitted for the degree of
Doctor of Philosophy
in
Engineering and Advanced Technologies

April 2017

I would like to dedicate this thesis to my loving parents, Safia Teyar and Mohamed Ahyoune and all my family.

Agradecimientos

En primer lugar y de forma especial, quiero dar mis más sincero agradecimiento a mis directores, Dr. Javier José Sieiro Córdoba, y Dra. María Nieves Vidal Martínez, y a mi tutor Dr. José María López Villegas, por sus valiosas orientaciónes, asesoramientos y un fuerte apoyo durante estos años. Que sin sus guías y ayudas, esta tesis no habría sido terminada.

También doy un agradecimiento a la empresa Francisco Albero S. A. U. (FAE) por su colaboración en este proyecto de investigación.

Igualmente quiero agradecer a mis compañeros del Grupo de Radio Frecuencia (GRF) Pablo Benet, Aleix Garcia y Tomás Carrasco. Así mismo doy las gracias a mis compañeros del Laboratorio (H20), Albert, Josep, Pablo, Raquel, David, Frank y todos los demás compañeros y profesores del departamento de Ingenierías: Sección de Electrónica.

Ademas dar las gracias a los amigos de la Universidad de Barcelona, M. Kadaoui , Tarik Y., Islam, Musab, Allan, Cristina, Median, M. Khili, de la Universidad Politécnica de Cataluña, Ayoub, Sedik, Hamza, Mohcin, Hassan, Tarik B., de la Universidad de Autònoma, Abdelilah, Ghali, Ikbal. Y otros amigos Yudith, Yassin, Marina, Asri M., Azozi. Y todos los demás amigos dentro y fuera de la universidad.

Finalmente, quiero agradecer profundamente a mi madre, mi padre, mis hermanos, hermanas, sobrinos, mi abuela, y toda mi familia por haberme brindado su apoyo, por la comprensión, tolerancia e infinita paciencia. Y por haber cedido su tiempo para permitir que así yo haya podido llevar adelante satisfactoriamente el enorme trabajo que representa una tesis doctoral.

Abstract

The aim of this work is the development of a modelling methodology for the fast analysis of non-radiative multilayer RF passive components without compromising solution accuracy. Instead of following a compact model approach, oftenly used in integrated technologies, the method is based on a specialized quasi-static partial element equivalent circuit (PEEC) numerical solver. Besides speed and accuracy, the solver can be embedded in circuit simulators; thus, models are already available in the schematic entry. Using this framework, model scalability is enhanced in terms of geometry, substrate cross-section, material properties, topology and boundary conditions.

The dissertation starts showing the actual performance of the obtained solver and the motivations beneath its development. Then, the description about solver development is splitted in three parts, but all of them are interrelated. First, the PEEC formulation is adapted according to relevant electromagnetic behaviour of the component. It is worth stressing that a different perspective related to the principle of virtual work is used in this formulation. The second part deals with the evaluation of partial elements, the core of the solver. It is carried out using analytical space-domain close-form solutions of the Green's function (GF) of the substrate. Partial elements are then assembled into a mesh. Therefore, the importance of the mesh up on solution accuracy is discussed in the last part and a basic layout aware mesh generator is proposed.

Practical application of the methodology includes the implementation of a library of RF passives for multilayer substrate. For validation, the chosen substrate is a low temperature co-fired ceramics (LTCC) technology. Different set of devices have been fabricated, characterized and compared against model prediction. In addition, the obtained results are also verified using state-of-the-art electromagnetic solvers.

Table of contents

List of figures

List of tables

Nomenclature

Acronyms / Abbreviations

AC Alternating Current

ADS Advanced Design System

API Application Programming Interface

ASITIC Analysis and Simulation of Inductors and Transformers in Integrated Circuits

BC Boundary Conditions

BST Barium Strontium Titanate

CMOS Complementary Metal-Oxide-Semiconductor

CST Computer Simulation Technology

CTE Coefficient of Thermal Expansion

DC Direct Current

DCIM Discrete Complex Image Method

EDA Electronic Design Automatic

EFIE Electric Field Integral Equation

EM Electromagnetic

EMC Electromagnetic compatibility

EMPro Electromagnetic Professional

FAE Francisco Albero Electrónica S.A.U.

FDTD Finite Differences in Time Domain

FEM Finite Element Method

FR Flame Retardant

GF Green's Function

GMD Geometric Mean Distance

GSG Ground-Signal-Ground

HFSS High Frequency Structural Simulator

HTCC High Temperature Co-fired Ceramic

IC Integrated Circuit

KCL Kirchoff's Current Law

KVL Kirchoff's Voltage Law

LTCC Low Temperature Co-fired Ceramic

LUT Look Up Table

MEMS Micro-Electro-Mechanical Systems

MMIC Monolithic Microwave Integrated Circuits

MNA Modified Nodal Analysis

MoM Method of Moments

MPIE Mixed Potential Integral Equation

PCB Printed Circuit Board

PDK Process Design Kit

PEEC Partial Element Equivalent Circuit

PML Perfect Matched Layers

RF Radio Frequency

RFIC Radio Frequency Integrated Circuits

SAW Surface Acoustic Wave

SiP System-in-Package

SMD Surface-Mount Device

SoC System-on-Chip

SOLT Short-Open-Load-Through

SPICE Simulation Program with Integrated Circuits Emphasis

SRF Self Resonant Frequency

UCM User-Compiled Model

Chapter 1

Introduction

1.1 Heterogeneous integration

Within each technology node, there is an increase in design, manufacturability and test cost that can only be compensated by adding more functionality inside the chip [1]. Therefore, on top of the essential functions of a digital System on Chip (SoC), i.e. processing and storage, there is a trend in adding quantitative (passive components, sensors and actuators) and functional requirements (power consumption and communication bandwidth) that do not always scale according to Moore's Law [2]. One way to overcome this problem is through the implementation of novel design techniques that shifts the analog-digital interface to higher frequencies as demonstrated in Software Defined Radio front-ends [3–5]. However, issues related to the antenna or bandpass filter reconfigurability must be addressed with non-CMOS technologies because they are not CMOS scalable or compatible [6]. In other words, complex system implementation requires the combination of different heterogeneous technologies, not only CMOS. As shown in Fig.1.1, this new approach is named *More than Moore* or functional diversification and have been included in the International Technology Roadmap for Semiconductors since 2001.

The design concept underneath this framework is the System in Package (SiP). SiP is not only a way to assemble digital, analog, and memory dies surrounded by small SMT devices [7], but adds more functionality at the package level, e.g. through the implementation of 3D passives and subsystems. SiP versus SoC must not been interpreted as competitor methodologies. In fact, it is the final user applications that will favour one of the SiP (health) or SoC (information and entertainment) approaches or both (transport, energy, security and communications). As a trend for the coming years, the most high-demanding functions will migrate from board level to package level, and, whenever possible, to chip level.

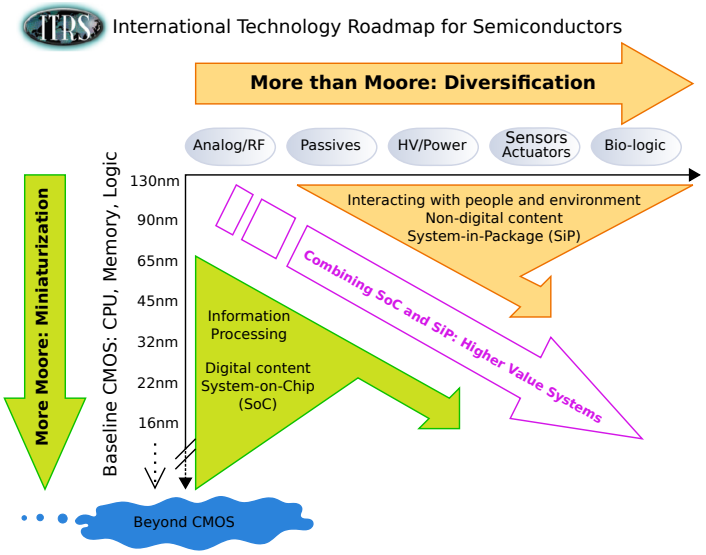

Fig. 1.1 Moore's Law vs More than Moore concept [1].

Taking into account the previous *More than Moore* scenario, one of the enabling technologies for the heterogeneous integration is the Low Temperature Co-fired Ceramic (LTCC) fabrication process as it has been demonstrated in [8]. It is a matured technology running since 20 years ago when Multichip Modules were an active research activity. Its driving force is based on the excellent properties of ceramic substrates, as it will be shown in the last section of this Chapter. It has been effectively applied in different industrial sectors, e.g., automotive [9–11], aerospace [12, 13], biosystems [14, 15], communications [16, 17], or power electronics [18, 19] among others. Actually, LTCC will play a central role in this work through the development of a library of components intended for this technology.

1.2 The EDA gap

In spite of the superior performance of LTCC, organic laminate technologies are used more frequently than LTCC. A possible cause could be its higher cost, but in many cases overall expenses are similar [8]. To shed some light on the actual reason for this limitation, it is necessary to review designer's role. Therefore, the question is how much functionality is able to handle the designer? The answer depends on three aspects:

- *Technology*: electromagnetic, thermal, and mechanical material parameters, and substrate topology (e.g. number of layers and minimum layout features) define the type of devices that can be built, their performance, and the ability to assembly different circuits and subsystems.

- *Electronic design automation (EDA) tools*: the higher the complexity of the technology, the higher the need for sophisticated EDA tools that help designers in meeting the stringent time-to-market and product yield constraints.

- *Designer's expertise*: heterogeneous integration demands designers with a wide knowledge in different fields (digital/analog/RF/power electronics, packaging, reliability, thermal design, ...) in order to combine effectively the best performance of each technology involved in the development of a product.

From the previous three points, the bottle-neck for a widespread use of the LTCC is the lack of efficient EDA tools. Thus, designers are not able to fully exploit all possibilities offered by the technology. This problem is known as *the EDA gap* [1]. It illustrates the fact that EDA tools are not developed at the same pace as technology increases its complexity. Not only LTCC, but many other technologies experience this gap when dealing with high-performance system design, for instance in the design of radiofrequency integrated circuits.

To better understand this problem, the paradigm in EDA is the translation of system specifications into an integrated or hybrid circuit just via a single mouse 'click' [20]. However, these tools are not still enough mature. As shown in Fig. 1.2, the design flow diagram followed by most RF EDA platforms is formed by two iterative procedures that rely on electromagnetic (EM) simulators [21]:

i. The first loop deals with the synthesis of passive components in order to account for their own parasitics.

ii. The second one is used to extract the EM coupling of distant parts of the circuit to assess the correct performance of the whole system.

Normally, the synthesis loop is recognized as the bottleneck of the RF design process because it is an iterative process that needs an accurate determination of the behaviour of the component, which is translated into a huge amount of computational resources and time. Clearly, an analog RF silicon compiler is still in its infancy, thus the actual challenge in RF EDA is to obtain an efficient tool which is able to reduce the number of iterations and/or the time employed for EM analysis. However, the need for high accuracy in the analysis of the component opposes to efficiency because it can only be achieved by using EM solvers.

1.3 Building a library of components

An alternative to solve the EDA gap is the development of a process design kit (PDK) that is formed by interconnect information (e.g. design rules, mask definition, material properties,

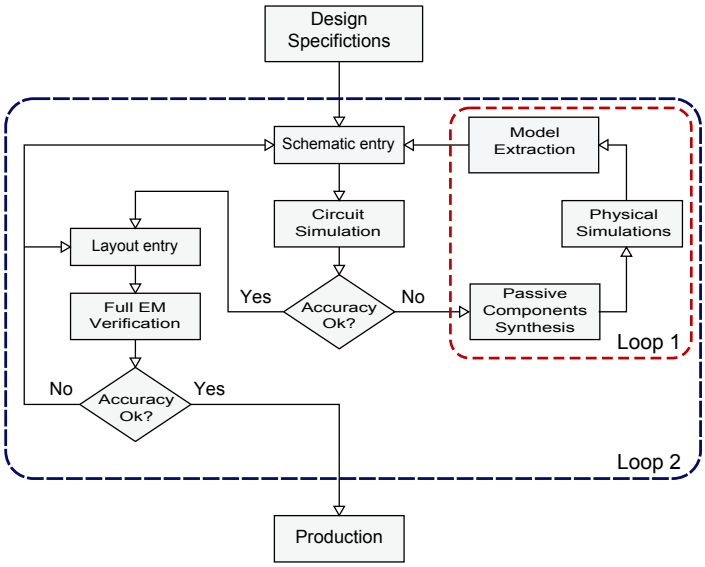

Fig. 1.2 RF Microwave design flow diagram.

...), libraries of components (device compatible SPICE models and their corresponding parameterized cells), standard cells or circuit blocks, Intellectual Property designs, and layout tools. Not all PDKs contain the same kind of information. Whereas a printed circuit board (PCB) PDK has only interconnect information, an IC one contains all information about any device that can be fabricated in the technology and, normally, it also offers a set of digital standard cells and basic analog cells. A PDK in LTCC process should be closer to an IC-PDK because the substrate must have an enhanced functionality. However, few attempts on LTCC-PDK development have been done [22] in spite of the huge number of passives that can be embedded. PDKs offered by LTCC foundries and material suppliers are closer to a PCB-PDK than to an IC-PDK. Only interconnect information is given to designers who are then forced to use EM simulators in their design flow methodology [23, 24] because of the lack of component libraries.

To better understand the complexity underneath the development of a component library, assume that a complete SPICE model for a film resistor embedded in LTCC should be developed, as the one shown in Fig. 1.3. This resistor can be made with different resistive materials (e.g. 10 Ω/sq, 100 Ω/sq, 1 $K\Omega/sq$, 10 $K\Omega/sq$), can be located at any layer of the LTCC substrate (the total number of layers is also a designer's choice), and can have rectangular or meander shape with different number of bends, width and length. Even more, a ground plane could be located underneath. If a single compact model (e.g. Fig. 1.4) must account for all parasitics in all of the previous configurations, the probable adopted solution would be the partition of the model according to its layer location, an a fixed technology cross-section. Otherwise, the description of parasitics becomes impractical. This situation

(a) cross section (b) rectangular resistor

(c) meander resistor

Fig. 1.3 Thick film resistor.

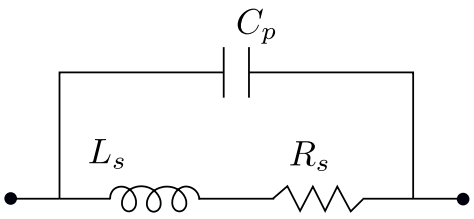

Fig. 1.4 Resistor equivalent compact model.

is even worsened for other passives such as capacitors, inductors and transformers, which geometrical shapes are further complex as illustrated in Fig. 1.5.

From the former example, one can conclude that the freedom to place passives on any layer level, which is a design advantage in LTCC, is an inconvenient for device model development. This picture is in opposition to IC design, where the device substrate cross-section is always fixed, i.e., components can only be located at their corresponding layer at not elsewhere. To solve this modelling problem, a new paradigm must be set. It is necessary to move away compact models and bring in physical tools at the core of device modelling. Using physical tools, material properties, substrate cross-section, component topology and geometry, and EM boundaries can be described effectively. Then, a true scalable PDK able to handle any complex technology can be implemented.

The proposed component library development demands the use of EM solvers that, as already explained, consume a huge amount of computational resources and time. Therefore, the challenge for changing this modelling paradigm is the development of fast, accurate and SPICE-compatible electromagnetic solvers. It is still possible to explore new solutions for improving efficiency (computation speed) without compromising accuracy; the key point is to realize that EM solvers are developed as general purpose tools able to cope with different technologies and device structures. Computational speed can be increased if previous knowledge about the EM behaviour of the component, its technological implementation and

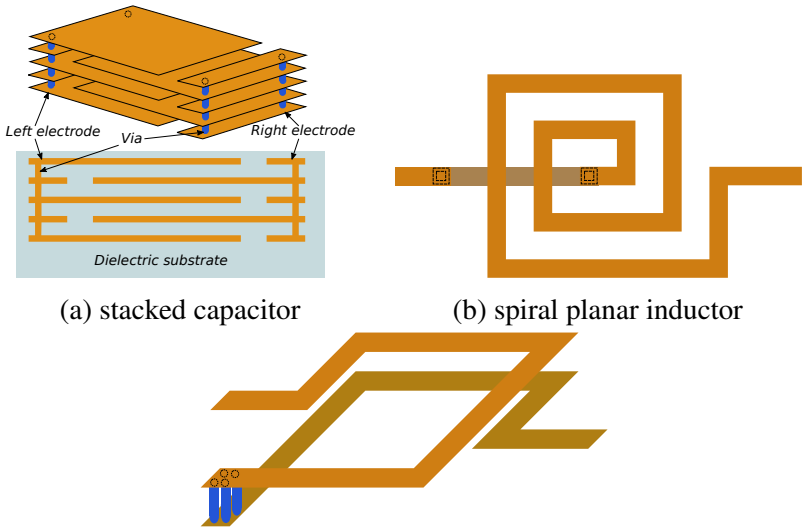

(a) stacked capacitor (b) spiral planar inductor

(c) stacked inductor

Fig. 1.5 Stacked capacitor and inductors in LTCC.

its targeted application is used as a way to specialize the solver. Then, it can be tuned out to become the core of a fast electromagnetic algorithm that can be used for building a reliable component library. This alternative must be understood as a kind of trade-off, i.e. generality vs. specialization of the solver tool and it will be the point of view taken in this work.

1.4 Objectives

The main goal of this work is the development of a fast and accurate 2.5D quasi-static electromagnetic solver that has the next characteristics:

- Simulation time must be on the order of circuit simulator (e.g., less than a second per frequency point for a typical inductor component).
- Accuracy must be within technology tolerance and measurement uncertainty.
- Stability of the method must be guaranteed by matrix elements formation.
- It must be useful for most laminated technologies (e.g. PCB, LTCC, high-frequency laminates) and, whenever possible, for RF integrated circuit design.
- It must be embedded seamlessly in a circuit simulator.

To arrive to this goal, it is necessary to develop additional numerical techniques, which can be viewed as secondary goals:

Table 1.1 Substrates parameters.

		Total thickness	layers	ε_r	$tg\delta$
LTCC	L8	840 μm	12	6.5	0.002
	Ferro-A6S	660 μm	6	6.1	0.002
RFIC	Silicon	400 μm	1	11.8	
	Oxide	10 μm	2	4	0.002
PCB		3.5 mm	12	6.5	0.02

- Substrate Green's functions must be available in close-forms, thus analytical procedures have to be developed.
- The mesh generator must be based on *physics aware*, i.e. the final mesh has to take into account not only the geometry, but it must be sensible to the physics of the component.

With the developed tool, the milestone of this thesis is the implementation of an LTCC PDK which contains, aside from interconnect information, component models based on the electromagnetic solver that can be used for any practical laminate system. Targeted devices are resistors, capacitors, inductors and transmission lines.

1.5 Performance of the developed EM solver

Instead of waiting until the last chapter of the thesis, the performance of the developed tool is next compared with other state-of-the-art commercial electromagnetic programs. Different devices (inductors, resistors and capacitors) using different technologies (PCB, LTCC, Silicon) are used in this benchmark. For a fair comparison, meshes are set to similar sizes.

The selected commercial tools are MoMemtum RF (keysight Technologies), Sonnet and CST studio. The two former are based on the method of momentts; the later is a finite element solver. Whenever possible, experimental values are also given as a reference for accuracy. To allow the checking of these results, Table 1.1 collects the substrate parameters used in the simulators.

With no doubt, planar inductor are the most amenable passive component for applying efficiently the PEEC method. This is due to the typical width/length/thickness aspect ratio of its layout metal strips. Three inductor shapes, each implemented in a different technology, have been simulated. Their geometrical parameters are shown in Table 1.2. For comparison, the selected electrical parameters are the inductance value at low frequency (L), the resistance

Table 1.2 Geometrical characteristics of inductors.

Inductor 1 (L1)	Substrate	LTCC-Ferro A6
	Number turns	3
	Length ports	1085 μm
	Width ports	185 μm
	Spacing Ports	920 μm
	Initial Length	964 μm
	Metal width	155 μm
	Metal spacing	340 μm
Inductor 2 (L2)	Substrate	PCB
	Number turns	3
	Length ports	4 mm
	Width ports	0.8 mm
	Spacing Ports	4.1 mm
	Initial Length	2.5 mm
	Metal widths	0.3 mm
	Metal spacing	0.5 mm
Inductor 3 (L3)	Substrate	Silicon
	Number turns	2
	Length ports	12 μm
	Width ports	40 μm
	Spacing Ports	310 μm
	Initial Length	0 μm
	Metal width 1	40 μm
	Metal width 2	16 μm
	Metal spacing	6 μm

at low frequency (R_{DC}), the maximum quality factor (Q_{max}), and the self resonant frequency (SRF).

For each solver and including experimental data, the predicted/measured performance of the inductors are shown in Table 1.3. In addition, the time required for computing the solution is also given. Two important remarks must be highlighted. First, the accuracy of integral solvers is higher than differential solvers under the constraint of similar meshes. Second, compared with other integral methods, the implemented PEEC solver is at least 30× faster for a one layer substrate (L2-L3) and up to 160× faster for a ten layer substrate (L1), while keeping on out performing accuracy. This superiority is achieved by tweaking the PEEC solver as an specialized tool, as it will be explained in Chapter 2.

Table 1.3 Measured vs. simulated data of inductors.

		L (nH)	R_{DC} (Ω)	Q_{max}	SRF (Ghz)	t_{comp} (51 points)
L1	PEEC	23.3	0.86	32	1.95	5.25s
	MoM	22.8	0.52	103	2.27	13min55s
	Sonnet	22.2	0.49	53	2.32	14min
	CST	20.4	0.10	124	2.24	6min17s
	Meas	23.8	1.01	46	2.03	**
L2	PEEC	141.0	0.138	80.9	333	1.89s
	MoM	143.2	0.19	66.9	334	1min27s
	Sonnet	144.8	0.17	84.1	335	2min3s
	CST	139.0	0.02	142.0	332	2min51s
	Meas	141.8	0.22	82.2	329	**
L3	PEEC	2.09	1.23	21.3	16.80	1.9s
	MoM	2.19	1.42	17.3	17.49	2min16s
	Sonnet	2.17	1.57	14.09	16.19	5min48s
	CST	2.27	0.06	38.7	16.41	3min48s
	Meas	2.00	1.11	29.8	18.75	**

Table 1.4 Geometrical characteristics of resistors.

Devide id	Ω/sq	No. bends	Length[μm]	Width[μm]	Gap[μm]
R1	10	2	1500	250	200
R2	100	2	1500	500	200
R3	1K	5	1500	250	200
R4	10K	5	1500	500	200

For resistors, performance figures are quite similar to inductors. In fact, from a simulation point of view, the only difference between resistors and inductors is the conductivity value of the strips. Table 1.4 collects the geometrical parameters of the simulated resistors, all of them placed on a LTCC substrate and having a meander shape. On Table 1.5, the comparison between solvers is shown. For this case, no experimental data is available.

The last component used in this comparison is a finger capacitor placed on a LTCC substrate. The main layout parameters are given in Table 1.6. Notice, on Table 1.7, that all

Table 1.5 Comparison of simulation results.

		Rdiff(Ω)	t_{comp} (51 points)
R1	PEEC	181.4	2.5s
	MoM	181.8	57s
	Sonnet	184.1	3min30
	CST	167.3	1min7s
R2	PEEC	925	1.12s
	MoM	1026	1min2s
	Sonnet	970	5min19s
	CST	735	1min6s
R3	PEEC	38.06K	5.35s
	MoM	34.17K	3min11s
	Sonnet	39.64K	3min25s
	CST	36.62K	1min57s
R4	PEEC	195.11K	5.42s
	MoM	195.76K	3min6s
	Sonnet	203.85K	6min27
	CST	146.72K	1min55s

Table 1.6 Geometrical characteristics of finger capacitors.

Devide id	No. Fingers	Length[μm]	Width[μm]	Gap[μm]
FC1	2	800	200	400
FC2	2	1000	400	200
FC3	2	1400	600	200

solvers the computation speed is between $2\times - 4\times$ faster. Compared to inductors, it is due to an increase in complexity of the PEEC solver, as it will be shown in Chapter 5.

Before finishing this section, it is important to notice that the improvement on speed and accuracy of the developed solver are accomplished through its specialization: depending on the device, the method is adapted accordingly. Nevertheless, a general purpose PEEC solver will perform quite similar to any other integral method. But this is the key point of this work: by tweaking the PEEC method, compact models can be replaced by EM models without an important speed penalty.

Table 1.7 Measured vs. simulated data.

		Cdiff(fF)	SRF(Ghz)	t_{comp} (51 points)
FC1	PEEC	209	7.91	51.27s
	MoM	205	8.36	4min15s
	Sonnet	202	9.15	2min13s
	CST	216	8.91	4min27s
	Meas	212	7.88	
FC2	PEEC	297	5.56	46.05s
	MoM	306	5.20	4min37s
	Sonnet	300	5.39	2min59s
	CST	333	5.54	3min37s
	Meas	285	5.41	
FC3	PEEC	424	4.88	46.16s
	MoM	443	4.44	5min51s
	Sonnet	426	4.88	3min23s
	CST	486	4.65	3min47s
	Meas	421	4.69	

1.6 Organisation of dissertation

The thesis is structured in six chapters. After introducing the purpose of this work, in the remaining part of this Chapter, it is explained the motivations for using the partial element equivalent circuit as the numerical framework of the developed fast solver, and the election of LTCC as the targeted technology for building the library of components. In addition, a summary of the most relevant parameters of the technologies used through this work is also collected.

The action of tranforming the description of a physical problem into a numerical form is called discretization. Instead of following the classical PEEC discretization procedure based on Galerkin method, an alternative point of view based on energy concepts is given in Chapter 2. For speeding up the computation time, three approximations are forced in the development: (i) the dismiss of the retarded potential (quasi-static approximation), then no radiation effects can be considered; (ii) the reduction of the dimension of the current density vector into only its axial component along the conductor; (iii) the infinitely thin metalstrip approximation for conductors in laminated substrates. System equations are then obtained in the form of modified nodal analysis (MNA). Here it is highlighted the role of the inductance

and capacitance partial elements. Practical programming implementation of the algorithm is described at the end of the Chapter which shows the importance on evaluating correctly the Green's function of the substrate and the construction of the geometrical mesh.

In Chapter 3, the computation of partial elements is carried out using an analytical procedure based on the development of closed-form spatial-domain Green's functions as a series expansion of image charges. With this analytical scheme, the formed system of equations is passive. Thus, solution stability is guaranteed. The method is applied to a multilayer one-dielectric problem, which encloses most of the available laminate technologies, and to a two-dielectric problem that is useful for RFIC analysis. Whereas the application of the one-dielectric Green's function solution is very effective, the two-dielectric one is computationally intensive. To overcome this difficulty, an heuristic reasoning for approching the two-dielectric problem into two one-dielectric problems is proposed. All developed expressions are compared to commercial solvers by calculating the capacitance between two metal patches placed on the substrate under study.

Arising from the meaning of the partial elements, a novel meshing algorithm is presented in Chapter 4. The simulation of high quality passives can only be achieved if a correct determination of the current density distribution inside the device is made. This computation is actually very sentitive to meshing conditions. Whereas many commercial tools use brute force techniques (e.g. a mesh refinement in all layout parts or an iterative adaptive meshing method), the path followed in this work consists in splitting the current distribution in two quasi-orthogonal mechanisms. In the one hand, the current distribution dependence along the thickness coordinate of a metalstrip is taken into account using an expression that is linked to the magnetic field generated by the self current passing through the strip. On the other hand, the dependence on the width is computed by generating a mesh that is able to sense, the influence of the remaining parts of the layout into a given metalstrip, prior to the solution of the complete model. In this way, an ab initio adapated mesh is generated using a reasonable number of cells. The method is verified using not only state-of-the-art commercial tools, but experimental data.

In Chapter 5, all developed techniques are collected in an analysis tool embedded in a circuit simulator. Device models are linked to this tool allowing the scalability in terms of geometry and substrate properties. Without any change, the same PDK can handle different LTCC tape systems and boundary conditions. All devices are verified at least using state-of-the-art tools.

To final with, the conclusions of this dissertation are presented in Chapter 6.

1.7 Selecting a numerical method framework

When dealing with the former objectives, the first concern is the selection of a correct numerical method framework. At least it should have the next requisites:

- Its integration in circuit simulators should be easy.
- Frequency and time domain description of a device must be allowed.
- It should be flexible enabling the possibility of a systematic model complexity reduction with little effort.
- It can deal with complex geometries that can use different metal layer levels.
- It must be stable (enforce passivity) and enough accurate.
- Although it is not a must, it should have a sounded circuit interpretation. With this requisite, the advantage is that the algorithm can be easily figure out as a parameter extractor.

To fullfill this requirements, it is quite tempting to use differential solvers, such as finite differences in time domain (FDTD) [25] or finite element method (FEM) [26], as they have been the power horse in computational electromagnetics. FDTD is the prefer solver for big volumes complex systems where transient response is of utmost importance. FEM can be formulated in both frequency and time domains, but it finds major applications in frequency device characterization. In addition, FEM offers the best geometry reproduction by using high-order elements. However, their most valuable characteristic for dealing with large size and complex problems, i.e. the local formulation of Maxwell's equations, is actually their drawback for a PDK development:

- The local interaction between mesh elements forces a fine mesh for keeping an accurate description of electromagnetic coupling between distant parts of the device.
- In differential solvers, primary variables are $\bar{E}$ and $\bar{H}$ or a suitable combination of their vector components. Therefore, their integration with circuit simulators, which primary variables are V and I, is difficult.
- Open boundaries need for additional modeling artifacts, such as Perfect Matched Layers (PML) in FDTD [27] or Sommerfeld boundary elements in FEM [28].
- The formulation is full-wave with no possibility to reduce the physics complexity without reformulating completely the method.

- The stability in both methods is linked to the actual ratio between large and small elements, and to the accuracy in their computed value.

Opposite to differential solvers, integral formulation establishes a link between distant parts of the model. Therefore, electromagnetic couplings are taken into account at mesh level. However, this characteristic has the drawback of generating dense matrices. In addition, it requires the knowledge of substrate Green's function. This last fact imposes a major restriction on the type of problems that can be solved, but it has the advantage that only source regions need to be meshed.

At a first glance, integral methods can be viewed as a set of specialized solvers, which can be much more interesting to the previous requirements. For instance, as far as RF and Microwave design involves the use of laminated substrates, devices in layered media are better described using integral methods. Actually, there are two methods dominating this application area: the method of moments (MoM) [29] and the Partial Element Equivalent Circuit (PEEC) [30–32]. Both are quite similar in their formal aspect because their starting point is the discretization of the Electric Field Integral Equation (EFIE). However, they differ in the way discretization is carried out. In the one hand, MoM uses the point collocation method [33] as weighting functions for the computation of matrix elements. The advantage is that elements are computed faster by avoiding one numerical integration. Although the obtained system matrix can be though as an impedance matrix, it cannot be interpreted as an actual circuit impedance matrix that could be embedded in a circuit simulator.

On the other hand, the discretization process in PEEC is based on Galerkin Method [34]. It involves an additional integral computation, compared with MoM, but the elements of the system matrix can be easily interpreted as circuit elements in the sense of a SPICE netlist. Moreover, the PEEC method can be formulated in both time and frequency domain[1]. A unique characteristic of PEEC, not found in other methods, is its systematic model complexity reduction: without too much effort, the method can be converted from full-wave, to quasi-static just by taking into account the type of circuit elements involved in the model [35]. Making a review on previous requisites, the PEEC method mostly fulfill all of them. Thus it is the numerical framework selected for the development of a fast solver for being the core of an LTCC component library.

[1]For linear elements and circuit simulators with convolution engine, it is not necessary to develop a time domain method if passivity is enforce in the model.

1.8 Selecting a carrier technology

Keeping in mind that the goal is to replace compact models with electromagnetic ones, many different technologies could be used for verifiying the solver. The reason for choosing an LTCC technology is two fold. In the one hand, it is one of the most promising technologies for developing SiP products. For being a true candidate for heterogenous integration, any technology must be highly mechanical, thermal and electromagnetical functionalized. In fact, these are the main characteristics of LTCC [36]:

- Materials can be punched or laser machined, allowing the formation of cavities and shaped preforms.
- Thermal expansion coefficient (CTE) has a good matching with integrated technologies.
- Thermal conductivity is one order of magnitude better than in organic laminates.
- Dielectric strength is over 1 KV/mil.
- Electromagnetic loss tangent, $tan\delta$, is $\sim 10^{-3}$ and relative dielectric permittivity, ε_r, ranges typically from 4 to 75.
- More than 30 interconnect levels can be stacked using both blind and through vias.
- Metal sheet resistance, based on Au and/or Ag, is normally below 5 $m\Omega$.
- It allows the inclusion of resistive, high-K and ferrite pastes; thus, resistances, capacitances and magnetic components can be embedded inside the substrate, as shown in Fig. 1.6 where the passives of a circuit have been patterned using the LTCC stack.

On the other hand, it has been possible to gain access to an LTCC process fabrication that has been provided by FAE-Francisco Albero Electrónica S.A.U. [37]. FAE is a local HTCC foundry supplier specialized in the fabrication of lambda sensors for automotion. As a long-term collaboration and thanks to their deep knowledge on ceramic material processing, an LTCC fabrication process for prototyping has been developed [36]. The main advantage in working with FAE has been the ability to change process steps, combine different LTCC tape systems materials and, more recently but outside of the scope of this thesis, to develop novel processes for co-firing magnetic materials and for exploring zero-shinkrage fabrication methods.

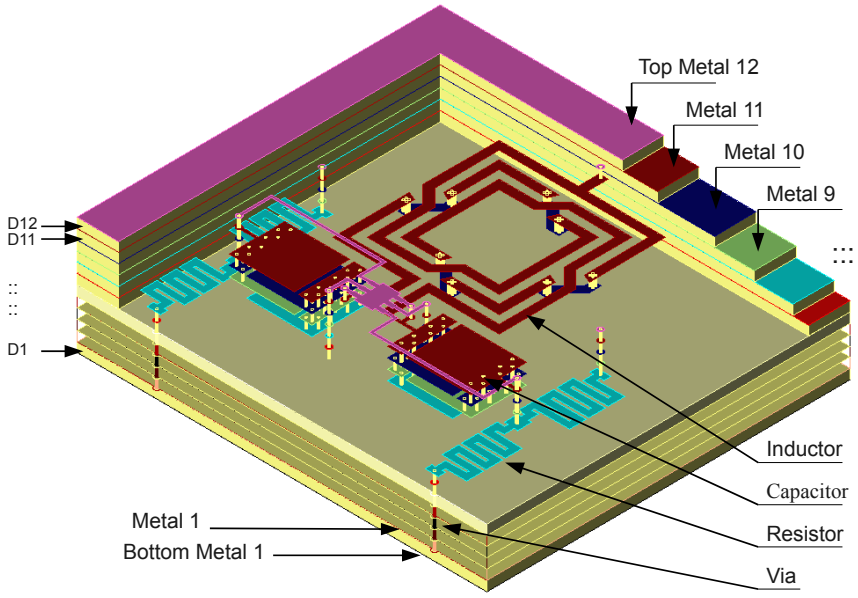

Fig. 1.6 3D section of LTCC substrate technology with embedded passives.

1.8.1 LTCC state of the art

For a better view about the possiblilies of the LTCC technology, next it is given a short review on the actual state-of-the-art in fabrication, system desing, and library development.

At the technology level, improvements have been driven by materials engineering trying to solve different challenges. The in-plane shrinkage can complicate the production of exact dimensions defining components or its geometry distortion due to metal fills [38]. Thus, zero-shrinkage methods have been developed. In materials integration, major efforts have been focused on the integration of electric controllable BST high-K tunable dielectric materials [39]. Related to power electronics, there has been also a big interest in the integration of ferromagnetic materials for shrinking the physical dimensions of high value inductors [40]. However, due to the ferromagnetic resonance phenomenon, its intended frequency application range is located below 1GHz. Another interesting technology development in LTCC is the addition of micro-electro-mechanical systems (MEMS) by using a thin film post-process module [41].

At the device level, the first steps where conducted to develop capacitors [42], film resistors [43] and inductors [44] in many flavours. The idea underneath was to provide a set of basic components that could be embedded inside the LTCC substrate. Most of these works had the inertia of planar technology and did not exploit the z-axis features. Nowadays,

via based resistors [45], stacked capacitors [46] or 3D inductors [40] are proposed to shrink system dimensions by using adequately the height of the substrate. Research related to RF-microwave systems and sub-systems (e.g. power amplifiers, mixers, transceivers) has been quite moderated. The main reason is the lack of well established design methodologies. First works about RF building blocks were targeted to power amplifiers [47]. On the transceivers field, the first SiP conception is found in [48]. The substrate is used at package level for placing a silicon tri-band receiver and SAW filters, and at functional level, for implementing 3D bandpass filters.

Concerning LTCC EDA tools, there has not been too much interest in this area. Design works at RF frequencies, mainly related to band pass filters [49], shows that the prefer design methodology is the one already depicted in Fig. 1.2 based on the intensive use of EM analysis tools, i.e., the classical SiP designing procedure [50], [23]. This is due to the high level of coupling between components that can be only extracted with physical tools. The same point of view is also found in antenna design [51]. Thus, RF/microwave LTCC designers are closer to electromagnetic engineering than to circuit design. This fact forces that design cycles are longer and designers must have an important expertise on physical tools.

Notwithstanding, some works have try to face the synthesis of circuits in LTCC [52–54]. All of them have a common point: a quasi-static partial element equivalent circuit (PEEC) method is used to make a simple model of the component/circuit. Then, optimization tools (e.g. non-linear, neural networks, aggressive space mapping, ...) are used to find the suitable layout. Here, the use of PEEC seems to be contradictory with the fact that, in most design works, the finite element method is the preferred simulation tool. Possibly, the reason for using PEEC in synthesis problems is that derived models are easily understood in terms of couplings between elements, which facilitates their physical interpretation.

1.8.2 LTCC material parameters

To final with, a summary of the properties of LTCC tape systems used in this work are collected. As shown in Table 1.8, three LTCC tape systems have been available. The number of K layers value is related to the fabricated samples used in this thesis. Stack-up of 30 layers has been demonstrated in free sintering. For zero-shrinkage, the maximum number is 12. For a description of the LTCC fabrication process, an explanation of the basic steps can be found in Appendix A.

Table 1.9, Table 1.10, and Table 1.11 shows the main mechanical, thermal and electrical parameters, respectively. They are collected here for having a reference of the material properties used through the remaining chapters of the thesis. Notice that these properties are better when compared against organic laminates.

Table 1.8 LTCC tape systems available at FAE.

Tape system	**Metals and components**	**0-shrinkage**	**Number of layers**
Ferro L8	Au, Ag, R, C, high-K	yes	12
Ferro A6S	Au	no	6
Heraeus CT702	Au, Ag, R, C, high-K	yes	12

Table 1.9 Mechanical parameters.

Parameter	**A6S**	**L8**	**CT702**
Typical Shrinkage XY (%)	15.2	13	14
Typical Shrinkage Z (%)	35	17	25
Fired density (g/cm^3)	2.5	3.1	3.1
Flexural strength (3 pt bend)	124 MPa	>275 MPa	150 MPa
Tape thickness (μm)	90-70	90	90-70
Young's modulus (GPa)	82	$\approx$ 100	$\approx$ 100

Table 1.10 Thermal parameters.

Parameter	**A6S**	**L8**	**CT702**
TCE ($25-300^oC$)	7.5 ppm/^oC	6 ppm/^oC	5.8 ppm/^oC
Thermal conductivity (W/mK)	2	>3	4.3
Specific heat (J/(kg.K))	$\approx$750	$\approx$750	$\approx$750

Table 1.11 Electrical parameters.

Parameter	**A6S**	**L8**	**CT702**
Permitivity	6.1	6.6	7.2
Loss tangent	<0.001	<0.002	<0.002
BreakDown voltage (V/mil)	>1000	>1250	>1000
Insulation resistance (Ω/cm)	$>10^{12}$	$>10^{12}$	$>10^{13}$

For component layout artwork, basic design rules are a minimum width and spacing of 200 μm for metal parts on the same layer, a via hole diameter of 150 μm and a pitch of three via diameters between non-related signal vias. A detailed design rules review is available in Appendix B as a Process Design Kit (PDK) document.

Chapter 2

A fast PEEC solver for laminated substrates

Abstract

In this chapter, the development of a fast quasi-static PEEC numerical method is presented. The algorithm is intended for being the core of an electromagnetic library of passive components that will be embedded in a circuit simulator. Starting from Maxwell's equations, the method is actually a derivation of Kirchoff's voltage and current laws. Nevertheless, instead of following Ruehli's procedure, a different point of view is taken: the goal is the evaluation of the total energy in a multiconductor system. With this approach, partial elements will be linked to the classical picture of capacitance and inductance matrices. To accelerate the computation speed of the numerical method, different assumptions and simplifications are made, heuristically justified, and, whenever possible, compared with other works. Guidelines for software implementation will be also highlighted.

2.1 The modeling hierarchy

From a designer's point of view, the modelling of analog/RF systems has the next three main requirements:

- It must relate design parameters with system performance using the physics of the device, instead of black-box models. With this scheme, it is easier to understand the importance of each parameter, the trade-offs, and the limitations of the model and/or device.

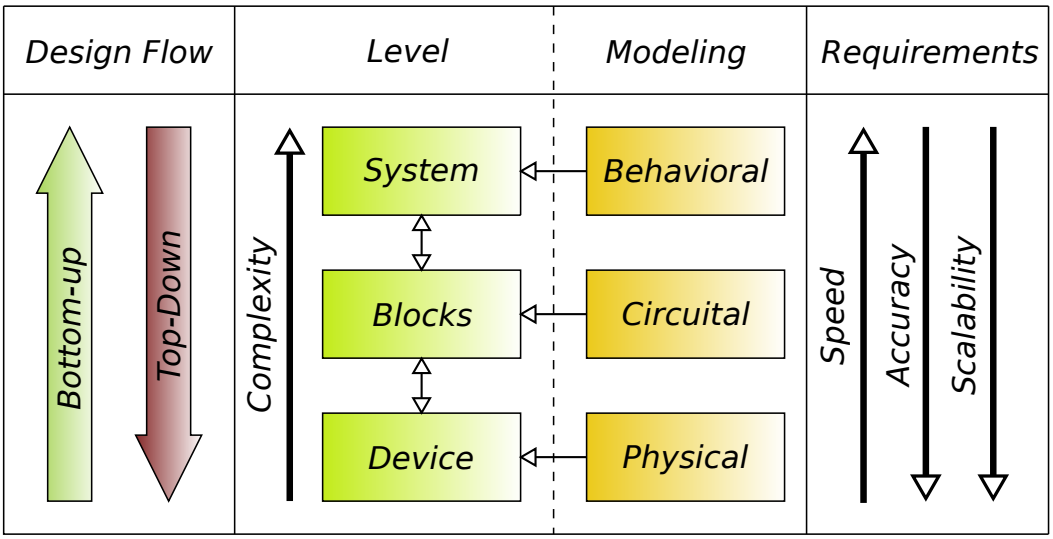

Fig. 2.1 Hierarchical modelling framework.

- Compared to experimental data, it must be accurate enough; thus, designers can rely on simulations for a proper design activity.
- It must be fast enough to allow the evaluation of different system architectures, topologies, and process yield that, normally, takes a huge amount of simulations.

A single tool cannot fulfill all these requirements. Therefore, engineers work using a hierarchical modelling framework, as shown in Fig. 2.1. At the top level, behavioral models are used for complex system description. The interaction between subsystems consists in an interchange of information/data flow without any worry about the physics of the system. Depending on the design flow, i.e. bottom-up or top-down, behavioral tools serve to assess overall system performance or as a way to translate system specifications to the lower levels of the design process.

Going down to the circuit level description, subsystems are partitioned in smaller units, named circuit blocks, having their own functionality and specs. Circuit blocks are formed by devices which are described using compact models. The main feature of compact models is that they take into account the energy/power transfer between devices or storage inside them. Thus, circuit models must obey conservation laws:

- energy conservation sets the physics of the device according to a given set of state variables, which are normally power-conjugate variables (e.g. V, I in circuit analysis).
- continuity law (charge/mass/heat flow/...) indicates the connectivity between devices.

Actually, this circuit level description is the realm of analog/RF/microwave designers. From their perspective, models are requested to be simple enough for hand calculations (thus

trade-offs are understood easily), but complex enough for obtaining accurated numerical results. Normally, this is accomplished by using compact models with different levels of description. As higher the level is, the more secondary effects it accounts for.

It would be desirable that any kind of device built in any type of technology could be modelled using analytical expressions based on its physical phenomena. However, few exceptions, linked to very simple techs and highly symmetric geometries, accept such kind of treatment. At this point, the designer enters the tough and time-consuming device modelling level. Many numerical methods are available ranging from differential to integral, time or frequency domain, fields (E, B) or mixed potentials description. The main benefits in using physical simulators are scalability (geometry and materials can be described precisely) and accuracy, but at the expense of a huge number of model unknowns which translates in a slower simulation time.

Gone so far in the description of the modelling hierarchy, it is clear that closing the gap between circuit and device modelling can make designer's life a better one. In some way, physical device modelling should be hidden inside compact models used at circuit level. Nevertheless, this process must be done keeping in mind that neither speed, accuracy or scalability performances can be compromised. This is the aim of this chapter: the development of a fast electromagnetic modelling tool that can be embedded inside a circuit simulator.

2.2 Energy and power in multiconductor systems

Passive devices fabricated in laminated substrates, as the ones shown in Fig. 2.2, can be viewed as multiconductor complex systems. In general, their description will be obtained from physical simulators. From the requirements stated in the previous section, it is important that model state variables of the device are linked to voltage and current, and their relationship must be related to the energy in the device. For these reasons, as it has been already discussed in Chapter 1, it seems that the PEEC method is a good framework for the development of fast EM modelling tool. However, prior to start this development, it is worth having a review on the energy associated to static fields in multiconductor systems. The aim of this section is to provide the designer with clear references about the meaning of capacitance and inductance partial elements. These concepts will be very useful when developing the PEEC methodology.

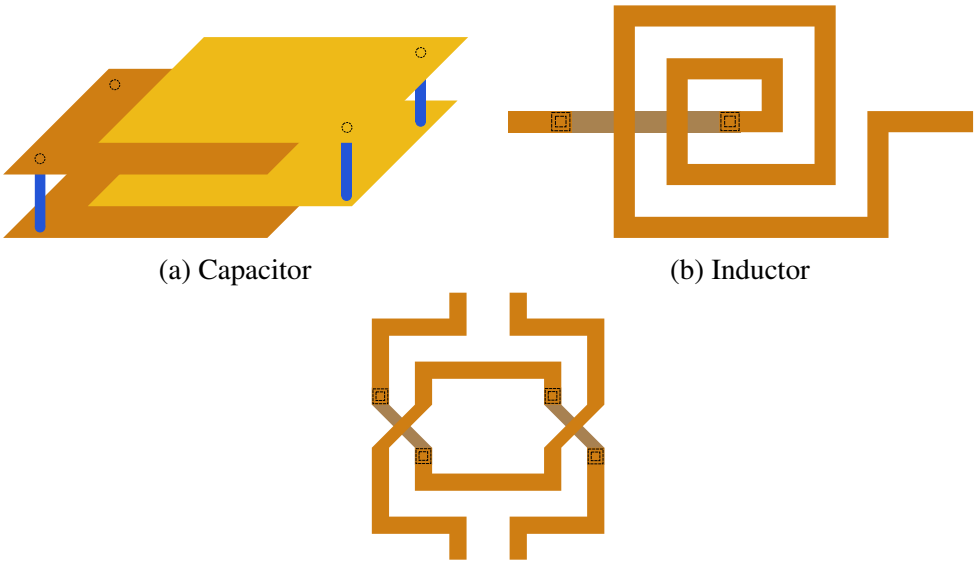

(a) Capacitor (b) Inductor

(c) Transformer

Fig. 2.2 Multiconductor based passive devices.

2.2.1 Electrostatic energy

The energy associated to an electrostatic field, W_e, in a linear media, e.g. a laminated substrate, is defined as:

$$W_e = \frac{1}{2}\int_v \bar{E}(\bar{r})\cdot\bar{D}(\bar{r})d^3r \tag{2.1}$$

where $\bar{E}$ is the electric field, $\bar{D}$ is the electric displacement field, $\bar{r}$ is the position vector and the integral extends over the volume v where both fields exist. The integrand in (2.1) has units of $[J/m^3]$; thus it can be understood as the energy density of the field. For numerical calculations, the main drawback of (2.1) is that, for unbounded fields, it extends over large volumes. Therefore, numerical artifacts, e.g. PML, must be incorporated for truncating the volume to a finite one. Nevertheless, eq. (2.1) can be cast in terms of the charge density distribution $\rho(\bar{r})$ and the scalar potential $\phi(\bar{r})$ using the fact that $\bar{E}(\bar{r}) = -\bar{\nabla}\phi(\bar{r})$ and $\bar{\nabla}\bar{D}(\bar{r}) = \rho(\bar{r})$:

$$\begin{aligned} W_e &= -\frac{1}{2}\int_v \bar{\nabla}\phi(\bar{r})\cdot\bar{D}(\bar{r})d^3r = \\ &= \left[-\frac{1}{2}\phi(\bar{r})\bar{D}(\bar{r})\right]_{\Gamma_v} + \frac{1}{2}\int_v \phi(\bar{r})\cdot\bar{\nabla}\bar{D}(\bar{r})d^3r = \\ &= \frac{1}{2}\int_v \phi(\bar{r})\rho(\bar{r})d^3r. \end{aligned} \tag{2.2}$$

Notice that the term $\left[-\frac{1}{2}\phi(\bar{r})\bar{D}(\bar{r})\right]_{\Gamma_v}$ is evaluated on the boundary of the volume, Γ_v, where $\phi(\bar{r}) \to 0$ or $D(\bar{r}) \to 0$. Now, the last integrand of (2.2) is non-zero only in the regions where charge exists, which are normally bounded in practical modelling problems.

The computation of (2.2) requires the knowledge of $\phi(\bar{r})$ due to $\rho(\bar{r})$. Using Green's function formalism, $\phi(\bar{r})$ is given by

$$\phi(\bar{r}) = \int_v G(\bar{r},\bar{r}')\rho(\bar{r}')d^3r' \tag{2.3}$$

where $G(\bar{r},\bar{r}')$ is the scalar potential at point $\bar{r}$ made by a unit point charge located at position $\bar{r}'$ inside the media of interest. Substitution of (2.3) into (2.2) yields the expression of the electrostatic energy of the system in terms of the charge density distribution:

$$W_e = \frac{1}{2}\int_v \rho(\bar{r})d^3r \int_{v'} G(\bar{r},\bar{r}')\rho(\bar{r}')d^3r'. \tag{2.4}$$

Notice that (2.4) is quite amenable for numerical computation as far as $G(\bar{r},\bar{r}')$ is known somehow. This process involves the discretization of (2.4). The $\rho(\bar{r})$ region can be divided in sufficiently small disjoint volumes, v_i, named cells, so that one can consider a constant charge density value inside each small cell $\rho_i = \frac{q_i}{v_i}$. Then, eq. (2.4) can be partitioned as

$$W_e = \frac{1}{2}\sum_i\sum_j \frac{q_i}{v_i}\frac{q_j}{v_j}\int_{v_i} d^3r \int_{v'_j} G(\bar{r},\bar{r}')d^3r'. \tag{2.5}$$

Using matrix notation, eq. (2.5) can be rewritten as

$$W_e = \frac{1}{2}\bar{q}^T[P]\bar{q} \tag{2.6}$$

where $\bar{q}$ is a column vector which entries are the charges q_i at each cell, $\bar{q}^T$ is its transpose and $[P]$ is the partial scalar potential matrix which coefficient entries are defined by:

$$P_{ij} = \frac{1}{v_i}\frac{1}{v_j}\int_{v_i} d^3\bar{r} \int_{v'_j} G(\bar{r},\bar{r}')d^3\bar{r}' \tag{2.7}$$

The meaning of P_{ij} is the measure of the potential energy value of the system formed by a uniformly distributed unit charge in cell i and another one in cell j. For this reason, in PEEC nomenclature, P_{ij} is named as partial potential coefficient. From the previous definition, it is clear that (2.6) is the total electrostatic potential (energy) due to all charges in the system. Notice that the partial potential matrix $[P]$ is symmetric because of the reciprocity of $G(\bar{r},\bar{r}')$ and it accounts for the media properties, through $G(\bar{r},\bar{r}')$, and the geometry of the device.

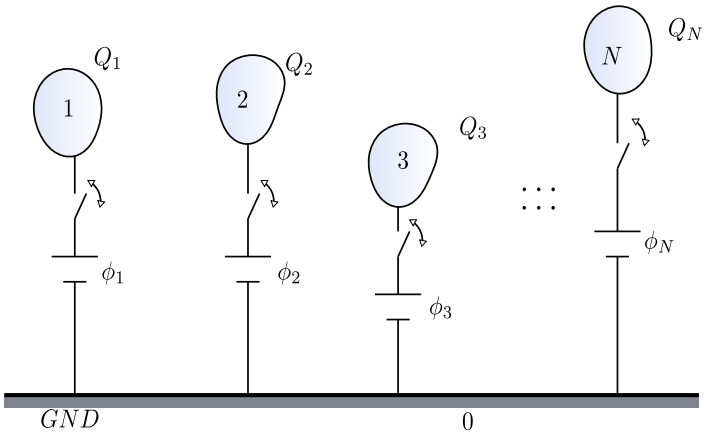

Fig. 2.3 Electrostatic multiconductor system.

2.2.2 Electrostatic energy in multiconductor system

Fig. 2.3 shows a multiconductor system formed by $N+1$ neutral conductors, all of them being at the same potential. As far as there is no electric field, the electrostatic energy of the system is null. Taking one of the conductors (e.g. conductor 0) as the ground potential reference, GND, a set of N voltage source ϕ_J, with $J = 1,2,...N$, are connected from GND to each of the remaining N conductors. Sources will drive charges between the $N+1$ conductors until the system arrives to an equilibrium where conductors have reached a ϕ_J potential value. At this point, sources are removed and an electrostatic field exists in the media.

Now, the question is how much work have been done by the sources for building the electric field. To compute this work, eq. (2.5) must be worked out because the entries of the problem are the conductor potential values ϕ_J, and not charge densities $\rho(\bar{r})$. This relationship between $\rho(\bar{r})$ and $\phi(\bar{r})$ is already stated in (2.3). Therefore, considering that conductors can be divided in small volume cells, the potential at any point of the space is rewritten as

$$\phi(\bar{r}) = \sum_j \frac{q_j}{v_j} \int_{v_j} G(\bar{r},\bar{r}')d^3r'. \tag{2.8}$$

Inside any conductor cell i, the potential ϕ_i is constant and equal to the voltage of the associated source ϕ_J (all cells belonging to conductor J will have the same potential ϕ_J). Thus, the evaluation of the mean voltage inside cell i is

$$\begin{aligned}\phi_i &= \frac{1}{v_i}\int_{v_i}\phi(\bar{r})d^3r = \sum_j \frac{1}{v_i}\frac{q_j}{v_j}\int_{v_i} d^3r \int_{v_j} G(\bar{r},\bar{r}')d^3r' \\ &= \sum_j P_{ij}\,q_j. \end{aligned} \tag{2.9}$$

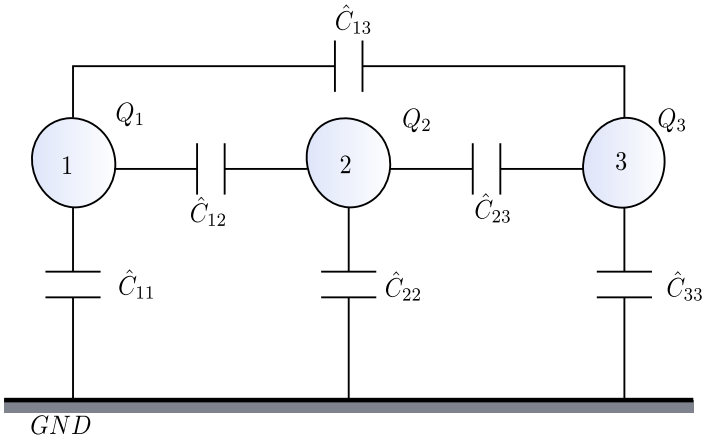

Fig. 2.4 Charge relationship between conductors in a multiconductor system.

So far, eq. (2.9) represents a transformation between ϕ_i and q_i. Using matrix formalism, it can be inverted as

$$\bar{q} = [P^{-1}]\bar{\phi}, \tag{2.10}$$

whereas the electrostatic energy can be cast as

$$W_e = \frac{1}{2}\left([P^{-1}]\bar{\phi}\right)^T [P]\left([P^{-1}]\bar{\phi}\right) = \frac{1}{2}\bar{\phi}^T\left([P^{-1}]\right)^T\bar{\phi} = \frac{1}{2}\bar{\phi}^T[P^{-1}]\bar{\phi} \tag{2.11}$$

where it has been used that $[P^{-1}] = [P^{-1}]^T$ due to symmetry. $[P^{-1}]$ is actually defined as the capacitance matrix $[C]$. Its coefficients C_{ij} represent the charge induced in cell i when all other cells are at 0 voltage except for cell j that has $1V$. In PEEC, C_{ij} is named as partial capacitance element. Care must be taken not to confuse $[C]$ with the mutual capacitance matrix $[\hat{C}]$. $[C]$ relates charges in conductors with their potentials

$$Q_i = C_{i1}V_1 + \ldots + C_{ii}V_i + \ldots + C_{iN}V_N\,, \tag{2.12}$$

whereas $\hat{C}$ relates charge in conductors with the potential difference between conductors, i.e.

$$Q_i = \hat{C}_{i1}(V_i - V_1) + \ldots + \hat{C}_{ii}(V_i - 0) + \ldots + \hat{C}_{iN}(V_i - V_N)\,. \tag{2.13}$$

This concept is illustrated in Fig. 2.4. Equating (2.12) and (2.13), the relationship between C_{ij} and $\hat{C}_{ij}$ is

$$C_{ij} = \begin{cases} \sum_{k=1}^{N}\hat{C}_{ik} & for \quad i = j \\ -\hat{C}_{ij} & for \quad i \neq j \end{cases}. \tag{2.14}$$

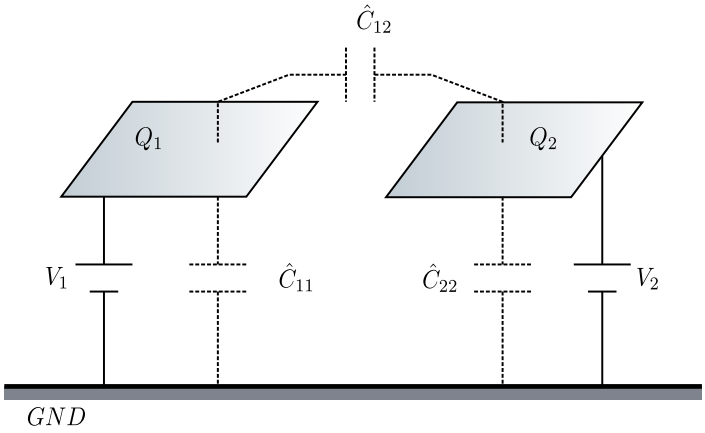

Fig. 2.5 Charge relationship between two patches.

When developing compact models, many authors use closed-form expressions for capacitances that are obtained from multiconductor transmission lines. Thus, it is important to write correctly the capacitances in terms of the nodal voltage values according to (2.14).

2.2.3 Mutual capacitance between two patches

To show the capability of the former formalism, it will be applied to the modeling of two patches placed above a ground plane, as shown in Fig. 2.5. The considered media is homogeneous, linear, and isotropic. This problem has been chosen because it will be used for verifying the analytical Green's functions expressions that will be developed in Chapter III against commercial tools.

The compact model of this system is the capacitance matrix $[C]$ that sets the relationship between (Q_1, Q_2)[1] with (V_1, V_2) as follows:

$$\begin{pmatrix} Q_1 \\ Q_2 \end{pmatrix} = \begin{pmatrix} C_{11} & C_{12} \\ C_{21} & C_{22} \end{pmatrix} \begin{pmatrix} V_1 \\ V_2 \end{pmatrix} . \tag{2.15}$$

To find $[C]$, the first step is the partitioning of the patches in smaller squares of area S_k, thus the associated surface charge density σ_k can be considered constant

$$q_k = \int_{S_k} \sigma_k ds = \sigma_k S_k . \tag{2.16}$$

[1] Using Fourier transform, $jwQ = I$.

Thereafter, as second step, $[P]$ matrix must be filled in by using the Green's function of the media, which is given by

$$G(\bar{r},\bar{r}') = \frac{1}{4\pi\varepsilon}\left(\frac{1}{|\bar{r}-\bar{r}'|} - \frac{1}{|\bar{r}-(\bar{r}')+2h\hat{z}|}\right) \tag{2.17}$$

where h is the distance between GND and any of the two patches, and ε is the permittivity of the media. The double surface integral of (2.7) has an analytical solution [55]. Once all P_{ij} are found, the third step is the formation of the algebraic system equations, which involves the knowledge of voltage sources (V_1, V_2), i.e.

$$\begin{pmatrix} V_1 \\ \vdots \\ V_1 \\ V_2 \\ \vdots \\ V_2 \end{pmatrix} = \left[P_{ij}\right] \begin{pmatrix} q_1 \\ \vdots \\ q_N \\ q_{N+1} \\ \vdots \\ q_{2N} \end{pmatrix}. \tag{2.18}$$

Notice that entries from $i = 1,...,N$ belong to patch 1, whereas the remaining $i = N+1,...2\cdot N$ are associated to patch 2. Solving q_i for $V_1 = 1$ and $V_2 = 0$, the values of C_{11} and C_{21} are found as

$$C_{11} = \left.\frac{Q_1}{V_1}\right|_{V_2=0} = \sum_{k=1}^{N} q_k \tag{2.19}$$

$$C_{21} = \left.\frac{-Q_2}{V_1}\right|_{V_2=0} = -\sum_{k=N+1}^{2N} q_k \tag{2.20}$$

in the forth step. The value of C_{22} is found by setting $V_1 = 0$ and $V_2 = 1$. Now, it is worth noting that, if the model must be used in a circuit simulator, mutual capacitances must be used, i.e.,

$$\hat{C}_{12} = \hat{C}_{21} = -C_{21} \quad ; \tag{2.21}$$

$$\hat{C}_{11} = C_{11} + C_{21} \quad ; \tag{2.22}$$

$$\hat{C}_{22} = C_{22} + C_{21} \quad . \tag{2.23}$$

2.2.4 Inductance

The concept of inductance, L, is commonly introduced as the ratio between the magnetic flux, Φ, through the area, S, and the current I defined by a current closed loop, as shown

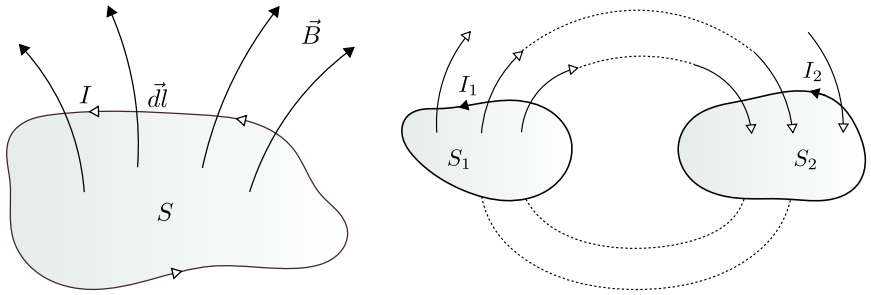

(a) autoinductance (b) mutual-inductance

Fig. 2.6 Magnetic coupling in multiconductor system.

in Fig. 2.6 for both auto-inductance and mutual-inductance cases. Taking Fig. 2.6(b) as the reference for this explanation, the flux generated by circuit I_1 traversing S_2, Φ_{21}, can be expressed in terms of the potential vector $\bar{A}_1$ as

$$\Phi_{21} = \oint_{l_2} \bar{A}_1(\bar{r}) \cdot d\bar{l}_2 \,. \tag{2.24}$$

For a linear homogeneous isotropic magnetic material, the value of $\bar{A}_1(\bar{r})$ is

$$\bar{A}_1(\bar{r}) = \frac{\mu}{4\pi} \oint_{l_1} \frac{I_1 d\bar{l}_1}{|\bar{r} - \bar{r}_1|} \,. \tag{2.25}$$

Thus, substituting (2.25) in (2.24) and making the ratio Φ_{21}/I_1, the well-known Neumann's integral formula for the mutual inductance is found:

$$L_{21} = \frac{\Phi_{21}}{I_1} = \frac{\mu}{4\pi} \oint_{l_2} \oint_{l_1} \frac{d\bar{l}_1 \cdot d\bar{l}_2}{|\bar{r}_2 - \bar{r}_1|} \,. \tag{2.26}$$

Notice that (2.26) implies a knowledge about the geometry of the loop. However, in laminated substrates, the return current path (through GND plane or substrate) is not known a priori, a fact that makes (2.26) useless for practical calculations. For this reason, other methods must be explored.

2.2.5 Magneto-static energy in multiconductor system

Fig. 2.7(a) shows a conducting region Ω where a current density distribution $\bar{J}(\bar{r})$ is circulating in. Notice that Ω is not a loop. The magnitude we are interested in is the amount of energy that has been needed for building up this current density distribution. Thanks to the duality between $\bar{E} \longrightarrow \bar{H}$ and $\bar{D} \longrightarrow \bar{B}$, the magnetic energy expression W_m is the dual of W_e,

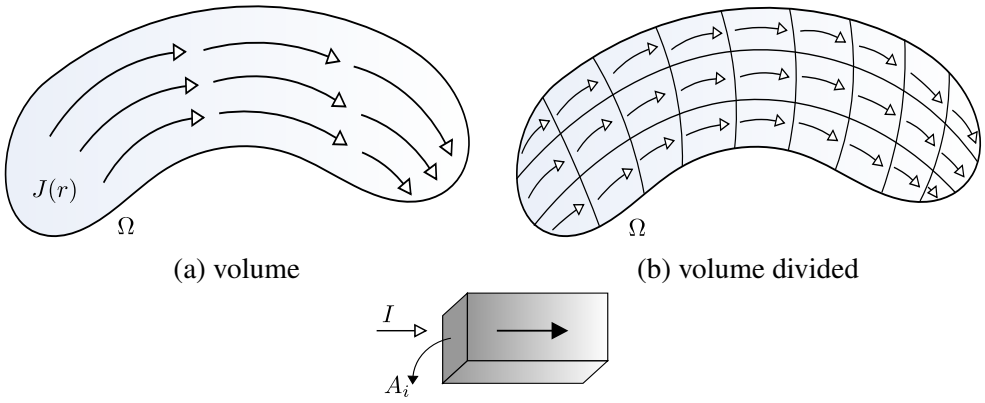

(a) volume (b) volume divided

(c) volume element

Fig. 2.7 A current distribution in a conductor volume.

eq.(2.4), i.e.,

$$W_m = \frac{1}{2}\int_v d^3r \int_{v'} d^3r' K(\bar{r},\bar{r}')\bar{J}(\bar{r})\cdot\bar{J}(\bar{r}') \tag{2.27}$$

where $K(\bar{r},\bar{r}')$ is the vector potential Green's function of the media.

For computing (2.27), the volume Ω is divided in N smaller partitions. Then, $\bar{J}(\bar{r})$ can be considered constant inside any cell, as shown in Fig. 2.7(b). An important fact to be accounted for is that the orientation of the cell k must match the $\bar{J}_k(\bar{r})$ vector. This is illustrated in Fig. 2.7(c). Thus, for a volume element, the relationship between the current I_k and the current density $\bar{J}_k(\bar{r})$ is given by

$$\bar{J}_k(\bar{r}) = \frac{I_k}{S_k}\cdot\hat{J}_k \tag{2.28}$$

where S_k is the area of the cell which vector points in the direction of the unit vector $\hat{J}_k$.

Using (2.28), W_m can be cast in the next form

$$W_m = \frac{1}{2}\sum_i^N\sum_j^N \frac{I_i}{A_i}\frac{I_j}{A_j}\int_{v_i}\int_{v'_j} K(\bar{r},\bar{r}')\hat{J}_i(\bar{r})\cdot\hat{J}_j(\bar{r}')d^3r d^3r'. \tag{2.29}$$

The quantity $\hat{J}_i(\bar{r})\cdot\hat{J}_j(\bar{r}')d^3r d^3r' \equiv da_i da'_j d\bar{l}_i\cdot d\bar{l}'_j \equiv dada'd\bar{l}\cdot d\bar{l}'$, thus

$$W_m = \frac{1}{2}\sum_{i,j}^N \frac{I_i}{A_i}\frac{I_j}{A_j}\int_{v_i}\int_{v'_j} K(\bar{r},\bar{r}')dada'd\bar{l}\cdot d\bar{l}'. \tag{2.30}$$

Eq. (2.30) can be rewritten in matrix form as

$$W_m = \frac{1}{2}\bar{I}^T[L]\bar{I} \tag{2.31}$$

where $\bar{I}$ is a column vector which entries are the currents I_i at each cell, $\bar{I}^T$ is its transpose, and $[L]$ is the inductance matrix which coefficients are defined by

$$L_{ij} = \frac{1}{A_i A_j} \int_{v_i} \int_{v'_j} K(\bar{r}, \bar{r}') da da' d\bar{l} \cdot d\bar{l}'. \tag{2.32}$$

In PEEC nomenclature, L_{ij} is known as partial inductance element[2]. For a linear homogeneous isotropic magnetic material, eq. (2.32) reads as

$$L_{ij} = \frac{1}{A_i A_j} \int_{v_i} \int_{v'_j} \frac{da da' \left[d\bar{l} \cdot d\bar{l}' \right]}{|\bar{r} - \bar{r}'|}. \tag{2.33}$$

If the section of the conductor is very small and the circuit is closed, eq. (2.33) is actually the definition of Neumann's integral (2.26). Eq. (2.32) is a rigorous expression for mutual inductance calculations without requiring the knowledge of the return current path, but $K(\bar{r}, \bar{r}')$.

2.2.6 Analytical circuit theory

In Maxwell's equations, the sources of fields are related to charge $\rho(\bar{r})$ and current $\bar{J}(\bar{r})$ density distributions. Eqs. (2.6) and (2.31) are actually the energy of the system defined by $\rho(\bar{r})$ and $\vec{J}(\bar{r})$ in a given media. This system has a set of constraints that are actually set by Kirchoff's current law, KCL. Notice that this description is equivalent to the one found in mechanical system: a set of particle distribution moving under the influence of a potential field (e.g. gravity) and forced to obey a set of constraints. Therefore, the question that arises is if is that possible to use the same mathematical formalism of analytical mechanics in circuit analysis. It can be done. In fact, this point of view can have advantages in some situations as

- in quantum computing for the definition of qubits in terms of LC circuits;
- in multiphysics problems, e.g. , electromechanical systems;
- in the investigation of new circuit solvers.

For the purpose of this thesis, we want to highlight that the PEEC method can be understood as the application of d'Alambert's principle of virtual work over and electrical circuit system [56] [3]. To better understand this statement, using (2.6) and (2.31), the Lagrangian of a circuit network is written as follows

[2] As far as P_{ij} is the *scalar* potential partial elements, L_{ij} could be named *vector* potential partial elements.
[3] Up to our knowledge, this point of view about the PEEC method has not been discussed elsewhere.

$$\mathscr{L} = W_m - W_e = \frac{1}{2}\bar{I}^T [L]\bar{I} - \frac{1}{2}\bar{q}^T [P]\bar{q} = \frac{1}{2}\bar{\dot{q}}^T [L]\bar{\dot{q}} - \bar{q}^T [P]\bar{q} \tag{2.34}$$

where $\dot{q} = \frac{dq}{dt} = I$. The Euler-Lagrange equations of motion, i.e. Kirchoff's Voltage Law, are obtained using the non-conservative equation of Hamilton's principle, i.e.

$$\frac{d}{dt}\left(\partial_{\dot{q}_i}\mathscr{L}\right) - \partial_{q_i}\mathscr{L} + \partial_{\dot{q}_i}R = \phi_i^{ext} \tag{2.35}$$

where ϕ_j^{ext} is the applied external voltage, and R is the Rayleigh dissipation factor that, for circuit analysis, is the loss due the resistive elements r_i

$$R = \frac{1}{2}\sum_i^N r_i \left(\dot{q}_i\right)^2 . \tag{2.36}$$

Therefore, after some algebra manipulation on (2.35) and using the Fourier transform $\frac{d}{dt} = j\omega$, the KVL equations are obtained as follows

$$\phi_i^{ext} = r_i I_i + j\omega \sum_j^N L_{ij} I_j + \sum_j^N P_{ij} q_j . \tag{2.37}$$

This is the discretization equation, derived in only two steps, that will be obtained when developing the PEEC method.

2.3 Development of a fast PEEC solver

The PEEC has become quite popular thanks to its flexibility allowing different kind of formulations (e.g., basic RC, quasi-static, full wave). Moreover, it shows Maxwell's equations from a circuit designer's perspective and it is easily integrated in circuit simulators [57]. In the previous section, it has been already introduced the concept of partial elements as a way to evaluate the energy of a multiconductor system. Now, the procedure will start from the mixed potential integral equation (MPIE), which can be derived from Maxwell's equations. Then its discretization will be carried out in terms of partial elements but using heuristic approximations related to the actual physics of the modelled devices, mainly inductors and transformers. In this way, the obtained numerical algorithm must be viewed as a specialized electromagnetic tool.

2.3.1 History of PEEC

The beginning of the PEEC method is linked to the computation of the auto-inductance and mutual-inductance in bus bars an multiconductor transmission lines. Actually, this kind of problem traces back to J.C. Maxwell [58] who introduced the concept of the geometric mean distance (GMD) for the calculus of components having a $\log R$ (2D) form of the media Green's function. Later, Rosa [59] and Terman [60] extended this work that was finally collected by Grover in his book "Inductance Calculations" [61]. Here, for the first time, it was shown that the inductance calculation of a conductor could be broken is smaller elements.

At the end of the sixties, driven by the IC industry for high speed electronics, there was an increasing interest on the computation of inductances for interconnects. Hoer and Love [55] extended the accuracy of Grover's method by substituting the GMD calculation by analytical integration, but only valid for Manhattan like layouts. Moreover, a study on the integration of inductors was developed by Greenhouse who made the first application of Grover's method in RFICs in 1974[62].

Nevertheless, the big impact contribution to this kind of methodology was made by A. Ruehli. He coined the term partial element equivalent circuit for referring to the actual computation of inductances. The key point was that Ruehli was looking for a formulation of Maxwell's equations in terms of circuits variables (V,I). He extended the partial element concept from magneto quasi-static formulation to full-wave, a fact that makes PEEC suitable for reduction model order complexity.

After a silent period during the eighties, the development of PEEC ramped up in the nineties thanks to the increasing performance of IC technology for radio-frequency applications. In the one hand, the lack of simulation tools stimulated the research for efficient algorithms. Based partly on PEEC, FastHenry [63] and FastCap [64] became quite popular as high frequency parasitic extraction tools, whereas ASITIC [65], developed by Niknejad, was intended for inductor and transformer RFIC design. On the other hand, PEEC modeling challenges were put on the electrically and magnetically induced losses in the substrate. Heeb and Ruehli made the effort to take into account these phenomena. In the last fifteen years, Antonini, Eckman and other authors, in collaboration with Ruehli, have widen the applicability of PEEC thanks to the introduction of non-orthogonal elements, time domain formalism, scattering, multi-physics, eddy current modeling and stability conditions. With these new features, the PEEC methodology can be applied to high speed IC and hybrid design, EMC, signal integrity, System in Package design, or power electronics among others.

2.3.2 Mixed potential integral equation

The starting point is the representation of the electric field in terms of the scalar and vector potentials,

$$\bar{E}(\bar{r},t) = -\partial_t \bar{A}(\bar{r},t) - \bar{\nabla}\phi(\bar{r},t) \tag{2.38}$$

that arises form Faraday's law, $\bar{\nabla} \times \bar{E} = -\partial_t \bar{B}$, where $\bar{B}$ has been replaced by $\bar{\nabla} \times \bar{A}$ and noting that the quantity $\bar{E} + \partial_t \bar{A}$ is in fact the minus gradient of the scalar field.

In the conductor region of a planar component, the current density $\bar{J}(\bar{r})$ and the total electric field $\bar{E}_T = \bar{E} + \bar{E}_s$ ($\bar{E}_s$ accounts for other electromotrice forces) are related through the constitutive Ohm's law

$$\bar{E}(\bar{r}) = \frac{\bar{J}(\bar{r})}{\sigma(\bar{r})} \tag{2.39}$$

where $\sigma(\bar{r})$ is the conductivity of the metal region. For the targeted technologies of this study, $\sigma(\bar{r})$ is considered linear, homogeneous and isotropic for any given conductor, but temperature dependent. Substitution of (2.39) in (2.38) and using the representation of $\bar{A}(\bar{r},t)$ and $\phi(\bar{r},t)$ in terms of their respective Green's functions,

$$\bar{A}(\bar{r},t) = \int_v K(\bar{r},\bar{r}')\bar{J}(\bar{r}',t')d^3r' \tag{2.40}$$

and

$$\phi(\bar{r},t) = \int_v G(\bar{r},\bar{r}')\rho(\bar{r}',t')d^3r', \tag{2.41}$$

the mixed potential integral equation

$$\bar{E}_s(\bar{r},t) = \frac{\bar{J}(\bar{r},t)}{\sigma(\bar{r})} + \partial_t \int_{v'} K(\bar{r},\bar{r}')\bar{J}(\bar{r}',t')dv' + \bar{\nabla}\int_{v'} G(\bar{r},\bar{r}')\rho(\bar{r}',t')d^3r' \tag{2.42}$$

arises, which is the actual starting point of the PEEC numerical method. Notice that (2.42) only contains sources $\bar{J}(\bar{r},t)$ and $\rho(\bar{r},t)$ as unknowns. In (2.42), $\bar{r}$ stands for the point of the space where the action of the field is being measured, $\bar{r}'$ is the coordinate of sources, t is the actual time and t' is the retarded time, i.e. $t' = t - \frac{|r-r'|}{c}$ where c is the speed of light.

The first assumption in this development towards an specialized tool is to dismiss the effect of any retarded time, thus $t = t'$. Of course, this trial imposes a limitation on the maximum frequency at which the component can be simulated, but normally it is beyond

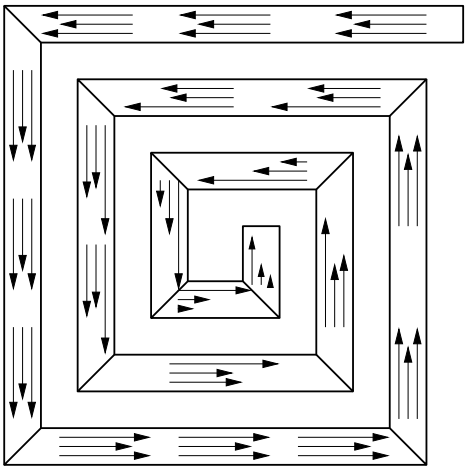

Fig. 2.8 Typical current distribution in metal strips of a spiral inductor.

its self resonant frequency [4]. For instance, a $350 \times 350 \mu m^2$ inductor on a silicon substrate will exhibit a characteristic maximum retarded time about $\sqrt{2} \cdot 350 \mu m \cdot \sqrt{\varepsilon_{Si}}/c \simeq 5.7 ps$, which is translated into a maximum simulation frequency of $20 GHz$. With this approach, the formalism has been converted from full-wave to quasi-static. (A more detailed study on the performance of quasi-static solvers can be found in [66].) Now, eq. (2.42) can be written as

$$\bar{E}_s(\bar{r},t) = \frac{\bar{J}(\bar{r},t)}{\sigma} + \partial_t \int_{v'} \bar{K}(\bar{r},\bar{r}')\bar{J}(\bar{r}',t)d^3r' + \nabla_r \int_{v'} \bar{G}(\bar{r},\bar{r}')\rho(\bar{r}',t)d^3r' . \tag{2.43}$$

This is a vector equation defined in the three directions of the space. Nevertheless, it can be reduced from 3D to 1D by taking the next assumption: the main component of the current density vector $\bar{J}$ inside a conductor (a cell in the model) points in the direction of the voltage gradient evaluated at DC. The unit vector in this direction of the space is named $\hat{J}_{DC}$[5] and sets the length direction of the conductor. As shown in Fig. 2.8, this approximation means that it is only necessary to establish one component for $\bar{J}(\bar{r},t)$ along its conductor length. Although this kind of approach has been previously used in [67], the definition given above is much more powerful because it allows to determine what kind of planar devices can be modeled using this strategy[6]. Keep in mind that (2.43) has not been reduced to a scalar equation, but to a vector equation where it is already known the orientation of $\bar{J}(\bar{r},t)$ at the conductor regions.

[4] In fact, the accuracy of this approximation depends on the compactness of the device. A transmission line component is the worst situation for this approach.

[5] In Chapter 4, *Meshing strategies*, a more rigorous definition of $\hat{J}_{DC}$ will be given.

[6] Gap components can still modelled using this definition as far as the dielectric part is considered as a very high resistivity material at DC. This point will be highlighted when developing the model for a finger capacitor in Chapter 5.

2.3.3 Discretization of MPIE

Eq. (2.43) can be spatially discretized into a mesh of disjoint cells small enough thus charge and current densities can be assumed constant. To take into account the previous consideration about $\bar{J}$ direction, current cells must be aligned with $\hat{J}_{DC}$. Then, $\bar{J}(\bar{r},t)$ is approximated as

$$\bar{J}(\bar{r},t) = \sum_{k=1}^{M} J_k(t)\,\psi_k(\bar{r})\hat{J}_k^{DC} \tag{2.44}$$

where $J_k(t)$ are the coefficients of the expansion which values represent the current density inside each cell k; $\psi_k(\bar{r})$ are the basis expansion functions; $\hat{J}_k^{DC}$ is the unitary vector pointing in the length of cell k; and M is the total number of current cells. In PEEC, $\psi_k(\bar{r})$ is defined as

$$\psi_k(\bar{r}) = \begin{cases} 1 & \bar{r} \in cell_k \\ 0 & \bar{r} \notin cell_k \end{cases} \tag{2.45}$$

thus $\psi_k(\bar{r})$ has support only inside the cell k. The charge density can also be developed in a similar expansion

$$\rho(\bar{r},t) = \sum_{k'=1}^{N} \rho_{k'}(t)\Theta_{k'}(\bar{r}) \tag{2.46}$$

where $\rho_{k'}(t)$ is the charge density inside cell k', $\Theta_{k'}(\bar{r})$ is the basis function with support into the cell; and N is the total number of charge density cells. Notice that $\Theta_{k'}(\bar{r})$ and $\psi_k(\bar{r})$ are different basis functions, i.e., there is a different mesh for currents and for charges. Substitution of (2.44) and (2.46) into (2.43) sets the next equation:

$$\bar{E}_s(\bar{r},t) = \sum_{k=1}^{M} \frac{1}{\sigma_k} J_k(t)\,\psi_k(\bar{r})\hat{J}_k^{DC} + \partial_t \sum_{k=1}^{M} J_k(t)\hat{J}_k^{DC} \int_{v'} K(\bar{r},\bar{r}')\,\psi_k(\bar{r}) d^3r' + \\ + \sum_{k'=1}^{N} \rho_{k'}(t)\bar{\nabla}_r \int_{v'} G(\bar{r},\bar{r}')\Theta_{k'}(\bar{r}) d^3r'. \tag{2.47}$$

The integrals in (2.47) can be computed if K and G are given, either numerically or analytically. To obtain a numerical solution, a further step must be done for converting (2.47) into a set of algebraic expressions. The normal procedure, which was derived by Ruehli in its seminal work [30], is to apply Galerkin's method to (2.47) using as weighting functions the same basis functions ψ_k and $\Theta_{k'}$. Instead of, d'Alembert's principle will be applied here. Thus it is necessary to calculate the work δW done by all terms in (2.47) over a virtual

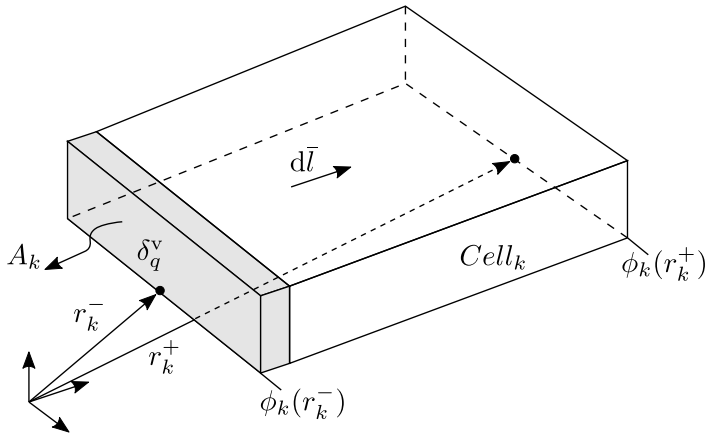

Fig. 2.9 Cell k with a virtual test unit charge ρ_{vq} crossing the cell in the direction dl.

infinitesimal charge δq_k^{v} that is translated from the input surface, located at $\bar{r}^-$, to the output surface, at $\bar{r}^+$, of the cell k[7]. This concept is illustrated in Fig. 2.9.

Before starting with this analysis, three remarks must be made.

- First, remember that the cell is oriented according to $\hat{J}^{DC}$; thus, the volume element is given by $d^3r = \mathrm{d}\bar{a} \cdot \mathrm{d}\bar{l} = \mathrm{da\,dl}$.
- Second, the virtual charge δq_k^{v} is supposed to be uniformly distributed in the volume of cell (A_k plane $\perp \hat{J}^{DC}$) of the cell; therefore δq_k^{v} is represented by a volume charge density defined as

$$\delta\rho_k^{\mathrm{v}} = \frac{\delta q_k^{\mathrm{v}}}{A_k \cdot l_k} \longrightarrow \int_{l_k}\int_{A_k} \rho_k^{\mathrm{v}}\,\mathrm{da}_k \cdot \mathrm{dl}_k = \rho_k^{\mathrm{v}} \int_{\mathrm{v}_k} d\mathrm{v} = \delta q_k^{\mathrm{v}}\,. \tag{2.48}$$

- Last, δq_{v} can be assumed to set a virtual current $I_k^{\delta q_{\mathrm{v}}}$ given by

$$\delta I_k^{\mathrm{v}} \equiv I_k^{\delta q_k^{\mathrm{v}}} = \frac{\delta q_k^{\mathrm{v}}}{\delta t} = J_k^{\delta q_k^{\mathrm{v}}} \cdot A_k \tag{2.49}$$

Virtual work due to E_s

By definition of the work exerted by a forced, the next expression must be integrated to obtain the work done by the external electromotrice field $\bar{E}_s$

[7] If the cell is enough small, this displacement is infinitesimal.

$$\delta W_k^s \equiv \int_{\bar{r}_k^-}^{\bar{r}_k^+} \bar{E}_s \cdot \delta q_k^{\mathrm{v}} \, \mathrm{d}\bar{\mathrm{l}} = \delta q_k^{\mathrm{v}} \int_{\bar{r}_k^-}^{\bar{r}_k^+} \bar{E}_S \, \mathrm{d}\bar{\mathrm{l}} = \delta q_k^{\mathrm{v}} \bar{E}_S \triangle \bar{r}_k =$$
$$= E_s \cdot l_k \cdot \delta q_k^{\mathrm{v}} \Rightarrow \frac{\delta W_k^s}{\delta q_k^{\mathrm{v}}} = V_k^s \tag{2.50}$$

where V_k^s is the value of the equivalent voltage source at cell k associated to the external field $\bar{E}_S$.

Energy loss

Using the previous definition, the work done by the first term on right hand of (2.47) is given by

$$\delta W_k^{loss} = \int_{\bar{r}_k^-}^{\bar{r}_k^+} \delta q_k^{\mathrm{v}} \cdot \frac{J_k(t)}{\sigma_k} \cdot \mathrm{dl} \tag{2.51}$$

By introducing the quantity $\delta t/\delta t$, where δt is the time employed by δq_k^{v} for passing through the cell k, eq. (2.51) can be arranged as

$$\delta W_k^{loss} = \int_{\bar{r}_k^-}^{\bar{r}_k^+} \frac{\delta q_k^{\mathrm{v}}}{\delta t} \cdot \frac{J_k(t)}{\sigma_k} \cdot \mathrm{d}\bar{\mathrm{l}} \, \delta t \tag{2.52}$$

Now, notice that $\delta q_k^{\mathrm{v}}/\delta t$ is δI_k^{v}, $\bar{J}_k(t) \parallel \mathrm{d}\bar{\mathrm{l}}$, and $J_k(t) = I_k(t)/A_k$. Therefore, the energy loss is given by

$$\delta W_k^{loss} = \delta t \cdot \delta I_k^{\mathrm{v}} \cdot I_k(t) \cdot \frac{l_k}{\sigma_k A_k} \cdot \tag{2.53}$$

$l_k/\sigma_k A_k$ is quickly recognized as the resistance value of cell k, called the partial equivalent resistor R_k. The product of $I_k \cdot R_k \equiv V_{R_k}$ is actually the voltage drop due to this resistor; thus $\delta I_k^{\mathrm{v}} \cdot V_{R_k} \equiv P_{loss}^{\delta I_k}$ is the power loss associated to the current δI_k^{v}. Finally, it is clear that the power loss times δt is the actual energy loss due to the displacement of δq_k^{v} inside cell k. Thus, the associated voltage is

$$V_k^R \equiv \frac{\delta W_k^{loss}}{\delta q_k^{\mathrm{v}}} = \frac{\delta W_k^{loss}}{\delta t \, \delta I_k^{\mathrm{v}}} = V_{R_k} = I_k(t) \cdot R_k \tag{2.54}$$

A subtle remark must be made on (2.53). Notice that δI_k^{v} does not contribute to the voltage drop across the resistance partial element. Keep in mind that the idea of a virtual charge for

computing the energy of the system should not change the 'forces' on the system (δq_k^{v} can be made as small as needed).

Magnetic energy

The evaluation of the second term reads as

$$\delta W_k^m \equiv \int_{\bar{r}_k^-}^{\bar{r}_k^+} dl \left(\delta q_k^{\mathrm{v}} \, \partial_t \sum_{l=1}^{M} J_l(t) \int_{\mathrm{v}_l'} K(\bar{r},\bar{r}') \psi_l(\bar{r}') d^3 r' \right), \tag{2.55}$$

which can be set in the next form:

$$\begin{aligned}
\delta W_k^m &= \sum_{l=1}^{M} \frac{\partial_t I_l(t)}{A_l} \int_{\bar{r}_k^-}^{\bar{r}_k^+} dl \, \delta q_k^{\mathrm{v}} \int_{\mathrm{v}_l'} K(\bar{r},\bar{r}') d^3 r' = \\
&= \sum_{l=1}^{M} \frac{\partial_t I_l(t) \delta I_k^{\mathrm{v}}}{A_l A_k} \cdot \delta t \, A_k \int_{\bar{r}_k^-}^{\bar{r}_k^+} dl \, \mathrm{da}_k \int_{\mathrm{v}_l'} \bar{K}(\bar{r},\bar{r}') d^3 r' = \\
&= \sum_{l=1}^{M} \partial_t I_l(t) \cdot \delta I_k^{\mathrm{v}} \cdot \delta t \frac{1}{A_l A_k} \cdot \int_{\mathrm{v}_k} d^3 r \int_{\mathrm{v}_l'} \bar{K}(\bar{r},\bar{r}') d^3 r' = \\
&= \sum_{l=1}^{M} \partial_t I_l(t) \cdot \delta I_k^{\mathrm{v}} \cdot \delta t \cdot L_{kl} \, .
\end{aligned} \tag{2.56}$$

Thus, the value of the associated potential $\delta W_k^m / \delta_t \, \delta I_k^{\mathrm{v}}$ is

$$V_k^m = \frac{\delta W_k^m}{\delta_t \, \delta I_k^{\mathrm{v}}} = \sum_{l=1}^{M} L_{kl} \, \partial_t \, I_l(t) \, . \tag{2.57}$$

The term L_{kl} is the definition already found in (2.28) and it is a partial inductance element. Clearly, $L_{kl} \, \partial_t \, I_l$ is contribution on the voltage due to the mutual magnetic coupling between all cells, including the self term L_{kk}.

Electric energy

The evaluation of the last term is related to the electrical energy associated to its conservative part, δW_k^e. Its expression is given by

$$\delta W_k^e = \int_{\bar{r}_k^-}^{\bar{r}_k^+} dl \, \delta q_k^{\mathrm{v}} \cdot \sum_{l=1}^{N} \rho_l(t) \cdot \bar{\nabla}_r \int_{\mathrm{v}'} G(\bar{r},\bar{r}') \, \Theta_l(\bar{r}') \, d^3 r' \tag{2.58}$$

Assuming that the metalization is very thin compared to the minimum width and separation between metal regions, a fact that is common in most laminate technologies, the charge

density can be considered as a surface one. Noticing that Θ_l is only defined in $cell_l$, δW_k^e is transformed to

$$\delta W_k^e = \sum_{l=1}^{N} \delta q_k^{\mathrm{v}} \sigma_l(t) \int_{\bar{r}_k^-}^{\bar{r}_k^+} dl \; \bar{\nabla}_r \int_{S_l'} G(\bar{r},\bar{r}')\, \Theta_l(\bar{r}')\, dl'\, dw' \tag{2.59}$$

where dw' is a differential length element along the width of the metal cell. To evaluate the double integral in (2.59), first it will be performed the integration on dl. Notice that using the definition of a definite integral, i.e.

$$F(b) - F(a) = \int_a^b F'(r) dr\,, \tag{2.60}$$

eq. (2.59) can be rearranged as

$$\delta W_k^e = \sum_{l=1}^{N} \delta q_k^{\mathrm{v}} \sigma_l(t) \int_{S_l'} \left[G(\bar{r}^+,\bar{r}') - G(\bar{r}^-,\bar{r}') \right] dl'\, dw'\,. \tag{2.61}$$

The quantity $\sigma_l(t) \int_{S_l'} G(\bar{r}^+,\bar{r}')\, ds'$ is the definition of the scalar potential contribution of the surface charge density σ_l in the position r^+ $\phi_l(r_k')$. When all contributions are added, this value is the electric potential related to the charge distribution in the system, i,e. $\phi_l(r_k^+)$. The same holds for $\phi_l(r_k^-)$. Therefore, the associated scalar voltage drop across the cell is

$$\frac{\delta W_k^e}{\delta q_k^{\mathrm{v}}} = \phi(\bar{r}_k^+, t) - \phi(\bar{r}_k^-, t). \tag{2.62}$$

Application of d'Alembert's principle: Kirchoff's voltage law

From and electrical point of view, d'Alembert's principle states that the total work done by generalized forces (i.e. voltage drop due to electric and magnetic field) over a virtual displacement of the generalized coordinates (e.g. δq_k in our case) is zero, i.e.

$$\delta W = \sum_i \delta W_i = \sum V_i \delta q_i = 0 \tag{2.63}$$

External forces and friction forces which are linear with velocity (i.e. ohmic materials) can also be added inside this definition, as it has been seen in Section 2.2.6.

Taking the results form (2.50), (2.54), (2.57), and (2.62), the application of d'Alembert's principle gives the next result

$$V_k^s = V_k^R + V_k^m + \phi(r_k^+) - \phi(r_k^-) \tag{2.64}$$

which is, in fact, Kirchoff's voltage law applied to cell k. Eq. (2.64) is the numerical discretization of (2.43). Thus, as k runs from 1 to M, a set of M equations are obtained from (2.64). By substituting the values of V_k^R and V_k^m in (2.64), which lead to

$$V_k^s = R_k I_k + \sum_l^M \partial_t I_l L_{kl} + \phi(r_k^+) - \phi(r_k^-), \tag{2.65}$$

it is shown that (2.65) sets a relationship between the cells related to unknown currents[8].

There is still the need to find out a set of N equations related to the approximation of the charge density (2.46). This will be obtained next through the constraint between current and charges dictated by the continuity equation. A final remark to be made on (2.65) is that it can be written as well in its harmonic form:

$$V_k^s(\omega) = R_k I_k(\omega) + j\omega \sum_l^M L_{kl}\, I_l(\omega) + \phi(r_k^+, \omega) - \phi(r_k^-, \omega) \tag{2.66}$$

where ω stands for the angular frequency. Thus, the PEEC formalism is easily translated from time domain to frequency domain.

2.3.4 Assembling law

The remaining N equations for charge unknowns are set by using the continuity equation

$$\bar{\nabla}\bar{J}(\bar{r}) + \partial_t \rho(\bar{r}) = 0 \Rightarrow \oint_S \bar{J}(\bar{r}) ds = -\int_{V_{in}} \partial_t \rho(\bar{r})\, d^3 r\,, \tag{2.67}$$

that must be applied to each charge density cell k of the model, as shown in Fig. 2.10. The currents flowing in and out of the boundary surface S_k of charge cell k are associated to its neighbour current cells. Therefore, a correct choice for both charge and current meshes is that they must be intercalated. In addition to that currents, there can be an external current source, I_k^s, connected to charge cell k. The application of (2.67) to cell k sets another algebraic equation

$$-I_{s_k} + \sum_i^K J_i^{(k)}(t)\, S_i^{(k)} + \partial_t \rho_k(t)\, v_k = 0 \tag{2.68}$$

where K is the number of current cells that crosses the boundary S_k, and v_k is the volume of the cell k. Taking into account that $J \cdot S = I$ and $\rho \cdot v = q$, it can be cast as

[8] In Section 2.2.6, the same result was derived from Hamilton's principle of least action.

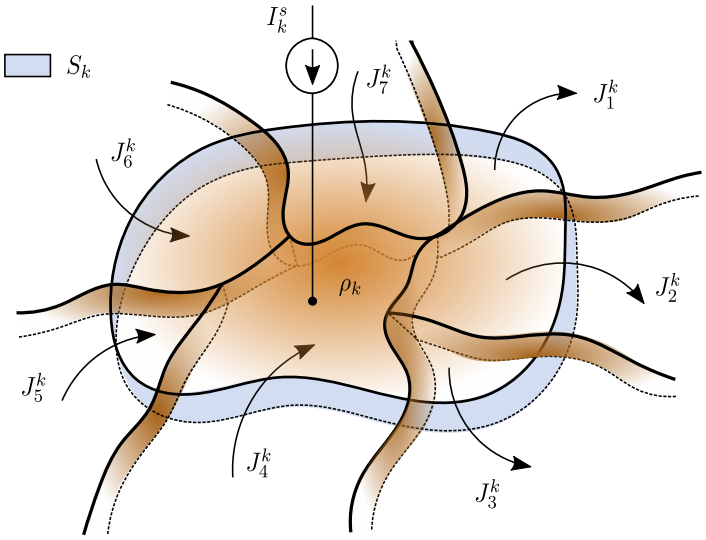

Fig. 2.10 Charge and current densities through cell k boundary surface S_k .

$$-I_{s_k}+\sum_{i}^{K} I_i^{(k)}+\frac{d}{dt}q_k=0\,. \tag{2.69}$$

Now, the currents associated to current cells can leave or enter the charge cell. Thus the terms in (2.69) can be reordered as follows

$$I_{s_k}=j\omega\, q_k+\sum_{i}^{N_{OUT_k}} I_i^{OUT_k}-\sum_{i}^{N_{IN_k}} I_i^{IN_k} \tag{2.70}$$

where N_{OUT_k} and N_{IN_k} are the total number of currents entering and leaving the cell. In (2.70), it has been used the harmonic form by changing $d/dt \rightarrow j\omega$. Notice that (2.70) is Kirchoff's current law, where the term dq_k/dt is related to the displacement current that enters in the cell. The index k runs over all charge cells. Therefore, a total of N algebraic equations are obtained. A further remark on (2.70) is that it sets the connectivity between both current and charge meshes defined by (2.44) and (2.46).

Eqs. (2.66) and (2.70) are the complete system of algebraic equations that describes numerically the behavior of the metal regions forming the component. Be aware that the unknowns in (2.66) are the currents I_k and scalar potentials $\phi(r_k^+)$, $\phi(r_k^-)$ whereas, in (2.70), they are the currents I_k and charges q_k. Therefore, it is necessary to establish a connection between scalar potentials, measured at the edges of current cells, and charges located inside charge cells. To perform this relationship, the best choice is to align the edges of currents cells with the centers of charge cells, thus the scalar potential of a charge cell is aligned with the edge of its neighbors current cells, where $\phi(r_k^+)$, $\phi(r_k^-)$ are evaluated. This idea is

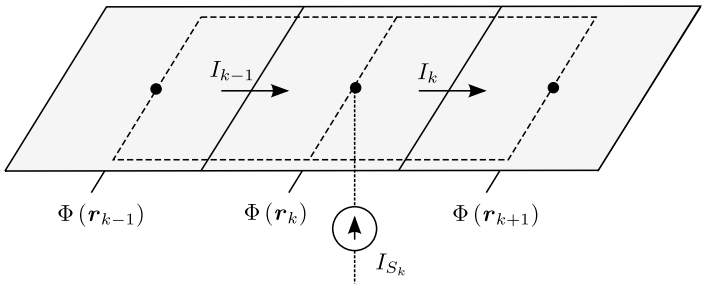

Fig. 2.11 Metal strip subdivided into three charge cells (solid line) and two current cells (dashed line). The black dots are actual circuit nodes.

shown in Fig. 2.11. Recalling (2.10), q_k can be expressed as a linear combination of scalar potentials

$$q_k = \sum_{l=1}^{N} P_{kl}^{-1}\,\phi(\bar{r}_l) = \sum_{l=1}^{N} C_{kl}\,\phi(\bar{r}_l) \tag{2.71}$$

where C_{kl} are the partial capacitance elements. Finally, the complete set of equations is given by

$$V_k^s = R_k I_k + j\omega \sum_{l}^{M} L_{kl}\, I_l + \phi(r_k^+) - \phi(r_k^-) \tag{2.72}$$

$$I_k^s = j\omega \sum_{l=1}^{N} C_{kl}\,\phi(r_l) + \sum_{m=1}^{N_{OUT_k}} I_m^{OUT_k} - \sum_{m=1}^{N_{IN_k}} I_m^{IN_k}\,. \tag{2.73}$$

It can be written in matrix form as

$$\begin{bmatrix} \bar{V}^s \\ \bar{I}^s \end{bmatrix} = \begin{bmatrix} \bar{\bar{R}}^s + j\omega\bar{\bar{L}} & D^T \\ D & j\omega\bar{\bar{C}} \end{bmatrix} \begin{bmatrix} \bar{I} \\ \bar{\phi} \end{bmatrix} \tag{2.74}$$

where $\bar{I}$ and $\bar{\phi}$ are the unknown current and voltage vector, $\bar{\bar{R}}$ is a diagonal matrix with R_k entries, $\bar{\bar{L}}$ is the partial inductance matrix, $\bar{\bar{C}}$ is the partial capacitance matrix, $\bar{\bar{D}}^T$ is the transpose of $\bar{\bar{D}}$ that describes the connection between nodes of the different branch elements, and $\bar{V}^s$ and $\bar{I}^s$ are the external voltage and current vector sources.

2.4 Implementation of PEEC method

2.4.1 General considerations

When implementing the numerical method, aside from selecting a correct linear algebra solver or using parallelization techniques, many other decisions must be taken on (2.74) to speed up its computation. The most remarkable are the next ones.

- How many M-current and N-charge cells are required for achieving an accurate solution?

  Taking into account that the employed time for solving (2.74) is $\mathrm{O}[(N+M)^2]$, an excessive number of cells for guaranteeing accuracy has a hughe penalty on speed. As it will be shown in Chapter 4, the challenge is to generate a mesh that is not only layout but physics aware. Then, mesh density can be selectively augmented in the areas of maximum variation of current/charge using a quantitative criteria.

- Which technique should be selected for computing Green's function $K(\bar{r},\bar{r}')$ and $G(\bar{r},\bar{r}')$?

  This is not a minor question. Nowadays, the preferred implementation in commercial softwares is to find their solution in the spectral domain and then convert them back to the spatial domain by using any fast transform technique (e.g. FFT). The problem of this anti-transform is that the spectral solution can have a big number of poles and branch-cuts in the complex plane that makes its evaluation quite difficult in terms of convergence and stability. This question will be addressed in Chapter 3 where an analytical procedure, instead of a numerical one, will be developed.

- How the double volume integral of partial elements P_{ij} and L_{ij}, eqs. (2.7) and (2.32), should be performed?

  After the meshing and the computation of Green's functions, this is the third source of error of the numerical method. A bad accuracy in its computation leads, once again, to instabilities that are normally related to the lack of passivity of the system matrix (2.74). This problem can be alleviated by considering the fact that the ratio of the width of metal strips vs. its thickness is bigger than 1 in laminated substrates. Then, volume integrals (2.7) and (2.32) can be casted as a double surface integral where the thickness dimension has been collapsed to an infinitely thin sheet approximation, i.e.,

$$P_{ij} = \frac{1}{a_i a_j} \int_{a_i} ds \int_{a_j} dS'\, G(\bar{r},\bar{r}') \tag{2.75}$$

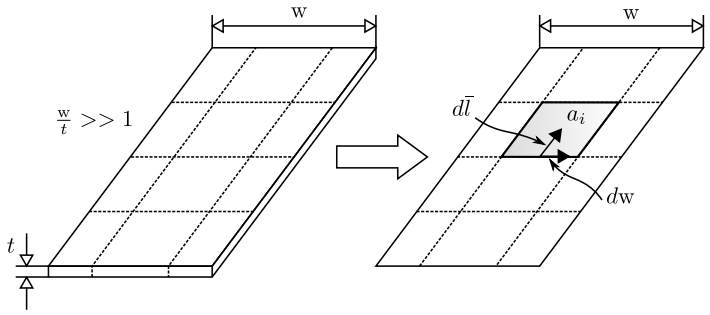

Fig. 2.12 An infinitesimal length element.

$$L_{ij} = \frac{1}{w_i w_j} \int_{a_i} \int_{a_j} G(\bar{r}, \bar{r}')\, dw_i \cdot dw'_j \left[d\bar{l}_i \cdot d\bar{l}'_j \right] \tag{2.76}$$

where $a_i(a_j)$ is the surface of the strip, $w_i(w_j)$ is its width, and $d\bar{l}_i$ is an infinitesimal length element, as shown in Fig.2.12.

Of course, this approximation demands, in addition, that the ratio of the spacing between metal parts vs. metal thickness is also bigger than 1. Otherwise, effects due to metal side walls proximity become important. With this approximation, the value of the sheet resistance of the metal strip is dependent on frequency due to the skin effect. This part will be deeply discussed in Chapter 4 and a simple method to calculate its value will be devised.

With this scheme, although the complexity in the calculation of P_{ij} and L_{ij} has been reduced, one has still to select the most suitable integration method. For enabling a fast algorithm implementation, analytical integration is the best option. This can be accomplished for rectangular shapes as it will be discussed in Chapter 3.

- How should non-Manhattan layout be treated?

  Fig.2.13 shows a component with a non-rectangular shape. In PEEC, the preferred meshing procedure is to approximate arcs with trapezoidal shapes following the $\hat{J}_{DC}$ path. For this case, the evaluation of P_{ij}/L_{ij} cannot be done analytically because cell pairs can be oriented out of 0° or 90°. Therefore, non-orthogonal numerical methods must be employed. However, this kind of problems will not be treated in this work and layout will be restricted to Manhattan-like. Even for these selected layouts, the meshing of 90° corners must be done carefully. From the accumulated experience, the best choice is the one illustrated in Fig.2.14. Notice that horizontal and vertical current cells are overlapped at their intersection. In fact, this picture is quite close to a true 2D mesh.

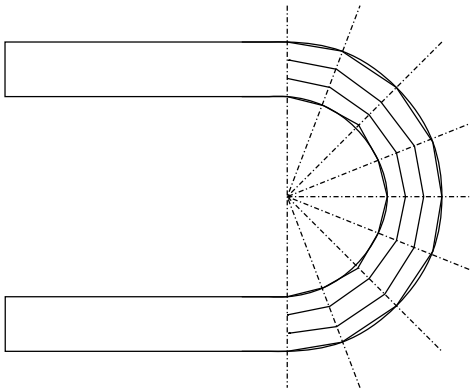

Fig. 2.13 Non rectangular shape.

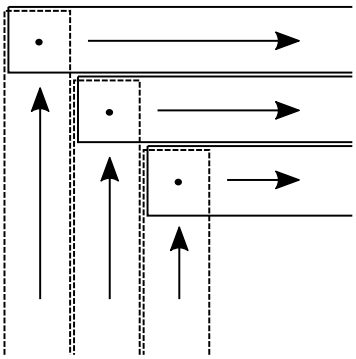

Fig. 2.14 Meshing in 90^o.

2.4.2 Embedding PEEC in a circuit simulator

In Chapter 1, it was stated that PEEC is suitable for embedding the method inside a circuit simulator. The reason is now completely clear: PEEC state variables are also V and I. To make this implementation, there are two alternatives:

a) Only Y-params, or any other Nport description, of actual component access ports is passed to the circuit simulator. This procedure can be performed whenever the circuit simulator has an application programming interface (API).

b) The system matrix is parsed as a netlist, as it is done when defining a subcircuit in SPICE. If no API is available, this is the only option for integrating PEEC in the circuit solver.

In this work, the chosen circuit simulator is *hpeesofsim* from Keysight Technologies [68]. It is a module of the EDA platform Advanced Design System, one of the most widespread tools for RF/microwave design. It offers an API though as a way to integrate

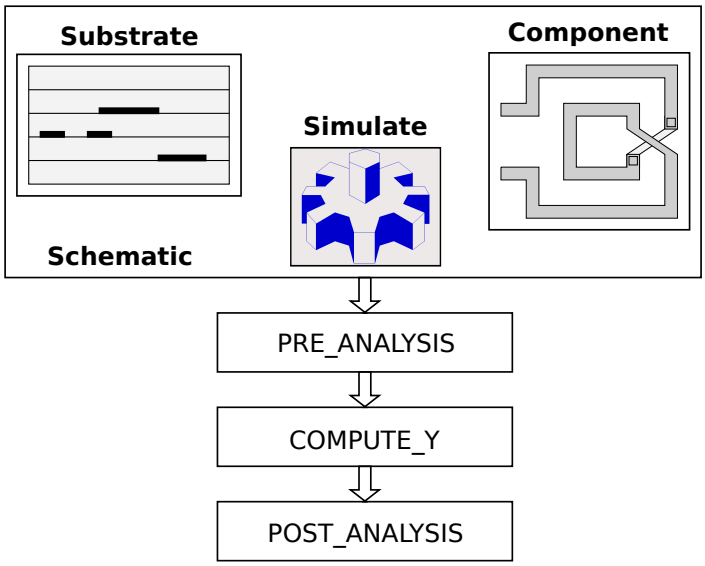

Fig. 2.15 Block diagram of User-Compiled Model.

(active component) compact models. Therefore, the PEEC solver is implemented via the API.

A. Simulation process

Fig. 2.15 is a simple representation of the aspects related to the development of a model in ADS. In ADS, this type of model implementation is named User-compiled model (UCM). The top part of the figure shows the schematic entry window where components are graphically placed and connected. Prior to the placement, the model developer has defined the corresponding parameterized cell using the *ael* syntax language of ADS. In this way, the symbol, parameter definition, layout artwork, and component netlist output are provided for user and circuit simulator. When the user starts a circuit simulation, by clicking on the simulate button, the next steps are issued for arriving to the numerical solution of the schematic:

1. The netlist is generated and it becomes the input argument of hpeesofsim. Then the simulator has to generate the handlers for instances. In addition, it has to load the required UCM models (dynamic libraries) for describing the component.

2. Each instance is processed using its corresponding coded library. Internally, the model has a modular structure that comprises a pre-analysis function, a function for computing the Y-param description of the device, and a post-processing function[9], as shown in

[9]There are many more modules, but to simplify the implementation explanations, the alrealy described functions are enough for our purposes.

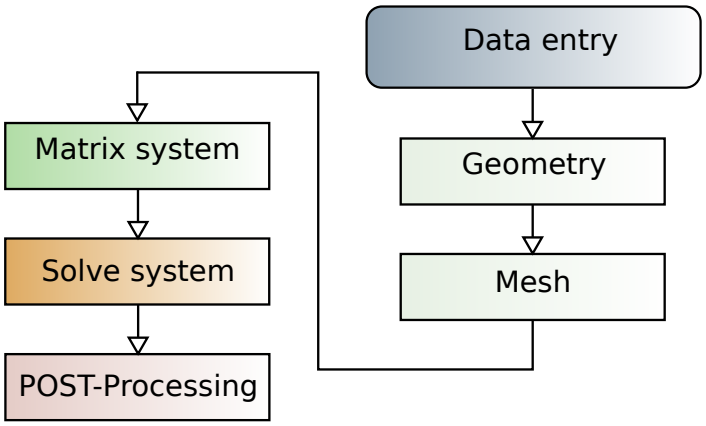

Fig. 2.16 Steps to make a physical simulation program.

the bottom part of Fig. 2.15. Then, hpeesofsim passes the instance handler to the pre-analysis function where all common procedures, basically those not depending on frequency, are processed.

3. Once finished, the control of the program is transfered to the compute Y-param function. Both instance handler and frequency are given as input parameters. The Y-param matrix of the component is the returned argument to the simulator. Then, hpeesof assembles this matrix with the rest of the system equations of the schematic.

4. Once hpeesofsim has reached the solution of voltages and currents, it transfers the control to the post-analysis function. Here, output operations and memory management of intermediate variables are hanled. Then, hpeesofsim sources the date to disk and the simulation is finished.

B. Partition of the PEEC method as an UCM

Fig.2.16 shows the main parts of a physical solver code. Of course, this is also applicable to the developed PEEC method. Now the point is how to map each part onto the functions already available in the UCM. This is made as follows:

- Data entry is performed in the pre-analysis. It consists of
  - Substrate parameters initialization: the parameters are parsed for checking any user input errors. Then, this data is shared in a substrate located inside the instance handler for later use.
  - Component parameters initializations: as previously, parsing and storing of this data is carried out. In addition, it is also checked that the component is realizable

(design rules) and compatible with the actual boundary condition (ground planes placement).

- The geometry/layout of the component is also performed in the *pre-analysis* function. Normally, the layout is described using the combination of rectangular metal strip elements. In spite of the simulation frequency, the layout has no change.

- The mesh generation is frequency dependent ($\lambda/20$ cells division criteria along propagation direction); thus, it should be attached to the *compute-y* function. Nonetheless, for computation time efficiency, it is better to make a single mesh at maximum simulation frequency. Therefore, the mesh generator has also been mapped in the *pre-analysis*.

- System matrix: the formation of this matrix and that of vectors sources has been splitted into the *pre-analysis* and *compute-y* functions. To understood this division, note that the system matrix is

$$\begin{bmatrix} \bar{\bar{R}} + j\omega\bar{\bar{L}} & D \\ D^T & \bar{\bar{G}} + j\omega\bar{\bar{C}} \end{bmatrix} \begin{bmatrix} \bar{I} \\ \bar{\phi} \end{bmatrix} = \begin{bmatrix} \bar{V}^s \\ \bar{I}^s \end{bmatrix}. \tag{2.77}$$

  Therefore, $\bar{\bar{L}}$, $\bar{\bar{C}}$, D and D^T do not depend on frequency, i.e. they are common for all frequencies. On the contrary, $\bar{\bar{R}}$ and $\bar{\bar{G}}$ are frequency dependent due to losses. This last part is calculated in the *compute-Y* function. The final assembly of the matrix is also performed in *compute-y* due to the explicit apparition of ω.

- Matrix solution is carried out in *compute-y*. It is necessary to obtain the N-port Y-param matrix describing the component. Thus, the component is solved by exciting canonically its ports; that is, one port is exciting at 1 V whereas remaining ports are hold at 0 V.

- Finally, post analysis functions, mainly related to memory deal location, are coded in the *post-analysis* module of the API.

C. Discretization

Discretization is one of the key point to make a fast and accurate solver. In this work, we have used 1D, 2D, and 1D/2D hybrid discretization models in order to minimize the required number of mesh cells. Fig.2.17 and 2.18 represents the partition and the equivalent circuit model for 1D and 2D cells.

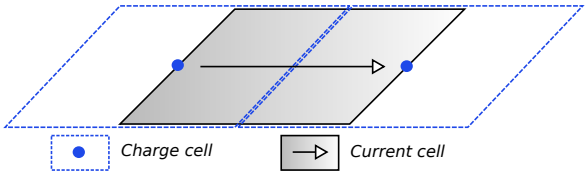

(a) 1D mesh of cell.

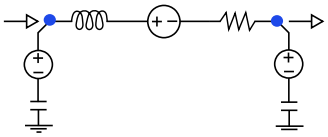

(b) 1D equivalent circuit of cell.

Fig. 2.17 1D discretization of one cell.

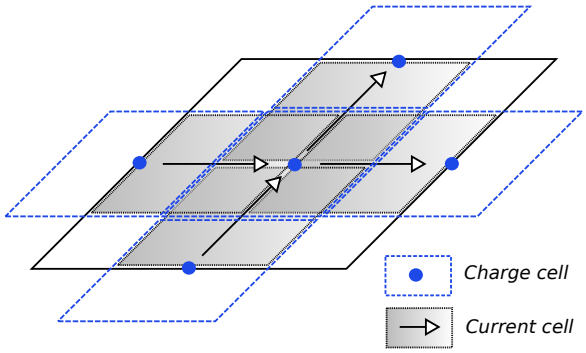

(a) 2D mesh of cell.

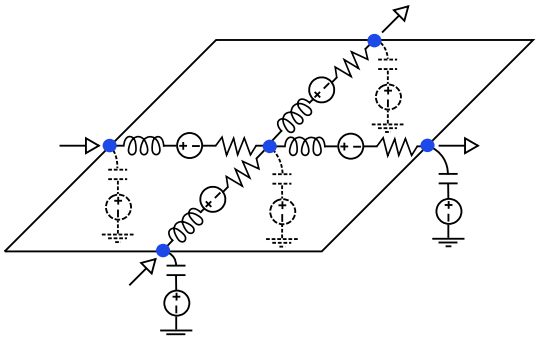

(b) 2D equivalent circuit of cell.

Fig. 2.18 2D discretization of one cell.

Chapter 3

Analytical Green's functions for laminated substrates

Abstract

When dealing with integral methods for low/medium size complexity problems, the speed computation bottle-neck is the formation of the system matrix elements. In this Chapter, an analytical approach is developed which consists in two different ingredients: (i) the Green's function of the substrate is obtained analytically in terms of a series of discrete images; (ii) the terms of the series are analytically integrated by using Hover-Love inductance expressions. The main advantage of the method is its exactness and speed for Manhattan like layouts. Although it can only be efficiently applied to a one dielectric material substrate, most LTCC tape systems fall in this category because they use the same dielectric material for all layers.

For two dielectric materials, an analytical expression is found as well. However, it is computationally intensive and cannot be used in a fast simulator. Instead, an heuristic procedure is derived that treats the two material problem as a two single-material problems. In all cases, comparisons with state-of-the-art commercial software are done.

3.1 Introduction

The PEEC algorithm developed in Chapter 2 has been specialized for the computation of microstrip complex structures up to a frequency where the quasi-static assumption still holds, which it is normally beyond the self-resonance of the component. Notice that, to speed the

computation time, the introduced simplifications have been directed to the reduction of the model order complexity, i.e.

- dismiss of the retarded potential;
- reduction of the vector components of $\bar{J}$ to only one, $\bar{J} \propto \hat{J}_{DC}$;
- consideration of a infinitely thin sheet conductor.

In this Chapter, the goal is to develop a fast procedure for the formation of the system matrix

$$\begin{bmatrix} \bar{V}^s \\ \bar{I}^s \end{bmatrix} = \begin{bmatrix} \bar{\bar{R}} + j\omega\bar{\bar{L}} & D^T \\ D & j\omega\bar{\bar{C}} \end{bmatrix} \begin{bmatrix} \bar{I} \\ \bar{\phi} \end{bmatrix}, \tag{3.1}$$

which involves the computation of the different partial elements. Whereas $\bar{\bar{D}}$, $\bar{\bar{D}}^T$ and $\bar{\bar{R}}$ are obtained quite straight forward, the computation of $\bar{\bar{L}}$ and $\bar{\bar{C}}$, i.e.

$$L_{ij} = \frac{1}{w_i w_j} \int_{a_i} dw_i \int_{a_j} dw_j K(\bar{r}, \bar{r}') \left[d\mathbf{l} \cdot d\mathbf{l}' \right] \tag{3.2}$$

$$C_{ij} = P_{ij}^{-1} \rightarrow P_{ij} = \frac{1}{a_i a_j} \int_{a_i} dS \int_{a_j} dS' G(\bar{r}, \bar{r}'), \tag{3.3}$$

is quite challenging because it involves the knowledge of Green's functions $K(\bar{r}, \bar{r}')$ and $G(\bar{r}, \bar{r}')$, and the evaluation of two surface integrals. It must be stressed that a too coarse computation of (3.2)-(3.3) can lead to inaccuracies, and instability of the numerical solution [69, 70]. On top of that and for large size problems (which is not the case for the passives that will be modelled in this work), eq.(3.1) should be sparsified somehow; otherwise, its solution becomes impractical.

Since the introduction of MoM [29], the challenge for developing fast and accurate GFs algorithms for multilayer media has been a topic of major interest.[1] Initial works showed that spectral methods were easier to implement computationally [71]. In 1987, Das & Pozar introduced a general spectral-domain procedure for obtaining full-wave GFs [72]. Although this formal methodology was quite straightforward, the main problem was related to GF anti-transform back to the space-domain, a required step for integrating (3.2) and (3.3). Nowadays, the most promising numerical method is the Discrete Complex Image Method (DCIM) [73] where the spectral-domain GF is approximated, using some fitting procedure, as a series of complex exponential functions. With this approach, the anti-transformation to

[1] As it has been mention in Chapter 1, 2.5D integral methods avoid the meshing of the substrate.

Table 3.1 Properties of LTCC ceramic materials.

Tape System	ε_r	tg δ	thickness (mil)	Metals
Dupont 951	7.8	0.014	1.8-3.8-5.5-8.5	Au-Ag-Mix
Dupont 9K7	7.1	0.001	4.2-8.4	Au-Ag
Heraeus CT702	7.2	0.002	2.7-3.5	Au-Ag-Mix
Ferro A6S	6.1	0.001	3.5	Au-Ag

the space domain should be easier. However, the obtained series expansion has many poles and branch-cuts in the complex plane that makes difficult its evaluation [74].

In the PEEC method, authors do not have put too much effort in the development of GFs. The reason is that most works have been directed to obtain a 3D, full-wave, full-spectrum, time and frequency domain EM solver. Thus, it is only required to use e^{jkR}/R (full-wave) or $1/R$ (quasi-static) kernels [75][2]. Nevertheless, Niknejad showed the possibility to use numerical spectral-domain methods in a 2.5D PEEC [67]. More recently, other authors are using DCIM methods for implementing PEEC-like EM solvers [76].

In this work, instead of pursuing a general purpose DCIM algorithm, the strategy for GF computation is to specialize the algorithm according to the characteristics of the LTCC substrate. To understand this starting point, Table 3.1 shows the basic EM properties of different commercial LTCC tape systems [77], [78]. The substrate is made by stacking the corresponding dielectric material sheets intercalating printings of metals (Au,Ag). This situation is depicted on the left side of Fig.3.1. Usually, state-of-the-art solvers will compute all necessary GFs between all layers; thus, the required GF computation time can be quite large if the substrate has many layers. To overcome this problem, a fully analytical GF solution is developed in this chapter that is valid for most LTCC tape systems. The key point is to notice that all dielectric layers of a given tape system, which could have different thickness, are made with the same material; thus, they have the same EM properties. Therefore, the actual substrate to deal with is the one shown on the right part of Fig.3.1. For practical cases, two configurations of the substrate will be work out: with and without GND plane.

Aside from GF computation, eqs. (3.2) and (3.3) require the evaluation of two surface integrals. These integrals can only be obtained analytically for the case of orthogonal structures [55]. On the contrary, it is necessary to use numerical integration [79–81] for non-orthogonal shaped components. Nevertheless, the components addressed in the library have Manhattan like layouts; thus, the analytical integration will be performed.

[2] In PEEC, the presence of dielectrics is treated using equivalence principles.

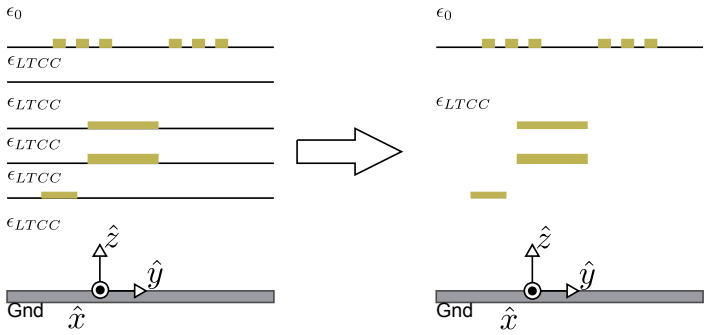

Fig. 3.1 Typical cross-section of an LTCC multilayer tape system.

3.2 Mathematical aspects

The Green's function method was developed by the british mathematician George Green in the 1830s. It is the impulsive response of an inhomogeneous differential equation constrained to specific boundary/initial conditions in a certain domain. In this section, the formalism of the chosen spectral-domain technique, which is based on Hankel transform, is described. It is applied to the well-known solution of the potential made by a point charge over a perfect GND plane in homogeneous media. For validating the obtained expression, it is also explained the procedure for comparing the analytical solution with other solvers.

3.2.1 Poisson's equation in multilayer substrate

When developing quasi-static solvers for non-conductive substrates, both $K(\bar{r},\bar{r}')$ and $G(\bar{r},\bar{r}')$ are obtained from the solution of a Poisson's equation

$$\nabla^2 G = K \cdot \delta(\bar{r}-\bar{r}_q) \tag{3.4}$$

applied to a multilayer problem, where $K\cdot\delta(\bar{r}-\bar{r}_q)$ is the point source located at $\bar{r_q}$. K equals $-1/\varepsilon$ for electrical problems; and μ, for magnetic ones. From now on, let us assume that a solution of the electrical part $G(\bar{r},\bar{r}')$ must be found. Due to the angular symmetry of planar substrates, the system is better described using cylindrical coordinates $(\rho,\ \theta,\ z)$[3]; then, eq. (3.4) has the next form

$$\partial_\rho^2 G + \frac{1}{\rho}\partial_\rho G + \partial_z^2 G = -\frac{1}{\rho\varepsilon}\delta(\rho)\delta(\theta)\delta(z-z_q). \tag{3.5}$$

[3]Through all this Chapter, be aware that ρ stands for the radial cylindrical coordinate and not for charge density which is normally named as $\rho(\bar{r})$.

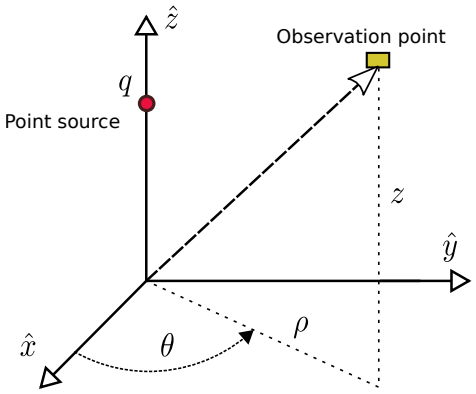

Fig. 3.2 Cylindrical coordinate reference system for Green's function computation.

In (3.5), it has been used that $G(\vec{r},\vec{r}')$ depends only on the distance between the source and the observation point, i.e., $G(\rho,\theta,z;\rho_q,\theta_q,z_q) \equiv G((\rho-\rho_q),(z-z_q))$. This fact has two consequences: (i) the source has been placed at $(0,0,z_q)$ due to the freedom in assigning the origin of the reference coordinate system, as shown in Fig. 3.2; (ii) there is no dependence on θ. Then, θ can be integrated out as follows

$$\int_0^{2\pi} d\theta \left[\partial_\rho^2 G + \frac{1}{r}\partial_\rho G + \partial_z^2 G\right] = -\int_0^{2\pi} d\theta \frac{1}{\varepsilon\rho}\delta(\rho)\delta(\theta)\delta(z-z_q) \Rightarrow \tag{3.6}$$

$$2\pi\left[\partial_\rho^2 G + \frac{1}{\rho}\partial_\rho G + \partial_z^2 G\right] = -\frac{1}{\varepsilon\rho}\delta(\rho)\delta(z-z_q) \Rightarrow \tag{3.7}$$

$$\Rightarrow \left[\partial_\rho^2 G + \frac{1}{\rho}\partial_\rho G + \partial_z^2 G\right] = \frac{-1}{2\pi\varepsilon\rho}\delta(\rho)\delta(z-z_q); \tag{3.8}$$

thus $G(\rho,\theta,z) \to G(\rho,z)$. Aside from the local physics described by this partial differential equation, boundary conditions (BC) must be set as well. At each layer interface z_i, the Green's function and its first derivative must be continuous, i.e.,

$$G(\rho,z_i^+) - G(\rho,z_i^-) = 0 \tag{3.9}$$

$$\partial_z G(\rho,z_i^+) - \partial_z G(\rho,z_i^-) = 0, \tag{3.10}$$

except at $z = z_q$ where the first derivative is equal to the point source value

$$\partial_z G(\rho,z_q^+) - \partial_z G(\rho,z_q^-) = \frac{-1}{2\pi\varepsilon\rho}\delta(\rho)\delta(z-z_q). \tag{3.11}$$

In addition to continuity BC, if a GND plane exists at the bottom of the multilayer substrate, it is defined through the condition

$$G(\rho,0)=0\,. \tag{3.12}$$

Open boundaries, top and/or bottom, are set as

$$G(\rho,z\to\pm\infty)=0. \tag{3.13}$$

For solving analytically (3.8) with its BC, different methods can be chosen. For instance, the well-known separation of variables could be applied in the spatial-domain. Nonetheless, the one that will be applied in this work is a spectral-domain method based on the Hankel transform because it will provide a solution as a series of charge images.

3.2.2 The Hankel transform

The zero order Hankel transform[4],

$$G^{H_0}(m,z)\equiv H_0\left\{G(\rho,z)\right\}\equiv\int_0^\infty \rho d\rho G(\rho,z)J_0(\rho m), \tag{3.14}$$

is the two-dimensional Fourier transform of a circularly symmetric function [82] which spatial variable is ρ and the spectral one is m. The advantage of using this transform for solving (3.8) is that the partial differential equation is converted to a second order ordinary differential equation. In this step, it is necessary to make use of the properties of the transform about the derivatives of a function

$$\left.\begin{aligned} H_0\left\{\tfrac{1}{\rho}\tfrac{d}{d\rho}(\rho f(\rho))\right\}&=mH_1\left\{f(\rho)\right\}\\ H_1\left\{f'(\rho)\right\}&=-mH_0\left\{f(\rho)\right\}\end{aligned}\right\}, \tag{3.15}$$

where $H_1\left\{f(\rho)\right\}$ is the first order Hankel transform. Then, the application of the transform on the left side of (3.8) is

$$H_0\left\{\partial_\rho^2 G+\frac{1}{\rho}\partial_\rho G+\partial_z^2 G\right\}=-m^2G^{H_0}(m,z)+\partial_z^2G^{H_0}(m,z), \tag{3.16}$$

[4] A summary of its basic properties can be found in Appendix C.

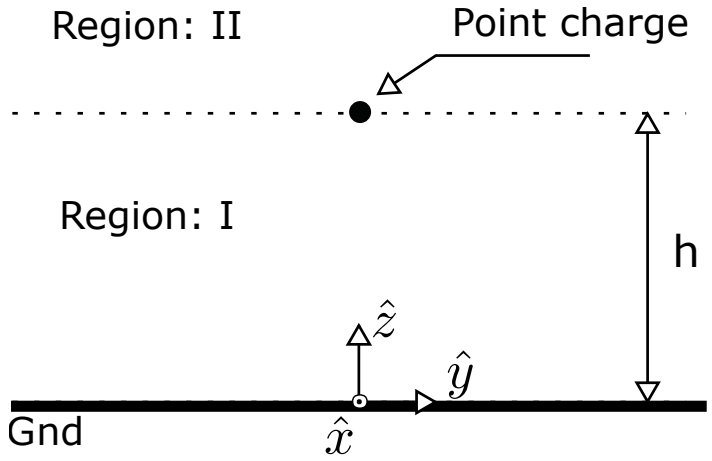

Fig. 3.3 Half free-space problem.

and, on the right side, the source term is

$$-\int_0^\infty \frac{1}{2\pi\varepsilon\rho} r\delta(\rho)\delta(z-z_q)J_0(\rho m)d\rho = -\frac{1}{2\pi\varepsilon}\delta(z-z_q)J_0(0). \tag{3.17}$$

Joining both results, the spectral domain ordinary differential equation is

$$-m^2 G^{H_0}(m,z) + \frac{d^2}{dz^2}G^{H_0}(m,z) = -\frac{1}{2\pi\varepsilon}\delta(z-z_q). \tag{3.18}$$

Notice that (3.18) is the telegraph equation. For each layer i of the substrate, its general solution is:

$$G^{H_0}(m,z) = A_i e^{mz} + B_i e^{-mz}, \tag{3.19}$$

where $z_{i-1} < z < z_i$, and z_i is the layer interface. A total of $2N$ unknown integration coefficients $\{A_i, B_i\}$ must be solved using the algebraic system of equations obtained from the $2N$ constraints introduced by BC. Once $\{A_i, B_i\}$ are substituted back into (3.19), the difficult task is to anti-transform the solution to the space domain. Only few substrate configurations are amenable for analytical solutions, as the one shown next.

3.2.3 Half free space Green's function

Fig. 3.3 depicts a point charge source placed at a distance h over a GND plane. From image theory, it is well-known that the potential on the half free space ($z > 0$) is the linear combination of the potential made by the charge itself and an image charge of the same value, but opposite sign, located symmetrically with respect to the GND plane. By using the former mathematical spectral formalism, let us try to find this solution.

The plane $z = h$, where the charge is located, divides the space in two regions (region I and II). Therefore, the Green's function solution is

$$G_I^{H_0}(m,z) = A_I e^{mz} + B_I e^{-mz} \quad if\ 0 < z < h\ (region\ I) \tag{3.20}$$

$$G_{II}^{H_0}(m,z) = A_{II} e^{mz} + B_{II} e^{-mz} \quad if\ z > h\ (region\ II). \tag{3.21}$$

Integration coefficients $\{A_I, A_{II}, B_I, B_{II}\}$) are found by applying corresponding BC. From GND plane condition

$$G_I^{H^0}(m, z = 0) = 0$$

and top open boundary

$$G_{II}^{H^0}(m, z \to \infty) = 0,$$

it is straight forward that $A_I = -B_I$ and $A_{II} = 0$. From continuity of GFs at the interface of both regions

$$G_I^{H_0}(m, z = h) = G_{II}^{H_0}(m, z = h),$$

and charge discontinuity

$$\varepsilon_0 \frac{d}{dz} G_I^{H_0}(m, z = h) - \varepsilon_0 \frac{d}{dz} G_{II}^{H_0}(m, z = h) = 1/2\pi,$$

the next two equations are found

$$A_I(e^{mh} - e^{-mh}) = B_{II} e^{-mh} \tag{3.22}$$

$$A_I(e^{mh} + e^{-mh}) + B_{II} e^{-mh} = -\frac{1}{2\pi\varepsilon m}. \tag{3.23}$$

From (3.22), B_{II} can be expressed in terms of A_I; then, B_{II} can be substituted in (3.23) for solving A_I as

$$A_I = \frac{e^{-mh}}{4\pi m\varepsilon}. \tag{3.24}$$

Then, A_I can be replaced back into (3.22); thus, B_{II} arises as

$$B_{II} = \frac{1}{4\pi m\varepsilon}\left(e^{mh} - e^{-mh}\right). \tag{3.25}$$

Using (3.24) and (3.25), the GF spectral domain expressions for each region are

$$G_I^{H_0}(m,z) = \frac{1}{4\pi\varepsilon m}\left(e^{m(z-h)} - e^{-m(z+h)}\right) \quad if\ 0 < z < h\ (region\ I) \tag{3.26}$$

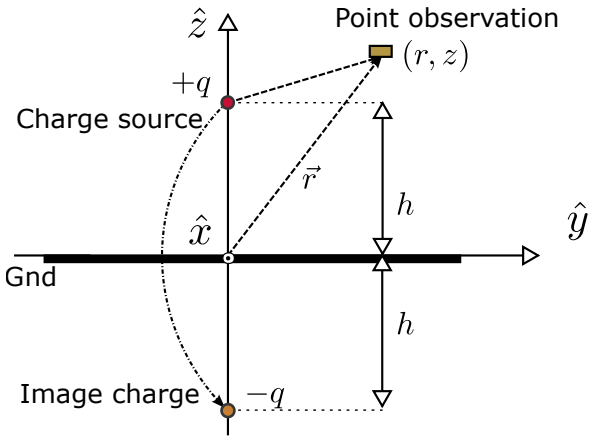

Fig. 3.4 Image charge situation in half free-space.

$$G_{II}^{H_0}(m,z) = \frac{1}{4\pi\varepsilon m}\left(e^{m(h-z)} - e^{-m(h+z)}\right) \quad if\ z > h\ (region\ II) \tag{3.27}$$

Using the analytical Hankel anti-transform

$$H_0^{-1}\left\{\frac{Ke^{-m|z|}}{m}\right\} = \frac{K}{\sqrt{r^2+z^2}}, \tag{3.28}$$

eqs. (3.26) and (3.27) are converted back to the spectral domain

$$G_I(\rho,z) = \frac{1}{4\pi\varepsilon}\left[\frac{1}{\sqrt{\rho^2+(z-h)^2}} - \frac{1}{\sqrt{\rho^2+(z+h)^2}}\right] \tag{3.29}$$

$$G_{II}(\rho,z) = \frac{1}{4\pi\varepsilon}\left[\frac{1}{\sqrt{\rho^2+(h-z)^2}} - \frac{1}{\sqrt{\rho^2+(z+h)^2}}\right]. \tag{3.30}$$

Notice that (3.29) and (3.30) have two terms: the first one is related to the potential made by the charge itself and the second one is the potential related to the image. This last term is negative, has the same charge value and it is located at $z = -h$, as shown in Fig. 3.4.

3.2.4 Procedure for verification

Once the analytical GF expression has been derived, it is compared with a state-of-the-art commercial software based on the method of moments (MoM). This comparison must be done indirectly through the computation of the capacitance matrix C of a simple multiconductor systems [5], because it is not possible to access the GF data calculated by the commercial

[5]The procedure for computing C has been already explained in Chapter 2, section 2.2.

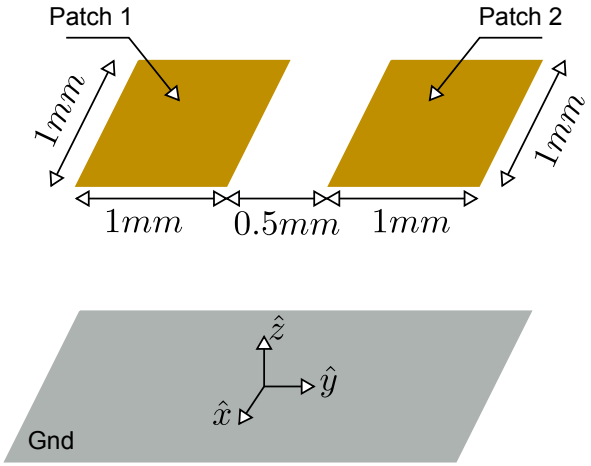

Fig. 3.5 Two patches in half free-space.

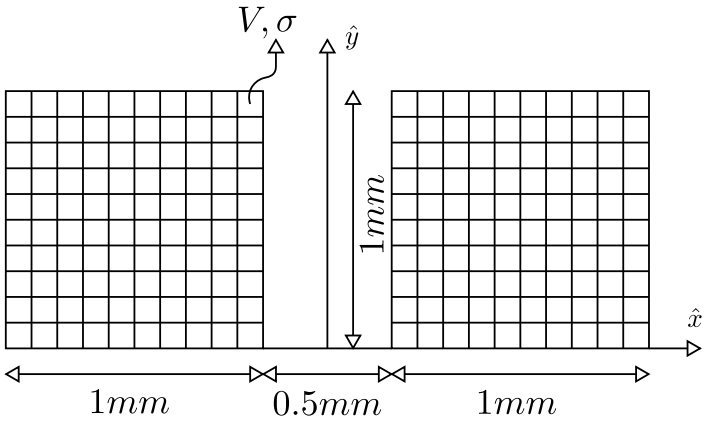

Fig. 3.6 Uniform mesh of the two patches problem.

software. For the computation of C, the analytical GF is used in the formation of the elements of the partial potential matrix, P_{ij} in (3.3). Keep in mind that the double surface integral is also computed analytically using Hoer-Love expressions [55], whereas MoM uses the numerical point collocation method.

The layout of the system is shown in Fig. 3.5. It is formed by two coplanar $1 \times 1mm^2$ patches separated by a distance of $0.5mm$. Patches are placed on the dielectric interface corresponding to the GF under study and are divided uniformly as shown in Fig.3.6. Although it is not a good mesh for a capacitance computation, the important point here is to be sure that both meshes, from commercial solver and analytical GF, are identical for a fair comparison.

Table 3.2 collects the results of the capacitance matrix coefficients using the analytical expression (3.29), the MoM software, and their relative difference. It is clear that differences are quite small; nonetheless, it must be kept in mind that the only approximation of the

Table 3.2 Capacitance matrix comparison for the two patches problem.

	Eq. (3.29) [fF]	MoM [fF]	Difference
C_{11}	61.44	61.71	0.43 %
C_{12}	-3.95	-3.96	0.25 %
C_{21}	-3.95	-3.96	0.25 %
C_{22}	61.44	61.71	0.43 %

C_{12} and C_{21} are negative by definition.

analytical procedure has been the mesh of the geometry itself, whereas the GF and surface integral computations in MoM have been evaluated numerically.

After demonstrating the procedure for the development and verification of analytical GF expressions, it will be next applied to the modelling of LTCC substrate. Later on, an extension to RFIC substrate will be also worked.

3.3 Analytical GFs for LTCC tape systems

Fig. 3.7 shows the four cross-sections of the LTCC substrate that will be used for the development of GFs:

a) The bottom of the substrate, which is located at $z = 0$, is bounded by a GND plane. The point source charge is placed on the LTCC dielectric-air interface at a distance d from GND.

b) The difference with Fig. 3.7a is that the point source charge is located inside the LTCC dielectric at a distance $h < d$.

c) Top and bottom interfaces are open boundaries and the point source charge is located at the LTCC dielectric-air interface. The bottom interface is the origin of the z coordinate.

d) The difference with Fig. 3.7c is that the point source charge is located inside the LTCC dielectric.

Charge plane ($z = h$) and dielectric-air interfaces ($z = d$) define the different regions of the domain. Notice that the components that will be implemented in the LTCC substrate will be always located at the interface or inside the dielectric. Therefore, regions of interest are those contained inside the LTCC.

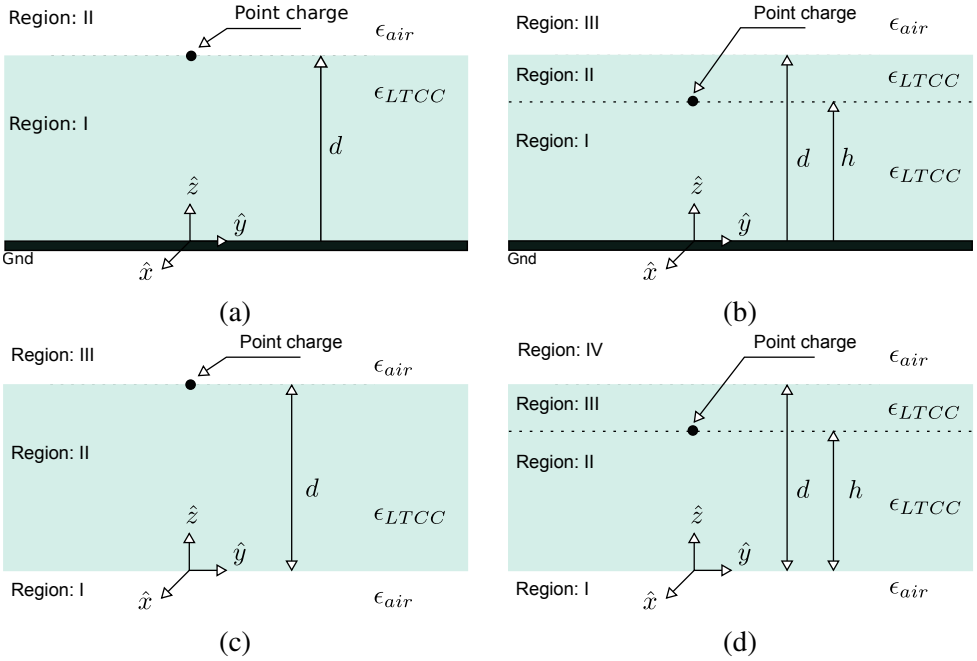

Fig. 3.7 LTCC cross-sections: (a) GND with point source on the dielectric-air interface; (b) GND with point source inside the LTCC; (c) open boundary with point source on the dielectric-air interface; (d) open boundary with point source inside the LTCC.

3.3.1 LTCC with GND plane

Point source located on the dielectric-air interface

This cross-section has two regions. The interesting GF is the one associated to region I, where the device will be embedded. The application of the GND bottom boundary and open top boundary on the general solution of the GFs, as it has been shown in Section 3.2.3, gives the next expressions for the different regions

$$G_I^{H_0}(m,z) = A_I\left(e^{mz} - e^{-mz}\right) \quad z \in \textit{region I} \tag{3.31}$$

$$G_{II}^{H_0}(m,z) = B_{II}e^{-mz} \quad z \in \textit{region II}. \tag{3.32}$$

To determine constants A_I and B_{II}, the continuity through the interface plane

$$G_I^{H_0}(m,d) = G_{II}^{H_0}(m,d)$$

and charge discontinuity

$$\varepsilon_{LTCC}\frac{d}{dz}G_I^{H_0}(m,d) - \varepsilon_{air}\frac{d}{dz}G_{II}^{H_0}(m,d) = 1/2\pi$$

are applied to (3.31) and (3.32), which leads to

$$A_I(e^{md} - e^{-md}) = B_{II}e^{-md} \tag{3.33}$$

$$\varepsilon_{LTCC}A_I(e^{md} + e^{-md}) + \varepsilon_{air}B_{II}e^{-md} = -\frac{1}{2\pi\varepsilon m} \tag{3.34}$$

Then, A_I is

$$A_I = \frac{e^{-md}}{4\pi m\varepsilon_M}\frac{1}{1+ke^{-2md}}, \tag{3.35}$$

and the constant B_{II} is

$$B_{II} = \frac{e^{md} - e^{-md}}{4\pi m\varepsilon_M}\frac{1}{1+ke^{-2md}} \tag{3.36}$$

where $\varepsilon_M = \frac{\varepsilon_{LTCC}+\varepsilon_{air}}{2}$ and $k = \frac{\varepsilon_{LTCC}-\varepsilon_{air}}{\varepsilon_{LTCC}+\varepsilon_{air}}$. Notice that $0 \leqslant k < 1$ a fact that will be important to assure the convergence in the spatial domain. Using (3.35) and (3.36), the Green's functions of the two regions are

$$G_I^{H_0}(m,z) = \frac{1}{4\pi m\varepsilon_M}\frac{e^{m(z-d)} - e^{-m(z+d)}}{1+ke^{-2md}} \tag{3.37}$$

$$G_{II}^{H_0}(m,z) = \frac{1}{4\pi m\varepsilon_M}\frac{e^{m(d-z)} - e^{-m(d+z)}}{1+ke^{-2md}}. \tag{3.38}$$

At the interface ($z = d$), $G_I^{H_0}(m,z)$ equals $G_{II}^{H_0}(m,z)$. Moreover, if $\varepsilon_{LTCC} = \varepsilon_{air} \Rightarrow k = 0$, then the solution found is the half free space GF.

Now, the challenge is to find the analytical anti-transform of (3.37) and (3.38). Let us define its denominator as $1+X$, with $X = ke^{-2md}$, and develop its Taylor's series

$$\frac{a}{1+X} = 1 + \sum_{n=1}^{\infty} a(-1)^n X^n, \qquad |X| < 1. \tag{3.39}$$

The condition for convergence, $|X| < 1$, is always guaranteed because $|k| < 1$, and $m \cdot d \geqslant 0$. Then, the denominator becomes

$$\frac{1}{1+ke^{-2md}} = 1 + \sum_{l=1}^{\infty}(-1)^l \cdot k^l \cdot e^{-2mdl}, \tag{3.40}$$

and both GFs are rewritten as

$$G_I^{H_0}(m,z) = \frac{e^{m(z-d)} - e^{-m(z+d)}}{4\pi m\varepsilon_M} \cdot \left(1 + \sum_{l=1}^{\infty}(-1)^l \cdot k^l \cdot e^{-2mdl}\right) \tag{3.41}$$

$$G_{II}^{H_0}(m,z) = \frac{e^{m(d-z)} - e^{-m(d+z)}}{4\pi m \varepsilon_M} \cdot \left(1 + \sum_{l=1}^{\infty} (-1)^l \cdot k^l \cdot e^{-2mdl}\right). \tag{3.42}$$

Using (3.28), i.e.

$$H_0^{-1}\left\{\frac{Ke^{-m|z|}}{m}\right\} = \frac{K}{\sqrt{\rho^2+z^2}}$$

where $K = \frac{1}{4\pi\varepsilon_M}$, the spatial domain Green's functions for both regions are

$$G_I(\rho,z) = \frac{1}{4\pi\varepsilon_M}\left\{\frac{1}{\sqrt{\rho^2+(d-z)^2}} - \frac{1}{\sqrt{\rho^2+(d+z)^2}} + \right.$$
$$\left. + \sum_{l=1}^{\infty}(-1)^l k^l \left[\frac{1}{\sqrt{\rho^2+(d-z+2d\cdot l)^2}} - \frac{1}{\sqrt{\rho^2+(d+z+2d\cdot l)^2}}\right]\right\} \tag{3.43}$$

$$G_{II}(\rho,z) = \frac{1}{4\pi\varepsilon_M}\left\{\frac{1}{\sqrt{\rho^2+(z-d)^2}} - \frac{1}{\sqrt{\rho^2+(d+z)^2}} + \right.$$
$$\left. + \sum_{l=1}^{\infty}(-1)^l k^l \left[\frac{1}{\sqrt{\rho^2+(z-d+2d\cdot l)^2}} - \frac{1}{\sqrt{\rho^2+(d+z+2d\cdot l)^2}}\right]\right\}. \tag{3.44}$$

The way (3.43) and (3.44) have been arranged is to illustrate the next properties in both GFs, a fact that is quite complicated to visualize with numerical techniques:

- Both terms out of the summation are the solution of the half space with a dielectric permittivity equal to ε_M.
- Each term l of the summation is formed by a charge of value $(-k)^l$ located at $2\cdot h\cdot l$ above the LTCC-air interface and its image through the GND plane, as shown in Fig. 3.8.
- Charges have been grouped in pairs, the charge and its image, thus it is possible to see them as dipoles of value $p = 2d(l+1)\cdot(-k)^l$. This interpretation can be very helpful when developing asymptotic expressions for large distance interactions.
- If the series is truncated at term l, the error in the calculation is defined by the term $l+1$. Thus, a priori robust error estimation of the expression is available.
- The summation can be interpreted as a perturbation of the half space solution. The higher the permittivity of the LTCC, the more terms of the summation are needed to compute GF accurately.

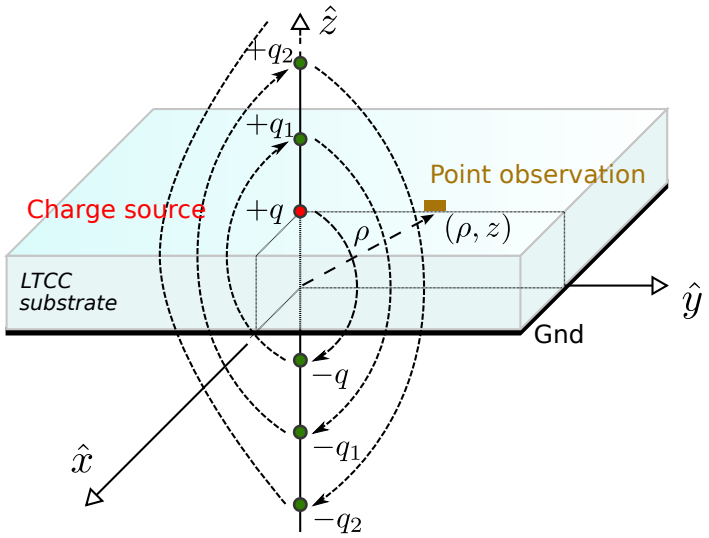

Fig. 3.8 Image charge situation in LTCC substrate with GND.

These features of the solution are mainly due to the GND plane. Therefore, they will be also obtained for the remaining GF when the charge is placed inside the LTCC, but a subtle difference will be highlighted.

Point source located inside the dielectric

As it was shown in Fig. 3.7b, the substrate cross-section is divided in three regions. Nonetheless, it is only necessary to solve the GF at region *II* where the component will be placed. After applying the GND bottom and open top boundary conditions, the general solution is

$$G_I^{H_0}(m,z) = A_I(e^{mz} - e^{-mz}) \tag{3.45}$$

$$G_{II}^{H_0}(m,z) = A_{II}e^{mz} + B_{II}e^{-mz} \tag{3.46}$$

$$G_{III}^{H_0}(m,z) = B_{III}e^{-mz}. \tag{3.47}$$

The remaining boundary conditions, i.e., the two continuity equations at $z = h$

$$G_I^{H_0}(m,h) = G_{II}^{H_0}(m,h)$$

and at $z = d$

$$G_{II}^{H_0}(m,d) = G_{III}^{H_0}(m,d),$$

the continuity of the first derivative at $z = d$

$$\varepsilon_{LTCC}\frac{d}{dz}G_{II}^{H_0}(m,d) = \varepsilon_{air}\frac{d}{dz}G_{III}^{H_0}(m,d),$$

and the charge discontinuity at $z = h$

$$\varepsilon_{LTCC}\frac{d}{dz}G_{II}^{H_0}(m,h) - \varepsilon_{air}\frac{d}{dz}G_{III}^{H_0}(m,h) = 1/2\pi\,,$$

provide the next relationships between integration constants A_I, A_{II}, B_{II}, and B_{III}

$$A_I(e^{mh} - e^{-mh}) = A_{II}e^{mh} + B_{II}e^{-mh} \tag{3.48}$$

$$A_{II}e^{md} + B_{II}e^{-md} = B_{III}e^{-md} \tag{3.49}$$

$$-m\varepsilon_{air}B_{III}e^{-md} - \varepsilon_{LTCC}m(A_{II}e^{md} - B_{II}e^{-md}) = 0. \tag{3.50}$$

$$-mA_I(e^{mh} + e^{-mh}) + m(A_{II}e^{mh} - B_{II}e^{-mh}) = \frac{-1}{2\pi\varepsilon_{LTCC}} \tag{3.51}$$

As the interest is placed in region II, it is only required to solve A_{II} and B_{II} which expressions are given by

$$A_{II} = \frac{e^{mh} - e^{-mh}}{4\pi\varepsilon_M m} \cdot \frac{ke^{-2md}}{1 + ke^{-2md}} \tag{3.52}$$

$$B_{II} = \frac{e^{mh} - e^{-mh}}{4\pi\varepsilon_M m} \cdot \frac{1}{1 + ke^{-2md}} \tag{3.53}$$

with $k = \frac{\varepsilon_{LTCC} - \varepsilon_{air}}{\varepsilon_{LTCC} + \varepsilon_{air}}$, and $\varepsilon_M = \frac{\varepsilon_{LTCC} + \varepsilon_{air}}{2}$.

Now, we can write the Green's function solution of region II in the transformed domain:

$$G_{II}^{H_0} = \frac{1}{4\pi\varepsilon_M m} \cdot \frac{e^{-m(z-h)} - e^{-m(z+h)} + ke^{-m(2d-z-h)} - ke^{-m(2d-z+h)}}{1 + ke^{-2md}}\,. \tag{3.54}$$

Using the Taylor series expansion (3.40), eq. (3.54) is cast in the next form

$$\begin{aligned} G_{II}^{H_0}(m,z) = \frac{1}{4\pi\varepsilon_M m}\Big[\, & e^{-m(z-h)} - e^{-m(z+h)} + ke^{-m(2d-z-h)} - \\ & - ke^{-m(2d-z+h)} + \sum_{l=1}^{\infty}(-1)^l k^l \Big(e^{-m(z-h+2dl)} - e^{-m(z+h+2dl)} + \\ & + ke^{-m(2d-z-h+2dl)} - ke^{-m(2d-z+h+2dl)}\Big)\Big]\,. \end{aligned} \tag{3.55}$$

Applying the Hankel anti-transform (3.28), the space domain GF in region II is given by

$$G_{II}(\rho,z) = \frac{1}{4\pi\varepsilon_M}\left\{\frac{1}{\sqrt{\rho^2+(z-h)^2}} - \frac{1}{\sqrt{\rho^2+(z+h)^2}} + \right.$$
$$+\frac{k}{\sqrt{\rho^2+(2d-z-h)^2}} - \frac{k}{\sqrt{\rho^2+(2d-z+h)^2}} +$$
$$+\sum_{l=1}^{\infty}(-1)^l k^l\left[\frac{1}{\sqrt{\rho^2+(z-h+2dl)^2}} - \frac{1}{\sqrt{\rho^2+(z+h+2dl)}} + \right.$$
$$\left.\left.+\frac{k}{\sqrt{\rho^2+(-z-h+2d(1+l))^2}} - \frac{k}{\sqrt{\rho^2+(-z+h+2d(1+l))^2}}\right]\right\}. \quad (3.56)$$

Once again, the expression has been rearranged to show the relation between charge images. Looking at the terms outside of the summation in l, the first two are easily recognized as the half space GF. The other two are, for the positive one, the image of the original charge through the dielectric-air interface, which has a value of k; for the negative one, it corresponds to the image through the GND plane of the later image, which value is $-k$. The charges of the summation are the iterative back and forth images through the planes defined by GND and dielectric-air interface. It is worth noting that, as in the previous GF derivation, the terms could be rearranged as a summation of electric dipoles.

3.3.2 LTCC with bottom and top open boundaries

Point source located on the dielectric-air interface

The substrate cross-section for this case, which is divided in three regions, has been already shown in Fig. 3.7c. The total thickness of the LTCC dielectric is d and the source is located on the top interface. After applying the two open boundary conditions, the general solutions are

$$G_I^{H_0}(m,z) = A_I \cdot e^{mz} \quad (3.57)$$

$$G_{II}^{H_0}(m,z) = A_{II} \cdot e^{mz} + B_{II} \cdot e^{-mz} \quad (3.58)$$

$$G_{III}^{H_0}(m,z) = B_{III} \cdot e^{-mz} \quad (3.59)$$

The remaining BCs (continuity at interfaces, first derivative continuity at bottom interface, and charge discontinuity at top interface) set the next relationships between integration constants

$$A_I = A_{II} + B_{II} \quad (3.60)$$

$$A_{II}e^{md} + B_{II}e^{-md} = B_{III}e^{-md} \tag{3.61}$$

$$\varepsilon_{air}A_I = \varepsilon_{LTCC}(A_{II} - B_{II}) \tag{3.62}$$

$$\varepsilon_{air}B_{III}e^{-md} + \varepsilon_{LTTC}(A_{II}e^{md} - B_{II}e^{-md}) = \frac{1}{2\pi m}. \tag{3.63}$$

It is only necessary to obtain the values of A_{II} and B_{II} because components are only located in region II. Their expressions are given as follows

$$A_{II} = \frac{e^{-md}}{4\pi m\varepsilon_M} \cdot \frac{1}{1-k^2e^{-2md}} \tag{3.64}$$

$$B_{II} = \frac{e^{-mD}}{4\pi m\varepsilon_M} \cdot \frac{k}{1-k^2e^{-2md}} \tag{3.65}$$

where $k = \frac{\varepsilon_{LTCC}-\varepsilon_{air}}{\varepsilon_{LTCC}+\varepsilon_{air}}$, and $\varepsilon_M = \frac{\varepsilon_{LTCC}+\varepsilon_{air}}{2}$.

The procedure for obtaining the space domain solution is identical to the previous cases. By using the Taylor series expansion in (3.40), the spectral domain GF is

$$G_{II}^{H_0}(m,z) = \frac{1}{4\pi\varepsilon_M}\left\{\left[\frac{e^{-m(d-z)}}{m} + \frac{k\cdot e^{-m(z+d)}}{m}\right]\cdot\left[1+\sum_{l=1}^{\infty}k^{2l}e^{-2mdl}\right]\right\}. \tag{3.66}$$

The application of the Hankel anti-transform (3.28) translates the spectral domain GF to the spatial domain as

$$G_{II}^{H_0}(\rho,z) = \frac{1}{4\pi\varepsilon_M}\left\{\frac{1}{\sqrt{\rho^2+(d-z)^2}} + \frac{k}{\sqrt{r^2+(z+d)^2}} + \right.$$
$$\left. + \sum_{l=1}^{\infty}\left[\frac{k^{2l}}{\sqrt{\rho^2+(D-z+2dl)^2}} + \frac{k^{2l+1}}{\sqrt{\rho^2+(z+D+2dl)^2}}\right]\right\}. \tag{3.67}$$

As expected, images are built through both interface planes. The main difference with the previous GND case is that all images have the same sign; therefore the GF is not related to a summation of dipoles, but charges. This has important consequences on the interaction at large distance between component parts. In the GND case, it will decay as $1/R^2$, whereas for the open boundary it will be $1/R$.

Point source inside the dielectric

The substrate cross-section of the last case, represented in 3.7d, is divided in four regions and the source is located inside the LTCC. The general solutions of the Green's function, after

applying the two open boundary conditions are

$$G_I^{H_0}(m,z) = A_I e^{mz} \tag{3.68}$$
$$G_{II}^{H_0}(m,z) = A_{II} e^{mz} + B_{II} e^{-mz} \tag{3.69}$$
$$G_{III}^{H_0}(m,z) = A_{III} e^{mz} + B_{III} e^{-mz} \tag{3.70}$$
$$G_{IV}^{H_0}(m,z) = B_{IV} e^{-mz}. \tag{3.71}$$

From the remaining BC, six relationships between integration constants are obtained, i.e.,

$$A_I = A_{II} + B_{II} \tag{3.72}$$
$$A_{II} e^{mh} + B_{II} e^{-mh} = A_{III} e^{mh} + B_{III} e^{-mh} \tag{3.73}$$
$$B_{IV} e^{-md} = A_{III} e^{md} + B_{III} e^{-md} \tag{3.74}$$
$$\varepsilon_{air} A_I = \varepsilon_{LTCC}(A_{II} - B_{II}) \tag{3.75}$$
$$-\varepsilon_{air} B_{IV} e^{-md} = \varepsilon_{LTCC}(A_{III} e^{md} - B_{III} e^{-md}) \tag{3.76}$$
$$-A_{II} e^{mh} + B_{II} e^{-mh} + A_{III} e^{mh} - B_{III} e^{-mh} = -\frac{1}{2\pi\varepsilon_{LTCC} m}. \tag{3.77}$$

Region III is the one of interested. Thus, A_{III} and B_{III} are derived as

$$A_{III} = \frac{k e^{m(h-2d)} + k^2 e^{-m(h+2d)}}{4\pi m \varepsilon_{LTCC}\left(1 - k^2 e^{-2md}\right)} \tag{3.78}$$

$$B_{III} = \frac{e^{mh} + k e^{-mh}}{4\pi m \varepsilon_{LTCC}\left(1 - k^2 e^{-2md}\right)} \tag{3.79}$$

where $k = \frac{\varepsilon_{LTCC} - \varepsilon_{air}}{\varepsilon_{LTCC} + \varepsilon_{air}}$.

Using Taylor series expansion (3.40) and the Hankel anti-transform (3.28), $G_{III}(r,z)$ is expressed as

$$G_{III}(\rho,z) = \frac{1}{4\pi\varepsilon_{LTCC}} \left\{ \frac{1}{\sqrt{\rho^2+(z-h)^2}} + \frac{k}{\sqrt{\rho^2+(z+h)^2}} + \right.$$
$$\frac{k}{\sqrt{\rho^2+(2d-z-h)^2}} + \frac{k^2}{\sqrt{\rho^2+(2d+h-z)^2}} +$$
$$+ \sum_{l=1}^{\infty} k^{2l} \left[\frac{1}{\sqrt{\rho^2+(z-h+2dl)^2}} + \frac{k}{\sqrt{\rho^2+(z+h+2dl)^2}} + \right.$$
$$\left. \left. + \frac{k}{\sqrt{\rho^2+(2d(l+1)-z-h)^2}} + \frac{k^2}{\sqrt{\rho^2+(2d(l+1)+h-z)^2}} \right] \right\}. \quad (3.80)$$

Compared to the previous case, an additional set of image charges has appeared.

3.3.3 Verification

Green's function (3.44), (3.56), (3.67), and (3.80) are going now to be tested using a six layers A6S tape system from Ferro. Each sinterized layer has a thickness of $70\mu m$, a relative permittivity value of $\varepsilon_{LTCC} = 5.6$ and a loss tangent $tg\delta < 0.002$. In this substrate, there can be six metal layers plus a GND plane on the bottom surface. Metals are based on Au with a typical thickness of $5\mu m$; thus, the sheet resistance is about $5.6m\Omega_{\square}$.

Two numerical experiments are carried out. The first one is a study of the convergence of the capacitance value of two $1 \times 1mm^2$ patches separated by a distance of $0.5mm$ using the former GFs. The second one is the comparison of the matrix capacitance coefficients C_{ij} of those patches computed with the analytical expressions and with a method of moments commercial simulator. For the source located on the LTCC-air interface cases, i.e. (3.44) and (3.67), patches are implemented on the interface, whereas for the other two internal source cases, (3.56) and (3.80), patches are embedded at the substrate thickness midpoint, at $210\mu m$. These situations are depicted in Fig.3.9.

A remark on Green's functions behaviour

Before starting with the numerical experiments, it is worth to inspect the qualitative behaviour of the analytical GFs. Fig. 3.10 shows the graphs for the four developed cases. In all of them, the observation point, where a virtual point charge should be placed, is within the z plane of the source; thus, the radial distance ρ is the independent variable (the singularity at $\rho = 0$ has been avoided). In each graph, there are two plots. The continuous line corresponds

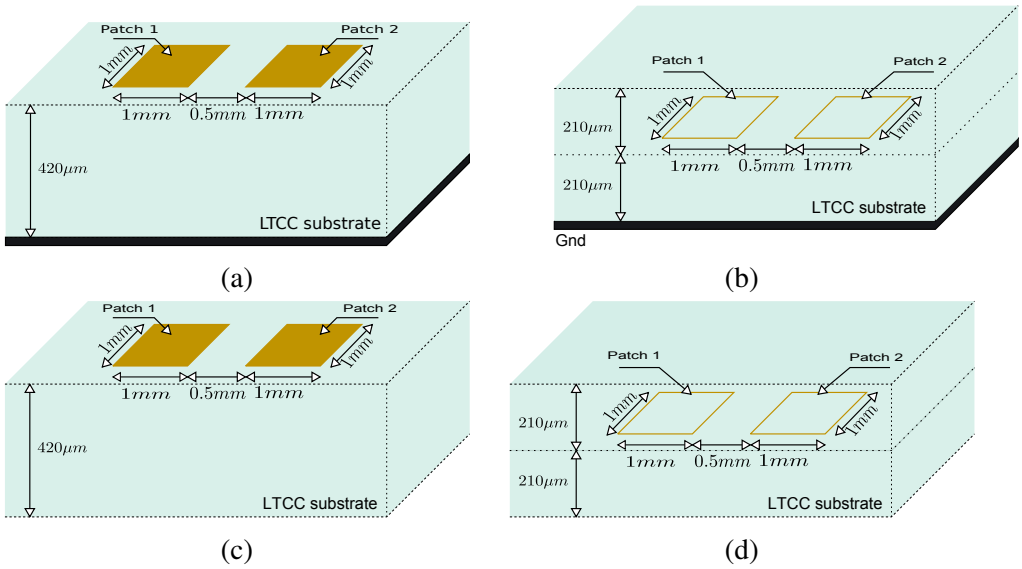

Fig. 3.9 Geometry of the two patches in LTCC substrate: (a) on top of the substrate and with a GND plane; (b) at the midpoint and GND plane; (c) on top, with open boundaries; (b) at the midpoint, with open boundaries.

to the terms out of the summation in (3.44), (3.56), (3.67), and (3.80), i.e. the half space solution. The dashed line is the complete expression where the summation has been trucated at $l = 100$.

The results are quite interesting and they reflect the comments made after the derivation of each analytical GF. For the GND boundary condition (Fig. 3.10a, and Fig. 3.10b), there are two different behaviours for short and large distances being the transition zone a distance of the order of the total substrate thickness d:

- For $\rho << d$, the partial potential value between the point source and a virtual point charge at a distance ρ has a $1/\rho$ shape. This means that the interaction is mainly between both charges; the GND plane (image charge) has no role. Therefore, the evaluation at short distances could be carried out without computing the summation term.

- For $\rho >> d$, the voltage has a $1/\rho^2$ shape, i.e., a dipole decay. Taking as reference the dipole formed by the source and its first image (continuous line), it is clear that the summation of all dipoles has a lower value than this reference. This is easily explained because the sign of dipoles alternates, i.e., $p = 2d(l+1)\cdot(-k)^l$; thus, they cancel partially each other.

- At the transition zone $\rho \approx d$, each term l of the summation can be viewed as a perturbation of the half space solution. This point of view is very interesting because it

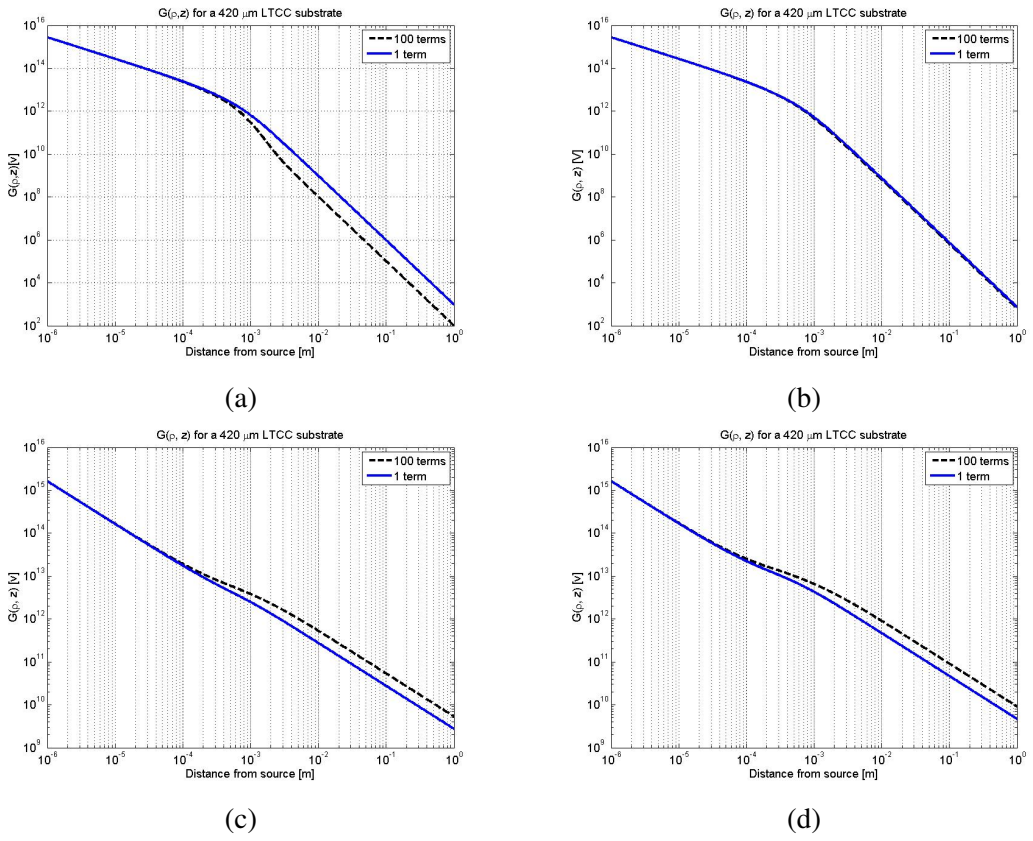

Fig. 3.10 Computation of the four cases of GFs equations, (a) case 1 (eq.3.43), (b) case 2 (eq.3.56), (c) case 3 (eq.3.67) and (d) case 4 (eq. 3.80): (solid line) only the charge source an its first image are considered; (dashed line) 100 terms are considered.

defines the way for truncating the computation of the series according to the distance between elements.

- An additional remark is that, for large distances, the difference between the half space solution and the complete solution is increased when $k \to 1$, i.e. when $\varepsilon_{LTCC} >> \varepsilon_{air}$.

Open boundary cases (Fig. 3.10c, and Fig. 3.10d) show a different behaviour than the GND ones. In the full ρ range, the shape of the partial potential is $1/\rho$. Thus, the influence of all images can be interpreted as a single charge source. The perturbation introduced by the summation terms is an increase of the effective value of the charge source. Thus,

- For $\rho << d$, the main contribution to the potential value is due to the source charge itself.

- For $\rho >> d$, all images must be taken into account, but their effect is like a single point charge source which value is bigger than the original point source.

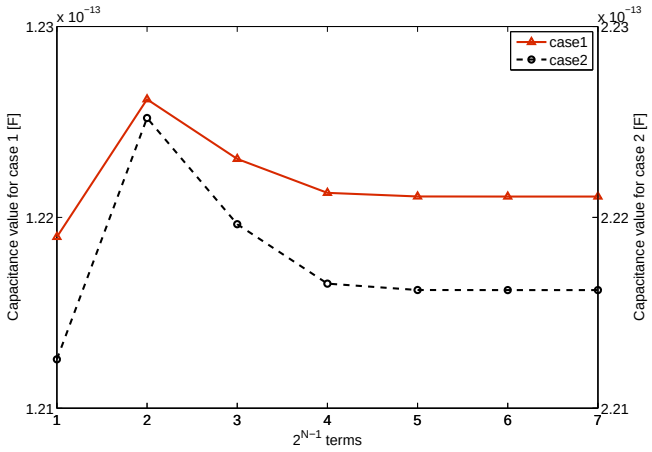

Fig. 3.11 Capacitance vs 2^{N-1} number of terms for LTCC with GND plane: (red $\triangle$) eq. (3.44); (black $\bullet$) eq. (3.56).

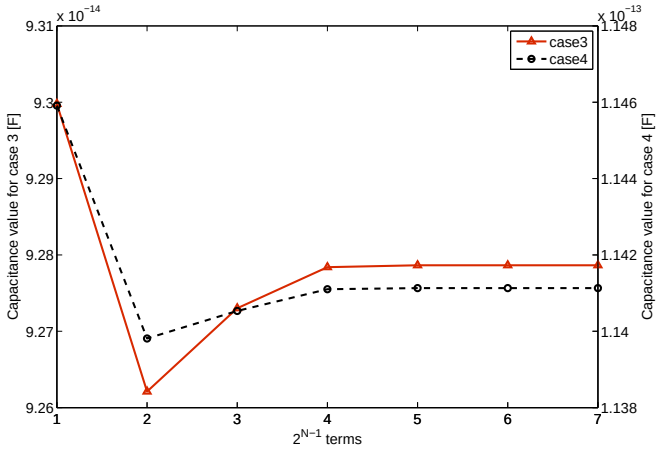

Fig. 3.12 Capacitance vs 2^{N-1} number of terms for LTCC with open boundaries: (red $\triangle$) eq. (3.67); (black $\bullet$) eq. (3.80).

Experiment 1: Convergence

The capacitance between patches, illustrated in Fig. 3.9, is computed with the analytical GF equations (3.44), (3.56), (3.67), and (3.80) as a function of the number of terms used for truncating their respective summation image charges terms. For the calculation, the employed mesh is the one already shown in Fig. 3.6 where patches are divided in square elements of $100 \times 100 \mu m^2$ size. The spatial range where GFs are evaluated is $0 \leq \rho/d \leq 7.7$ that covers the different behaviours of GFs. Notice that the evaluation of GF at $\rho = 0$ does not raise up any singularity when evaluating the double surface integral of the partial potential because the charge is distributed uniformly on the surface of the element.

Table 3.3 Comparison of C_{ij} matrix coefficients with a commercial simulator.

		Eq. (3.44) [fF]	MoM [fF]	Difference
case 1	C_{11}	230.5	231.6	0.475 %
	C_{12}	-6.8	-6.839	0.570 %
	C_{21}	-6.8	-6.839	0.570 %
	C_{22}	230.5	231.6	0.475 %
		Eq. (3.56) [fF]	MoM [fF]	Difference
case 2	C_{11}	424.1	426	0.446 %
	C_{12}	-9.6	-9.557	0.449 %
	C_{21}	-9.6	-9.557	0.449 %
	C_{22}	424.1	426	0.446 %
		Eq. (3.67) [fF]	MoM [fF]	Difference
case 3	C_{11}	101.5	101.9	0.392 %
	C_{12}	-42.1	-42.22	0.284 %
	C_{21}	-42.1	-42.22	0.284 %
	C_{22}	101.5	101.9	0.392 %
		Eq. (3.80) [fF]	MoM [fF]	Difference
case 4	C_{11}	118.4	118.9	0.421 %
	C_{12}	-54.9	-55.1	0.363 %
	C_{21}	-54.9	-55.1	0.363 %
	C_{22}	118.4	118.9	0.421 %

C_{12} and C_{21} are negative by definition.

The results are given in Fig. 3.11 for the GND plane cases and in Fig. 3.12 for the top and bottom open boundaries cases. For all cases, from $N = 5$ (or equivalently $l = 16$) in the truncation of the summation, the capacitance value is almost constant indicating that it has converged without requiring a large computation time.

Experiment 2: computation of the capacitance matrix coefficients C_{ij}

The results obtained from the computation of patches capacitance in the previous experiment are now compared with the values obtained using a method of moments 2.5D full-wave commercial solver. These results are shown in Table 3.3. The maximum difference in any of the coefficients is below 0.6% that denotes that (3.44), (3.56), (3.67), and (3.80) are enough accurate for numerical computation.

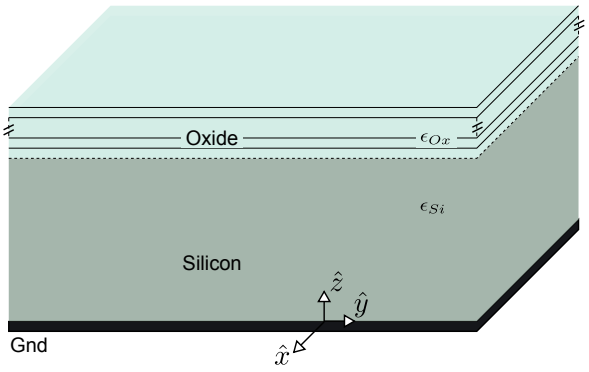

Fig. 3.13 Silicon multilayer substrate.

3.4 Analytical GFs for two-dielectric substrate

Normally, LTCC tape systems do not mix dielectric layers, except for film capacitors implementation where a high-K material is added locally. Then, what are the motivations for developing analytical GF closed-forms for two-dielectric substrates in the spatial domain?

- The first one is that, after the good performance achieved in the development of one-dielectric substrate GFs, it is quite tempting to follow the same path for the two-dielectric substrate GFs.
- The second one is that RFIC silicon substrates could be described with this kind of GFs. Therefore, RFIC components could be modelled using the developed fast PEEC method instead of using compact models. Signal integrity tools could also benefit from this development.
- And last, up to our knowledge, there has not been any previous attempt in the literature to do this task[6].

In actual IC technologies, the substrate is quite complex because a large number (> 10) of metal layers can be stacked up, as shown in Fig. 3.13. As a consequence, the search for an analytical GF is impractical. Nonetheless, by assuming that all dielectric layers are of the same type (silicon oxide), except for the silicon, the substrate can be reduced to a two-dielectric problem with a GND bottom plane and a top open boundary condition. Thus, the substrate is divided in three different permittivity regions: silicon ($\varepsilon_1 = 11.7 \cdot \varepsilon_0$), oxide ($\varepsilon_2 = 3.9 \cdot \varepsilon_0$), and free space ($\varepsilon_3 = 1 \cdot \varepsilon_0$). It is only interesting to find the solution inside the oxide region, including both silicon and air interfaces, because metals can only be placed

[6] In the literature, there are many works related to closed-form Green's function, but they are developed in the spectral domain. The spatial domain anti-transform is only indicated with its integral operator. The same happens with one-dielectric substrates.

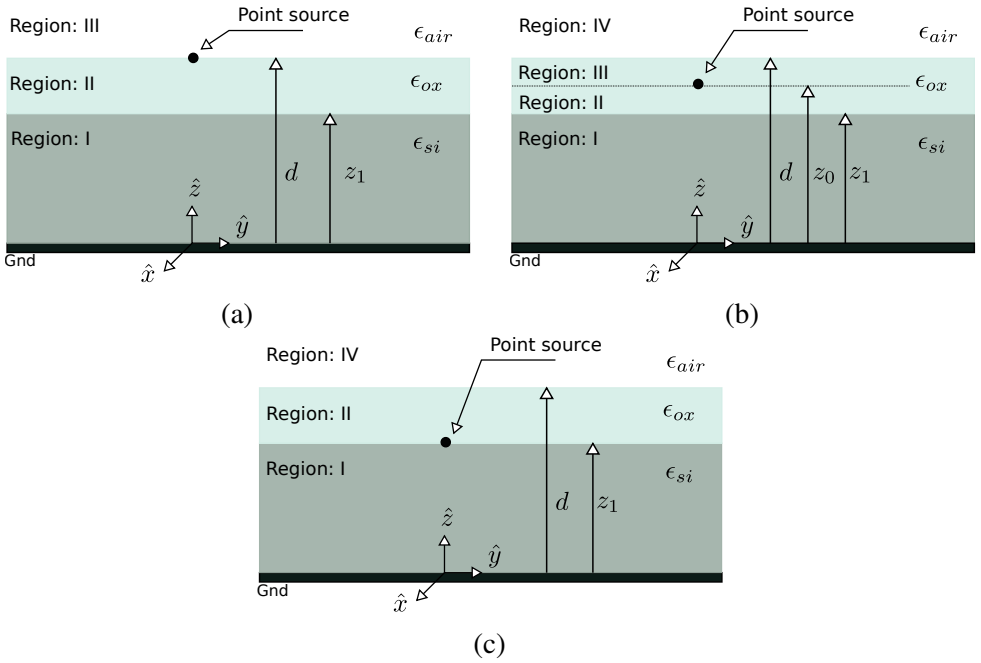

Fig. 3.14 Simplified silicon substrate cross-section showing the location of the charge source: (a) at the top boundary $(\varepsilon_3 - \varepsilon_2)$ interface; (b) inside the oxide (ε_2); (c) at the silicon-oxide $(\varepsilon_1 - \varepsilon_2)$ interface.

there. The calculation is divided in three cases, which are related to the location of the source charge in the oxide region: (i) on the top boundary ($\varepsilon_3 - \varepsilon_2$ interface); (2) inside the oxide dielectric (ε_2); (iii) on the silicon-dielectric boundary ($\varepsilon_1 - \varepsilon_2$ interface).

3.4.1 Analytical GFs closed-forms

Before starting with the analytical development, two comments are issued:

- Be aware that the expressions found are strictly convergent for $\varepsilon_1 \geqslant \varepsilon_2 \geqslant \varepsilon_3$, which is luckily the condition met in silicon substrates. Any other configuration must be studied carefully to avoid the singularities of the spectral domain solution.
- It will be shown that these analytical GFs are not computationally efficient. Nevertheless, their development is by itself enough relevant as a way to test other methods, as it will be shown in Section 3.4.2.

Point source on the dielectric-air interface (case 1)

The cross-section of the substrate is shown in Fig. 3.14a, which is divided in three parts: region I (silicon) has a thickness z_1; region II (oxide) extends the substrate up to d; and region

III (free space) extends indefinitely. The charge source is located at the top boundary of the substrate. As it has been previously mention, the GF of interest is the one related to region II.

After applying the GND and top boundary conditions, the general forms of Green's function at each region are given by

$$G_I^{H_0}(m,z) = A_I\left(e^{mz} - e^{-mz}\right) \tag{3.81}$$

$$G_{II}^{H_0}(m,z) = A_{II}e^{mz} + B_{II}e^{-mz} \tag{3.82}$$

$$G_{III}^{H_0}(m,z) = B_{III}e^{-mz}. \tag{3.83}$$

Using the remaining four boundary conditions

- two continuity at both dielectric interfaces,
- one continuity equation on the derivative at the interface $z = z_1$,
- and the charge discontinuity at $z = d$,

the following system of equations is found for the integration constants

$$A_I\left(e^{mz_1} - e^{-mz_1}\right) = A_{II}e^{mz_1} + B_{II}e^{-mz_1} \tag{3.84}$$

$$A_{II}e^{md} + B_{II}e^{-md} = B_{III}e^{-md} \tag{3.85}$$

$$\varepsilon_1 A_I\left(e^{mz_1} + e^{-mz_1}\right) = \varepsilon_2\left(A_{II}e^{mz_1} - B_{II}e^{-mz_1}\right) \tag{3.86}$$

$$\varepsilon_2\left(A_{II}e^{md} - B_{II}e^{-md}\right) + \varepsilon_3 B_{III}e^{-md} = \frac{1}{2m\pi} \tag{3.87}$$

It is only of interest the determination of constants A_{II} and B_{II}. With (3.84) and (3.86), A_I is cancelled out and a relationship between A_{II} and B_{II} is found:

$$\left(1 + k_1 e^{2mz_1}\right)A_{II} = -\left(1 + k_1 e^{-2mz_1}\right)B_{II} \qquad \textit{where} \quad k_1 = \frac{\varepsilon_1 - \varepsilon_2}{\varepsilon_1 + \varepsilon_2}. \tag{3.88}$$

From (3.85) and (3.87), B_{III} is also cancelled out and another relationship between A_{II} and B_{II} arises:

$$A_{II} - k_2 B_{II}e^{-2md} = \frac{e^{-md}}{2\pi(\varepsilon_2 + \varepsilon_3)} \qquad \textit{where} \quad k_2 = \frac{\varepsilon_2 - \varepsilon_3}{\varepsilon_2 + \varepsilon_3}. \tag{3.89}$$

Solving (3.88) and (3.89), the next expressions are obtained:

$$A_{II} = \frac{1}{4m\pi\varepsilon_m} \cdot \frac{(1 + k_1 e^{-2mz_1})e^{-md}}{1 + k_1 e^{-2mz_1} + k_2 e^{-2md} + k_1 k_2 e^{-2m(d-z_1)}} \tag{3.90}$$

$$B_{II} = \frac{-1}{4m\pi\varepsilon_m} \cdot \frac{(1+k_1 e^{2mz_1})e^{-md}}{1+k_1 e^{-2mz_1}+k_2 e^{-2md}+k_1 k_2 e^{-2m(d-z_1)}} \tag{3.91}$$

where $\varepsilon_m = (\varepsilon_2+\varepsilon_3)/2$.

The substitution of (3.90) and (3.91) back into (3.85) gives the GF expression of region II in the transformed domain, i.e.,

$$G_{II}^{H_0}(m,z) = \frac{1}{4m\pi\varepsilon_m} \frac{(1+k_1 e^{-2mz_1})e^{-m(d-z)} - (1+k_1 e^{2mz_1})e^{-m(d+z)}}{1+k_1 e^{-2mz_1}+k_2 e^{-2md}+k_1 k_2 e^{-2m(d-z_1)}} \tag{3.92}$$

where

$$k_1 = \frac{\varepsilon_1-\varepsilon_2}{\varepsilon_1+\varepsilon_2}, \qquad k_2 = \frac{\varepsilon_2-\varepsilon_3}{\varepsilon_2+\varepsilon_3}, \quad \textit{and} \quad \varepsilon_m = \frac{\varepsilon_2+\varepsilon_3}{2}.$$

Now, the key point is to find the Hankel anti-transform of (3.92). Let us define its denominator as $1+X$ where $X = 1+k_1 e^{-2mz_1}+k_2 e^{-2md}+k_1 k_2 e^{-2m(d-z_1)}$. The factor $1/(1+X)$ can be substituted by its Taylor's series if one assures the convergence of the expansion. Instead of developing around $X=0$, it must be done around $X = k_1+k_2+k_1k_2 \equiv K$, thus the distance to the singularity, at $X=-1$, is far enough from the domain of interest. Then, the denominator becomes

$$\left.\frac{1}{1+X}\right|_{X=K} = \frac{1}{1+K}\sum_{n=0}^{\infty} a_n (X-K)^n \tag{3.93}$$

where $a_n = \left(\frac{-1}{1+K}\right)^n$. The term $\sum_{n=0}^{\infty} a_n (X-K)^n$ must be further developed by applying the binomial expansion, i.e.

$$\begin{aligned} G_{II}^{H_0}(m,z) = \frac{1}{4m\pi\varepsilon_m(K+1)} &\left(e^{-m(d-z)} - e^{-m(d+z)} + \right. \\ &\left. + k_1 e^{-m(2z_1+d-z)} - k_1 e^{-m(-2z_1+d+z)}\right) \cdot \left[1 + \sum_{n=1}^{\infty}\sum_{i=0}^{n}\sum_{j=0}^{i}\sum_{k=0}^{j}\binom{n}{i}\cdot\right. \\ &\left.\cdot\binom{i}{j}\binom{j}{k}\frac{(-1)^{n+k}}{(c+1)^n}(k_1)^{n-i+j-k}(k_2)^{i-k}c^k e^{-2m(z_1(n-i-j+k)+d(i-k)}\right] \end{aligned} \tag{3.94}$$

This expression can be now anti-transformed by noting that

$$H_0^{-1}\left\{\frac{k e^{m|z-z'|}}{m}\right\} = \frac{k}{\sqrt{\rho^2+(z-z')^2}}. \tag{3.95}$$

Therefore, the spectral domain GF expression of the region II is the next one:

$$
\begin{aligned}
G_{II}(\rho,z) = \frac{1}{4\pi\varepsilon_m(K+1)}\Bigg[& \frac{1}{\sqrt{\rho^2+(-z+d)^2}} - \frac{1}{\sqrt{\rho^2+(z+d)^2}} + \\
& + \frac{k_1}{\sqrt{\rho^2+(-z+d+2z_1)^2}} - \frac{k_1}{\sqrt{\rho^2+(z+d-2z_1)^2}} + \\
& + \sum_{n=1}^{\infty}\sum_{i=0}^{n}\sum_{j=0}^{i}\sum_{l=0}^{j}\binom{n}{i}\binom{i}{j}\binom{j}{l}\frac{(-1)^{n+l}}{(K+1)^n}(k_1)^{n-i+j-l}(k_2)^{i-l}K^l \cdot \\
& \cdot\Bigg(\frac{1}{\sqrt{\rho^2+(-z+d(2i-2l+1)+2z_1(n-i-j+l)))^2}} - \\
& - \frac{1}{\sqrt{\rho^2+(z+d(2i-2l+1)+2z_1(n-i-j+l))^2}} + \\
& + \frac{k_1}{\sqrt{\rho^2+(-z+d(2i-2l+1)+2z_1(n-i-j+l+1))^2}} - \\
& - \frac{k_1}{\sqrt{\rho^2+(z+d(2i-2l+1)+2z_1(n-i-j+l-1))^2}}\Bigg)\Bigg]
\end{aligned}
\tag{3.96}
$$

where

$$
k_1 = \frac{\varepsilon_1-\varepsilon_2}{\varepsilon_1+\varepsilon_2}; \qquad k_2 = \frac{\varepsilon_2-\varepsilon_3}{\varepsilon_2+\varepsilon_3} \qquad \textit{and} \qquad K = k_1+k_2+k_1k_2.
$$

Point source inside the dielectric (case 2)

The substrate cross-section is shown in Fig. 3.14b, which is divided in four regions. Silicon extends to $z = z_1$; oxide, to $z = d$; and the charge source is located at z_0 where the condition $z_1 < z_0 < d$ holds. Boundary conditions are defined next:

- bottom GND plane and top open boundary;
- continuity between regions I and II, where $z = z_1$;
- continuity between regions *II* and *III*, where $z = z_0$;
- continuity between regions *III* and *IV*, where $z = d$;
- continuity on GF derivative between regions *I* and *II*, where $z = z_1$;
- continuity on GF derivative between regions *III* and *IV*, where $z = d$;
- and discontinuity caused by the source between regions *II* and *III*, where $z = z_0$.

Their application to the general form of GFs leads to the next relationships between integration constants:

$$A_I\left(e^{mz_1}-e^{-mz_1}\right)=A_{II}e^{mz_1}+B_{II}e^{-mz_1} \tag{3.97}$$

$$A_{II}e^{mz_0}+B_{II}e^{-mz_0}=A_{III}e^{mz_0}+B_{III}e^{-mz_0} \tag{3.98}$$

$$B_{IV}e^{-md}=A_{III}e^{md}+B_{III}e^{-md} \tag{3.99}$$

$$\varepsilon_1 A_I\left(e^{mz_1}+e^{-mz_1}\right)=\varepsilon_2\left(A_{II}e^{mz_1}-B_{II}e^{-mz_1}\right) \tag{3.100}$$

$$\varepsilon_2\left(A_{III}e^{md}-B_{III}e^{-md}\right)=-\varepsilon_3 B_{IV}e^{-md} \tag{3.101}$$

$$A_{III}e^{mz_0}-B_{III}e^{-mz_0}-A_{II}e^{mz_0}+B_{II}e^{-mz_0}=-\frac{1}{2\pi\varepsilon_2 m}. \tag{3.102}$$

GFs of interest are G_{II} and G_{III}[7]. With (3.97) and (3.100), A_I is eliminated and the next relationship between A_{II} and B_{II} is obtained:

$$A_{II}=-\frac{k_1e^{-2mz_1}+1}{k_1e^{2mz_1}+1}B_{II} \qquad where \quad k_1=\frac{\varepsilon_1-\varepsilon_2}{\varepsilon_1+\varepsilon_2}. \tag{3.103}$$

Using (3.99) and (3.101), A_I is again cancelled out, thus A_{III} and B_{III} are related by

$$A_{III}=k_2e^{-2md}B_{III} \quad where \quad k_2=\frac{\varepsilon_2-\varepsilon_3}{\varepsilon_2+\varepsilon_3}. \tag{3.104}$$

Adding and subtracting (3.102) and (3.98), two more relationships between A_{II} and A_{III}, and between B_{II} and B_{III} are found, i.e.,

$$A_{II}-A_{III}=\frac{e^{-mz_0}}{4\pi\varepsilon_2 m} \tag{3.105}$$

$$B_{II}-B_{III}=-\frac{e^{mz_0}}{4\pi\varepsilon_2 m}. \tag{3.106}$$

Eqs. (3.103), (3.104), (3.105) and (3.106) form an algebraic system for solving A_{II}, B_{II}, A_{III} and B_{III}, i.e., the coefficients of G_{II} and G_{III}. Their solution are given by

$$A_{II}=\frac{1}{4\pi\varepsilon_2 m}\cdot\frac{e^{-mz_0}\left[1+k_1e^{-2mz_1}\right]\left[1+k_2e^{-2m(d-z_0)}\right]}{1+k_1^{-2mz_1}+k_2e^{-2md}+k_1k_2e^{-2m(d-z_1)}}, \tag{3.107}$$

[7]In fact, it is only necessary to calculate G_{II} or G_{III}, not both, because the materials of the substrate are reciprocal.

$$B_{II} = \frac{-1}{4\pi\varepsilon_2 m} \cdot \frac{e^{-mz_0}\left[1+k_1e^{2mz_1}\right]\left[1+k_2e^{-2m(d-z_0)}\right]}{1+k_1^{-2mz_1}+k_2e^{-2md}+k_1k_2e^{-2m(d-z_1)}}, \tag{3.108}$$

$$A_{III} = \frac{1}{4\pi\varepsilon_2 m} \cdot \frac{k_2e^{-2mD}\left(e^{mz_0}\left[1+k_1e^{-2mz_1}\right]-e^{-mz_0}\left[1+k_1e^{2mz_1}\right]\right)}{1+k_1^{-2mz_1}+k_2e^{-2md}+k_1k_2e^{-2m(d-z_1)}}, \tag{3.109}$$

$$B_{III} = \frac{1}{4\pi\varepsilon_2 m} \cdot \frac{e^{mz_0}\left[1+k_1e^{-2mz_1}\right]-e^{-mz_0}\left[1+k_1e^{2mz_1}\right]}{1+k_1^{-2mz_1}+k_2e^{-2md}+k_1k_2e^{-2m(d-z_1)}}. \tag{3.110}$$

Then, both Green's functions in the transformed domain read as follows

$$\begin{aligned} G_{II}^{H_0}(m,z) = \frac{1}{2\pi m\varepsilon_2} \cdot \frac{1}{1+K} \cdot \Big\{ & e^{-m(z_0-z)} - e^{-m(z_0+z)} + \\ & + k_1e^{-m(2z_1+z_0-z)} - k_1e^{-m(-2z_1+z_0+z)} + k_2e^{-m(2z_1+z_0-z)} - \\ & - k_2e^{-m(2d-z_0+z)} + k_1k_2e^{-m(2d+2z_1-z_0-z)} - k_1k_2e^{-m(2d-2z_1-z_0+z)} \Big\}, \end{aligned} \tag{3.111}$$

$$\begin{aligned} G_{III}^{H_0}(m,z) = \frac{1}{2\pi m\varepsilon_2} \cdot \frac{1}{1+K} \cdot \Big\{ & e^{-m(z-z_0)} - e^{-m(z+z_0)} + \\ & + k_1e^{-m(2z_1-z_0+z)} - k_1e^{-m(-2z_1+z_0+z)} + k_2e^{-m(2d-z_0-z)} - \\ & - k_2e^{-m(2d+z_0-z)} + k_1k_2e^{-m(2d+2z_1-z_0-z)} - k_1k_2e^{-m(2d-2z_1+z_0-z)} \Big\} \end{aligned} \tag{3.112}$$

where $k_1 = \frac{\varepsilon_1-\varepsilon_2}{\varepsilon_1+\varepsilon_2}$, $k_2 = \frac{\varepsilon_2-\varepsilon_3}{\varepsilon_2+\varepsilon_3}$, and $K = k_1e^{-2mz_1} + k_2e^{-2mz_0} + k_1k_2e^{-2m(z_0-z_1)}$. Eqs. (3.111) and (3.112) can be anti-transformed back to the spatial domain by applying the same former procedure for *case 1*. Using the Taylor's series expansion (3.93) for developing the denominator as a series of charges, spectral domain expressions are rearranged as

$$\begin{aligned} G_{II}^{H_0}(m,z) = \frac{1}{4\pi\varepsilon_2 m(1+K)} \Big\{ & k_1k_2e^{-m(2d+2z_1-z_0-z)} - \\ & - k_1k_2e^{-m(2d-2z_1-z_0+z)} + k_2e^{-m(2d-z_0-z)} - k_2e^{-m(2d-z_0+z)} + \\ & + k_1e^{-m(2z_1+z_0-z)} - k_1e^{-m(-2z_1+z_0+z)} + e^{-m(z_0-z)} - \\ & - e^{-m(z_0+z)} \Big\} \cdot \left(1 + \sum_{n=1}^{\infty} \sum_{i=0}^{n} \sum_{j=0}^{i} \sum_{l=0}^{j} \binom{n}{i} \binom{i}{j} \binom{j}{l} \cdot \right. \\ & \left. \cdot \frac{(-1)^{n+l}}{(C+1)^n} \cdot (k_1)^{n-i+j-l} \cdot (k_2)^{i-l} \cdot K^l \cdot e^{-2m(z_1(n-i-j+l)+d(i-l))} \right) \end{aligned} \tag{3.113}$$

$$G_{III}^{H_0}(m,z) = \frac{1}{4\pi\varepsilon_2 m(1+K)} \Big\{ k_1 k_2 e^{-m(2d+2z_1-z_0-z)} - \\ - k_1 k_2 e^{-m(2d-2z_1+z_0-z)} + k_2 e^{-m(2d-z_0-z)} - k_2 e^{-m(2d+z_0-z)} + \\ + k_1 e^{-m(2z_1-z_0+z)} - k_1 e^{-m(-2z_1+z_0+z)} + e^{-m(-z_0+z)} - \\ - e^{-m(z_0+z)} \Big\} \cdot \Bigg(1 + \sum_{n=1}^{\infty} \sum_{i=0}^{n} \sum_{j=0}^{i} \sum_{l=0}^{j} \binom{n}{i} \binom{i}{j} \binom{j}{l} \cdot \\ \cdot \frac{(-1)^{n+l}}{(K+1)^n} \cdot (k_1)^{n-i+j-l} \cdot (k_2)^{i-l} \cdot K^l \cdot e^{-2m(z_1(n-i-j+l)+d(i-l))} \Bigg). \quad (3.114)$$

To final with, the anti-transformation pair (3.95) is used to recover the spatial domain analytical solution of (3.113) and (3.114), i.e.,

$$
\begin{aligned}
G_{II}(\rho,z) = \frac{1}{4\pi\varepsilon_2(1+K)} \cdot \Bigg(& \frac{1}{\sqrt{\rho^2+(z_0-z)^2}} - \frac{1}{\sqrt{\rho^2+(z_0+z)^2}} + \\
& + \frac{k_1}{\sqrt{\rho^2+(2z_1+z_0-z)^2}} - \frac{k_1}{\sqrt{\rho^2+(-2z_1+z_0+z)^2}} + \\
& \frac{k_2}{\sqrt{\rho^2+(2d-z_0-z)^2}} - \frac{k_2}{\sqrt{\rho^2+(2d-z_0+z)^2}} + \\
& + \frac{k_1k_2}{\sqrt{\rho^2+(2d+2z_1-z_0-z)^2}} - \frac{k_1k_2}{\sqrt{\rho^2+(2d-2z_1-z_0+z)^2}} + \\
& + \sum_{n=1}^{\infty}\sum_{i=0}^{n}\sum_{j=0}^{i}\sum_{l=0}^{j} \binom{n}{i}\binom{i}{j}\binom{j}{l} \cdot \frac{(-1)^{n+l}}{(K+1)^n} \cdot (k_1)^{n-i+j-l} \cdot (k_2)^{i-l} \cdot K^l \cdot \\
& \cdot \Bigg[\frac{1}{\sqrt{\rho^2+(z_0-z+2z_1(n-i-j+l)+2d(i-l))^2}} - \\
& - \frac{1}{\sqrt{\rho^2+(z_0+z+2z_1(n-i-j+l)+2d(i-l))^2}} + \\
& + \frac{k_1}{\sqrt{\rho^2+(2z_1+z_0-z+2z_1(n-i-j+l)+2d(i-l))^2}} - \\
& - \frac{k_1}{\sqrt{\rho^2+(-2z_1+z_0+z+2z_1(n-i-j+l)+2d(i-l))^2}} \\
& + \frac{k_2}{\sqrt{\rho^2+(2d-z_0-z+2z_1(n-i-j+l)+2d(i-l))^2}} - \\
& - \frac{k_2}{\sqrt{\rho^2+(2d-z_0+z+2z_1(n-i-j+l)+2d(i-l))^2}} \\
& + \frac{k_1k_2}{\sqrt{\rho^2+(2d+2z_1-z_0-z+2z_1(n-i-j+l)+2d(i-l))^2}} - \\
& - \frac{k_1k_2}{\sqrt{\rho^2+(2d-2z_1-z_0+z+2z_1(n-i-j+l)+2d(i-l))^2}} \Bigg] \Bigg)
\end{aligned}
\tag{3.115}
$$

$$
\begin{aligned}
G_{III}(\rho,z) = \frac{1}{4\pi\varepsilon_2(1+K)} \cdot \Bigg(& \frac{1}{\sqrt{\rho^2+(-z_0+z)^2}} - \frac{1}{\sqrt{\rho^2+(z_0+z)^2}} + \\
& + \frac{k_1}{\sqrt{\rho^2+(2z_1-z_0+z)^2}} - \frac{k_1}{\sqrt{\rho^2+(-2z_1+z_0+z)^2}} + \\
& + \frac{k_2}{\sqrt{\rho^2+(2d-z_0-z)^2}} - \frac{k_2}{\sqrt{\rho^2+(2d+z_0-z)^2}} + \\
& + \frac{k_1k_2}{\sqrt{\rho^2+(2d+2z_1-z_0-z)^2}} - \frac{k_1k_2}{\sqrt{\rho^2+(2d-2z_1+z_0-z)^2}} + \\
& + \sum_{n=1}^{\infty}\sum_{i=0}^{n}\sum_{j=0}^{i}\sum_{l=0}^{j} \binom{n}{i}\binom{i}{j}\binom{j}{l} \cdot \frac{(-1)^{n+l}}{(K+1)^n} \cdot (k_1)^{n-i+j-l} \cdot (k_2)^{i-l} \cdot K^l \cdot \\
& \cdot \Bigg[\frac{1}{\sqrt{\rho^2+(-z_0+z+2z_1(n-i-j+l)+2d(i-l))^2}} - \\
& - \frac{1}{\sqrt{\rho^2+(z_0+z+2z_1(n-i-j+l)+2d(i-l))^2}} + \\
& + \frac{k_1}{\sqrt{\rho^2+(2z_1-z_0+z+2z_1(n-i-j+l)+2d(i-l))^2}} - \\
& - \frac{k_1}{\sqrt{\rho^2+(-2z_1+z_0+z+2z_1(n-i-j+l)+2d(i-k))^2}} \\
& + \frac{k_2}{\sqrt{\rho^2+(2d-z_0-z+2z_1(n-i-j+l)+2d(i-k))^2}} - \\
& - \frac{k_2}{\sqrt{\rho^2+(2d+z_0-z+2z_1(n-i-j+l)+2d(i-k))^2}} \\
& + \frac{k_1k_2}{\sqrt{\rho^2+(2d+2z_1-z_0-z+2z_1(n-i-j+l)+2d(i-l))^2}} - \\
& - \frac{k_1k_2}{\sqrt{\rho^2+(2d-2z_1+z_0-z+2z_1(n-i-j+l)+2d(i-l))^2}} \Bigg] \Bigg)
\end{aligned}
\tag{3.116}
$$

where

$$
k_1 = \frac{\varepsilon_1-\varepsilon_2}{\varepsilon_1+\varepsilon_2}; \qquad k_2 = \frac{\varepsilon_2-\varepsilon_3}{\varepsilon_2+\varepsilon_3} \qquad \textit{and} \qquad K = k_1+k_2+k_1k_2.
$$

Point source on the silicon-dielectric interface (case 3)

In this last case, the charge source is located at the silicon-oxide interface $z = z_1$. The region of interest is number II, the one associated to the oxide region. In Fig. 3.14c, the cross-section of the substrate is depicted.

After applying the ground plane condition, $G_I^{H_0}(m,0) = 0$, and the top open boundary, $G_{III}^{H_0}(m, z \to \infty) = 0$, the remaining BCs give the next relationships between integration constants

- from the continuity of $G_I^{H_0}$ and $G_{II}^{H_0}$ at $z = z_1$

$$A_I \left(e^{mz_1} - e^{-mz_1}\right) = A_{II} e^{mz_1} + B_{II} e^{-mz_1}, \tag{3.117}$$

- from the continuity between regions *II* and *III* at $z = d$

$$B_{III} e^{-md} = A_{II} e^{md} + B_{II} e^{-md}, \tag{3.118}$$

- from the continuity of the derivative of GF at $z = d$

$$-\varepsilon_3 B_{III} e^{-md} = \varepsilon_2 \left(A_{II} e^{md} - B_{II} e^{-md}\right), \tag{3.119}$$

- and, from the discontinuity in the first derivative at $z = z_1$ due to the source

$$\varepsilon_2 \left(A_{II} e^{mz_1} - B_{II} e^{-mz_1}\right) - \varepsilon_1 A_I \left(e^{mz_1} + e^{-mz_1}\right) = -\frac{1}{2\pi m}. \tag{3.120}$$

It is only necessary to determine constants A_{II} and B_{II}. From (3.118) and (3.119), the next relationship between A_{II} and B_{II} is found by cancelling out B_{III}:

$$A_{II} = k_2 \cdot B_{II} \cdot e^{-2md} \tag{3.121}$$

where $k_2 = (\varepsilon_2 - \varepsilon_3)/(\varepsilon_2 + \varepsilon_3)$. Then, eqs. (3.117) and (3.120) are used to find a second relationship between A_{II} and B_{II} through the elimination of A_I, i.e.,

$$A_{II} \left(k_1 e^{2mz_1} + 1\right) + B_{II} \left(k_1 e^{-2mz_1} + 1\right) = \frac{e^{mz_1} - e^{-mz_1}}{2\pi m(\varepsilon_1 + \varepsilon_2)} \tag{3.122}$$

where $k_1 = (\varepsilon_1 - \varepsilon_2)/(\varepsilon_1 + \varepsilon_2)$. From (3.121) and (3.122), A_{II} and B_{II} are solved, i.e.,

$$A_{II} = \frac{1}{4\pi m \varepsilon_m} \cdot \frac{k_2 e^{-2md}\left(e^{mz_1} - e^{-mz_1}\right)}{1 + k_1 e^{-2mz_1} + k_2 e^{-2md} + k_1 k_2 e^{-2m(d-z_1)}} \tag{3.123}$$

$$B_{II} = \frac{1}{4\pi m \varepsilon_m} \cdot \frac{e^{mz_1} - e^{-mz_1}}{1 + k_1 e^{-2mz_1} + k_2 e^{-2md} + k_1 k_2 e^{-2m(d-z_1)}} \tag{3.124}$$

where $\varepsilon_m = (\varepsilon_1 + \varepsilon_2)/2$ and $G_{II}^{H_0}(m,z)$ is written as

$$G_{II}^{H_0}(m,z) = \frac{1}{4\pi m \varepsilon_m} \cdot \frac{(k_2 e^{-m(2d-z)} + e^{-mz})(e^{mz_1} - e^{-mz_1})}{1 + k_1 e^{-2mz_1} + k_2 e^{-2md} + k_1 k_2 e^{-2m(d-z_1)}} \tag{3.125}$$

where

$$k_1 = \frac{\varepsilon_1 - \varepsilon_2}{\varepsilon_1 + \varepsilon_2}, \quad k_2 = \frac{\varepsilon_2 - \varepsilon_3}{\varepsilon_2 + \varepsilon_3}, \ \textit{and} \quad \varepsilon_m = \frac{\varepsilon_1 + \varepsilon_2}{2}.$$

As formerly done, the application of the Taylor's series expansion (3.93) casts (3.125) as a summation in term of charge images as follows

$$\begin{aligned} G_{II}^{H_0}(m,z) = \frac{1}{4\pi m \varepsilon_m (K+1)} \left(k_2 e^{-m(2d-z)} + e^{-mz}\right) \left(e^{mz_1} - e^{-mz_1}\right) \cdot \\ \cdot \left(1 + \sum_{n=1}^{\infty} \sum_{i=0}^{n} \sum_{j=0}^{i} \sum_{l=0}^{j} \binom{n}{i} \binom{i}{j} \binom{j}{l} \frac{(-1)^{n+l}}{(K+1)^n} k_1^{n-i+j-l} \cdot k_2^{i-l} \cdot \right. \\ \left. \cdot K^l \cdot e^{-2m[z_1(n-i-j+l)+d(i-l)]} \right), \end{aligned} \tag{3.126}$$

from which the spatial domain analytical expression is found by applying the anti-transformed pair (3.95), i.e.,

$$\begin{aligned} G(\rho,z)_{II} = \frac{1}{4\pi\varepsilon_m(K+1)} \left[\frac{1}{\sqrt{\rho^2 + (z-z_1)^2}} - \frac{1}{\sqrt{\rho^2 + (z+z_1)^2}} + \right. \\ + \frac{k_2}{\sqrt{\rho^2 + (2d - z_1 - z)^2}} - \frac{k_2}{\sqrt{\rho^2 + (2d + z_1 - z)^2}} + \\ + \sum_{n=1}^{\infty} \sum_{i=0}^{n} \sum_{j=0}^{i} \sum_{l=0}^{j} \binom{n}{i} \binom{i}{j} \binom{j}{l} \frac{(-1)^{n+l}}{(K+1)^n} (k_1)^{n-i+j-l} (k_2)^{i-l} K^l * \\ * \left(\frac{1}{\sqrt{\rho^2 + (z - z_1 + 2z_1(n-i-j+l) + 2d(i-l))^2}} - \right. \\ - \frac{1}{\sqrt{\rho^2 + (z + z_1 + 2z_1(n-i-j+l) + 2d(i-l))^2}} + \\ + \frac{k_2}{\sqrt{\rho^2 + (2d - z_1 - z + 2z_1(n-i-j+l) + 2d(i-l))^2}} - \\ \left. \left. - \frac{k_2}{\sqrt{\rho^2 + (2d + z_1 - z + 2z_1(n-i-j+l) + 2d(i-l))^2}} \right) \right] \end{aligned} \tag{3.127}$$

Table 3.4 Characteristics of Silicon substrate

Property	Value
Oxide relative permittivity	ε_r=11.7
Silicon relative permittivity	ε_r=3.9
Silicon thickness	725 μm
Oxide thickness	5 μm

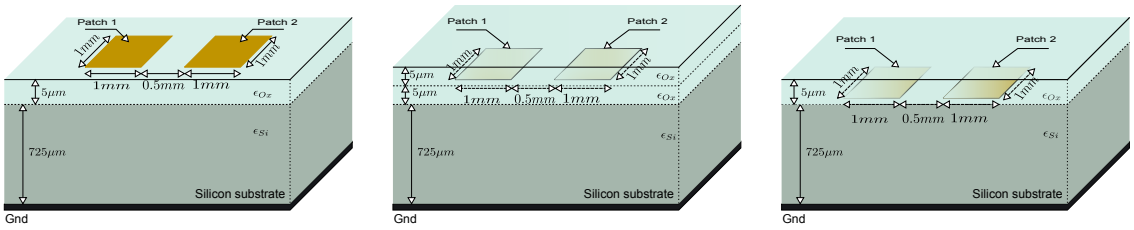

(a) case 1 (b) case 2 (c) case 3

Fig. 3.15 3D geometry of silicon substrate showing the location of the two patches: (a) on the dielectric-air interface, (b) inside the dielectric , and (c) on the silicon-dielectric interface.

where

$$k_1 = \frac{\varepsilon_1 - \varepsilon_2}{\varepsilon_1 + \varepsilon_2}; \qquad k_2 = \frac{\varepsilon_2 - \varepsilon_3}{\varepsilon_2 + \varepsilon_3} \qquad \textit{and} \qquad K = k_1 + k_2 + k_1 k_2.$$

Verification

To demonstrate the validity of (3.96), (3.115), and (3.127), they have been compared with a method of moments 2.5D commercial software. In Table 3.4, the main properties of the substrate are listed. For the three involved cases, the geometry of the problem is shown in Fig. 3.15 and the mesh is the one already shown in Fig. 3.6.

Before proceeding with the validation, the convergence of the analytical expressions is checked by simulating the capacitance value between patches as a function of the numbers of terms used for truncating the quadruple summation of (3.96), (3.115), and (3.127). The results are given in Fig.3.16. For $N \geqslant 5$, the capacitance value has reached a constant value for the three cases.

The comparison with the MoM simulator is given on Table 3.5. Differences in the computation of the capacitance matrix coefficients is less than 0.5 % for the three cases. Although the accuracy of developed GF is good enough, the number of terms of the quadruple summation in the three cases above (3.96), (3.115), and (3.127) increases very fast with increasing n. For instance, setting $n = 12$, the calculation of one partial coefficient P_{ij} (see eqn.(3.3)) involves the evaluation of $8 \cdot 10^3$ double surface integral terms. This brute force

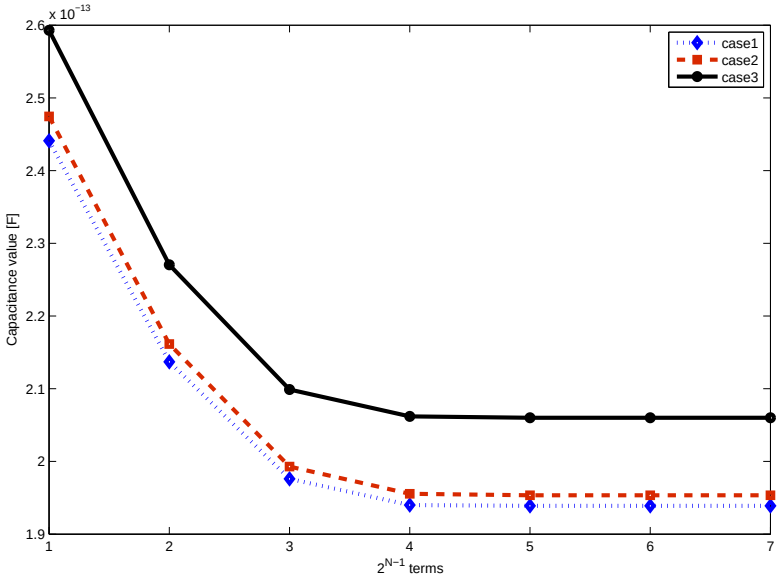

Fig. 3.16 Capacitance value depending on 2^{N-1} terms: (blue $\Diamond$) case 1; (red $\square$) case 2; (black $\bullet$) case 3.

Table 3.5 Comparison of the capacitance matrix coefficients C_{ij}

		GF (eq.3.96) [fF]	MoM [fF]	Difference
case 1	C_{11}	345	346.6	0.46 %
	C_{12}	-21.4	-21.39	0.047 %
	C_{21}	-21.4	-21.39	0.047 %
	C_{22}	345	346.6	0.46 %
		GF (eq.3.115) [fF]	MoM [fF]	Difference
case 2	C_{11}	347.3	348.8	0.43 %
	C_{12}	-21.7	-21.7	0.0 %
	C_{21}	-21.7	-21.7	0.0 %
	C_{22}	347.3	348.8	0.43 %
		GF (eq.3.127) [fF]	MoM [fF]	Difference
case 3	C_{11}	364.2	365.8	0.16 %
	C_{12}	-23.9	-23.96	0.25 %
	C_{21}	-23.9	-23.96	0.25 %
	C_{22}	364.2	365.8	0.16 %

C_{12} and C_{21} are negative by definition.

computation cannot compete with actual numerical methods unless the evaluation can be lowered to a few tens of integrals. An alternative is found next.

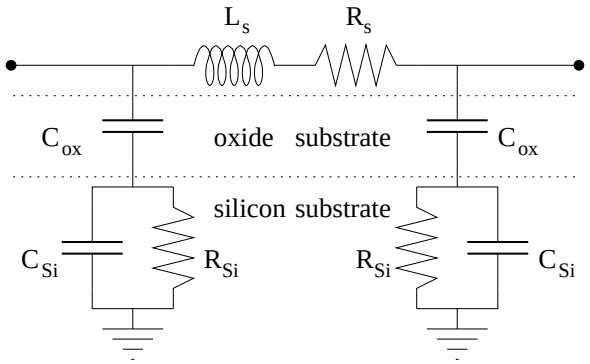

Fig. 3.17 Classical compact model for an integrated inductor.

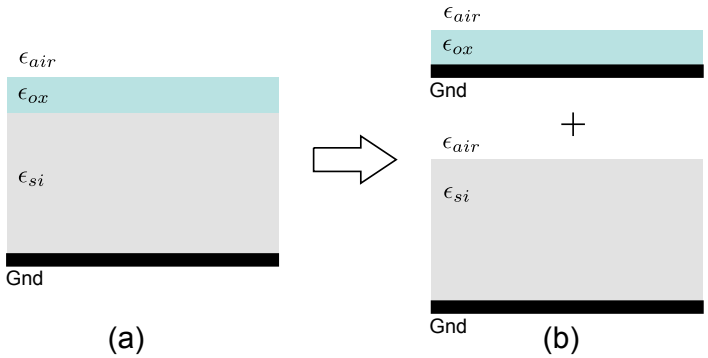

Fig. 3.18 (a) Silicon substrate, (b) substrate separation into two sections.

3.4.2 Heuristic approach

Eqs. (3.96), (3.115), and (3.127) have shown the feasibility and accuracy to describe the electrical part of an IC substrate using an analytical Green's function. However, some sort of designer's wisdom is lost when the computation of capacitance is viewed as a complex infinite series expansion of equivalent images. To recover the designer's perspective, we explore an heuristic approximation for the two-dielectric substrate problem that has its roots in the compact modeling of integrated inductors. In that framework, as shown in Fig. 3.17, the substrate is typically described using the C_{ox}, C_{Si}, and R_{Si} lumped components. The reason for choosing this description is because the electrical part of the model resembles a capacitor made with two dielectric materials, the oxide and the silicon. This view can be extrapolated to the computation of Green's function by assuming that the IC substrate can be divided in two parts: the complete set of dielectric layers, all them having the same permittivity value; and the silicon substrate. This idea is sketched in Fig. 3.18. Notice that the two new substrates inherit the top open boundary condition of the initial substrate. This approximation is valid meanwhile the thickness of the oxide is very small compared to the silicon. The analytical Green's function of this approach is simply evaluated by adding the

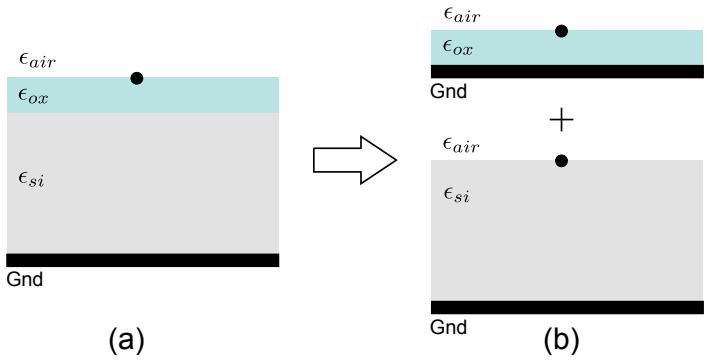

Fig. 3.19 (a) Silicon substrate, (b) silicon substrate approach for case 1.

Green's function of the new oxide and silicon substrate

$$G(\rho,z) = G(\rho,z)_{silicon} + G(\rho,z)_{oxide}. \tag{3.128}$$

With this decomposition, the actual two-layer problem is transformed into two one-layer problems.

Now we apply this concept on the three previous cases related to the location of the charge source.

Point source on the dielectric-air interface (case 1)

The two one-layer problems are shown in Fig. 3.19. Each one-layer problem has already been solved in Section 3.3.1, eq. (3.43). Thus it is only necessary to adapt the expression to the new substrate. Thus, $G(r,z)_{silicon}$ and $G(r,z)_{oxide}$ are given by

$$G(\rho,z)_{Si} = \frac{1}{4\pi\varepsilon_{M_1}} \sum_{l=0}^{\infty} (-1)^l k_1^l \left[\frac{1}{\sqrt{\rho^2 + (z-h+2h\cdot l)^2}} - \right. \\ \left. - \frac{1}{\sqrt{\rho^2 + (h+z+2h\cdot l)^2}} \right] \tag{3.129}$$

$$G(\rho,z)_{Ox} = \frac{1}{4\pi\varepsilon_{M_2}} \sum_{l=0}^{\infty} (-1)^l k_2^l \left[\frac{1}{\sqrt{\rho^2 + (z-h+2h\cdot l)^2}} - \right. \\ \left. - \frac{1}{\sqrt{\rho^2 + (h+z+2h\cdot l)^2}} \right] \tag{3.130}$$

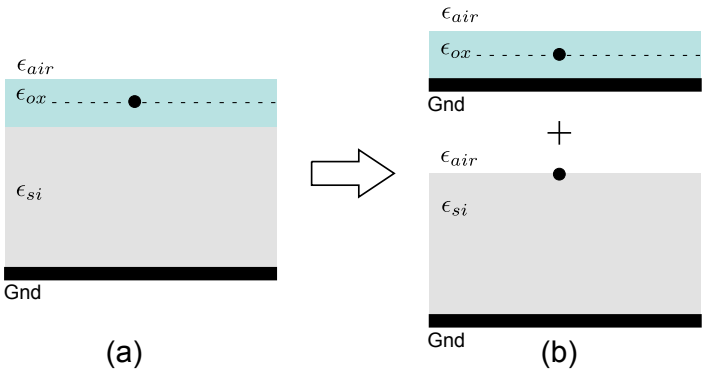

Fig. 3.20 (a) Silicon substrate, (b) silicon substrate approach for case 2.

where,

$$k_1 = \frac{\varepsilon_{si} - \varepsilon_{air}}{\varepsilon_{Si} + \varepsilon_{air}}, k_2 = \frac{\varepsilon_{Ox} - \varepsilon_{air}}{\varepsilon_{Ox} + \varepsilon_{air}}, \varepsilon_{M_1} = \frac{\varepsilon_{Si} + \varepsilon_{air}}{2}, \textit{and } \varepsilon_{M_2} = \frac{\varepsilon_{Ox} + \varepsilon_{air}}{2}.$$

Point source inside the dielectric (case 2)

The two one-layer problems are shown in Fig. 3.20. The one-layer problem concerning the oxide has been already solved in Section 3.3.1, eq. (3.56); whereas the one-layer silicon problem has been solved in the former section.

The expression of $G(r,z)_{silicon}$ and $G(r,z)_{oxide}$ are given by

$$G(\rho,z)_{Si} = \frac{1}{4\pi\varepsilon_{M_1}} \sum_{l=0}^{\infty} (-1)^l k_1^l \left[\frac{1}{\sqrt{\rho^2 + (z-h+2h\cdot l)^2}} - \right.$$
$$\left. - \frac{1}{\sqrt{\rho^2 + (h+z+2h\cdot l)^2}} \right], \quad (3.131)$$

$$G(\rho,z)_{ox} = \frac{1}{4\pi\varepsilon_{M_2}} \sum_{l=1}^{\infty} (-1)^l k_2^l \left[\frac{1}{\sqrt{\rho^2 + (h-z+2dl)^2}} - \right.$$
$$- \frac{1}{\sqrt{\rho^2 + (z+h+2dl)}} + \frac{k_2}{\sqrt{\rho^2 + (-h-z+2d(1+l))^2}} -$$
$$\left. - \frac{k_2}{\sqrt{\rho^2 + (-h+z+2d(1+l))^2}} \right] \quad (3.132)$$

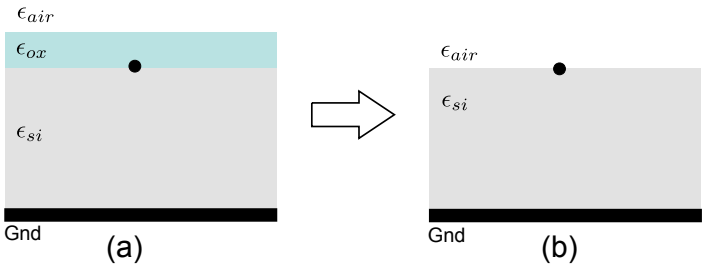

Fig. 3.21 (a) Silicon substrate, (b) silicon substrate approach for case 3.

where,

$$k_1 = \frac{\varepsilon_{si} - \varepsilon_{air}}{\varepsilon_{Si} + \varepsilon_{air}}, k_2 = \frac{\varepsilon_{Ox} - \varepsilon_{air}}{\varepsilon_{Ox} + \varepsilon_{air}}, \varepsilon_{M_1} = \frac{\varepsilon_{Si} + \varepsilon_{air}}{2}, \textit{and } \varepsilon_{M_2} = \frac{\varepsilon_{Ox} + \varepsilon_{air}}{2}.$$

Point source on the silicon-dielectric interface (case 3)

The last case is depicted in Fig. 3.21. Notice that the substrate is now transformed into a single one-layer problem concerning the silicon. This approximation is only acceptable for very narrow oxides when compared to the height of silicon. For this case, the solution is

$$G(\rho,z)_{Si} = \frac{1}{4\pi\varepsilon_{M_1}} \sum_{l=0}^{\infty} (-1)^l k_1^l \left[\frac{1}{\sqrt{\rho^2 + (z-h+2h\cdot l)^2}} - \right. \\ \left. - \frac{1}{\sqrt{\rho^2 + (h+z+2h\cdot l)^2}} \right] \quad (3.133)$$

where

$$k_1 = \frac{\varepsilon_{si} - \varepsilon_{air}}{\varepsilon_{Si} + \varepsilon_{air}} \textit{ and } \varepsilon_{M_1} = \frac{\varepsilon_{Si} + \varepsilon_{air}}{2}.$$

Verification

The validation of the heuristic approach is made taking as reference the complete analytical expressions already found in Section 3.4.1. The used component is once again the two patches problem which geometry was depicted in Fig. 3.15. Results are shown in Table 3.6. Error is less than 1% in case 1, less than 2 % in case 2, and less than 1.5% in case 3. Nevertheless, the computation time has been decreased in more than two orders of magnitude. Therefore, this procedure could be implemented in a fast PEEC tool for developing RFIC EM models.

Table 3.6 Results of the comparison between analytical and heuristic Green's function.

		Eqn. (3.96) [fF]	Eqn. (3.129) [fF]	Difference
case 1	C_{11}	345	344	0.31 %
	C_{12}	-21.4	-21.4	0 %
	C_{21}	-21.4	-21.4	0 %
	C_{22}	345	344	0.31 %
		Eqn. (3.115) [fF]	Eqn. (3.131) [fF]	Difference
case2	C_{11}	347.3	344.4	0.83 %
	C_{12}	-21.7	-21.3	1.84 %
	C_{21}	-21.7	-21.3	1.84 %
	C_{22}	347.3	344.4	0.83 %
		Eqn. (3.127) [fF]	Eqn. (3.133) [fF]	Difference
case 3	C_{11}	362.2	364.2	0.54 %
	C_{12}	-23.6	-23.9	1.25 %
	C_{21}	-23.6	-23.9	1.25 %
	C_{22}	362.2	364.2	0.54 %

C_{12} and C_{21} are negative by definition.

Chapter 4

Meshing strategies

Abstract

Following the pursuit for model order reduction, two novel meshing techniques are developed in this Chapter. Both techniques have the goal to minimize the number of cells of the mesh for having an accurate description of the component. The first technique deals with the concept of skin effect, i.e. the current density distribution related to the thickness of the metal strip. By means of a semi-analytical formulation, the effect of the skin depth on the sheet resistance value is captured within a reasonable accuracy. The second technique takes into account, at first order, the influence of the current crowding distribution along the width of a metal strip, thus an ab initio adaptive mesh is generated. These two strategies are validated through measurements in different LTCC laminated substrates.

4.1 Introduction

In the previous chapters, the PEEC method has been modified as a fast simulation tool by using different assumptions and analytical procedures, which have allowed to simplify the model order complexity of devices under study. In this development, an eye has been kept to avoid severe restrictions that could forbid the simulation of interesting devices and laminates. For now, RF passives with Manhattan layout can be simulated, e.g. planar/solenoidal/toroidal inductors/transformers, film resistors or interdigitized/stacked capacitors. On the contrary, aside from constant section transmission lines, microwave components cannot be modeled due to the dismiss of the retarded potential. Although this is a major drawback of the fast tool, it is important to keep in mind that the algorithm will be implemented in a fast EDA platform which has a large number of models for microwave components.

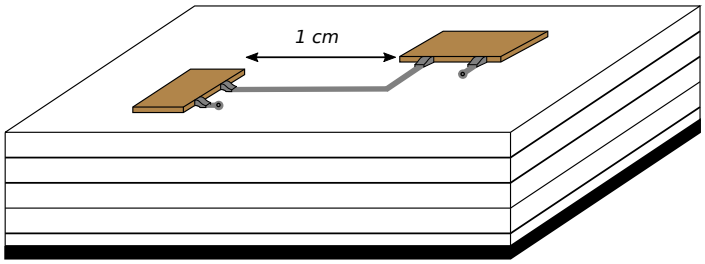

Fig. 4.1 Typical interconnection between two ICs placed on top of an FR4 PCB.

Table 4.1 Number of cells according to PCB technology and application frequency.

Class Technology	Trace size t×w×l	♯ cells @ 100 Mhz	♯ cells @ 1 Ghz	♯ cells @ 10 Ghz
3 - 1 oz	$35\times250\times10^4$	$3.0\cdot10^5$	$9.3\cdot10^6$	$3.0\cdot10^8$
6 - 1 oz	$35\times175\times10^4$	$2.1\cdot10^5$	$6.5\cdot10^6$	$2.1\cdot10^8$
3 - 1/2 oz	$12\times250\times10^4$	$1.0\cdot10^5$	$3.2\cdot10^6$	$1.0\cdot10^8$
6 - 1/2 oz	$12\times175\times10^4$	$0.7\cdot10^5$	$2.2\cdot10^6$	$0.7\cdot10^8$

Centering the modeling in the former set of RF components, the goal to arrive to in this Chapter is the forming of a numerical mesh able to predict accurately second order effects due to crowding and skin current distribution, but using a minimum number of cells in the mesh [1]. To understand the challenging aspects of this problem, Fig. 4.1 shows a typical interconnection between two ICs placed on top of an FR4 substrate. Without any knowledge about the excitation applied to the metal-strip, all directions of the conductor region should be equally discretized according to a skin depth criterion, i.e.

$$\delta = \sqrt{\frac{2}{\omega\mu\sigma}}\,, \tag{4.1}$$

where ω stands for the angular frequency, μ is the permeability of the material, and σ its conductivity. Table 4.1 shows the number of cells for different PCB class technologies and application frequency. Clearly, the number of cells grows quite fast by increasing either the frequency or the dimensions of the strip.

To alleviate this situation, additional information must be loaded into the definition of the problem. The first aspect to be introduced is the knowledge related to the excitation conditions on the metal strip as it sets the direction of propagation. Actually, this excitation in laminated technology can be though as the one shown in Fig. 4.2. Here, a microstrip line is excited between two reference planes, *ref 1* and *ref 2*, that set the direction of the wave

[1] Assuming an $O(N^2)$ solution time for planar solvers, being N the number of cells, the benefits of a mesh reduction are clear.

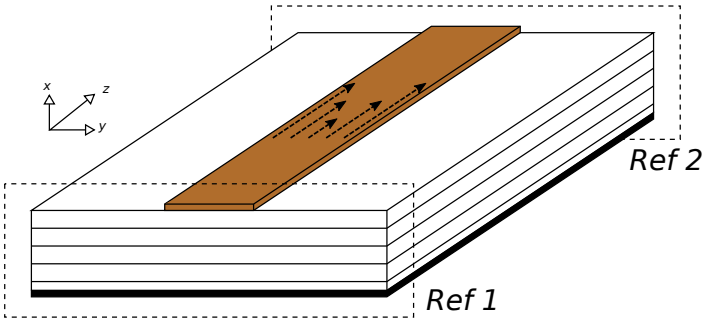

Fig. 4.2 Microstrip transmission line in a multilayered substrate.

propagation[2]. From a discretization point of view, this means that the size of a cell along the propagation axis must be set according to the wavelength, instead of using a δ criterion. Normally, the size is chosen as $\lambda/20$. At RF and microwave frequencies, $\lambda/20 \gg \delta$; thus the number of divisions is $20l/\lambda \ll l/\delta$ where l is the length of the microstrip line in the propagation direction. In spite of this important reduction of the number of cells, it is still a huge number to deal with for a fast simulator implementation because the current distribution in a given cross-section of the conductor has still a dependence on δ. Therefore, aside from the excitation knowledge, additional information related to the actual physics of the device should be used in order to find a suitable way for generating the numerical mesh. This means that it is necessary to understand the skin and current crowding effects in microstrip lines.

4.2 Skin effect and current crowding phenomena

Before starting with the study of non-stationary fields, it is worth to make a short review on some concepts related to the DC current distribution inside conducting regions that obey Ohm's law. Thereafter, eddy currents are analyzed splitting their contribution in terms of the own magnetic field generated by the metal strip (skin effect), and the external magnetic field generated by the remaining metal strips of the device (current crowding).

4.2.1 Static field current distribution

At DC, the current density distribution $\bar{J}_{DC}$ must obey the continuity equation at any differential volume of the space, i.e.

$$\bar{\nabla}\bar{J} + \partial_t \rho = 0 \;\Rightarrow\; \bar{\nabla}\bar{J} = 0 \tag{4.2}$$

[2]In laminated substrates, the length of a metal strip is defined as the distance between the references planes; the width is the substrate surface coplanar orthogonal dimension of the length; and the thickness is the remaining one.

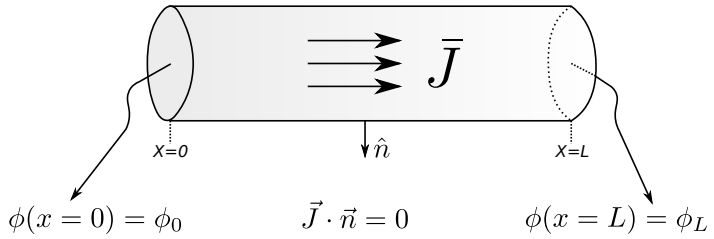

Fig. 4.3 Boundary conditions related to a battery driven conductor.

which indicates that $\bar{J}_{DC}$ is solenoidal. In addition, the electric field $\bar{E}$ at any point of the space is irrotational, $\bar{\nabla}\times\bar{E}=0$; thus $\bar{E}$ can be defined in terms of a potential function ϕ

$$\bar{E}=-\bar{\nabla}\phi. \tag{4.3}$$

Inside conductor regions, $\bar{J}$ and $\bar{E}$ are related via Ohm's law. Therefore, the potential distribution inside the conductor region is given by

$$\bar{\nabla}\bar{J}_{DC}=\bar{\nabla}(\sigma\bar{E})=\bar{\nabla}(-\sigma\bar{\nabla}\phi)=0\,. \tag{4.4}$$

For a linear homogeneous isotropic conductor, eq. (4.4) is a Poisson's equation

$$\nabla^2\phi=0 \tag{4.5}$$

which, for a battery driven conductor, has the boundary conditions shown in Fig. 4.3. Once $\phi(x)$ is found, $\bar{J}_{DC}$ can be obtained as

$$\bar{J}_{DC}=-\sigma\,\bar{\nabla}\phi\,. \tag{4.6}$$

From (4.6), some remarks must be made:

1. It sets the actual current direction in a given cell. Therefore, it is the formal solution of the restriction introduced in Chapter 2, i.e. *the main component of the current density vector inside a conductor (a cell in the model) points in the direction of the voltage gradient evaluated at DC*.

2. It is derived from the gradient of the scalar potential. From now on, a current having this characteristic is named as *impressed* current. Notice that it is the solenoidal component of the current distribution.

3. It predicts the existence of a charge density distribution at the surface of the conductor, $\sigma_S(r)$, that varies according to the scalar potential, as shown in Fig. 4.4. The value of

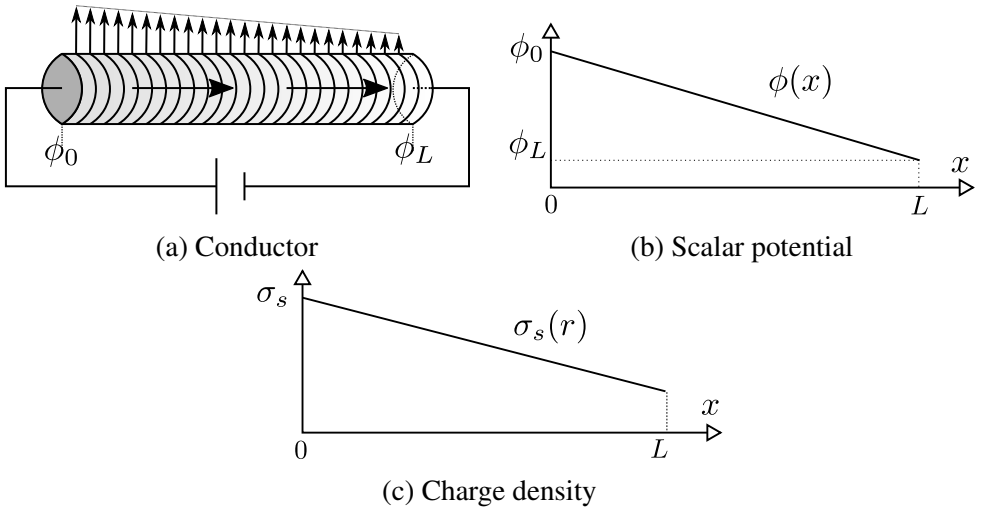

(a) Conductor (b) Scalar potential

(c) Charge density

Fig. 4.4 (a) Electric field distribution on the surface of the conductor; (b) scalar potential distribution; (c) $\sigma_S(r)$.

this charge is given by the integral equation[83]

$$\phi(r) = \int_{S'} G(r,r')\,\sigma_S(r')\,dS'\,. \tag{4.7}$$

Notice that substrate boundary conditions are embedded inside $G(r,r')$; thus different $\sigma_S(r)$ is obtained using different substrates, but, as stated by (4.6), $\bar{J}_{DC}$ is the same if the geometry of the conductor has not been changed and it has been submitted to the same potential difference.

Through this discussion, it is interesting to highlight that the DC conduction mechanism is quite complex. As instance, the existence of $\sigma_S(r)$ over the entire surface of the conductor means that a diffusion current should exist on the same surface. Some authors have pointed out that it is through the formation of such $\sigma_S(r)$ that the volume conduction exists [84–86]. However, the whole picture would require a deep study on solid-state physics for conductors. Nevertheless, for our purpose, the important aspect of this discussion is that the scalar potential sets the solenoidal impressed current.

4.2.2 Quasi-static magnetic field current distribution

In conductors, the quasi-stationary regime is characterized by time varying fields but with the restriction that $\partial_t \bar{D}$ is very small, thus $\bar{B}$ is mainly defined by $\bar{J}$. In fact, in many situations such as in the analysis of bus power connections, $\bar{\nabla}\bar{J} = 0$ still holds. The main difference with the DC stationary case is that $\bar{\nabla} \times \bar{E}$ is no longer 0 but $-\partial_t \bar{B}$. Therefore, the electric

field has a two term contribution, i.e.,

$$\bar{E} = -\partial_t \bar{A} - \bar{\nabla}\phi \,. \tag{4.8}$$

In the framework of massive conductors, $\bar{A}$ is forced to a Coulomb gauge $\bar{\nabla}\bar{A} = 0$. Therefore, (4.4) does not change as shown next:

$$\begin{aligned} \bar{\nabla}\bar{J} = \bar{\nabla}(\sigma\bar{E}) = \bar{\nabla}(\sigma(-\partial_t\bar{A} - \bar{\nabla}\phi)) = \partial_t\nabla(\sigma\bar{A}) + \bar{\nabla}(\sigma\bar{\nabla}\phi) = 0 \\ \Rightarrow \bar{\nabla}(\sigma\bar{\nabla}\phi) = 0\,, \end{aligned} \tag{4.9}$$

where it has been considered that σ is homogeneous inside the conductor. Although (4.4) and (4.9) are equal, it is important to understand that they do not reproduce the same physics, i.e. the same $\bar{J}$ distribution. It only tell us that $\bar{J}_{DC}$ and $\bar{J}$ are both solenoidal. In addtion, notice the next remarks on (4.9):

1. Ohm's law is now given by $\bar{J} = -\sigma(\partial_t\bar{A} + \bar{\nabla}\phi)$. If the conductor has a closed toroidal shape, there can be an existing net current flow due to the rotational part of the electric field ($\nabla\phi$ is conservative).

2. The scalar potential has the same spatial distribution as in the DC case if $\partial_t\rho \approx 0$ (otherwise, displacement current on the conductor surface must be account for, i.e. the non-solenoidal part of the current). From this point of view, the term $-\sigma\bar{\nabla}\phi$ is the impressed current and its distribution is the same as $\bar{J}_{DC}$. Thus, impressed current and $\bar{J}_{DC}$ are the same object.

3. $\bar{J}$ can be effectively divided into two parts: the impressed current $-\sigma\nabla\phi \equiv J_{DC}$; and the magnetically induced current $-\sigma\partial_t\bar{A} \equiv J_{\partial_t\bar{A}}$, as show in Fig. 4.5.

4. To find the actual $\bar{J}$, it is necessary to compute the vector potential $\bar{A}$ distribution inside the conductor volume. Using the definition of $\bar{A}$ with a Coulomb gauge and Ampere's law,

$$\begin{aligned} \bar{\nabla}\times\bar{B} = \bar{\nabla}\times(\bar{\nabla}\times\bar{A}) = \bar{\nabla}\cdot(\bar{\nabla}\cdot\bar{A}) - \nabla^2\bar{A} = -\nabla^2 A = \\ = \nabla\times\mu H = \mu\,\bar{J}, \end{aligned} \tag{4.10}$$

   the diffusion equation of $\bar{A}$ is

$$\nabla^2\bar{A} - \mu\,\sigma\,\partial_t\bar{A} = \mu\,\bar{J}_{DC}\,. \tag{4.11}$$

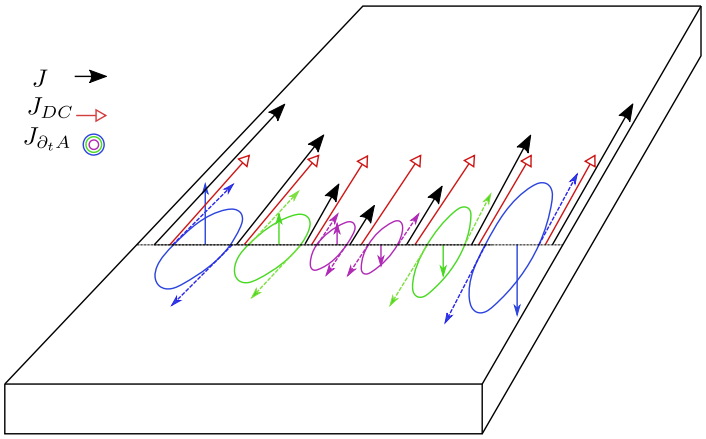

Fig. 4.5 Quasi-static current distribution in a metal strip conductor.

The diffusion constant associated to the homogeneous part of (4.11) sets the value of the penetration of $\bar{A}$ into a conductive region. Therefore,

$$k^2 - j\omega\mu\sigma = 0 \Rightarrow \delta_{qs} = \sqrt{\frac{2}{\mu\sigma\omega}} \tag{4.12}$$

is the quasi-static skin factor. It is worth noting that δ_{qs} is actually the same skin-depth δ definition given in (4.1) which is normally derived using full-wave formalism of Maxwell's equation.

Arrived to this point, one can wonder if the former description has put some light on the meshing problem as we have arrived to the already mentioned conclusion that δ sets the cell size criterion. The key point now is that, for a given conductor region, (4.8) and (4.11) split clearly the actual contribution to AC current distribution in two terms:

1. The term arising from $\bar{J}_{DC}$ in (4.11) will rise up the own-magnetic field of the conductor due to its own impressed current, $\bar{J}_{DC}$.

2. The boundary conditions of (4.11) can set the existence of an external $\bar{A}_{ext}$ field which will contribute to the AC current distribution even if $\bar{J}_{DC}$ is null.

To check out the contribution of both terms, a 3D quasi-static magnetic field solver has been used to evaluate the current distribution in both former situations. Fig.4.6 shows the simulated current distribution for a planar Cu metal strip of 40 μm width and 2 μm thickness when it is fed with a $1A$ impressed current. The evaluation has been performed at 3 different frequencies in order to compare the different current distribution patterns. At low frequencies, the current density is equally distributed across the section of the metal strip. At RF frequencies (few Ghz), $\bar{J}$ is mainly dependent on the width coordinate

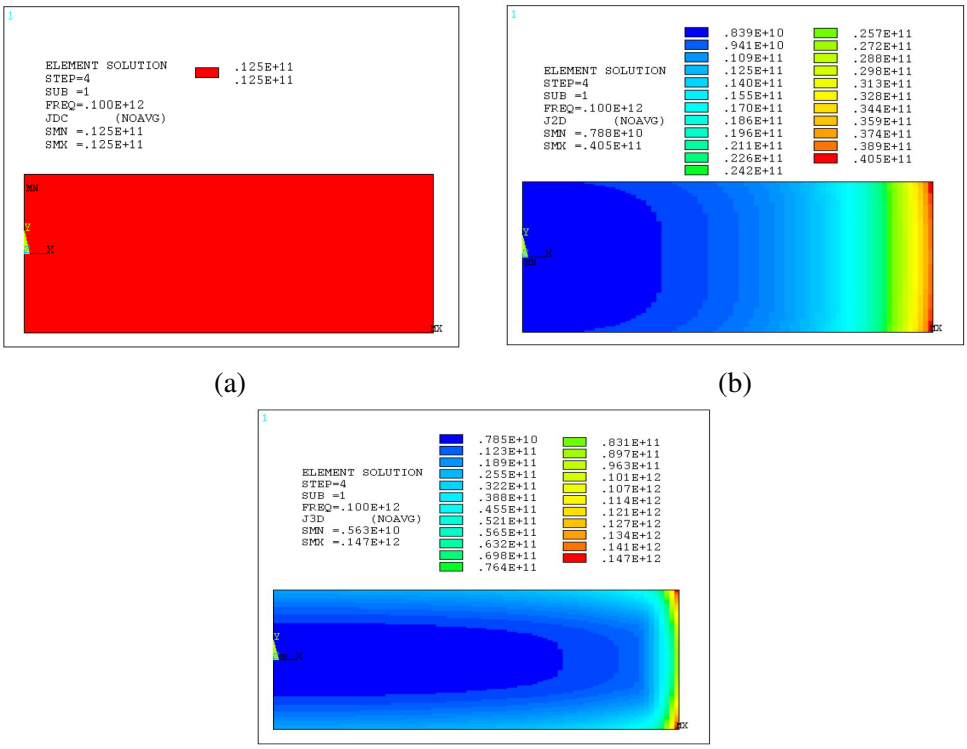

Fig. 4.6 $\bar{J}$ distribution cross-section of a microstrip line (width = 40μm and thicknees = 2 μm) due to an impressed current of 1A [87]. (a) 10MHz; (b) 3 GHz; (c) 30 GHz. Only half of the strip has been simulated due to symmetry.

(it is distributed lateraly) and there is an almost null influence on the thickness because $\delta_{Cu\,@\,3Ghz} \sim 1.22\mu m$. At very high frequencies, in the microwave range and beyond, the thickness plays an additional role which is commonly associated to the skin effect. However, both lateral and skin effect distributions have the same physical mechanism. An additional characteristic of the current distribution due to the impress current is its even symmetry, being the symmetry plane the length-thickness plane located at the middle of the strip width.

Fig.4.7 shows the current density due to an external $\bar{B}$ field (of 0.2T) perpendicular to the substrate and strip plane. No impressed current feeds the metal strip. Now the pattern has odd symmetry and it is worth noting that, even at very high frequencies, the distribution is mostly related to the width (and not to the thickness) because the induced electric field points in the strip length direction.

In the most general case of a planar device, as the one shown in Fig.4.8, its geometry can be broken into metal strips. Therefore, the current density distribution for each strip has two contributions:

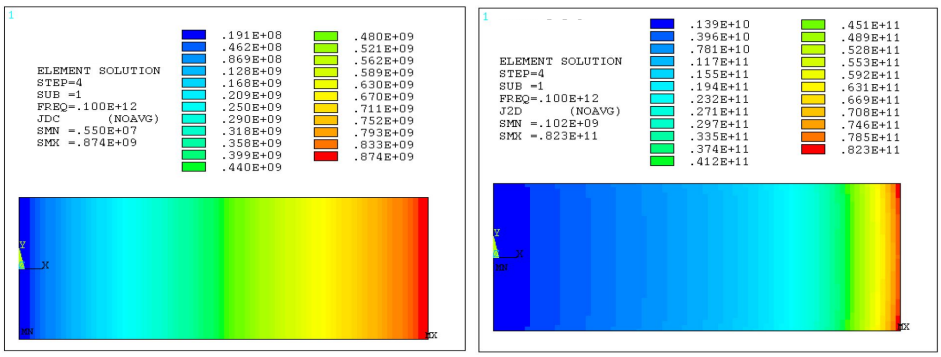

(a) (b)

Fig. 4.7 Cross-section current distribution in a metal strip line (width = 40μm and thickness = 2μm) due to an external field of 1T [87]. (a) 10MHz; (b) 3 GHz. Only half of the strip has been simulated due to the symmetry.

1. The own-magnetic field eddy current distribution due to the impress current in the strip, which shapes the skin effect behavior.

2. The external-magnetic field eddy current distribution due to the magnetic coupling with all of the remaining strips, which shapes the crowding behavior. Notice that each strip of the geometry will have a different current distribution pattern.

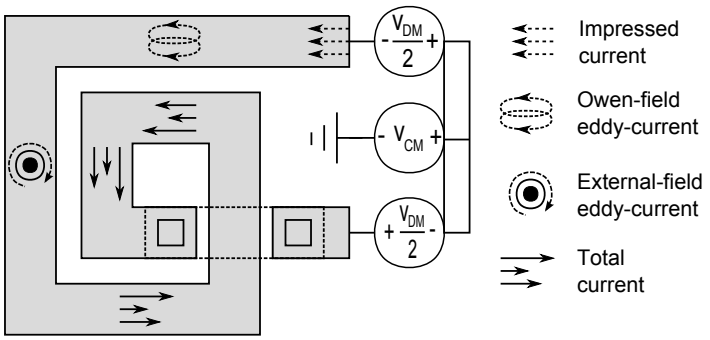

Fig. 4.8 Physical interpretation of current distribution in inductors.

Using this point of view, the meshing algorithm has been split in two quasi-orthogonal problems: (i) the meshing in the thickness of the metal which is related to the impress current; (ii) the meshing in the width direction, that depends on $\bar{A}_{ext}$ which actual value is a function of the global location of the metal strip in the device. The way to face these two problems is different, as it will be shown next with the development of the novel techniques presented hereafter.

4.3 Skin effect meshing

Commonly, the skin effect (defined as the actual current distributions across the thickness) is modeled as a surface impedance in most 2.5D commercial electromagnetic simulators. This surface impedance is derived by considering the effect of a magnetic field over a semi-infinite conductor material. When this development is applied to the evaluation of the sheet resistance, $R_{\square}$, in metal strips, the next expression is found

$$R_{\square} = R_{\square_{DC}} \cdot \frac{t}{\delta(1-e^{-t/\delta})} \tag{4.13}$$

where $R_{\square_{DC}}$ is the DC sheet resistance, t is the thickness of the conductor, and δ is the skin depth value at the frequency of interest[3]. In spite of its general usage, the application of this equation must be done carefully as it does not take into account the actual substrate where the metal strip is embedded.

To better understand the physics underlying the skin effect, a series of simulation experiments are proposed in order to check the correctness of (4.13) by evaluating the actual $\bar{J}$ current distribution in a given metal strip under different geometries, boundary conditions and electromagnetic parameters. Fig.4.9 shows schematically these experiments.

The chosen frequency for the evaluation is $1Ghz$ and the material is Cu ($\sigma_{Cu} \sim 5.7 \cdot 10^7 S/m$), thus $\delta \approx 2\mu m$ for a non-magnetic substrate. Notice that this δ value is actually smaller than the typical metal thickness of most laminates. Simulation results are obtained by using the numerical method already developed in Chapter 2 and 3. To take into account the thickness of the strip, it is divided in a given number of layers[4] [88] [29]. The meshes used in the computations are not uniform, but follow a δ criterion as shown in Fig. 4.10.

These structures are fed by a differential voltage source of **1V** placed between the edges of the length of the strip. Because the magnitude of interest is $\bar{J}$, the actual length of the strip is not important. In addition, the results of $\bar{J}$ are normalized, $\bar{J}_{norm}$, to $|\bar{J}|_{max}$ thus enabling a fair comparison between $\bar{J}$ profiles of different sized strips.

A. $\bar{J}(y,z)$ vs boundary conditions

To start with, a metal strip of $thickness = 5\mu m$ and $with = 100\mu m$ is placed on a single layer substrate of $500\mu m$ height. Three different boundary conditions are simulated (Fig. 4.9 (a)): (i) a suspended substrate where the strip is placed on top; (ii) a microstrip configuration; (iii) a stripline where the metal is located in the middle of the layer. This set of experiments is

[3] For a derivation of (4.13), see Appendix D.

[4] Although $\mathbf{J} = \mathbf{J}(y,z)$, be aware that the method is not full 3D.

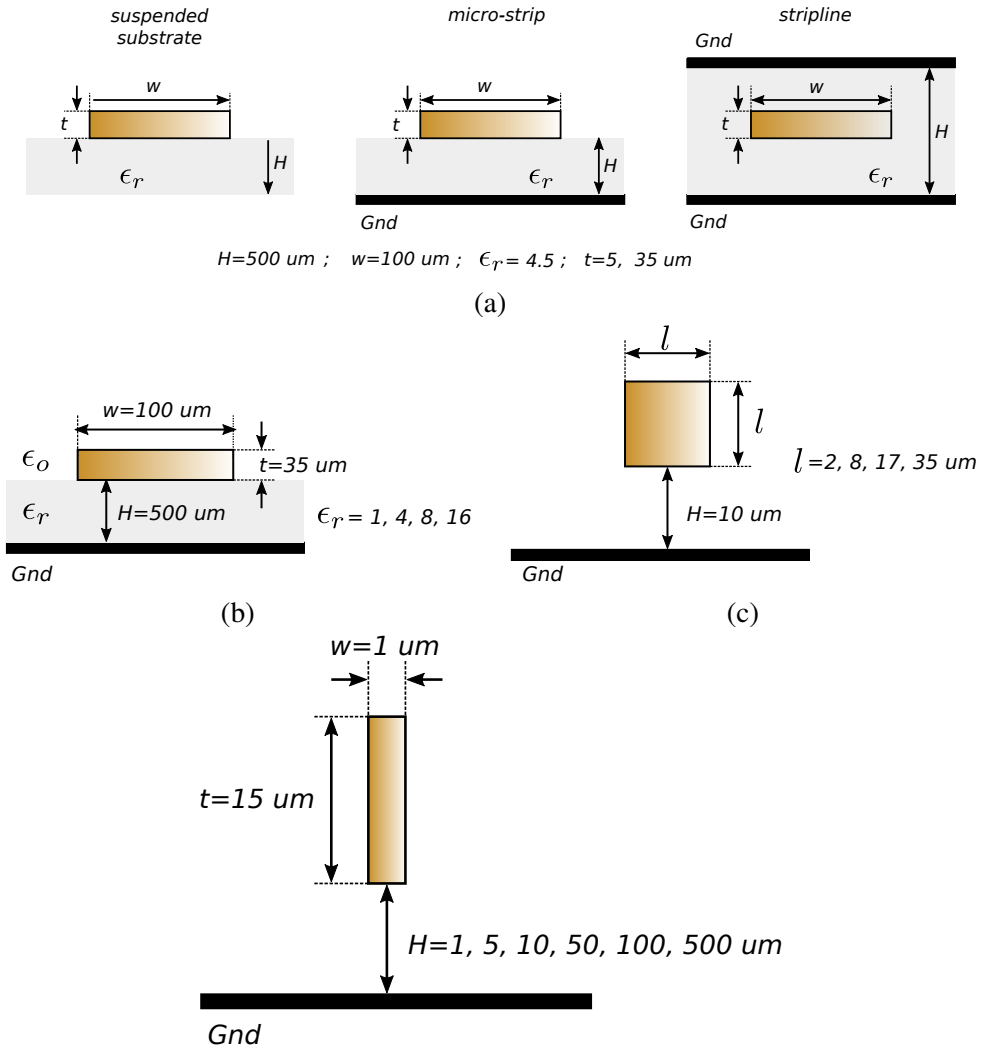

Fig. 4.9 Proposed experiments for the study of the skin effect: (a) vs boundary conditions; (b) vs permittivity value; (c) vs size of the conductor; (d) vs distance to GND plane.

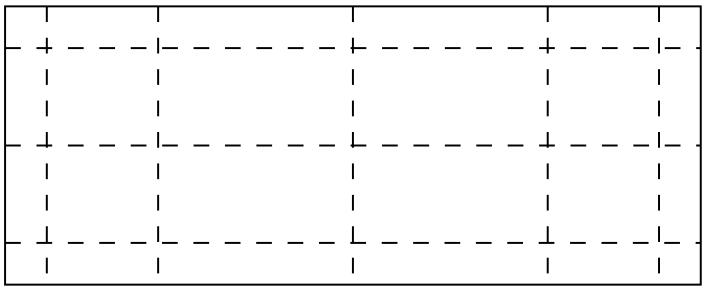

Fig. 4.10 Non-uniform mesh.

repeated for a metal $thickness = 35\mu m$. The goal of these computations is to have a picture of the typical current distribution in most hybrid laminated technologies. For the previous six cases, Fig.4.11 shows the obtained $|\bar{J}|_{norm}$ results. From these plots, it is worth stressing the next features:

- $thickness = 5\mu m$ cases: notice that the principal axis of current distribution is set along the width. On the contrary, the influence of δ on the thickness is at its onset as it can be seen at $|\bar{J}(y = \pm width/2, z)|$.
- $thickness = 35\mu m$ cases: $\bar{J}$ redistribution along the thickness is now fully depleted ($\delta \ll thickness$), but the redistribution along the width is still much more important. Notice that the level of $|\bar{J}_{norm}|$ at the perimeter of the strip is higher at locations $y = \pm width/2$ that at $z_{top} = H + thickness$ or $z_{bottom} = H$.
- All boundary conditions: all substrate configurations have the same $|\bar{J}_{norm}|$ profile (for each $thickness = 5\mu m, 35\mu m$ respectively). This result is very interesting because is shows that (4.13) is a plausible model for skin loss sheet resistance for a huge range of boundary conditions; but it is a little bit surprising, because it seems to contradict the microstrip vs suspended-substrate current distribution picture where $\bar{J}_{norm}(z_{top}) < \bar{J}_{norm}(z_{bottom})$ is assumed in the microstrip configuration, a fact that is used in many situations. Using the results from the remaining experiments, this apparent contradiction will be explained.

B. $\bar{J}(y,z)$ **vs** ε_r

In this experiment (Fig.4.9(b)), the goal is to check the influence of ε_r on $\bar{J}$. For the previous three substrate configurations and using a metal thickness of $35\mu m$, ε_r has been set to 1, 4, 8 and 16. Fig.4.12 shows the results for the microstrip configuration, which are all equal. This result should not be unexpected as the quasi-TEM propagation of a microstrip transmission line can be obtained from the uncoupled solutions of $\bar{A}$ and ϕ. For the remaining substrate configurations, the same kind of results are obtained. Notice that this result is in agreement with (4.13) which has no dependence on ε_r.

C. $\bar{J}(y,z)$ **vs strip size in microstrip configuration**

Following the pursuit for a clear understand of the skin effect, this experiment illustrates the influence of the strip size, thought as a square cross-section ($width = thickness$), on a microstrip substrate. By using this symmetric section, any asymmetry in $\bar{J}$ will become more

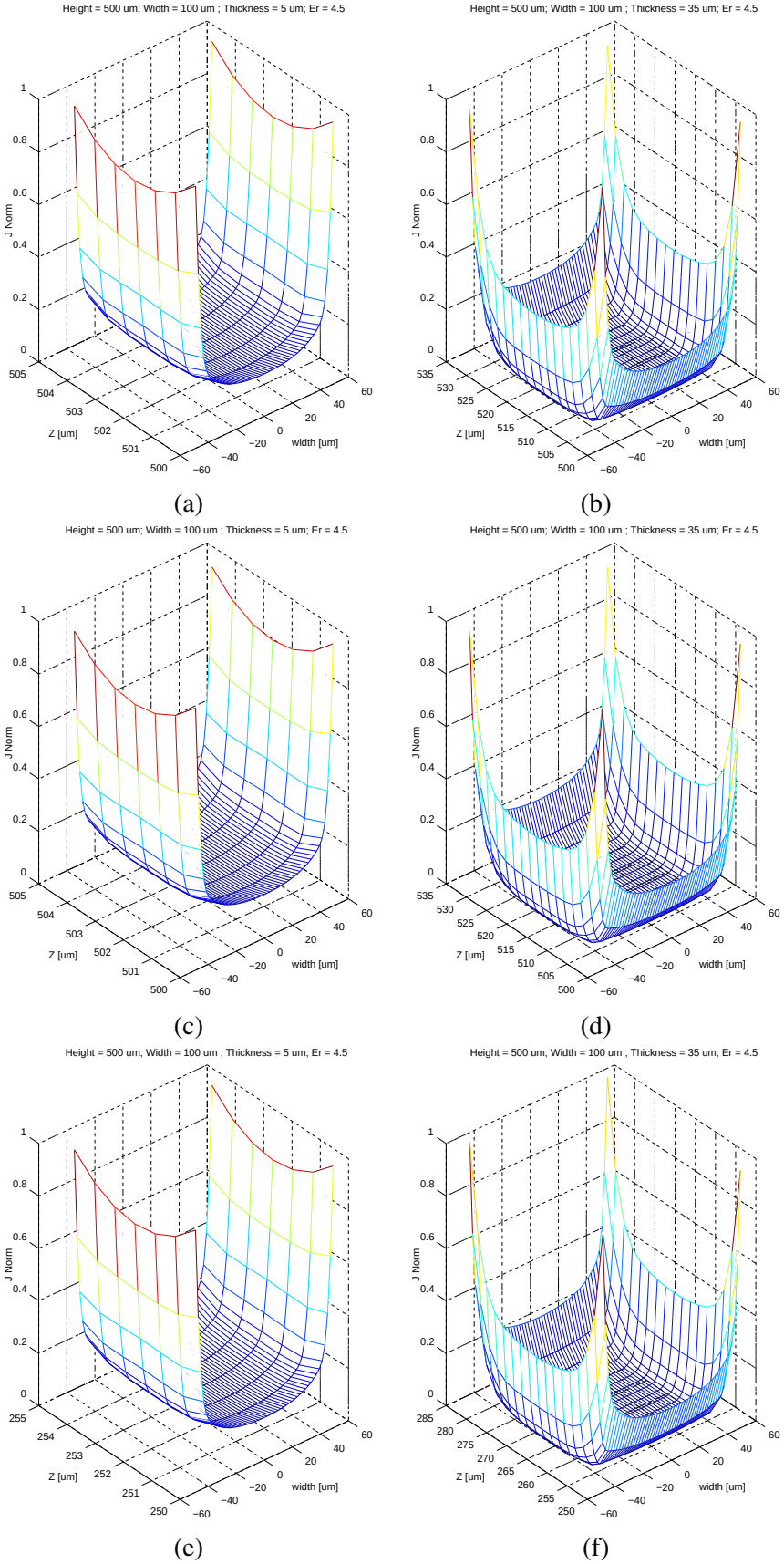

Fig. 4.11 $|\bar{J}(y,z)|_{norm}$ vs boundary conditions for thickness=5μm (a, c, and e) and thickness=35μm (b, d, and f).

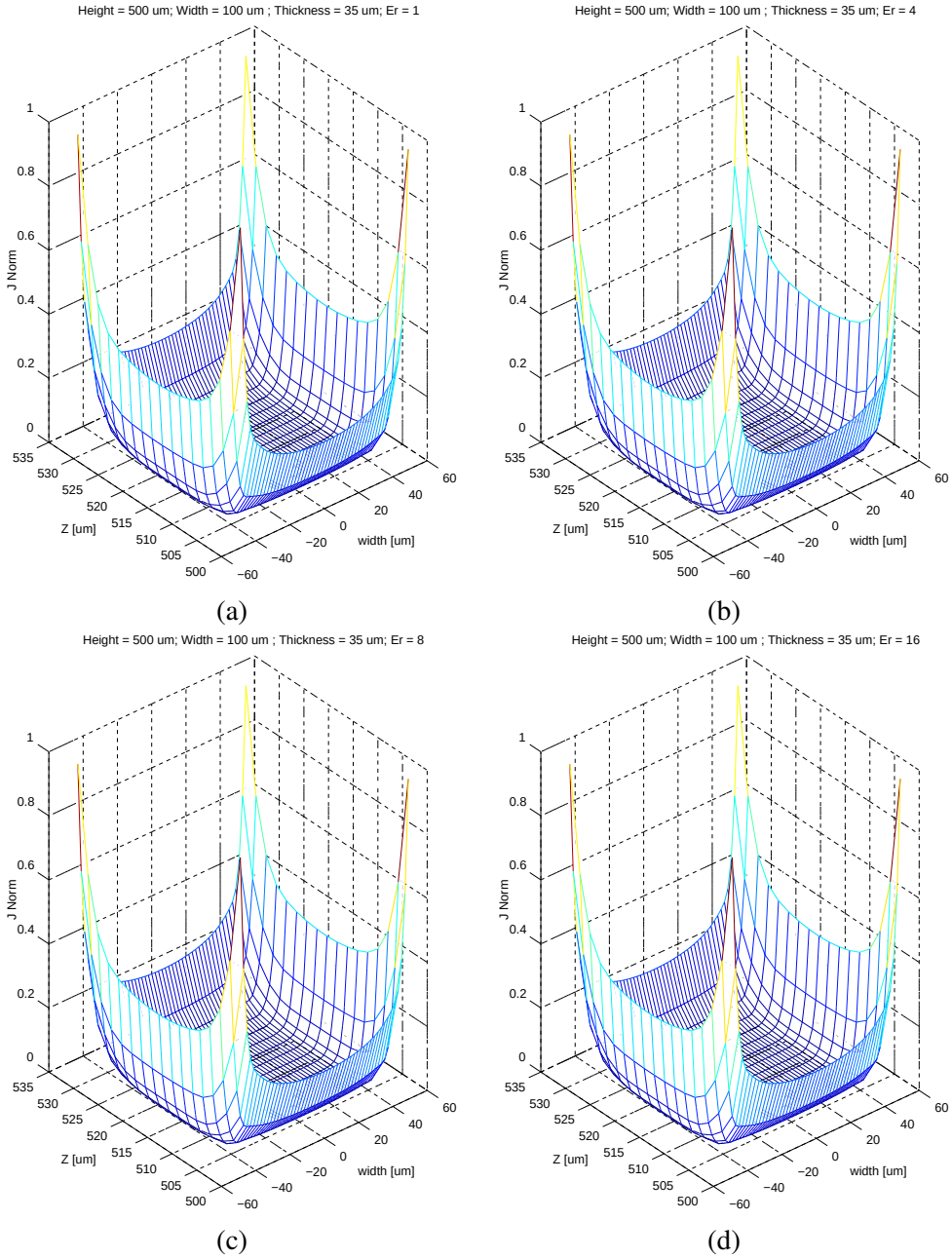

Fig. 4.12 $\bar{J}(y,z)$ vs ε_r: (a) $\varepsilon_r = 1$; (b) $\varepsilon_r = 4$; (c) $\varepsilon_r = 8$; (d) $\varepsilon_r = 16$.

evident. To increase the influence of the GND plane, the strip is place at only $10\mu m$ distance of the GND plane.

The results are plotted in Fig.4.13. Whereas $\delta < size$, $|\bar{J}_{norm}|$ is roughly constant all over the cross-section. As $\delta \gg size$, $|\bar{J}_{norm}|$ redistribution becomes evident. Moreover, as bigger the size of the cross-section is, the bigger the difference between $|\bar{J}_{norm}(z_{bottom})|$ and $|\bar{J}_{norm}(z_{top})|$. Therefore, the classical picture of $\bar{J}$ in microstrip configuration is obtained, but notice the close proximity to the GND plane. This last result suggests that, under asymmetric boundary conditions, the actual $\bar{J}$ distribution seems to be a quite complex function of the substrate height, strip width and thickness. In consequence, eq. (4.13) cannot be the complete picture for all substrate configurations. Some sort of modification should be introduced which will required further explorations about the influence of the substrate in $\bar{J}$.

D. $\bar{J}(y,z)$ vs microstrip substrate height H

In this experiment, it is evaluated the $\bar{J}$ dependence on the microstrip substrate height H. To get ride-off of the influence of the width, the strip dimensions are set to $width = 1\mu m$ and $thickness = 15\mu m$. The distance to the GND plane is changed for different simulations, i.e. $1\mu m$, $5\mu m$, $10\mu m$, $50\mu m$, $100\mu m$, and $500\mu m$.

In Fig. 4.14, it is clearly shown that $|\bar{J}_{norm}|$ distribution depends on H. For narrow substrates, the influence of the GND plane is so strong that most of the current in the microstrip is confined in the bottom surface. As the distance H is increased, the distribution becomes more symmetric and both top/bottom surfaces carry the same amount of current. Although it seems to be a quite complicated behavior, the truth is that it can be simply explained by considering the equivalent problem shown in Fig. 4.15. $|\bar{J}_{norm}|$ is the same as the one obtained considering two coupled metal strips separated by a distance $2H$, driven differentially, and having the same reversed width-thickness dimensions of the original problem. To state this in other words, the actual $\bar{J}$ in microstrip substrates is not only due to the impressed current, but to the magnetic coupling of the image current of the strip.

The point now is to find a suitable procedure for taking into account the influence of t and H on $R_{\square}$. Fig.4.15 is actually the clue for developing a fast algorithm. Using this concept, a new set of simulations is performed: for a given strip thickness, and fixing its $width = 1\mu m$, the normalized loss of the strip is evaluated vs the independent variable (t/H) for a fixed frequency of 1GHz. This normalized loss is defined as

$$R_{\square_{norm}} = \frac{R_{\square}(t/H)}{R_{\square}(t/H \to \infty)} - 1, \tag{4.14}$$

thus it is a fair comparison of the relative importance on the increase of the loss due to (t/H).

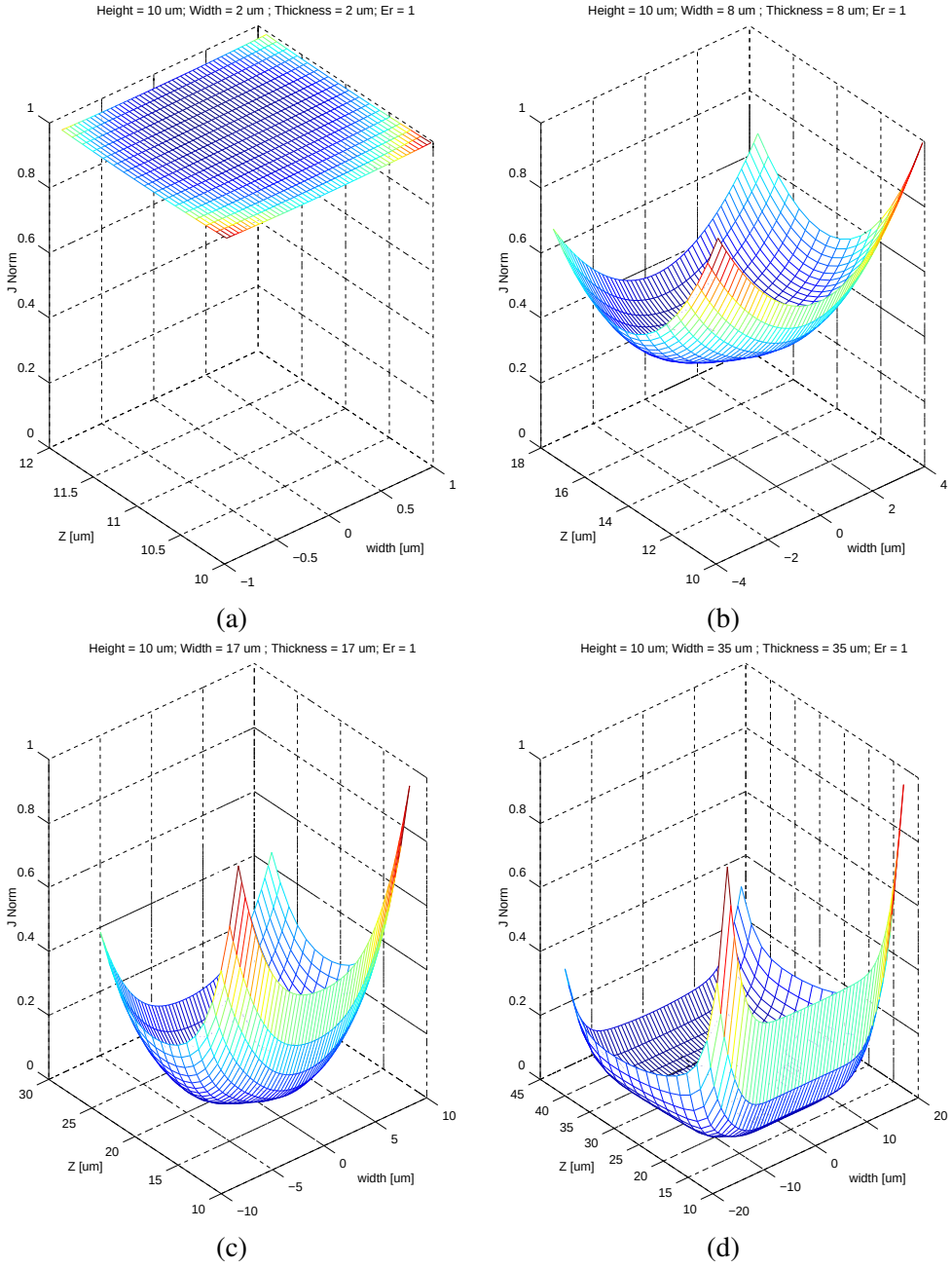

Fig. 4.13 $\bar{J}(y,z)$ vs strip size ($H = 10\mu m$): (a) size=$2\mu m$; (b) size=$8\mu m$; (c) size=$20\mu m$; (d) size=$40\mu m$.

Fig. 4.16 shows the results for different values of the thickness. The interesting point in these plots is that all of them have the same functional form which is given by

$$f(t/H) = \frac{A(t/H)^2}{1+B(t/H)^2}. \tag{4.15}$$

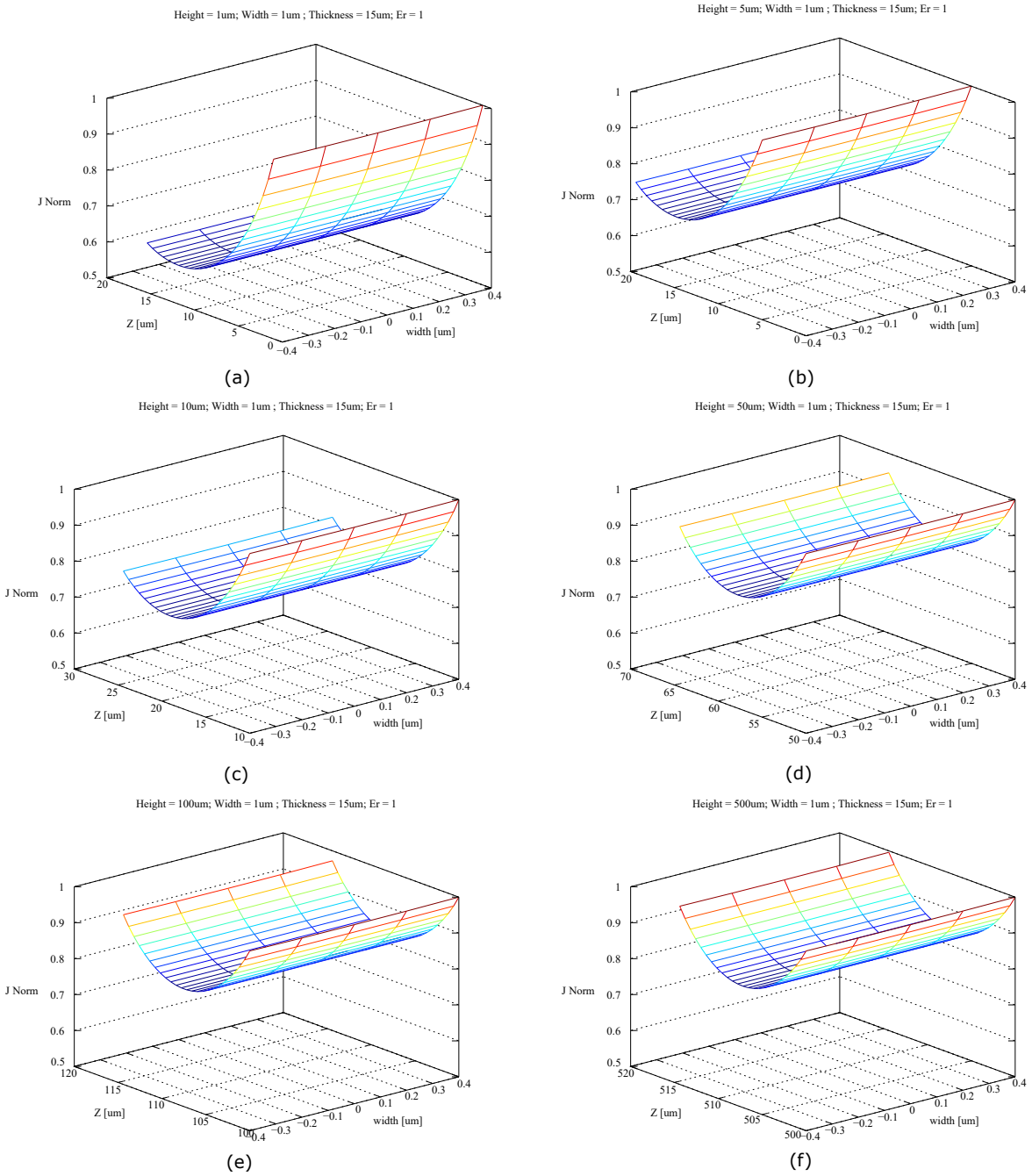

Fig. 4.14 $\bar{J}(y,z)$ vs microstrip substrate height H: (a) H=1μm; (b) H=5μm; (c) H=10μm; (d) H=50μm; (e) H=100μm; (f) H=500μm.

The values of A and B are dependent on frequency (they must vanish for $\omega \to 0$) and on the width because they carry the information related to the magnetic coupling between the strip and its image. In fact, the dependence of $\bar{J}$ profile along the thickness is also a strong function of the width, as it can be understood from Fig. 4.17. By increasing the width, the magnetic

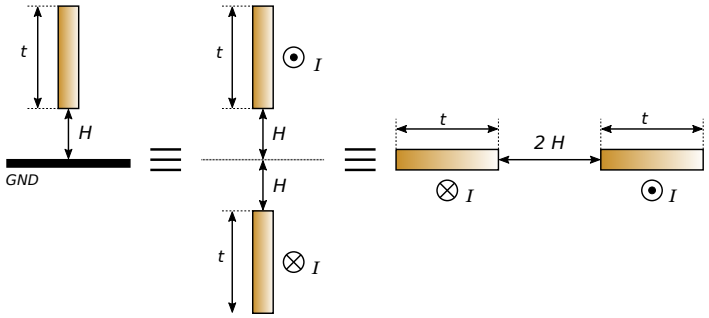

Fig. 4.15 Equivalent problem for the computation of $\bar{J}$ in microstrip configuration.

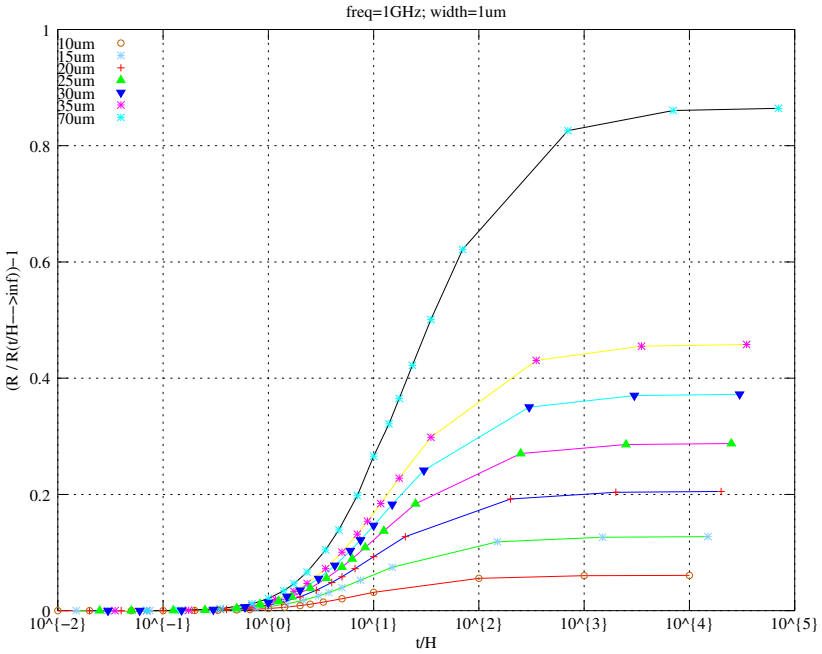

Fig. 4.16 Normalized loss of the strip vs (t/H).

field lines of the image cross the strip at different orientations. The main consequence is that $\bar{B}_{Image}$ has components directed in both the thickness-length and width-length planes. The former component is responsible for the the broken symmetry of $\bar{J}$ in microstrip configuration not as impressed current, but as an external field. The latter component (width-length plane) modifies the $\bar{J}$ distribution along the width itself by actually subtracting the total magnetic field.

To sum up, next it is proposed a simple and fast procedure for calculating the skin effect without increasing the mesh of a device under simulation in its thickness direction (i.e., only one cell division is issued on the thickness, thus the Green's function procedure developed in the previous chapter can be applied):

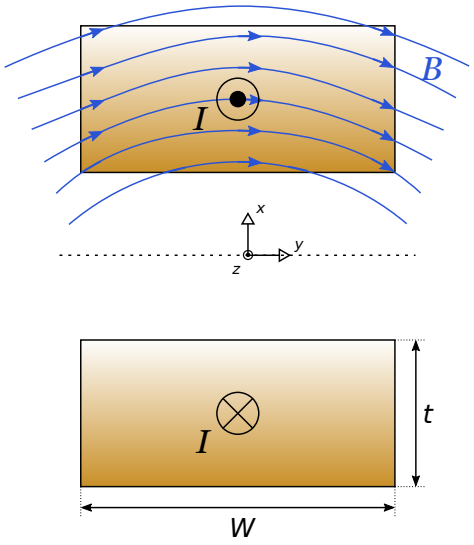

Fig. 4.17 $\bar{B}_{Image}$ field lines crossing the metal strip.

1. For a microstrip or stripline substrate, calculate the value (t/H) (in stripline configuration, H is the minimum distance between the strip and each of both GND planes).

2. If the strip has $(t/H) > 0.5$ or it is located in a suspended substrate, use (4.13) as $R_{\square}$; otherwise, use the next modified expression:

$$R_{\square} = R_{\square_{DC}} \cdot \frac{t}{\delta(1-e^{t/\delta})} \cdot \frac{A(t/H)^2}{1+B(t/H)^2} \tag{4.16}$$

3. A and B coefficients are obtained by performing the previous simulations. Notice that for a given technology the metal thickness and substrate height are fixed. Therefore, it is only necessary to make this computation once for a given frequency and width values. This means that the third factor in (4.16) can be tabulated and stored inside the PEEC algorithm.

At this point, it is worth stressing that $t/H < 0.1$ for most hybrid technologies; thus (4.16) is seldom used as a way to compute $R_{\square}$.

4.4 Proximity effect meshing

In planar device modelling, the proximity effect is defined as the current distribution along the width of the strip due to the influence of other parts/strips of the device itself or to other components located nearby. Here, the goal is the development of a suitable meshing algorithm for computing this current distribution with a reasonable accuracy, but using a

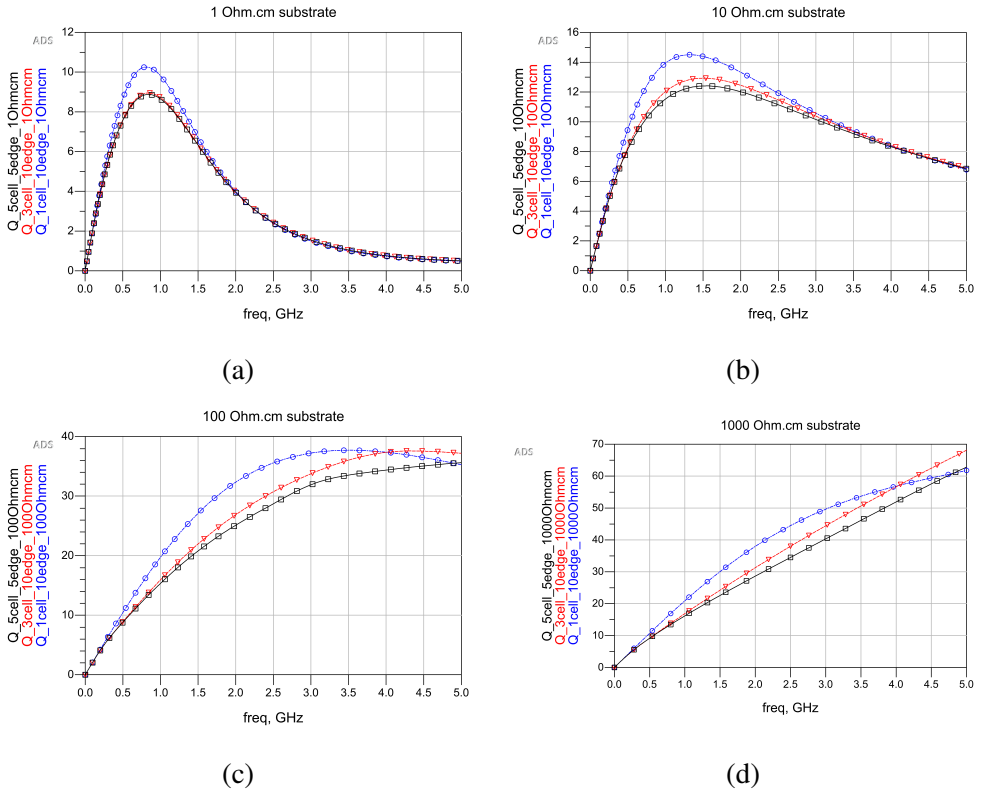

Fig. 4.18 Q factor of a metal strip for different substrate conductivities: (a) $\sigma_{subs} = 1\Omega \cdot cm$; (b) $\sigma_{subs} = 10\Omega \cdot cm$; (c) $\sigma_{subs} = 100\Omega \cdot cm$; (d) $\sigma_{subs} = 1K\Omega \cdot cm$.

minimum number of cell divisions along the width. With no doubt, the mesh plays a central role on the accuracy and speed of the solver, thus the benefits of an optimum mesh are two fold. As instance, in the evaluation of high Q inductors, losses are mainly dominated by metal losses; thus, meshing errors become evident in the calculation of proximity effects. To have a better idea on this issue, Fig.4.18 shows the simulation of the Q factor of a metal strip placed over a conductive substrate ($\sigma_{subs} = 1, 10, 10^2, 10^3\,\Omega \cdot cm$) using different meshing characteristics, i.e. $1\,cell$, $3\,cells$ at 10% edge mesh and $5\,cells$ at 5% edge mesh. Whereas it is only necessary to have 3 cells for an accurate description in high loss substrate, it is not enough in high resistivity substrates. This effect is even more severe in complex structures such as inductors, as shown in Fig. 4.19 [89]. This plot shows a cross-section of the current distribution of a 4 turn circular spiral. Notice that each turn has a completely different current distribution pattern. This fact points out that the mesh for each turn should be adapted accordingly.

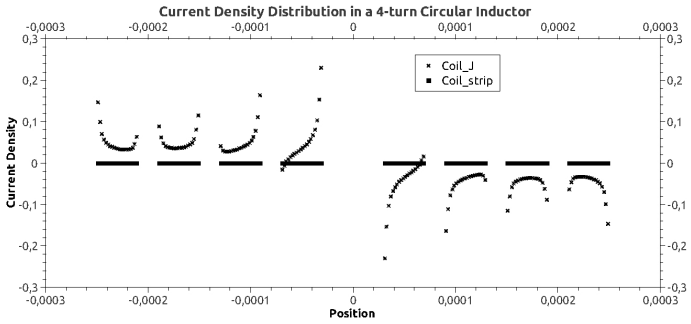

Fig. 4.19 Cross section current density distribution of 4 turn circular inductor.

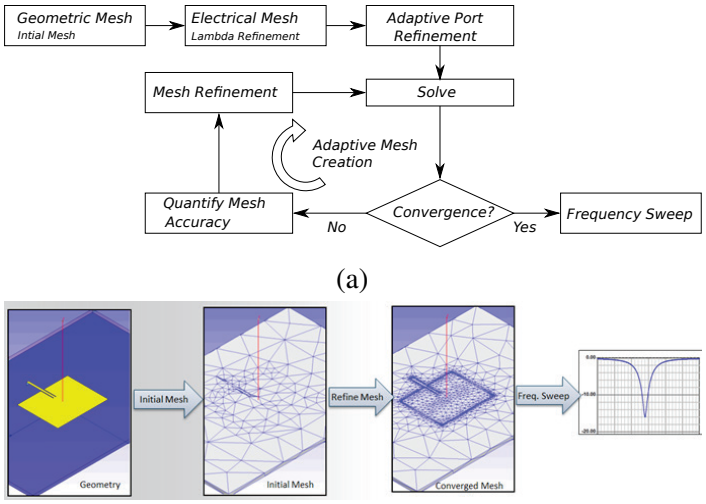

(a)

(b)

Fig. 4.20 HFSS adaptive mesh refinement [91]:(a) process flow; (b) initial mesh is refined untill convergence.

A. Ad hoc adaptive meshing

Before starting with the development of the proposed meshing algorithm, here it is made a short description of one of the most advanced mesh generator procedures: the adaptive meshing[5].

Fig. 4.20a show the block diagram of the adaptive meshing. Starting from an initial mesh, it is refined using a λ/N criterion. Then, the model is solved and the mesh is recomputed based on the actual solution. Normally, a finer mesh is built on model zones where there is a maximum gradient. This process is repeated until convergence is reached, i.e. the solution is stable between iterations according to a tolerance value. Fig. 4.20b shows an example of the final mesh obtained for a patch antenna in HFSS.

[5]This description is based on the HFSS user's Manual [90].

Adaptive meshing provides a high degree of accuracy at the cost of an increased computational time. Normally, it takes around 10 iterations for a converged solution. The term ad hoc used at the beginning of the subsection shows the fact that the refinement of the mesh is made once the complete EM solution is available. Next, we will show that the proposed meshing algorithm does not need a valid solution for generating the adaptive mesh. In this sense, the method is named 'ab initio'.

B. Ab initio adaptive mesh

As already mention, the implementation of an adaptive meshing technique can compromise the solution speed of a fast solver.

Here, it is introduced a novel technique that avoids the iterative procedure of the classical adaptive meshing technique by providing a knowledge about the actual AC loss of a strip, but without solving the complete device $\bar{J}$ distribution. It has its roots in the PEEC formalism. In fact, the development of the technique will illustrate that PEEC is not only suitable for numerical computation, but for hand calculations.

To start with, a simple model of an strip, which belongs to a given device, is devised in Fig. 4.21(a). It is formed by three equal cells[6], laterals l_1, l_2 and central c, carrying their respectives currents I_{l_1}, I_{l_2} and I_C. The influence of the remaining strips is captured with $B_{ext_{l_1}}$, $B_{ext_{l_2}}$ and B_{ext_c}. Using a quasi-static magnetic formalism, the actual PEEC model of the strip is sketched in Fig. 4.21(b). Each cell has its own impedance $j\omega L + R$, and the magnetic mutual couplings are established between the cells themselves, i.e. M_c and M_l, and with the remaining strips of the device, i.e. $M_{ext_{l_1}}$, $M_{ext_{l_2}}$ and M_{ext_c}. L_{ext} and R_{ext} are related to the impedance of the remaining parts of the device. With this simple model, it is possible to evaluate, at first order, the redistribution of current I_{l_1}, I_{l_2} and I_C in the strip without solving the complete system. In other words, instead of solving a $4N \times 4N$ system of equations for the complete N strip device, it is only necessary to solve N 2×2 problems formed with the KVL loop equations from I_{l_1} and I_{l_2}, i.e.

$$\begin{bmatrix} 2s(L+M_c)+2R & s(L+M_l-2M_c)+R \\ s(L+M_l-2M_c)+R & 2s(L+M_c)+2R \end{bmatrix} \begin{bmatrix} I_{l_1}/I_{in} \\ I_{l_2}/I_{in} \end{bmatrix} =$$

[6] It is not necessary to force an equal size for the three cells. However, the development is a little bit more complicated.

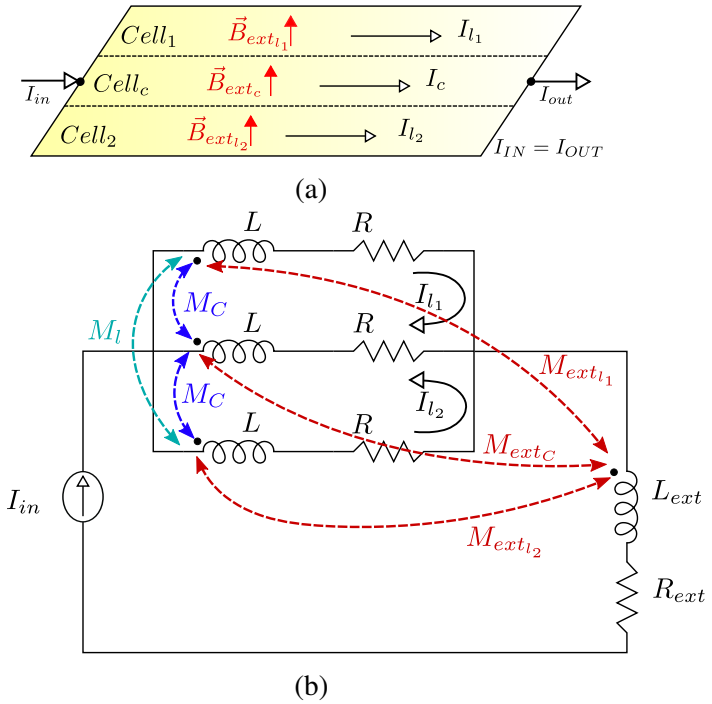

Fig. 4.21 (a) Simple mesh of a metal strip; (b) equivalent circuit model.

$$= \begin{bmatrix} s\left(L - M_c - M_{ext_{l_1}} + M_{ext_c}\right) + R \\ \\ s\left(L - M_c - M_{ext_{l_2}} + M_{ext_c}\right) + R \end{bmatrix}. \tag{4.17}$$

As expected, the 2×2 matrix is symmetric, but the independent term has a broken symmetry with the $M_{ext_{l_1}}$ and $M_{ext_{l_2}}$. This fact shows that I_{l_1} and I_{l_2} will be different when $s \neq 0$ and $M_{ext_{l_1}} \neq M_{ext_{l_2}}$, i.e. when a non-stationary net magnetic field transverses the strip.

Once (4.17) is solved, the ratio of the AC losses vs DC losses is evaluated as:

$$\begin{aligned} \frac{P_{AC\,loss}}{P_{DC\,loss}} &= \frac{\frac{1}{2}|I_{in}|^2 R \left[\left|\frac{I_{l_1}}{I_{in}}\right|^2 + \left|\frac{I_{l_2}}{I_{in}}\right|^2 + \left|1 - \frac{I_{l_1}}{I_{in}} - \frac{I_{l_2}}{I_{in}}\right|^2 \right]}{\frac{1}{2}|I_{in}|^2 \cdot (R//R//R)} \\ &= 3\left[\left|\frac{I_{l_1}}{I_{in}}\right|^2 + \left|\frac{I_{l_2}}{I_{in}}\right|^2 + \left|1 - \frac{I_{l_1} + I_{l_2}}{I_{in}}\right|^2 \right] \end{aligned} \tag{4.18}$$

This ratio is a first order computation on how important the current distribution is. Therefore, based on its value, the number of cells and the % of edge-mesh is selected for the given strip.

Now, the ab intio adaptive meshing algorithm can be defined as follows:

1. A simple mesh of the device is built that consists in three cells per strip.

Table 4.2 Number of cell divisions along the width.

$P_{ACloss}/P_{DCloss} = x$	♯ cells
$x < 1.5$	3
$1.5 < x < 2.5$	5
$2.5 < x < 4$	7
$4 < x$	9

2. For each strip, the values of M_l, M_c, $M_{ext_{l_1}}$, $M_{ext_{l_2}}$,M_{ext_c}, L and R are calculated:

   2.1 Calculate the partial elements of this three cells: L & R are common for the three cells; by symmetry, M_c and M_l need to be calculated once.

   2.2 For each subdivision of the strip, i.e. l_1, l_2 and c, evaluate $M_{ext_{l_1}}$, $M_{ext_{l_2}}$ and M_{ext_c} by summing up all the couplings with the remaining strips.

3. Built the system (4.17), using the adequate mesh frequency; solve it; and calculate the AC/DC power loss ratio, using (4.18), for each strip of the device.

4. Based on the accumulated experience, the criteria shown in Table 4.2 is used to assign the divisions.

Fig.4.22 shows the typical meshes obtained for a given inductor component. Notice that the meshing at $1Ghz$ has a different number of cells and distribution than its $1Mhz$ counterpart. In addition, comparison with experimental data is given in Fig.4.23 for two different inductor geometries and LTCC technologies. In both simulations the user has not been led to tune the parameters defining the mesh. Clearly, the method is effective for the study of low loss devices.

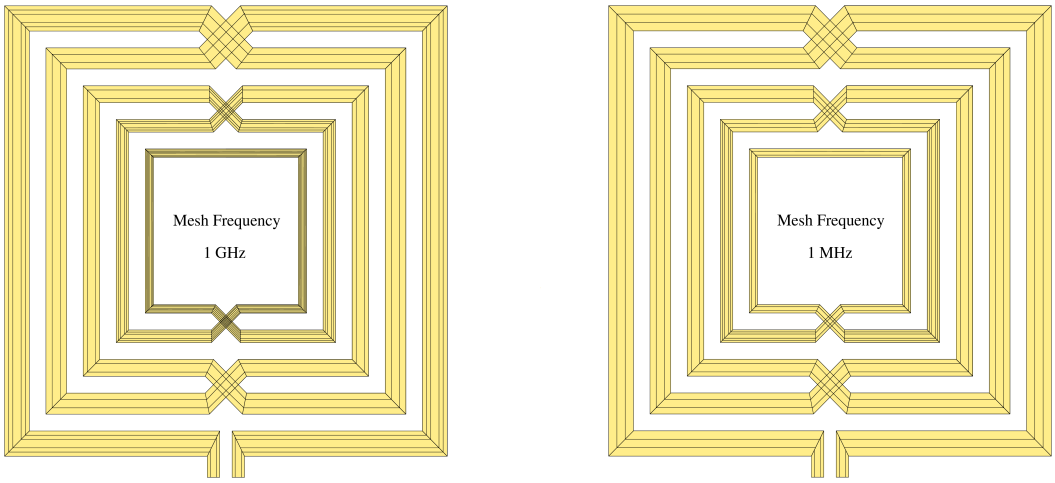

Fig. 4.22 Meshing of symmetric square inductor, (a) for frequency of 1Ghz and (b) for 1 Mhz.

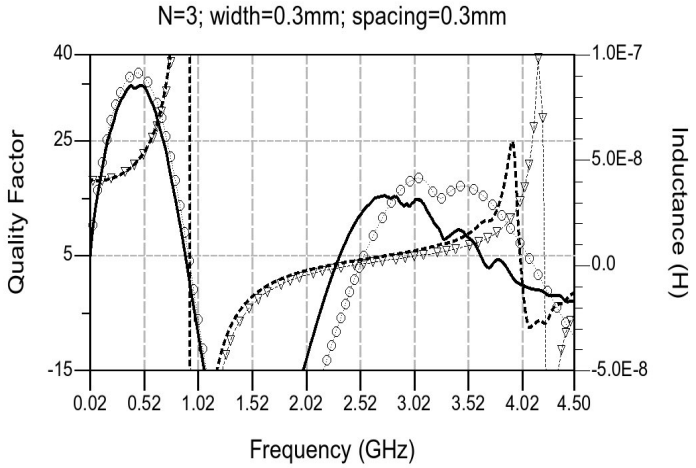

(a) LTCC-L8 inductor

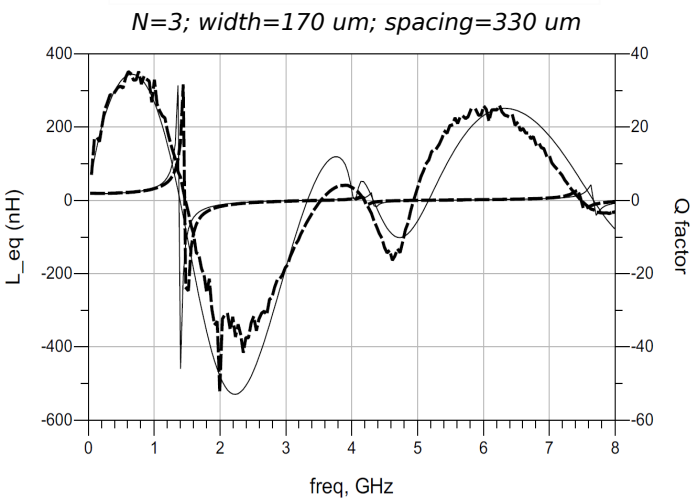

(b) LTCC-A6S inductor with GND-ring

Fig. 4.23 Measured vs. simulated data: (a)(solid line) measured Q; (o) simulated Q; (dashed line) measured L_{eq}; ($\bigtriangledown$) simulated L_{eq}, (b) (dasehd line) measurements; (solid line) simulation.

Chapter 5

Passive component library

Abstract

In this chapter, a library of planar components based on the already implemented fast electromagnetic solver is developed. The library is formed by film resistors, finger/stacked/film capacitors, and symmetric inductors. For each of them, the geometry is described, the relevant modelling features are discussed, and comparison with measurements is given. The library is a part of a complete Process Design Kit that has been implemented in the EDA platform Advanced Design System (ADS). Although it has been tuned for LTCC laminates, minor modifications in the substrate definition are only necessary to extend the library to other practical laminated technologies.

5.1 Introduction

A review on PDKs distributed by LTCC companies reveals that models for embedded components are seldom available. Table 5.1 collects PDK data found on a recent scan on websites, company brochures, and EDA platforms[1]. Four levels of PDKs are found:

A. *Basic*: fabrication process and design rules are described; but no EDA files, neither for masks, are provided.

B. *Basic with EDA files*: technology definition files are added, and, to some extent, design rule check files, though as a PCB PDK.

[1]There are more LTCC fab companies (Kyocera, Barry LTCC, Via electronics, Selmic, ...), but it has been impossible to find information related to their LTCC PDK.

Table 5.1 PDKs review of different LTCC companies.

Company	Ref.	PDK type	Observations
Anaren	[92]	*A*	None.
Murata	[93]	*A*	None.
NeoTech	[94]	*A*	None.
Dupont	[95]	*B-C*	Basic PDK for ADS.
DT Microcircuits	[96]	*D*	Compact models for passives.
IMST	[97]	*D*	3D FDTD core. No revision since 2002.

C. *Advanced I*: microstrip/stripline embedded components are included that are based on already existing models in the associated EDA platform.

D. *Advanced II*: embedded passives (R, C, L) are also provided.

Most LTCC foundries give the information related to the design guidelines which are normally obtained from material vendors (e.g., Heraeus, Ferro, Dupont). Then, the design flow methodology offered by EDA vendors [98]-[99] requires the use of EM simulators, a fact that makes the LTCC design a hand-crafted work. For its GreenTape 943 tape system, Dupont has a PDK library for ADS but only microstrip like components are scalable and are based on the already implemented components in ADS. DT Microcircuits has a library of passives based on compact models, but it seems that layouts and component placement are fixed. In 2002, IMST developed a 3D FDTD full solver for the modelling of LTCC components that could be embedded inside ADS. However, this option seems to be obsolete when compared with actual SiP design flow in ADS using the EMPro [100] environment as a co-simulation tool.

Although first works in LTCC device modelling were closer to the RFIC-MMIC compact models design paradigm, [44], [101], actual research is mainly focussed on the design of subsystems using EM solvers [49], [102]. The reason beneath is that the development of LTCC compact models is very complex because it has to take into account all LTCC fabrication possibilities, device topologies, geometries and placement.

Nevertheless, a change in the modelling paradigm has appeared in the last years due to the pursuit for automated synthesis tools [103]. In synthesis, the entry of the problem is the electrical parameters that are used in an optimization process. The goal is to find out an equivalent SPICE model and the corresponding layout of the passive that best matches the specified data. Due to the low accuracy of compact models for spanning correctly the design space, researches have accommodated EM solvers, in an automated way, as evaluation tools in the synthesis algorithm. For minimising the number of EM simulations, the common strategy is to use a sort of look up table (LUT) library or a surrogate model which have been

computed using EM solver. However, under a miss on the LUT/surrogate model, or a need for a larger design space, or a change in the technology (e.g., a last minute change in the number of layers of the LTCC stack), the synthesis procedure will require a relative large set of EM simulations, slowing-down the design phase. A possible alternative to minimise the required synthesis time is through the used of specialized EM solvers, as the one developed in the former chapters. In fact, it has been already applied to the synthesis of inductors in LTCC [104]. Other authors have also used the PEEC method for developing automated synthesis tools [105]-[106]. However, the main difference of those works with this one is the heuristic approach that uses information about the physics of the device for reducing the model order complexity.

Although synthesis tools are very useful for circuit design, in this chapter, the interest is set around device modelling itself. The key point is the replacement of compact models by EM ones based on fast and accurate solvers. This modelling procedure is made in two steps. First, using full-wave simulators, the physics of the LTCC component is analysed in order to identify the relevant phenomena that describes its behaviour. Second, the former information is loaded into the specialized solver: mesh parameters, Green's function truncation and equations describing the necessary physics are set accordingly. To check the goodness of this procedure, derived models are applied to film resistors, capacitors, inductors and compared with measurements.

5.2 Film resistors

Description

Resistors are made using a thick film process based on ruthenium oxide inks. They can be place inside (buried resistors) or on top of the LTCC substrate (surface resistors). For having a wide range of values, inks can have four different sheet resistance values: $10\Omega/sq$, $100\Omega/sq$, $1K\Omega/sq$ and $10K\Omega/sq$. As specified by material vendor, these values have typically a 30% formulation tolerance. On top of that, the control on the thickness of deposited material, is another source of process missmatch. Therefore, buried resistors should be used in ratio based designs, e.g. in polarization circuits. In that case, matched resistors are around 5%. When precision resistors are required, they can be placed on the LTCC surface for final laser trimming. Compared to SMD components, the advantage of using film resistors is the co-sintering, which minimizes cost and increases reliability; the drawback is that the printing area is a little bit bigger (this is only applicable to surface resistors because buried resistors do not occupy surface area where another component could be mounted on).

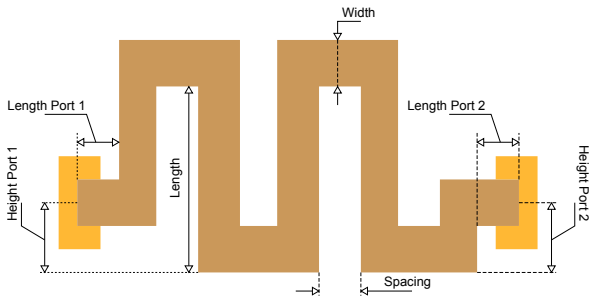

Fig. 5.1 Layout parameters of the film resistor.

Table 5.2 Geometrical values for the simulated resistor.

Length Ports	Height Ports	Length	Width	Spacing	Bends
$500\mu m$	$750\mu m$	$2.0mm$	$500\mu m$	$200\mu m$	5

The actual geometry shape is a meander which facilitates the compactness of the layout. Fig. 5.1 shows the parameters used in the definition of the geometry for developing the parameterized cell (pcell) in the PDK. To allow for any location of contact pins, variables *length port 1*, *length port 2*, *heigth port 1* and *heigth port 2* are defined. It includes metal pads that are automatically dimensioned according to design rules. Besides these parameters, the number of bends and layer level are added to the component. Notice that by selecting zero bends, the resistor topology is converted to a rectangular one.

Modelling

Fig. 5.2 shows the current distribution, computed at DC and at 1 GHz, in a $10\Omega/sq$ meander resistor having the geometrical parameters shown in Table 5.2. This plot has been obtained using a commercial MoM solver. It can be a little bit surprising that both distributions are almost equal. This is easily explained because the skin value for this material is about $250\mu m$ at $1GHz$. The picture for the remaining sheet resistance values is quite similar. Therefore, no crowding or skin effects are important in resistors.

Nevertheless, it is necessary to compute adequately the high frequency behaviour because capacitive effects introduce an imaginary component on the actual impedance of the device. This is depicted in Fig. 5.3 where the 1-port differential mixed made S-parameter frequency response is plotted in a Smith chart. Notice that this response is dependent on the actual layer where the resistor has been placed, i.e., it is affected by the coupling to the GND plane. Here, it is clear that a component model based on an EM solver will be able to reproduce the influence of capacitive parasitics; on the contrary, a compact model should be built for each layer location and each substrate definition.

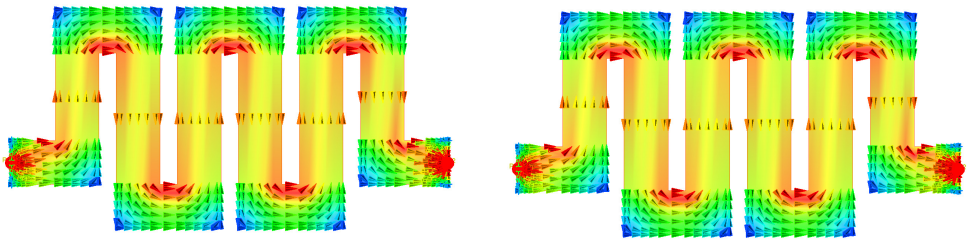

(a) DC (b) 1 GHz

Fig. 5.2 Current distribution in a $10\Omega/sq$ resistor at (a) DC and (b) 1GHz.

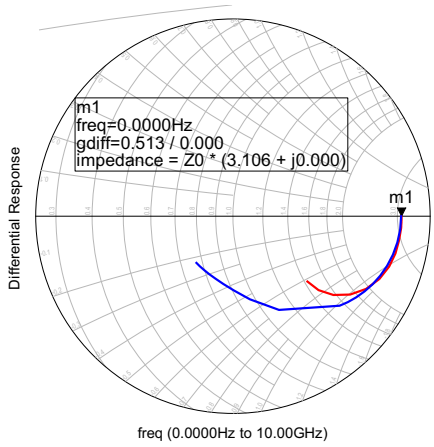

Fig. 5.3 Differential resistance response vs frequency (DC-10GHz): (blue) located at layer 1; (red) located at layer 12.

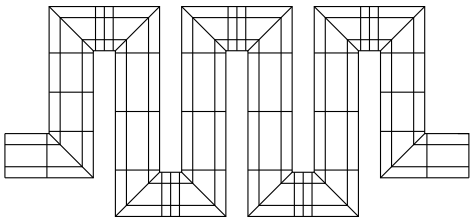

Fig. 5.4 Mesh partition for the computation of the current distribution in a film resistor.

The physics that describes the behaviour of the resistor fits inside the heuristic approach of the developed EM solver. The proposed mesh for computing resistors is shown in Fig. 5.4, which follows a Manhattan layout. Each corner of the meander in divided in two parts. In this way, the redistribution on the inner corner of each bend is better achieved. The influence of the magnetic part could be skipped, a fact that would accelerate the actual computation time. Although not drawn, metal pads are also taken into account in the model.

Table 5.3 Geometrical characteristics of resistors.

	No. bends	width	resistivity	R_{DC} (Ω)		time (51 points)	
R1	2	250 μm	10 Ω	PEEC	181.4	PEEC	2.5s
				MoM	181.8	MoM	57s
R2	2	500 μm	100 Ω	PEEC	925	PEEC	1.12s
				MoM	1026	MoM	1min2s
R3	5	250 μm	1K Ω	PEEC	38.06 K	PEEC	5.35s
				MoM	34.17	MoM	3min11s
R4	5	500 μm	10 K Ω	PEEC	195.11 K	PEEC	5.42s
				MoM	195.76K	MoM	3min6s

Verification

Due to materials compatibility problems between resistor inks and LTCC ceramic, it has not been possible to obtain reliable components for checking the PEEC model against experimental values. Instead, the PEEC solver for resistor modelling has been verified with MoMentum. In addition to geometry variations, the resistivity value has also been checked in this verification. Table 5.3 collects the parameter values used in simulation time. Whereas the obtained R_{DC} value are quite similar between both methods (differences lower than 1 %), the PEEC solver is 20 times faster thanks to the 1D current approximation. For a large number of bends and large width, the 1D approximation would decrease its accuracy. Nevertheless, such kind of resistors are seldom used.

The predicted behavior in a large frequency range is depicted in Fig. 5.5 for a section of the resistors in Table 5.3 that includes all variations of width, bends and resistivity. Differences are lower than 5 %, increasing at higher frequencies due to dismiss of retarded potential; qualitatively, i.e. parasitic behaviour, both methods produce similar results. Therefore, the developed solver can be used for LTCC film resistor modelling.

5.3 Capacitor

Capacitance values range from $0.14pF$ to $30nF$ for the LTCC tape systems used in this work. To achieve this wide range, three different type of capacitors have been developed: finger, stacked and thick film. Table 5.4 collects some general characteristics.

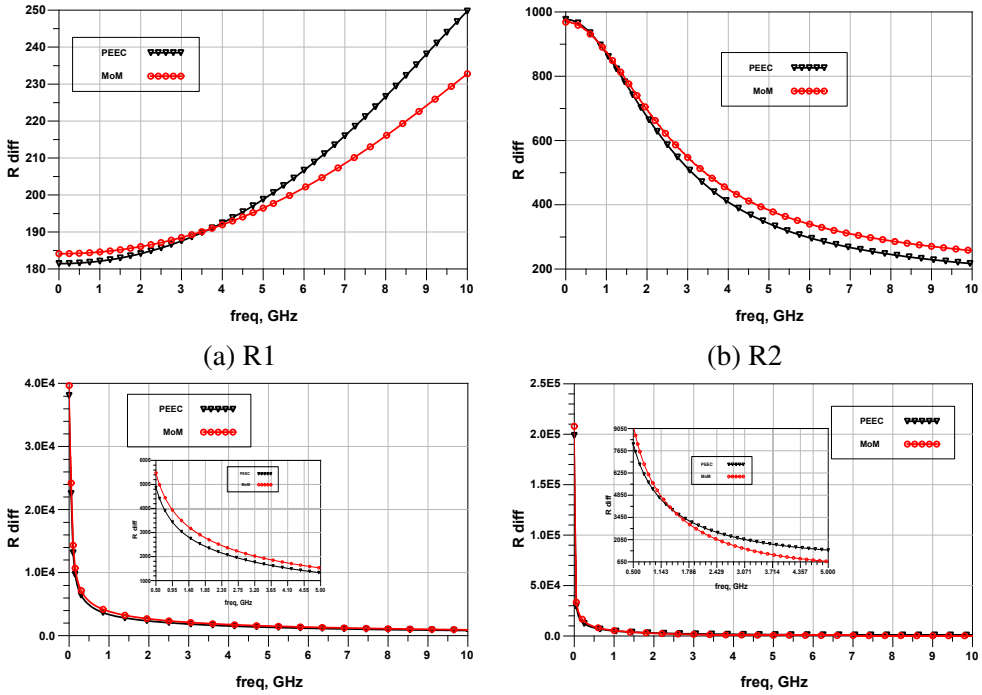

(a) R1 (b) R2

(c) R3 (d) R4

Fig. 5.5 Simulation data comparison of a film resistor.

Table 5.4 Type of capacitors in LTCC tape systems.

Type	Range	Tolerance	Observations
Finger	$0.14-20pF$	5%	filter design; high SRF
Stacked	$0.7-300pF$	5%	compactness; medium SRF
Thick film	$20-3000pF$	30%	DC block

5.3.1 Finger capacitor

Description

It is an inter-digitized coplanar metalstrip based component. Fig. 5.6 shows the geometrical parameters which are the *width* and *length* of fingers and the *gap* distance between them, and the length and width of access ports. It can be located at any layer and the number of *fingers* can be selected as well. A guard ring structure can be located as well. Note that the layout is Manhattan. The range of capacitance values varies from $140fF$, for minimum device dimensions and located on the top layer, upto $21.5pF$ for an embedded $10x10mm^2$ one, which is a quite large area. This type of capacitors are intended for precise values that can be required in matching circuits and filter design. Its tolerance is linked to the screen printing process of metal parts. Designers must take care when this component is placed

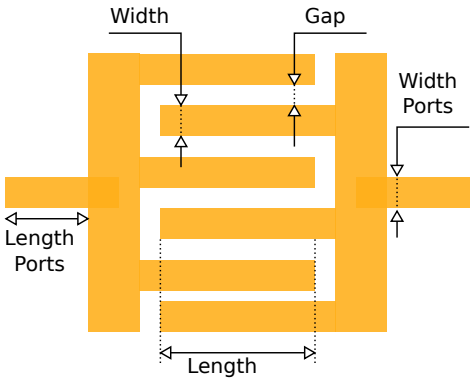

Fig. 5.6 Layout parameters of the finger capacitor.

near a GND plane because the parasitic capacitance can be very large, a fact that is taken into account using the EM model.

Modelling

Opposite to the resistor case, the behaviour of $\bar{J}$ is not so intuitive in a finger capacitor; thus, it is not clear if using the developed PEEC solver can be applied for the modelling of this device. In addition, it is not sure if the dismiss of the retarded potential can still cover a wide frequency range description, upto its self resonance (SRF), with enough accuracy. To study qualitatively these issues, the 2.5D planar solver MoMemtum is used. The advantage in using MoMemtum is that a full-wave (fw) or a quasi-static (qs) solver can be chosen. Thus, by plotting both solver solutions, it is possible to figure out the typical maximum simulation frequency using a quasi-static solver. With the post-processing capabilities of the software, the actual $\bar{J}$ will be plotted at different and interesting frequency points.

Fig.5.7 shows the differential impedance of a $1.2pF$ finger capacitor ($width = 200\mu m$, $length = 3mm$, $gap = 200\mu m$, $layer = 12$) calculated using both MoMentum solvers. For a typical dimension of $4.7mm$ of the finger capacitor, the retarded time is about $40ps$ that represents a maximum simulation frequency of $25GHz$. However, for an error lower than $\lambda/10$ and taken into account that the maximum distance from any of the two ports to any other point of the device is about $3.7mm$, the error in phase computation can start to be large above $3GHz$. Nonetheless, the difference in SRF is about 2% ($SRF_{fw} = 5.09GHz$, $SRF_{qs} = 5.20GHz$) although the value is beyond the $3GHz$ limit. Moreover, the second resonance, which is located at $7.73GHz$, is still predicted satisfactorily with the quasi-static solver. The reason because the quasi-static solver works so well with this device is due to the fact that the main mechanism responsible for the capacitance behaviour is due to the EM couplings and not to the delay of signals travelling through the device. For the equivalent capacitance, both

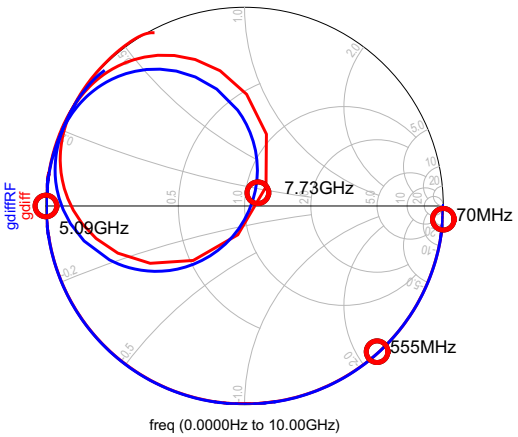

Fig. 5.7 Comparison of the differential impedance calculated using (red) full-wave, and (blue) quasi-static solvers.

solvers predict almost the same value: $C_{fw} = 1.207pF$, $C_{qs} = 1.201pF$. However, notice that, at large frequencies, the difference in electrical length is important.

Following with this qualitative analysis, the next goal is to make a picture of the actual current distribution $\bar{J}$ evaluated at different frequency points, which are marked in Fig.5.7. This evaluation is shown in Fig.5.8. Interestingly, the current is directed along the length of fingers, and the crowding effect is quite similar in all fingers. Up to SRF, the maximum value of the current is produced at the beginning of the finger and, due to the capacitive coupling with neighbour fingers, it losses its current when running into the opposite gap. For the vertical strips collecting fingers, $\bar{J}$ is dependent on frequency and it has a 2D distribution. At $70MHz$, $555MHz$ and SRF, most of the current flows parallel to strip edges except in the locations where fingers are connected [2]. At $7.73GHz$ (2^{nd} SRF), the plot shows that the resonance is due to the generation of symmetric double current loop that is closed thanks to vertical strips; but still $\bar{J}$ has a clear principal axis along fingers.

To sum up with this qualitative study, the important point is that $\bar{J}$ can be treated as an 1D object for fingers and 2D for the strip connecting all fingers. However, as heuristic rule, it was dictated that this 1D object should be directed along $\bar{J}_{DC}$. To check this point, it was pointed out in Chapter II that the DC regime for a capacitor component could be simulated by adding a small conductivity to the substrate. Once again,

At fingers, $\vec{J}$ is 1D, but the electrode region connecting the access port and fingers has a 2D nature. A fail in computing correctly this distribution will impact on the accuracy of the

[2]For $70MHz$ and $555MHz$ the voltage excitation has a phase lag of $90°$, thus $\bar{J}$ is maximised. At resonance, although the picture is quite similar it must be stressed that the actual picture is taken at $0°$ phase, which means that voltage and current are in-phase.

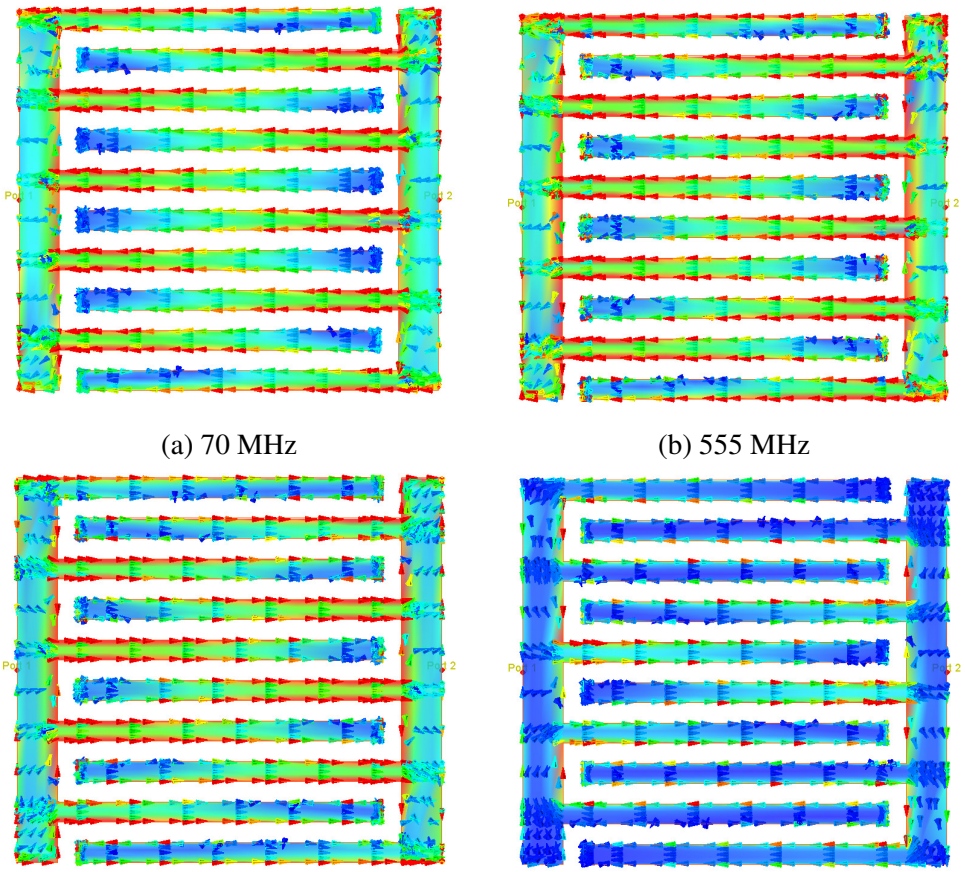

(a) 70 MHz (b) 555 MHz

(c) 5.09 GHz (d) 7.73 GHz

Fig. 5.8 $\bar{J}$ at frequency values corresponding to the circles shown in Fig.5.7.

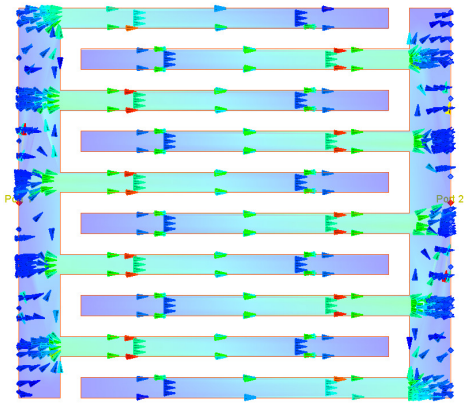

Fig. 5.9 Evaluation of the finger capacitor at DC using a conductive substrate.

determination of its self resonant frequency. With this example, notice that a 1D/2D hybrid mesh methodology can enhance the computing performance of the PEEC solver. To do that,

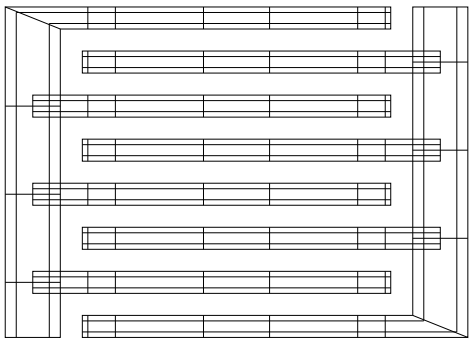

Fig. 5.10 Mesh distribution used for the evaluation of finger capacitors.

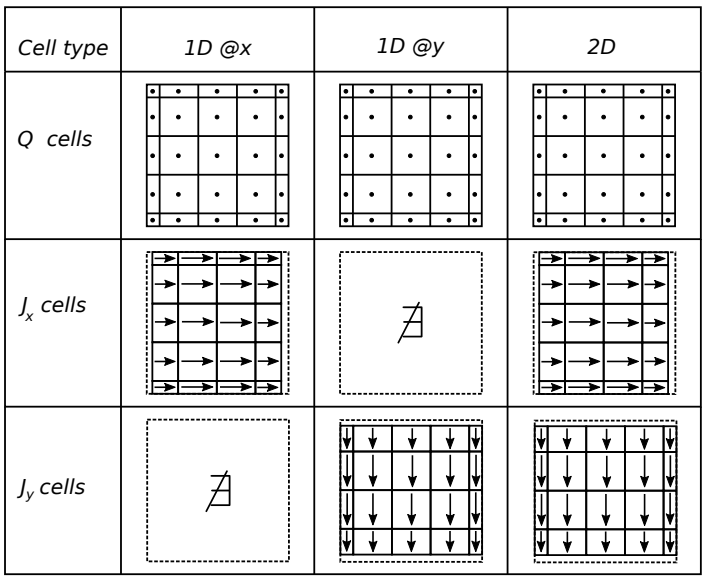

Fig. 5.11 1D/2D mesh.

the different metal regions are labelled as 1D or 2D $\vec{J}$ distribution. According to its label, Fig.5.11 shows how a quad region (from now on, a rectangular primitive) is divided in. All regions have the same kind of charge mesh discretization, which cells are represented by their central node, but no J_y current mesh is provided for a 1D-$\hat{x}$ area (and viceversa). This means that 1D-$\hat{x}$ primitives cannot share an electrical border, i.e. a current passing through, with 1D-$\hat{y}$ ones. Nonetheless, they can share the geometry of the border; however, it will be understood as electrically disconnected. 2D areas have both J_x and J_y current meshes; thus they can be connected to any border.

In the same Fig.5.11, notice that only internal current meshes have been plotted. Current cells at the border can be formed once the information of the charge mesh is projected onto these borders. To better understand this idea, Fig. 5.12 shows two compatible touching primitives. Be aware that any intersection of borders is allowed, the number of nodes touching

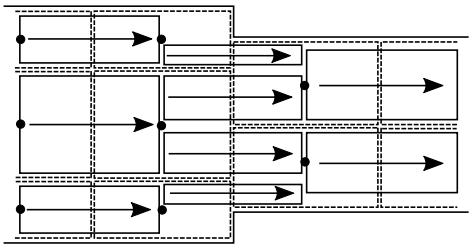

Fig. 5.12 Current cells at the border.

the border can be different in either primitive as well as their size. Starting from the lower end point of the border of the primitive on the left, the current (arrow) flowing out of the charge cell (dashed rectangle) enters in its neighbour charge cell located in the primitive on the right. The current flows just across the shared frontier between both charge cells that defines the width of the new current cell (solid rectangle). Its length is given by the distance between nodes (black circles), and its electrical connection by the corresponding node numbers. This procedure is repeated until the top end point of the primitive on the left is reached. Notice that isolated segments belonging to the border do not generate any additional current mesh. The generated current mesh at the border can be viewed as an unstructured PEEC mesh because a charge cell can have more than one current cell entering or leaving its domain, getting this way the possibility to decouple the mesh density of different regions. When using this 2D un-structured mesh the penalty is an increase in computation time.

Verification

Three finger capacitors have been used to verify the solver. Their geometric characteristics are collected in Table 5.5. They have been fabricated in a 12-layer LTCC process with a total thickness of $840\mu m$, and a relative permittivity of 6.5 [37]. Measurements have been performed using a GSG-$500\mu m$ probe and a SOLT calibration procedure.

The main obtained electrical characteristics from measurement, from PEEC simulation, and from a commercial method of moments (MoM) solver are shown in Table 5.6. PEEC solver has about the same accuracy as MoM, but the total simulation time is five times lower. To check the predicted behaviour upto the SRF, it is represented the differential capacitance value in Fig. 5.13. The plot inset is a zoom of the low frequency range; the picture inset is the image of the measured device. Notice that, in spite of the quasi-static approximation, the solver is able to predict the behaviour in a wide frequency range.

Table 5.5 Geometrical characteristics of finger capacitors.

Devide id	Length[μm]	Width[μm]	Gap[μm]
FC1	800	200	400
FC2	1000	400	200
FC3	1400	600	200

Table 5.6 Measured vs. simulated data.

		Cdiff(fF)	SRF(Ghz)	t_{comp} (51 points)
FC1	PEEC	209	7.9	51.27s
	MoM	205	8.3	4min15s
	Meas	212	7.8	
FC2	PEEC	297	5.5	46.05s
	MoM	306	5.3	4min37s
	Meas	285	5.4	
FC3	PEEC	424	4.8	46.16s
	MoM	443	4.4	5min51s
	Meas	421	4.6	

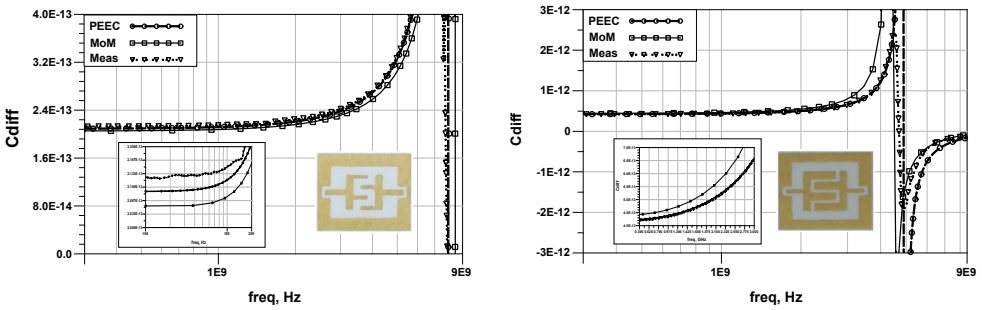

(a) (b)

Fig. 5.13 Measured vs. simulated data of a finger capacitor:(a) Finger capacitor 1 (FC1) and (b) Finger capacitor 2 (FC2).

5.3.2 Stacked capacitor

Description

It is a 3D stacked parallel plate topology using any number of layers where plates are intercalated and joined with vias. The dielectric material is the LTCC itself. The component can be located anywhere under the constraint that the total number of layers is lower than

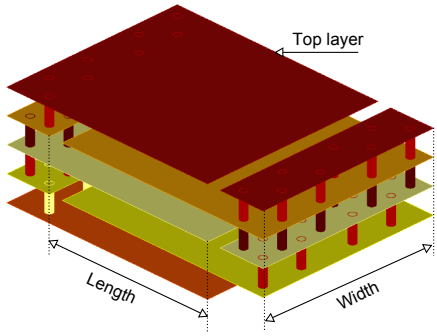

Fig. 5.14 3D-View of stacked capacitor layout indicating the layout parameters.

that of the technology. Geometrical parameters are restricted to *length* and *width* of plates, without counting the area required for via connection. Pin locations are placed opposite each other and symmetrically according to layout. Nonetheless, pins can be located at any layer level where the device exists, getting this way an easier connection to other circuit devices. The range of capacitance values varies from $0.7pF$ fF, for a minimum device dimensions, upto xx fF for a fully depleted $5x5mm^2$ stacked capacitor in a 12 layers zero-shrinkage L8 process[3]. Similarly to finger capacitors, this device is devoted to matching, filters, or AC signal coupling. Designers must take into account that the tolerance of the component is linked to LTCC dielectric thickness control.

Modelling

In fact, the stacked capacitor is a sort of vertical version of the finger capacitor. Therefore, the behaviour related to the retarded potential and the current distribution on the different plates will be similar to the finger case[4]. In Fig.5.15, it is represented $\bar{J}$ for a 4 layer stacked capacitor implemented in an L8 process, which nominal value is 21.5pF. $\bar{J}$ is directed along the line connecting both ports. Via connections are important for distributing evenly the current through the plates. Actually, the modelling of this component will follow the same guidelines of previous capacitor. The only additional consideration is that the projection of meshing cells at different plates must be coincident for a reliable capacitance computation.

Verification

To verify the stacked capacitor model two stacked capacitors have been compared with MoM commercial software. The geometry of stacked capacitors are showing in Table 5.7, the mesh of model is based on 1D/2D hybrid explained in the previous section.

[3]Range values are dependent on the total number of layers of the technology and dielectric properties.
[4]Plots in Fig.5.8 could be interpreted as cross-section cuts of a stacked capacitor.

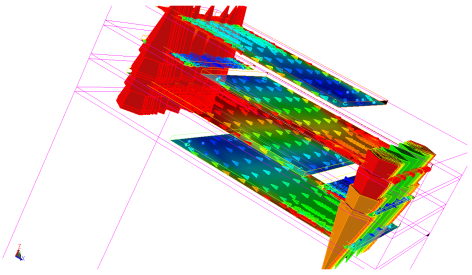

Fig. 5.15 $\bar{J}$ at 10MHz for a 21.5pF stacked capacitor.

Table 5.7 Geometrical characteristics of finger capacitors.

Devide id	Length [mm]	Width [mm]	No. layers
FC1	2	2	4
FC2	2	2	6

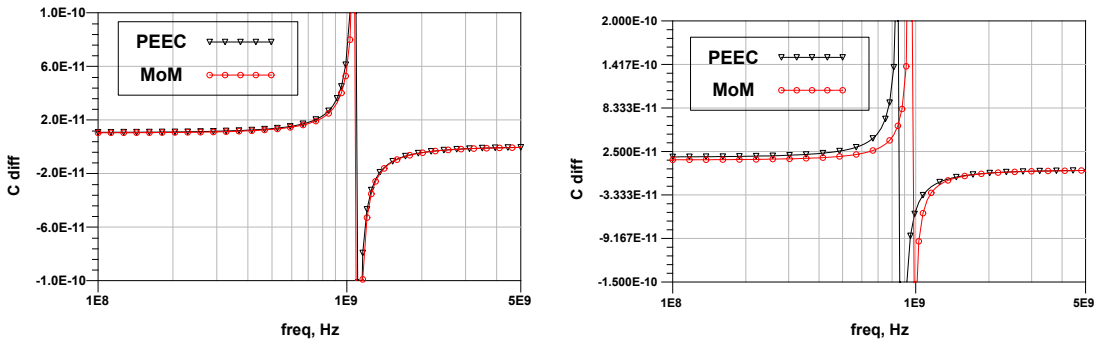

(a) (b)

Fig. 5.16 Simulation data comparison of a stacked capacitor: (a) 4 layers; (b) 6 layers.

The comparison result of two stacked capacitors are showing in Fig. 5.16, the difference between MoM commercial software and PEEC model is less than 1 % in all frequency range comparison. No experimental data is available for this component.

5.3.3 Film capacitor

Description

The film capacitor is a parallel plate capacitor made from an added high-K dielectric ($\varepsilon_r \approx 250$) sandwiched between two metal layers placed on the same LTCC dielectric layer. The thickness of this high-K dielectric is about $35\mu m$. This value is quite thick, but minimizes tolerances by providing a uniform and flat surface. To avoid cracking of the high-K dielectric, it is recommend to located the component on the central layers (e.g., for a 12 layers process,

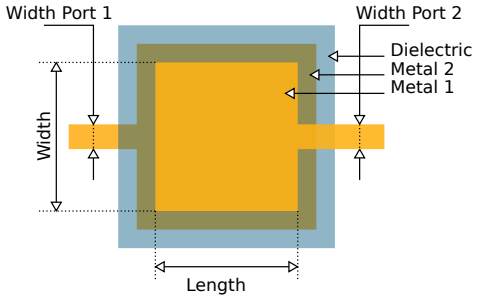

Fig. 5.17 Layout parameters of the film capacitor.

the allowed layer levels would be 5, 6 and 7). Fig. 5.17 shows the layout of the component indicating the defined geometrical parameters. Capacitance values range from 20 pF up to 30 nF. Similarly to the film resistor component, variables *width port 1*, *width port 2*, and *angle of port 2* are used to facilitate pin connection. This last variable sets the orientation of the second port pin, which can be placed at the bottom/rigth/top side of the device. The primary application of film capacitors is for DC bias filtering due its large tolerance value ($> 30\%$).

Modelling

Film capacitors are expected to have a behaviour similar to a two layer stacked capacitor. However, the inclusion of a high-K dielectric can have additional effects. Moreover, the second port connection can be located in different positions, thus $\bar{J}$ is expected to be affected by this fact. Fig.5.18a shows the simulated $\bar{J}$ for an $1.5nF$ film capacitor ($width = 4mm$, $length = 4mm$, $layer = 6$) embedded in a 12-layer L8 tape system where port1 and port2 are aligned. Once again, $\bar{J}$ is basically directed along the line connecting both ports, except at the sides of both plates where the current follows the perimeter path between input and output ports. For the case where ports are located at 90°, the results are depicted in Fig.5.18b. It is very interesting to notice that, at each plate, $\bar{J}$ is directed according to its port direction, except at the sides nearby both ports, where the current tends to follow the perimeter.

The introduction of the high-K dielectric layer modifies the substrate cross-section. Therefore, the associated Green's function does not correspond to a homogeneous media; thus, the formalism developed in chapter 3 cannot be applied directly. This problem has has forced to find an alternative heuristic solution that consists in dividing the original computation in two homogeneous substrate problems. For a better understanding of the method, Fig. 5.19 shows a transversal cut of a film capacitor and its actual π compact model. Notice that the elements Y_{TP} and Y_{BP}, i.e. the top/bottom plate admittance to ground, are associated to the fields embedded in the LTCC- air media; Y_{TBP}, the top to bottom plates admittance, is mainly related to the fields in the high-K dielectric. Keeping in mind thus

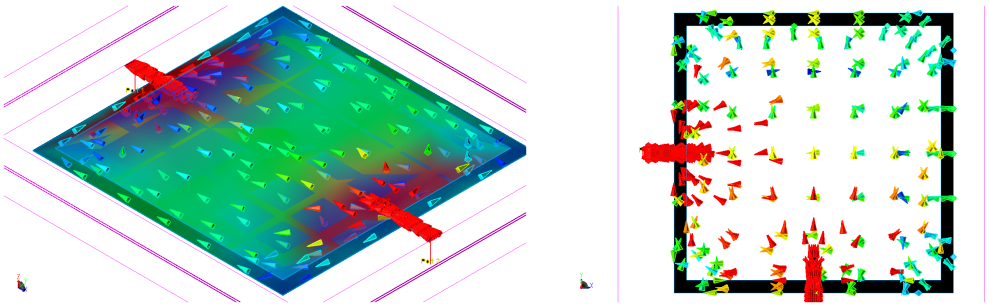

(a) (b)

Fig. 5.18 $\bar{J}$ at 1MHz for a 1.5nF film capacitor: (a) ports in opposite configuration; (b) ports in 90°.

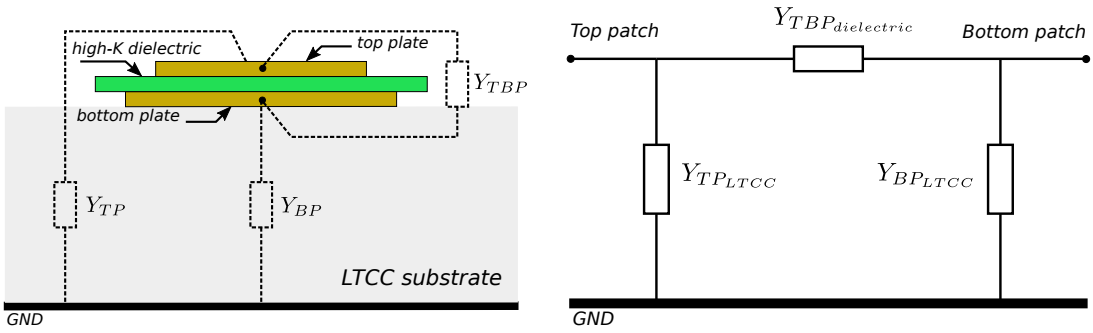

(a) (b)

Fig. 5.19 Y matrix approach of a film capacitor: (a) substrate approach, and (b) Y matrix.

configuration, first it is calculated the Y-parameter matrix of the film capacitor where all dielectrics are of LTCC type by solving the corresponding canonical problems of both ports. The Y-parameters are obtained as

$$Y_{11} = \left.\frac{I_1}{V_1}\right|_{V_2=0} ; Y_{22} = \left.\frac{I_2}{V_2}\right|_{V_1=0} ; Y_{12} = Y_{21} = \left.\frac{I_1}{V_2}\right|_{V_1=0} . \tag{5.1}$$

From these values, $Y_{TP_{LTCC}}$ and $Y_{BP_{LTCC}}$ are extracted as

$$Y_{TP_{LTCC}} \equiv Y_{11_{LTCC}} + Y_{12_{LTCC}} \tag{5.2}$$

$$Y_{BP_{LTCC}} \equiv Y_{22_{LTCC}} + Y_{21_{LTCC}} . \tag{5.3}$$

Table 5.8 Geometrical characteristics of film capacitors.

Devide id	Length	Width	Ring	Port 2	high-K value
film capacitor 1	740 μm	740 μm	no	180○	250
film capacitor 2	740 μm	740 μm	no	90○	250
film capacitor 3	1420 μm	1420 μm	yes	180○	250

Second, the same problem is solved once again but changing the LTCC by the high-K dielectric for all layers. Then, the value of $Y_{TBP_{dielectric}}$ is found as

$$Y_{TBP_{dielectric}} \equiv -Y_{12_{high-K}}\,. \tag{5.4}$$

Eqs.(5.2)-(5.4) are combined for obtaining the actual Y-parameter model of the heterogeneous substrate as it is shown next:

$$Y_{11} \equiv Y_{TP_{LTCC}} - Y_{TBP_{high-K}} \tag{5.5}$$

$$Y_{22} \equiv Y_{BP_{LTCC}} - Y_{TBP_{high-K}} \tag{5.6}$$

$$Y_{12} = Y_{21} \equiv Y_{TBP_{high-K}}\,. \tag{5.7}$$

The mesh used in this model is hybrid 1D/2D mesh, in length ports we use 1D and in the patches we use 2D.

Verification

Three different capacitor configurations, which main parameters are shown in Table 5.8, have been used for checking the proposed methodology. The first two capacitors are are evaluated using MoMentum and the PEEC method and results are plotted in Fig. 5.20. For both input/output ports configuration (180° and 90°) differences between both simulators are within 1 % up to the SRF.

The third capacitor has also been characterized experimentally. It has been fabricated in a 10-layer LTCC process with a total thickness of 1000 μm, and a relative permittivity of 6.5 [37]. Measurements have been performed using a GSG-500μm probe and a SOLT calibration procedure. Fig. 5.21 shows the comparison between MoM, PEEC and experimental data. At low frequencies, the PEEC solver predicts a capacitance value closer to the actual one; MoM has a better accuracy about the SRF. To sum up, the proposed model can be used for the evaluation of film capacitors.

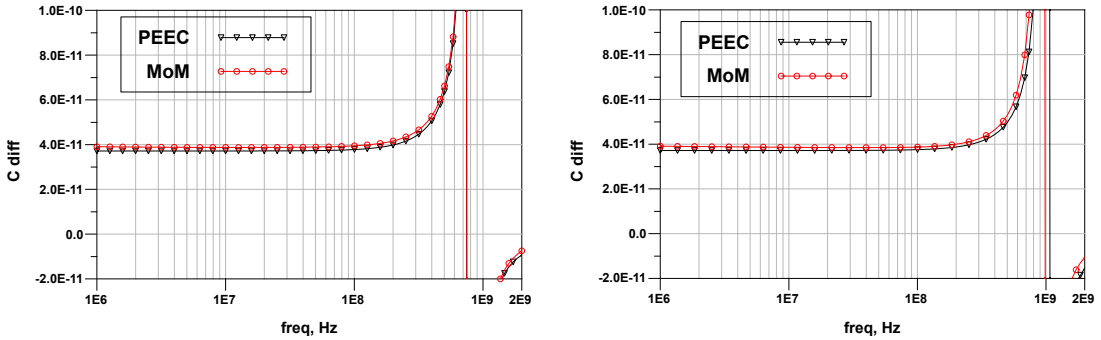

(a) (b)

Fig. 5.20 Simulation data comparison of a film capacitor: (a) ports in opposite configuration; (b) ports in 90°.

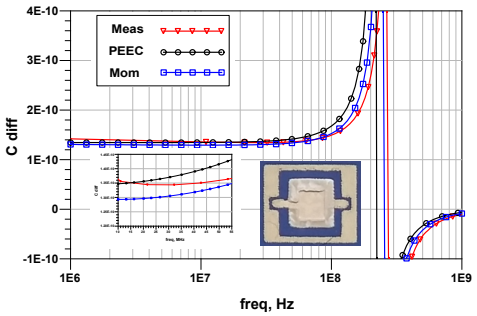

Fig. 5.21 Measured vs. simulated data of a film capacitor.

5.4 Inductor

LTCC inductors can be implemented in different ways. Attending to the orientation of the $\bar{B}$ field according to the substrate plane, they can be classified as follows

- *In plane* $\bar{B}$. These inductors exploit the z dimension of the substrate for building 3D structures, toroids and solenoids, that confine the magnetic field inside the substrate. This is a suitable property because the component has a better electromagnetic interference robustness. Due to their typical large size, they are used in applications below GHz (EMI filters, power converters, ...). Moreover, ferrite materials can be also embedded inside the inductor core.

- *Out of plane* $\bar{B}$. The layout is mainly planar; vias are only used for avoiding short-circuits between turns of the inductor. It is the type of inductor used in RFIC design. Different spiral shapes can be constructed (circular, octagonal, square, ...) and they can be laid out following an Arquimedes spiral path or as symmetric structures. They

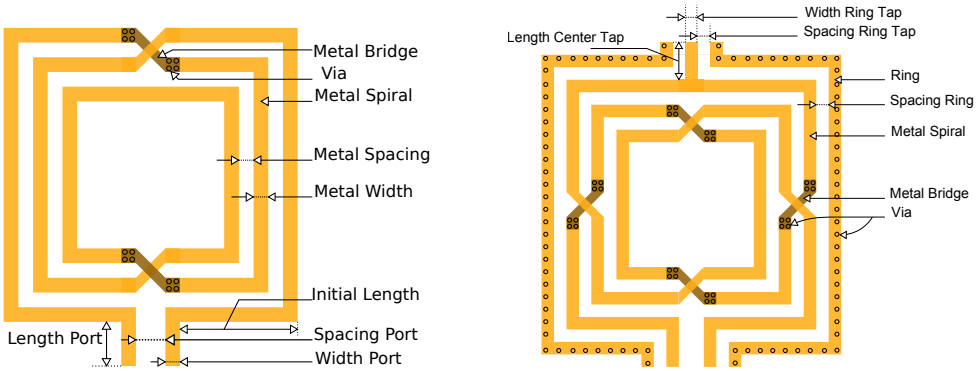

(a) no center-tap (b) with center-tap

Fig. 5.22 Geometrical parameters of square symmetric inductors: (a) no center-tap layout connection; (b) with center-tap. Guard-ring can be placed in both components.

can be used above few GHz. Typical applications are the implementation of diplexers, matching circuits, RF chokes, resonant tanks, etc.

For the library developed in this Chapter, the selected topology is the symmetric square spiral inductor because it fits quite well the heuristic rules of the developed solver. To account for toroids/solenoids, additional features should be included in the PEEC algorithm, being the most important the incorporation of non-orthogonal elements. Inductances can range from 1nH up to 100 nH using a reasonable LTCC area.

Description

Fig. 5.22 shows the layout of the two implemented symmetric square inductors. The center-tap configuration has the advantage of providing a common-mode node. It can be used for different purposes, e.g., as DC feed of active devices in differential circuits where the inductor is attached to. Compared to resistors and capacitors, the geometrical description of inductors is further more complex. The necessary parameters are illustrated in Fig. 5.22. It must taken into account that metal width and spacing between turns are not fixed, but can be changed at each turn of the inductor. With this feature, optimization design space is broaden, thus tapered inductors can be considered [107].

In addition to geometrical parameters, a considerable number of topological parameters must be included for a complete description of the component, i.e.,

- *Number of turns*. It sets the number of turns of the inductor. For the center-tap case, it must be and odd number.

- *Guard-ring*. It is a flag that helps the designer to make use of a guard-ring structure. In Fig. 5.22b, the additional geometrical parameters associated to the ring are shown. When using the guard, vias can be added to provide a contact to actual ground planes.
- *Spiral layer level*. The layer location of the main spiral metal strips is set with this value. Of course, it must be compatible with the remaining topological parameters and the maximum number of layers of the LTCC stack.
- *Bridge layer level*. To avoid short-circuits, the bridge can be placed as well in any layer, except the one occupied by the spiral layer.
- *Bottom GND plane*. The inductor can have no GND plane, a GND plane at the bottom of the LTCC substrate, or even it can be located at any layer below the spiral and bridge layers.
- *Top GND plane*. It is the top counter-part of the previous variable.

With such a large number of parameters, it is obvious that the development of LTCC compact models, if not impossible, is a tough and cumbersome task. On the contrary, using an EM solver, it is only necessary to develop the geometrical instances according to the mentioned parameters.

Modelling

Planar inductors are devices which behaviour is mainly determined through the magnetic coupling between metalstrips, a phenomena that has been discussed exhaustively in Chapter 4. As a reminder, Fig.5.23 shows the current distribution of a $18nH$ inductor that contains a guard-ring. Not only spiral metallizations, but the guard-ring structure has a 1D $\bar{J}$ distribution. Notice the crowding effect at each turn of the inductor, which has a different pattern. Therefore, inductors can be modelled beyond their SRF using the proposed PEEC solver . The adaptive mesh used for the modelling of inductors has been already studied in the last chapter; thus no additional information is given here.

Verification

The developed EM inductor model is applied to the study of the performance of planar inductors due to the presence of shielding structures [108]. Two experiments are proposed. In the first one, identical inductor geometries are evaluated under three different electromagnetic boundary conditions: (i) as a stand-alone device, (ii) surrounded by a guard-ring structure, and (iii) adding a ground plane connected to the guard-ring with solid through vias. In the

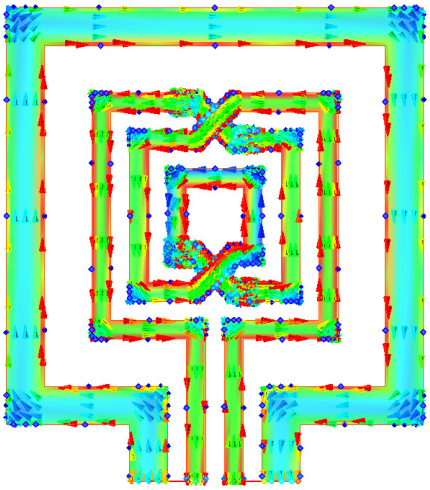

Fig. 5.23 Current distribution of a 18 nH inductor contains a guard ring.

second one, the influence of the width of the guard-ring is studied. Of course, experimental results are compared with simulations.

The chosen LTCC substrate is formed by stacking six layers of Ferro A6S ceramic material ($\varepsilon_r = 6.0$, $tg\delta < 0.001$). The thickness of each dielectric is about $110\mu m$. Gold metallizations have a thickness of $8\mu m$; thus, the sheet resistance is lower than $5m\Omega$.

The geometry of the inductors used for the experiments is the one already defined in Fig. 5.22 and a photograph of the fabricated structures is shown in Fig. 5.24. Some of the geometrical parameters are common to all devices: number of turns is always 3; metal width of input ports is set to $185\mu m$ and their separation is $850\mu m$; for shielded structures, ports are $200\mu m$ apart from guard-ring. The remaining parameters are collected in Table 5.9 and Table 5.10 for the first and second experiment set, respectively. Notice that, for the first experiment, three different kind of devices are fabricated: the difference between them is the change in metal width and separation, thus the pitch between turns is always fixed. In addition, the selected geometries have another common fact: the inner side of inductors is always $800\mu m$. The reason for this choice is that, by maintaining both inner side and pitch identical, all inductors will have a similar L_{eq}.

Both experimental and simulation data are obtained as two-port device. Then, one-port Z_{eq} impedance must be derived at the post-processing step. In order to maximise the effects of shields, the one-port single-ended configuration with a short-circuited output port is chosen. Using Y two-port admittance parameters, $Z_{eq} = 1/Y_{11}$. From Z_{eq}, equivalent inductance (L_{eq}), quality factor (Q) and self resonance (SRF) are chosen as figures of merit. Measurements have been performed using an HP 8720C network analyser, GSGSG 500 μm Picoprobe RF probes and SOLT calibration method in a frequency range from 50MHz to 8GHz.

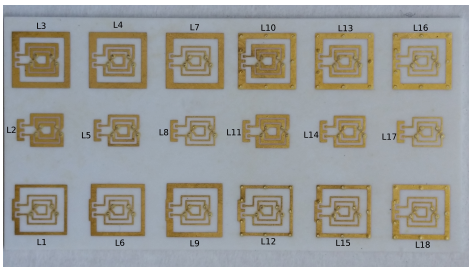

Fig. 5.24 Complete set of LTCC inductors used in both experiments.

Table 5.9 Geometry [μm] of inductors for first experiment.

# induc	type	length port	initial length	metal width	metal sep	ring width	ring sep
L2 & L11	no-ring	1160	1200	370	130	–	–
L3	ring	1180	1220	370	130	625	600
L10	GND-ring	1210	1190	370	130	625	600
L5 & L14	no-ring	1260	1150	270	230	–	–
L4	ring	1295	1095	270	230	625	700
L13	GND-ring	1380	1035	270	230	625	700
L8 & L17	no-ring	1370	1010	170	330	–	–
L7	ring	1415	995	170	330	625	800
L16	GND-ring	1450	1030	170	330	625	800

Table 5.10 Geometry [μm] of inductors for second experiment.

ring	L1	L6	L9	L7
GND-ring	L12	L15	L18	L16
width ring	325	425	525	625

In the commercial tool, meshing options have been set to automatic edge-mesh, five cells per width, and a mesh frequency of $5GHz$, which are typical values used by designers. For the PEEC based model, the mesh frequency has been also set to $5GHz$, but no additional meshing parameters are needed. Fig. 5.25 shows a comparison of the obtained meshes, for an inductor that has 3 turns, a width of $350\mu m$, a spacing of $150\mu m$ between turns, and an initial length of $1100\mu m$. Notice that PEEC mesh has a considerable lower number of cells and vias are considered as lumped elements. For this inductor, a comparison with experimental values is given in Fig. 5.26 for both numerical methods.

For the equivalent inductance plot, the behavior below SRF is within a 2% error for the PEEC method and a 10% for the commercial software. This difference in simulation performance is due to the exactness in the computation of partial inductance using analytical

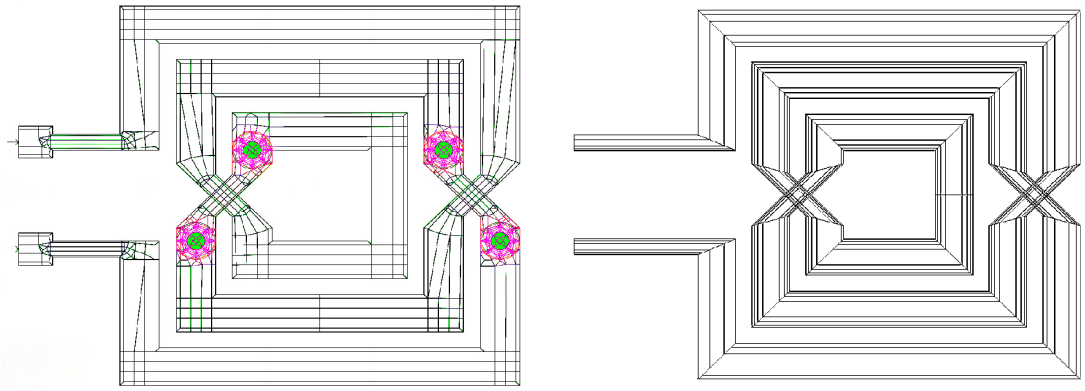

(a) (b)

Fig. 5.25 Inductor mesh: (a) MoM; (b) PEEC.

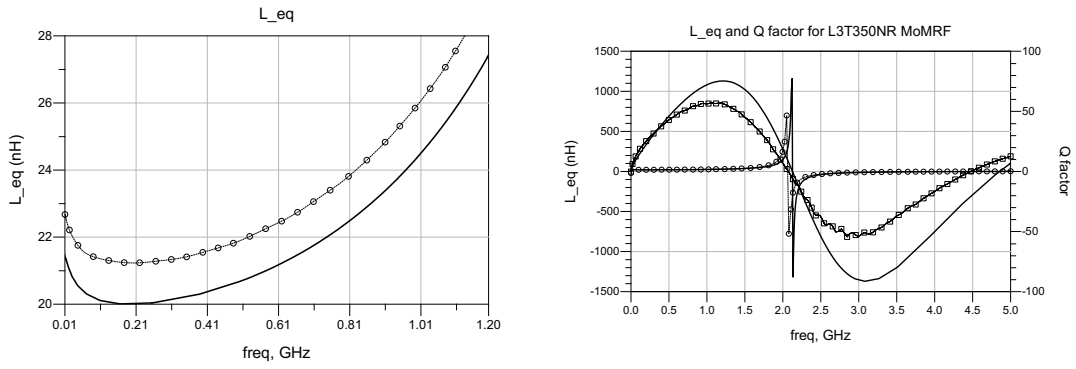

(a) (b)

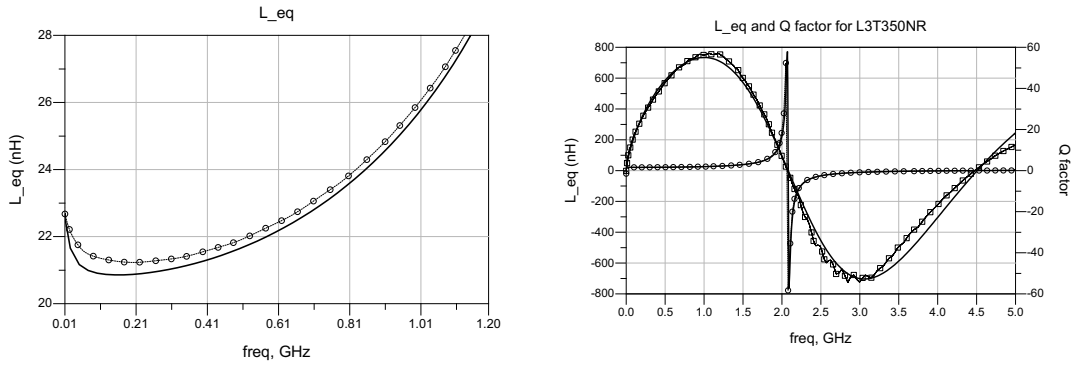

(c) (d)

Fig. 5.26 Results of MoM and PEEC methods vs experimental data: (a) MoM; (b) MoM; (c) PEEC; (d) PEEC.

expressions. Nevertheless, the differences in the prediction of the Q factor behaviour are much more important. The PEEC model is able to match Q plot with in a 5% error up to the first resonance and beyond. However, the mesh produced by the other tool cannot catch

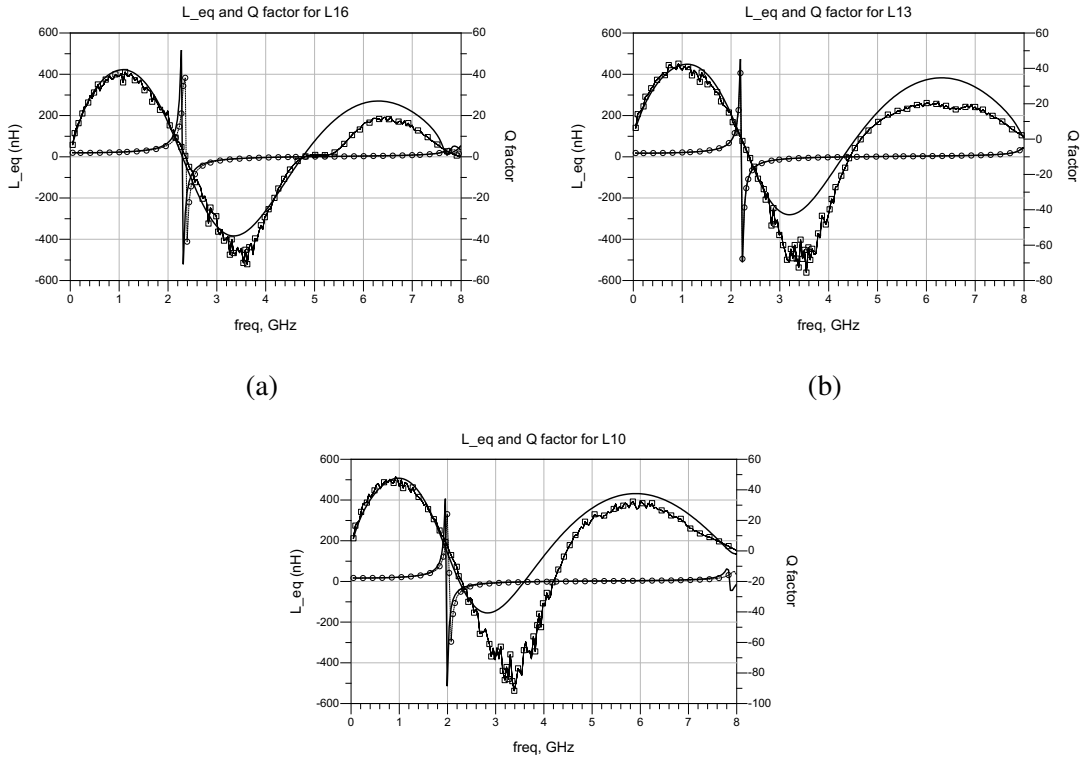

Fig. 5.27 Equivalent inductance L_{eq} and quality factor Q for (a) inductor L16 ; (b) inductor 13; (c) inductor L10.

up accurately the crowding effect, thus errors are higher than 40%. In addition, the second resonance is still well predicted in the PEEC model. To check that this accuracy can be also obtained for other inductors, having guard-ring and GND planes, Fig. 5.27 shows the performance of the method. Both simulation and experimental data have been extended up to $8GHz$ in order to check the prediction of the third resonance. To final with, Table 5.11 and 5.12 collect the figure of merit of the complete series on inductors in Fig. 5.24 calculated with PEEC and compared to experimental data.

Table 5.11 $L_{dc}(nH)$, Q, and $SRF(GHz)$ measured (m) and simulated (s) values for experiment I

	w=370μm s=130μm			w=270μm s=230μm			w=170μm s=330μm		
	L2	L3	L10	L5	L4	L13	L8	L7	L16
L_{dc} m	21.3	19.7	16.8	22.1	20.4	17.9	23.5	21.9	19.2
L_{dc} s	21.4	19.0	16.3	22.3	20.1	16.8	23.0	21.0	18.8
Q_{max} m	51.0	44.1	36.5	50.0	47.4	35.1	43.0	43.0	31.4
Q_{max} m	56.0	47.2	36.5	59.7	48.0	37.0	47.5	50.0	33.8
SRF m	1.76	1.60	1.36	1.87	1.72	1.40	1.95	1.84	1.48
SRF s	1.64	1.52	1.24	1.68	1.52	1.40	1.84	1.91	1.36

Table 5.12 $L_{dc}(nH)$, Q, and $SRF(GHz)$ measured (m) and simulated (s) values for experiment II

	Guard-ring				GND guard-ring			
	L1	L6	L9	L7	L12	L15	L18	L16
width (μm)	325	425	525	625	325	425	525	625
L_{dc} m	22.1	21.8	21.6	21.9	19.1	19.0	19.3	19.2
L_{dc} s	22.1	21.7	21.3	21.0	18.4	18.7	18.0	18.8
Q_{max} m	42.7	43.7	49.1	43.1	34.4	34	34.4	31.4
Q_{max} s	48.3	50.2	49.6	50	34.4	34.0	34.4	33.8
SRF m	1.80	1.81	1.80	1.80	1.47	1.47	1.48	1.47
SRF s	1.76	1.76	1.80	1.90	1.40	1.36	1.40	1.36

Chapter 6

Conclusions

In this work, a fast planar electromagnetic solver based on the PEEC method has been implemented, and embedded in a circuit simulator. It is intended for the modelling of passive components in laminated technologies under the assumption of a quasi-static behaviour. For achieving this goal, it has been necessary to develop original contributions at different levels of the method:

- It has been demonstrated that the PEEC method can be derived from the application of d'Alembert's principle of virtual work to a multiconductor system.
- For reducing model order complexity, a heuristic, but rigorous, criterion based on the density current distribution evaluated at DC has been formulated and correctly applied to the modelling of resistors, capacitors and inductors at RF frequencies.
- The robustness of the method, in terms of stability and convergence, is guaranteed thanks to the development of an analytical procedure for the calculation of the spatial domain Green's function of the substrate.
- For one-dielectric substrates, the developed GF spanned as a series of charge images is computationally efficient. Moreover, it can take into account any value of the homogeneous permittivity, any number of layers, and different boundary conditions (GND plane, open boundary).
- It has also been developed an analytical two-dielectric substrate GF. However, it is computationally inefficient. Instead, it has been developed a heuristic approach that consists in dividing the two-dielectric substrate GF problem in two one-dielectric homogeneous problems. It has been shown a good agreement when compared with general purpose solvers.

- An ab initio adaptive meshing technique has been developed and effectively applied to the computation of high Q inductors. This technique splits the mesh generation in two parts, i.e., one related to the own magnetic field of the involved metal strip and the other related to the external magnetic field.
- An hybrid 1D/2D meshing technique has also been developed for combining regions of 2D current distribution with these of 1D nature inside the same layout. In addition, this technique has allowed the implementation of unstructured meshes.
- Using the proposed EM solver, a PDK able to handle any LTCC tape system has been implemented. Resistors and inductors are simulated about 60 times faster when compared with commercial solvers while keeping the same degree of accuracy; for capacitors, the speed is 4 times faster.

To sum up, with the developed electromagnetic solver, it has been demonstrated a change of paradigm in the development of RF passive component models and libraries through the introduction of a specialized EM solver.

References

[1] ITRS, "The International Technology Roadmap for Semiconductors: 2009 Edition Executive Summary," 2009.

[2] G. E. Moore, "Cramming More Components onto Integrated Circuits," *Electronics Magazine*, vol. 38, April 1965.

[3] J. Mitola, "The software radio architecture," *IEEE Communications Magazine*, vol. 33, pp. 26–38, May 1995.

[4] P. Cruz, N. B. Carvalho, and K. A. Remley, "Designing and testing software-defined radios," *IEEE Microwave Magazine*, vol. 11, pp. 83–94, June 2010.

[5] V. Giannini, J. Craninckx, S. D'Amico, and A. Baschirotto, "Flexible Baseband Analog Circuits for Software-Defined Radio Front-Ends," *IEEE Journal of Solid-State Circuits*, vol. 42, pp. 1501–1512, July 2007.

[6] G. Q. Zhang, F. van Roosmalen, and M. Graef, "The paradigm of "more than Moore"," in *2005 6th International Conference on Electronic Packaging Technology*, pp. 17–24, Aug 2005.

[7] A. Maurelli, D. Belot, and G. Campardo, "SoC and SiP, the Yin and Yang of the Tao for the New Electronic Era," *Proceedings of the IEEE*, vol. 97, pp. 9–17, Jan 2009.

[8] F. Bechtold, "A comprehensive overview on today's ceramic substrate technologies," in *Microelectronics and Packaging Conference, 2009. EMPC 2009. European*, pp. 1–12, June 2009.

[9] F. A. Ghaffar, M. U. Khalid, A. Shamim, and K. N. Salama, "Gain-enhanced ltcc system-on-package for automotive umrr applications," in *2010 53rd IEEE International Midwest Symposium on Circuits and Systems*, pp. 934–937, Aug 2010.

[10] T. Mobley, S. Cardona, and D. Nair, "A novel front end module for 77 ghz automotive radar implemented on low temperature co-fired ceramic technology," in *Radar Conference (EuRAD), 2011 European*, pp. 109–112, Oct 2011.

[11] A. C. Bunea, D. Neculoiu, M. Lahti, and T. Vähä-Heikkilä, "Ltcc microstrip parasitic patch antenna for 77 ghz automotive applications," in *Microwaves, Communications, Antennas and Electronics Systems (COMCAS), 2013 IEEE International Conference on*, pp. 1–4, Oct 2013.

[12] A. C. Scogna and F. Zanella, "Design and optimization of ltcc digital demodulator used for aerospace satellite applications," in *2006 IEEE International Symposium on Electromagnetic Compatibility, 2006. EMC 2006.*, vol. 3, pp. 802–806, Aug 2006.

[13] M. Rittweger, R. Kulke, R. Follmann, and I. Wolff, "Innovative technologies for rf circuitry in satellite payload," in *2009 3rd European Conference on Antennas and Propagation*, pp. 484–486, March 2009.

[14] P. Bembnowicz, M. Małodobra, W. Kubicki, P. Szczepańska, A. Górecka-Drzazga, J. Dziuban, A. Jonkisz, A. Karpiewska, T. Dobosz, and L. Golonka, "Preliminary studies on {LTCC} based {PCR} microreactor," *Sensors and Actuators B: Chemical*, vol. 150, no. 2, pp. 715 – 721, 2010.

[15] T. Qiulin, K. Hao, Q. Li, X. Jijun, L. Jun, X. Chenyang, Z. Wendong, and L. Tao, "High temperature characteristic for wireless pressure ltcc-based sensor," *Microsystem Technologies*, vol. 21, no. 1, pp. 209–214, 2015.

[16] T. Tajima, H. J. Song, and M. Yaita, "Compact thz ltcc receiver module for 300 ghz wireless communications," *IEEE Microwave and Wireless Components Letters*, vol. 26, pp. 291–293, April 2016.

[17] F. F. Manzillo, M. Ettorre, M. S. Lahti, K. T. Kautio, D. Lelaidier, E. Seguenot, and R. Sauleau, "A long slot array fed by a multilayer true-time delay network in ltcc for 60-ghz communications," in *2016 10th European Conference on Antennas and Propagation (EuCAP)*, pp. 1–5, April 2016.

[18] M. H. Lim, J. D. van Wyk, F. C. Lee, and K. D. T. Ngo, "A class of ceramic-based chip inductors for hybrid integration in power supplies," *IEEE Transactions on Power Electronics*, vol. 23, pp. 1556–1564, May 2008.

[19] Q. Li and F. C. Lee, "Winding ac resistance of low temperature co-fired ceramic inductor," in *2012 Twenty-Seventh Annual IEEE Applied Power Electronics Conference and Exposition (APEC)*, pp. 1790–1796, Feb 2012.

[20] R. C. López, F. V. Fernández, Óscar Guerra-Vinuesa, and Ángel Rodríguez-Vázquez, *Reuse-Based Methodologies and Tools in the Design of Analog and Mixed-Signal Integrated Circuits*. Springer, 1 ed., 2006.

[21] C. Bowick, *RF Circuit Design, Second Edition*. Newnes, 2 ed., 2007.

[22] "943 green tape™ design kit." [online] http://cp.literature.agilent.com/litweb/pdf/5989-9066EN.pdf.

[23] "Agilent EEsof EDA: A Faster and Effective RF Module/LTCC Design Flow with AM." [online] http://cp.literature.agilent.com/litweb/pdf/5989-9475EN.pdf.

[24] T. Mobley, G. Oliver, and T. Donisi, "Filter design flow and implementation in ltcc," *Dupont Electronic Technology: Ansoft corporation*, 2010.

[25] K. Yee, "Numerical solution of initial boundary value problems involving maxwell's equations in isotropic media," *IEEE Transactions on Antennas and Propagation*, vol. 14, pp. 302–307, May 1966.

[26] J. ming Jin, *The finite element method in electromagnetics*. John Wiley & Sons, third edition ed., 2014.

[27] J.-P. Berenger, "A perfectly matched layer for the absorption of electromagnetic waves," *Journal of Computational Physics*, vol. 114, no. 2, pp. 185 – 200, 1994.

[28] A. Sommerfeld, *Partial differential equations in physics*. Pure and Applied Mathematics: A Series of Monographs and Textbooks, Vol. 1, Academic Press, 1949.

[29] R. F. Harrington, *Field Computation by Moment Methods (IEEE Press Series on Electromagnetic Wave Theory)*. The IEEE PRESS Series in Electromagnetic Waves (Donald G. Dudley, Editor), Wiley-IEEE Press, 1993.

[30] A. E. Ruehli, "Equivalent circuit models for three-dimensional multiconductor systems," *Microwave Theory and Techniques, IEEE Transactions on*, vol. 22, pp. 216–221, Mar 1974.

[31] A. E. Ruehli and P. A. Brennan, "Efficient capacitance calculations for three-dimensional multiconductor systems," *Microwave Theory and Techniques, IEEE Transactions on*, vol. 21, pp. 76–82, Feb 1973.

[32] A. Ruehli, "Inductance calculations in a complex integrated circuit environment," *IBM Journal of Research and Development*, vol. 16, pp. 470–481, Sept 1972.

[33] H. Brunner, *Collocation Methods for Volterra Integral and Related Functional Differential Equations*. Cambridge Monographs on Applied and Computational Mathematics, Cambridge University Press, 2004.

[34] C. A. J. F. (auth.), *Computational Galerkin Methods*. Springer Series in Computational Physics, Springer-Verlag Berlin Heidelberg, 1 ed., 1984.

[35] G. Antonini, A. E. Ruehli, and C. Yang, "Peec modeling of dispersive and lossy dielectrics," *IEEE Transactions on Advanced Packaging*, vol. 31, pp. 768–782, Nov 2008.

[36] M. Blanes, J. M. Fernández, C. López, F. Ramos, F. Afsar, T. Carrasco, A. Cirera, F. Giordano, J. M. López-Villegas, J. G. Macías, J. Sieiro, and N. Vidal, "A Low Temperature Cofired Ceramic (LTCC) technology platform for heterogeneous integrated systems," in *Proceedings of the 8th Spanish Conference on Electron Devices, CDE'2011*, pp. 1–4, Feb 2011.

[37] "FRANCISCO ALBERO S.A.U.," [Accessed: 1- March- 2017]. [online] http://www.fae.es/en/.

[38] T. Maeder, C. Jacq, Y. Fournier, W. Hraiz, and P. Ryser, "Structuration of zero-shrinkage LTCC using mineral sacrificial materials," in *Microelectronics and Packaging Conference, 2009. EMPC 2009. European*, pp. 1–6, June 2009.

[39] S. G. (auth.), *Ferroelectrics in Microwave Devices, Circuits and Systems: Physics, Modeling, Fabrication and Measurements*. Engineering Materials and Processes, Springer-Verlag London, 1 ed., 2009.

[40] J. M. Lopez-Villegas, N. Vidal, and J. A. del Alamo, "Toroidal versus spiral inductors in multilayered technologies," in *2016 IEEE Radio Frequency Integrated Circuits Symposium (RFIC)*, pp. 55–58, May 2016.

[41] R. Buttiglione, S. Catoni, G. de Angelis, M. Dispenza, A. Fiorello, K. Kautio, M. Ladhes, R. Marcelli, and K. Ronka, "Alumina and LTCC Technology for RF MEMS Switches and True Time Delay Lines," in *Microwave Integrated Circuit Conference, 2008. EuMIC 2008. European*, pp. 366–369, Oct 2008.

[42] K. Delaney, J. Barrett, J. Barton, and R. Doyle, "Characterization and performance prediction for integral capacitors in low temperature co-fired ceramic technology," *IEEE Transactions on Advanced Packaging*, vol. 22, pp. 68–77, Feb 1999.

[43] K. Delaney, J. Barrett, J. Barton, and R. Doyle, "Characterization and performance prediction for integral resistors in low temperature co-fired ceramic technology," *IEEE Transactions on Advanced Packaging*, vol. 22, pp. 78–85, Feb 1999.

[44] A. Sutono, D. Heo, Y. J. E. Chen, and J. Laskar, "High-Q LTCC-based passive library for wireless system-on-package (SOP) module development," *IEEE Transactions on Microwave Theory and Techniques*, vol. 49, pp. 1715–1724, Oct 2001.

[45] M. Klíma and I. Szendiuch, "Possibilities of making 3D resistors in LTCC technology," in *2012 35th International Spring Seminar on Electronics Technology*, pp. 50–54, May 2012.

[46] S. Ahyoune, J. Sieiro, J. Lopez-Villegas, M. Vidal, T. Carrasco, F. Ramos, and J. Fernández-Sanjuán, "Scalable LTCC library for System-in-Package design," in *Conference on Design of Circuits and Integrated Systems, DCIS 2013*, Nov 2013.

[47] D. Heo, A. Sutono, E. Chen, Y. Suh, and J. Laskar, "A 1.9-GHz DECT CMOS power amplifier with fully integrated multilayer LTCC passives," *IEEE Microwave and Wireless Components Letters*, vol. 11, pp. 249–251, June 2001.

[48] Y.-S. Lin, C.-C. Liu, K.-M. Li, and C. H. Chen, "Design of an LTCC tri-band transceiver module for GPRS mobile applications," *IEEE Transactions on Microwave Theory and Techniques*, vol. 52, pp. 2718–2724, Dec 2004.

[49] J. X. Xu, X. Y. Zhang, X. L. Zhao, and Q. Xue, "Synthesis and Implementation of LTCC Bandpass Filter With Harmonic Suppression," *IEEE Transactions on Components, Packaging and Manufacturing Technology*, vol. 6, pp. 596–604, April 2016.

[50] J. Park, J. Hartung, and H. Dudek, "Complete Front-to-back RF SiP Design Implementation Flow," in *2007 Proceedings 57th Electronic Components and Technology Conference*, pp. 986–991, May 2007.

[51] U. Ullah, N. Mahyuddin, Z. Arifin, M. Z. Abdullah, and A. Marzuki, "Antenna in LTCC Technologies: A Review and the Current State of the Art," *IEEE Antennas and Propagation Magazine*, vol. 57, pp. 241–260, April 2015.

[52] H. Hu, K. Yang, K. L. Wu, and W. Y. Yin, "Quasi-Static Derived Physically Expressive Circuit Model for Lossy Integrated RF Passives," *IEEE Transactions on Microwave Theory and Techniques*, vol. 56, pp. 1954–1961, Aug 2008.

[53] X. J. Zhang and D. G. Fang, "Using circuit model from layout-level synthesis as coarse model in space mapping and its application in modelling low-temperature ceramic cofired radio frequency circuits," *IET Microwaves, Antennas Propagation*, vol. 1, pp. 881–886, Aug 2007.

[54] H. C. Lu, T. B. Chan, C. C. P. Chen, C. M. Liu, H. J. Hsing, and P. S. Huang, "LTCC Spiral Inductor Synthesis and Optimization With Measurement Verification," *IEEE Transactions on Advanced Packaging*, vol. 33, pp. 160–168, Feb 2010.

[55] C. Hoer and C. Love, "Exact inductance equations for rectangular conductors with applications to more complicated geometries," *J. Res. Natl. Bur. Stand. C*, vol. 62, pp. 127–137, Apr.-Jun. 1965.

[56] D. Mayer, "Hamilton´s principle and electric circuits tudory," *Advances in Electrical and Electronic Engineering*, vol. 5, no. 1, 2011.

[57] G. Antonini, J. Delsing, J. Ekman, A. Orlandi, and A. Ruehli, "Peec development road map 2007," tech. rep., Tech Rep 5. Lulea University of Technology, 2007.

[58] J. Maxwell, *A treatise on electricity and magnetism*. No. v. 1-2 in A Treatise on Electricity and Magnetism, Dover Publications, 1954.

[59] E. Rosa, "The self and mutual inductance of linear conductors," *Bulletin of the Bureau of Standards*, vol. 4, no. 2, pp. 301–344, 1908.

[60] F. Terman, *Radio Engineers's Handbook*. HcGraw-Hill handbooks, McGraw-Hill, 1943.

[61] F. Grover and I. S. of America, *Inductance Calculations: Working Formulas and Tables*. Dover books on engineering and engineering physics, Instrument Society of America, 1946.

[62] H. Greenhouse, "Design of planar rectangular microelectronic inductors," *IEEE Transactions on Parts, Hybrids, and Packaging*, vol. 10, pp. 101–109, Jun 1974.

[63] M. Kamon, M. Tsuk, and J. White, "Fasthenry: a multipole-accelerated 3-d inductance extraction program," *Microwave Theory and Techniques, IEEE Transactions on*, vol. 42, pp. 1750–1758, Sept 1994.

[64] K. Nabors and J. White, "Fastcap: a multipole accelerated 3-d capacitance extraction program," *Computer-Aided Design of Integrated Circuits and Systems, IEEE Transactions on*, vol. 10, pp. 1447–1459, Nov 1991.

[65] A. M. Niknejad, R. Gharpurey, and R. G. Meyer, "Numerically stable green function for modeling and analysis of substrate coupling in integrated circuits," *IEEE Transactions on Computer-Aided Design of Integrated Circuits and Systems*, vol. 17, pp. 305–315, Apr 1998.

[66] S. Ahyoune, J. Sieiro, J. M. López-Villegas, and M. N. Vidal, "Substrate coupling modeling in integrated circuits using analytical green's function," in *Design of Circuits and Integrated Circuits (DCIS), 2014 Conference on*, pp. 1–6, Nov 2014.

[67] A. M. Niknejad and R. G. Meyer, "Analysis of eddy-current losses over conductive substrates with applications to monolithic inductors and transformers," *IEEE Transactions on Microwave Theory and Techniques*, vol. 49, pp. 166–176, Jan 2001.

[68] "User-compiled model data structures and apis." [online] http://edadocs.software.keysight.com/display/ads201101/User-Compiled+Model+Data+Structures+and+APIs.

[69] A. E. Ruehli, G. Antonini, and L. Ljiang, "Passivization of em peec solutions in the frequency and time domain," in *Electromagnetics in Advanced Applications (ICEAA), 2013 International Conference on*, pp. 1273–1276, Sept 2013.

[70] J. Ekman, G. Antonini, A. Orlandi, and A. E. Ruehli, "Impact of partial element accuracy on peec model stability," *IEEE Transactions on Electromagnetic Compatibility*, vol. 48, pp. 19–32, Feb 2006.

[71] A. Farrar and A. T. Adams, "Multilayer microstrip transmission lines (short papers)," *IEEE Transactions on Microwave Theory and Techniques*, vol. 22, pp. 889–891, Oct 1974.

[72] N. K. Das and D. M. Pozar, "A generalized spectral-domain green's function for multilayer dielectric substrates with application to multilayer transmission lines," *IEEE Transactions on Microwave Theory and Techniques*, vol. 35, pp. 326–335, Mar 1987.

[73] A. Alparslan, M. I. Aksun, and K. A. Michalski, "Closed-form green's functions in planar layered media for all ranges and materials," *IEEE Transactions on Microwave Theory and Techniques*, vol. 58, pp. 602–613, March 2010.

[74] M. Yuan, T. K. Sarkar, and M. Salazar-Palma, "A direct discrete complex image method from the closed-form green's functions in multilayered media," *IEEE Transactions on Microwave Theory and Techniques*, vol. 54, pp. 1025–1032, March 2006.

[75] J. Ekman, *Electromagnetic Modeling Using the Partial Element Equivalent Circuit Method*. PhD thesis, Luleå University of Technology, 2003.

[76] N. Srivastava, R. Suaya, and K. Banerjee, "Analytical expressions for high-frequency vlsi interconnect impedance extraction in the presence of a multilayer conductive substrate," *IEEE Transactions on Computer-Aided Design of Integrated Circuits and Systems*, vol. 28, pp. 1047–1060, July 2009.

[77] Dupont, "Dupont low temperature co-fired ceramic (ltcc) material systems." http://www.dupont.com/products-and-services/electronic-electrical-materials/low-temperature-co-fire-ceramic-materials.html, 2016.

[78] Heraeus, "Ltcc materials." https://www.heraeus.com/en/het/products_and_solutions_het/thick_film_materials/ltcc_materials/ltcc_materials_page.aspx, 2016.

[79] G. Antonini, A. Orlandi, and A. E. Ruehli, "Analytical integration of quasi-static potential integrals on nonorthogonal coplanar quadrilaterals for the peec method," *IEEE Transactions on Electromagnetic Compatibility*, vol. 44, pp. 399–403, May 2002.

[80] D. Daroui and J. Ekman, "Performance analysis of parallel non-orthogonal peec-based solver for emc applications," *Progress in Electromagnetics Research B*, vol. 41, pp. 77–100, 2012.

[81] Y. Hackl, P. Scholz, W. Ackermann, and T. Weiland, "Multifunction approach and specialized numerical integration algorithms for fast inductance evaluations in nonorthogonal peec systems," *IEEE Transactions on Electromagnetic Compatibility*, vol. 57, pp. 1155–1163, Oct 2015.

[82] A. D. Poularikas, *The transforms and applications handbook*. The electrical engineering handbook series, CRC Press, 2nd ed ed., 2000.

[83] J. D. Jackson, *Classical electrodynamics*. New York, NY: Wiley, 3rd ed. ed., 1999.

[84] J. D. Jackson, "Surface charges on circuit wires and resistors play three roles," *American Journal of Physics*, vol. 64, no. 7, pp. 855–870, 1996.

[85] W. G. V. Rosser, "What makes an electric current "flow"," *American Journal of Physics*, vol. 31, no. 11, pp. 884–885, 1963.

[86] O. Jefimenko, "Demonstration of the electric fields of current-carrying conductors," *American Journal of Physics*, vol. 30, no. 1, pp. 19–21, 1962.

[87] J. J. siero Cordoba, *Modelling of Integrated Passive Componnents for RFIC's*. PhD thesis, Universitat de Barcelona, Departament d'Electronica, 2001.

[88] J. C. Rautio and V. Demir, "Microstrip conductor loss models for electromagnetic analysis," *IEEE Transactions on Microwave Theory and Techniques*, vol. 51, pp. 915–921, Mar 2003.

[89] T. C. Carrillo, *Methods and tools for the design of RFICs*. PhD thesis, Universitat de Barcelona, Departament d'Electronica, 2013.

[90] ANSYS, Inc., *HFSS Online Help*. 2016.

[91] ANSYS, Inc., "ANSYS HFSS for Antenna Simulation." http://resource.ansys.com/staticassets/ANSYS/staticassets/resourcelibrary/techbrief/ab-ansys-hfss-for-antenna-simulation.pdf, 2014.

[92] Anaren®, "Ceramics design guide." https://www.anaren.com/sites/default/files/uploads/File/CeramicsDesignGuide-for-website.pdf.

[93] M. Manufacturing, "Low temperature co-fired ceramics (ltcc) multi-layer module boards." http://www.murata.com/~/media/webrenewal/support/library/catalog/products/substrate/ltcc/n20e.ashx, 2014.

[94] NEOTech, "Ceramics Substrate Design Guide." http://www.neotech.com/ceramic-substrates-design-guides/.

[95] K. Technologies, "An LTCC modeling and design example." http://edadocs.software.keysight.com/display/ads201101/An+LTCC+modeling+and+design+example.

[96] DTmicrocircuits. http://www.dtmicrocircuits.com/ltcc{_}foundry/foun{_}design{_}frame.htm.

[97] MultiLib™. http://www.multilib.de/main/MultiLIB/en/home.php.

[98] Ansys®, "Ansys hfss." http://www.ansys.com/Products/Electronics/ANSYS-HFSS.

[99] K. Technologies, "Advanced design system (ads)." http://www.keysight.com/en/pc-1297113/advanced-design-system-ads?nid=-34346.0&cc=ES&lc=spa.

[100] K. Technologies, "Electromagnetic professional (empro)." http://www.keysight.com/en/pc-1297143/empro-3d-em-simulation-software?nid=-34278.0&cc=ES&lc=spa.

[101] S.-M. Lin, L.-Q. Yang, and H.-Y. Chang, "Scalable lumped model with multiple physical parameters for embedded passives," in *Proceedings Electronic Components and Technology, 2005. ECTC '05.*, pp. 1842–1845 Vol. 2, May 2005.

[102] Y. Wu, K. S. Chin, W. Che, K. C. Chang, and W. Feng, "LTCC multilayered helical filters with a mixed electric and magnetic coupling structure," *IEEE Transactions on Components, Packaging and Manufacturing Technology*, vol. 5, pp. 1050–1059, Aug 2015.

[103] J. Esteban-Muller, R. González-Echevarría, C. Sánchez-López, E. Roca, R. Castro-López, F. V. Fernández, J. M. López-Villegas, J. Sieiro, and N. Vidal, "Multi-objective performance optimization of planar inductors," in *Symbolic and Numerical Methods, Modeling and Applications to Circuit Design (SM2ACD), 2010 XIth International Workshop on*, pp. 1–4, Oct 2010.

[104] J. Sieiro, T. C. Carrillo, S. Ahyoune, N. Vidal, J. M. López-Villegas, and J. A. Osorio, "Synthesis of planar inductors in low temperature co-fired ceramic technology," *Analog Integrated Circuits and Signal Processing*, vol. 78, no. 1, pp. 77–86, 2013.

[105] H. C. Lu, T. B. Chan, C. C. P. Chen, C. M. Liu, H. J. Hsing, and P. S. Huang, "LTCC spiral inductor synthesis and optimization with measurement verification," *IEEE Transactions on Advanced Packaging*, vol. 33, pp. 160–168, Feb 2010.

[106] H. Hu, K. Yang, K. L. Wu, and W. Y. Yin, "Quasi-static derived physically expressive circuit model for lossy integrated RF passives," *IEEE Transactions on Microwave Theory and Techniques*, vol. 56, pp. 1954–1961, Aug 2008.

[107] J. M. Lopez-Villegas, J. Samitier, C. Cane, P. Losantos, and J. Bausells, "Improvement of the quality factor of RF integrated inductors by layout optimization," *IEEE Transactions on Microwave Theory and Techniques*, vol. 48, pp. 76–83, Jan 2000.

[108] S. Ahyoune, J. Lopez-Villegas, J. Sieiro, M. Vidal, T. Carrasco, and F. Ramos, "Effects of shielding structures on the performance of planar inductors," in *Conference on Design of Circuits and Integrated Systems, DCIS 2016*, Nov 2016.

Appendix A

LTCC process

Fig. A.1 illustrates the different processing steps involved in the fabrication of an LTCC circuit. Starting from the reel tape green material, the main steps are the following ones

- **Blank:** tape may be blanked using standard techniques such as hot knife, die cutting, or lasering. Nominal size of blankets is $8'' \times 8''$ which provides a nominal $7'' \times 7''$ circuit design area.
- **Punch:** Vias may be formed in the blankets using mechanical punches. A minimum via diameter of 200 μm is suggested for production, although lower dimensions could be achieved in prototypes. Cavities are also formed at this step. When using punching (nibbling technique), possible shapes are only rectangular type. If other shapes are required, cavities can be formed at the laser process step.
- **Via filling:** Vias are filled with a conventional thick film stencil printer. Through the aperture according to circuit pattern, paste is applied above via holes and it is drawn with a vacuum pump into the holes to fill them. The tape has to be placed on a sheet of nonspread paper which lays on a porous stone to avoid the leak of the paste. Fig. A.2 shows the process of stencil printing.
- **Printing:** Once vias have been filled, conductors, resistors and capacitors are printed using screen printing technique. As shown in Fig. A.3, the squeegee pushes the paste through the openings in the mask. For avoiding the shifting of the LTCC blanket, it is fixed to the table with vacuum.
- **Stacking:** Blankets are inspected optically and then are collated using an alignment tool and fiducial marks.

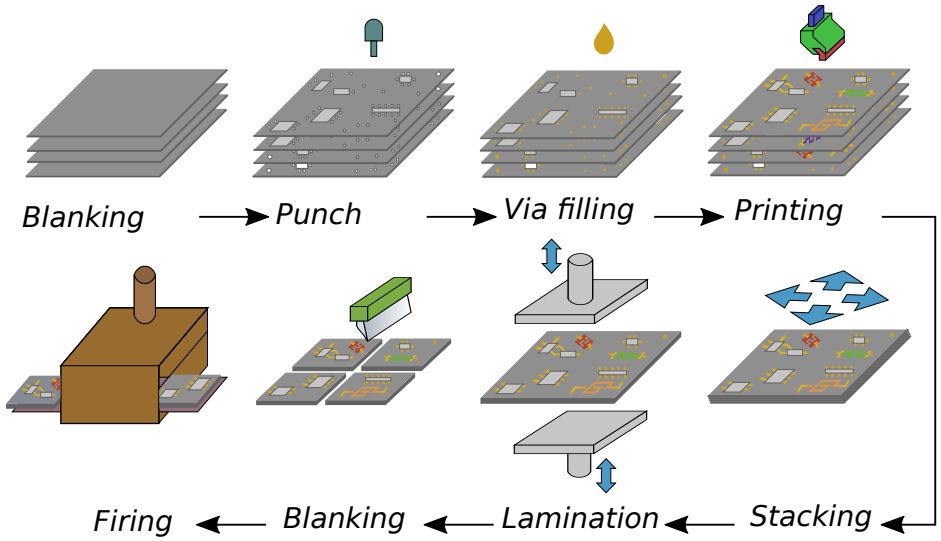

Fig. A.1 The different processing steps involved in the fabrication of an LTCC circuit.

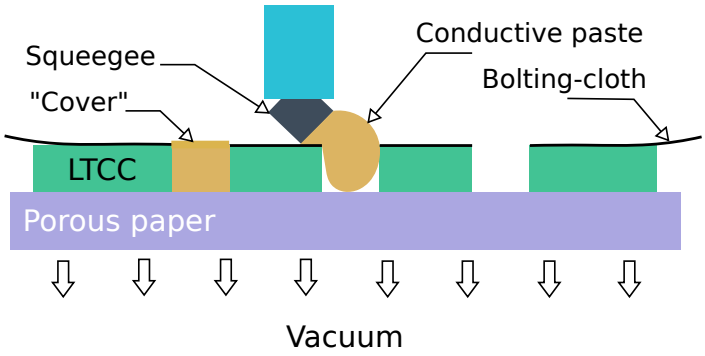

Fig. A.2 Via filling using thick film stencil paper.

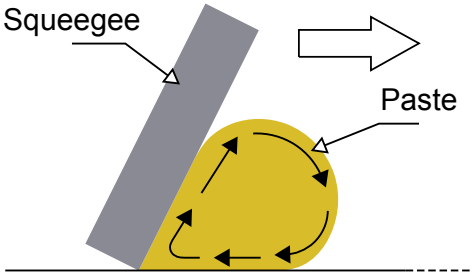

Fig. A.3 Screen printing process: the squeegee the paste.

- **Lamination:** All layers are heated and pressed together to obtain a single substrate. For avoiding delamination, an isostatic pressure technique is used.
- **Blanking:** circuit units are separated before firing using hot-knife technique. Cut-line is about 200 μm width.

- **Firing:** The organic ingredients of the green sheet are burn-out in a furnance using an adequate temperature profile. In this process, the material shrinks about 15% in the *x*-*y* direction, depending on tape system. For *z* direction, it depends on the chosen process (normal: 15-25%; 0-shrinkage about 30%).

Appendix B

LTCC design rules

The terms used in creating design rules are defined in the following illustrations:

- Minimum size of a feature is the minimum distance between parallel edges (Fig. B.1 a), i.e. min(A, B).
- Spacing between features is the minimum distance A between edges of the features (Fig. B.1 b).
- Given two features named 1 and 2 (Fig. B.1 c),
  - Intrusion of feature 1 into feature 2 is the distance A.
  - Extension of feature 1 from feature 2 is the distance B.
  - Extension of feature 2 from feature 1 is the distance min(C1, C2, C3).
  - Inclusion of feature 1 within feature 2 is the distance min(A1, A2, A3).
  - Overlap of feature 2 over feature 1 is the distance min(A1, A2, A3).
- For a given conductor layer, the coverage is the ratio of total metalized surface over total singulated surface layer expressed in %. In this example, the total metalized surface is the black area; the total surface layer is the area of the rectangle defined by fiducial singulation marks.

B.1 Conductors

Rules description for Fig. B.2 a:

- Rule 1.1. Minimum size feature of buried and surface conductors.

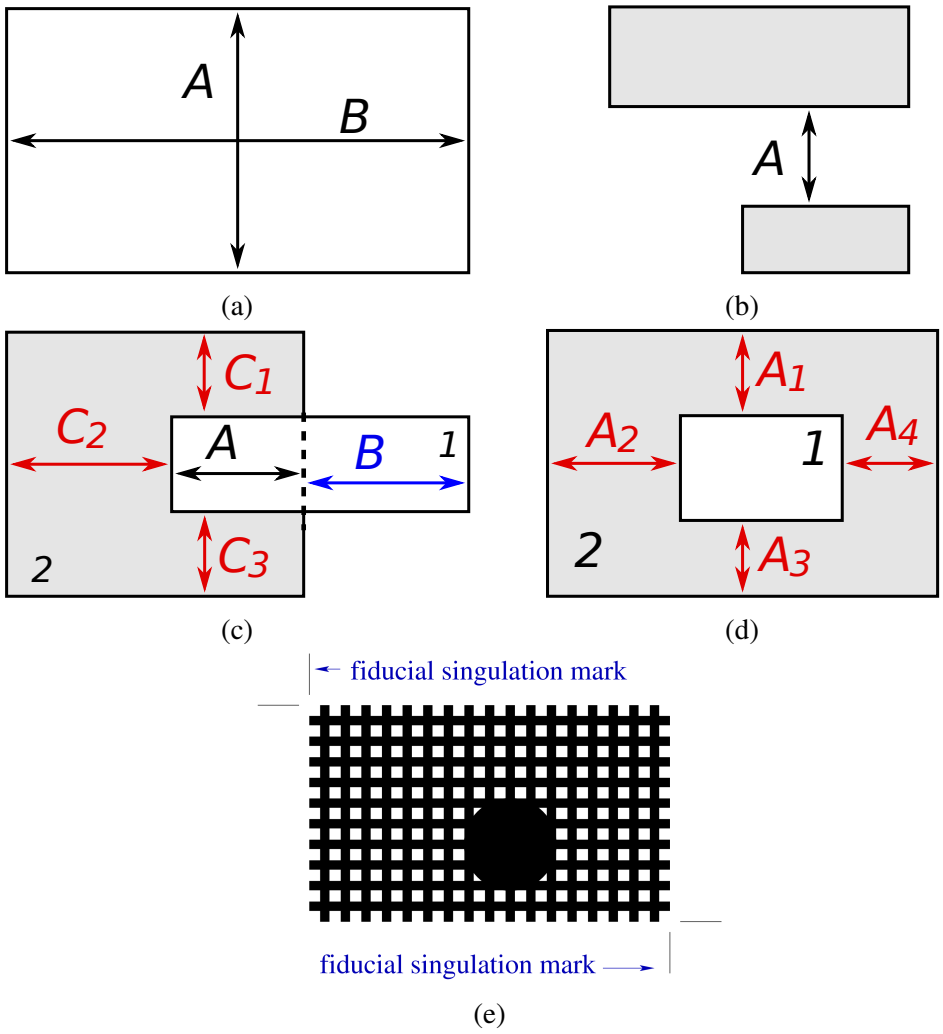

Fig. B.1 Definition for, (a) minimum size of a feature, (b) spacing between features, (c) intrusion and extension, (d) inclusion and overlap and (e) metal converge.

- Rule 1.2. Minimum distance between metal features on same layer.
- Rule 1.3. Minimum distance of metal feature to circuit edge (singulation line).

Rules description for Fig. B.2 b:

- Rule 1.4. Minimum metal width for buried GND/power grid.
- Rule 1.5. Minimum distance between metal parts of buried GND/power grid.
- Rule 1.6. Maximum coverage of metal on a given layer 50%.

[1]For RF GND it can be shrink to 75 μm.

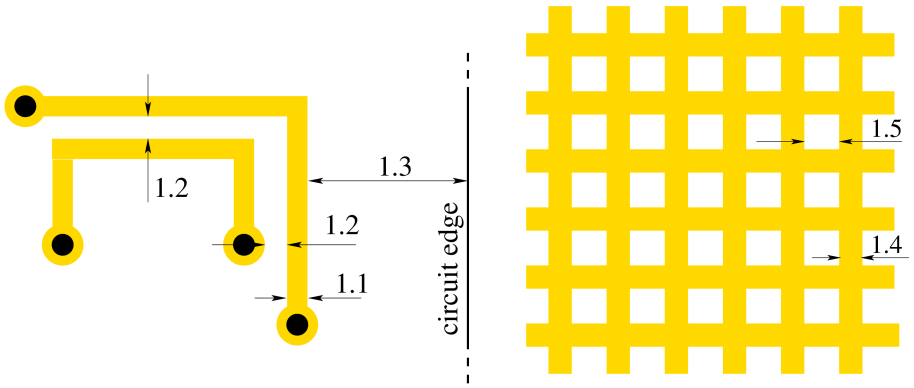

(a) (b)

Fig. B.2 Design rules: (a) for conductors on any layer, and (b) for buried ground/power planes.

Table B.1 Rules of conductors.

	Standard	Under approval
Rule 1.1	200 μm	100 μm
Rule 1.2	200 μm	100 μm
Rule 1.3	250 μm	250 μm [1]
Rule 1.4	250 μm	200 μm
Rule 1.5	300 μm	250 μm
Rule 1.6	50 %	50 %

B.2 Vias

Rules description for Fig. B.3:

- Rule 2.1 Minimum size feature of via hole.
- Rule 2.2 Minimum overlap of metal pad feature over via hole.
- Rule 2.3 Minimum distance between via holes in same dielectric layer.
- Rule 2.4 Minimum distance of via hole to circuit edge (singulation line).

Rules description for Fig. B.4:

- Rule 2.5 Minimum distance of staggered vias.
- Rule 2.6 Minimum distance of staggered vias in GND transmission line.

Additional recommendations:

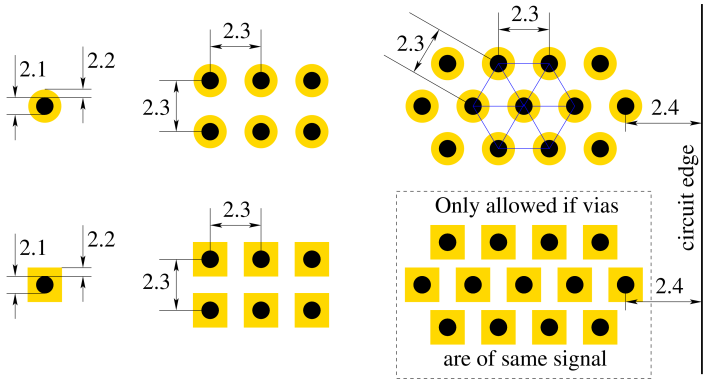

Fig. B.3 Design rules for vias at the same dielectric layer level.

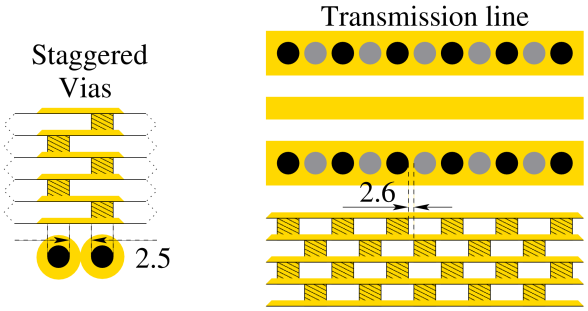

Fig. B.4 Design rules for staggered vias and GND RF vias.

Table B.2 Rules of vias.

	Standard	Under approval
Rule 2.1	200 μm	150 μm
Rule 2.2	100 μm	50 μm
Rule 2.3	3 $\oslash$ via	2.5 $\oslash$ via
Rule 2.4	4 $\oslash$ via	3 $\oslash$ via
Rule 2.5	1 $\oslash$ via	1 $\oslash$ via
Rule 2.6	50 μm	50 μm

- Use catch pad whenever possible.
- Avoid using stacked vias because may not be hermetic.
- In high density via areas, vias should be placed horizontally staggered as indicated in Fig. B.5.

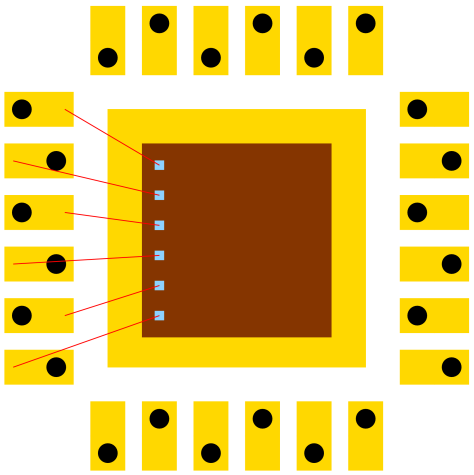

Fig. B.5 Land pattern for wire-bonding using routing at different layer level.

B.3 Cavities

Rules description for Fig. B.6:

- Rule 3.1. Cavity size range.
- Rule 3.2. Minimum cavity floor thickness.
- Rule 3.3. Minimum distance between two cavities
- Rule 3.4. Minimum distance from cavity wall to circuit edge.
- Rule 3.5. Maximum cavity wall height above bond shelf.
- Rule 3.6. Minimum distance between cavity wall and non-related buried metal.
- Rule 3.7. Minimum distance between cavity wall and via.
- Rule 3.8. Separation between cavity wall and metal flag (land for component).
- Rule 3.9. Minimum distance between bond shelf pad and cavity wall.
- Rule 3.10. Minimum intrusion of metal inside cavity.
- Rule 3.11. Minimum intrusion of bond shelf pad inside cavity wall above bond shelf.
- Rule 3.12. Minimum distance between cavity wall and non-related surface metal.

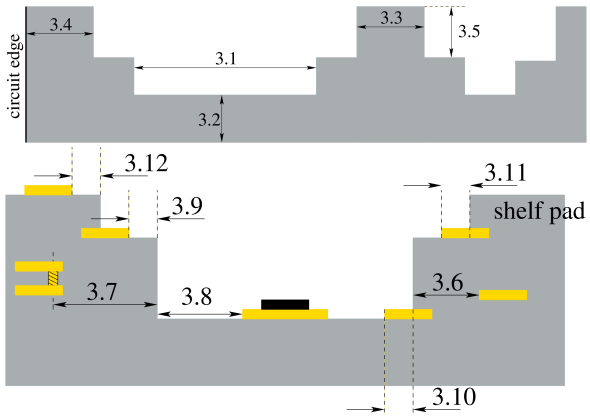

Fig. B.6 Design rules for cavities.

Table B.3 Rules of cavities.

	Standard	Under approval
Rule 3.1	700 μm - 6250 μm	500 μm - 6250 μm
Rule 3.2	1:2	1:3
Rule 3.3	1250 μm	1250 μm
Rule 3.4	1250 μm	1250 μm
Rule 3.5	1:2 -height IC	?
Rule 3.6	375 μm	250 μm
Rule 3.7	3 $\oslash$ via	2.5 $\oslash$ via
Rule 3.8	250 μm	50 μm
Rule 3.9	250 μm	50 μm
Rule 3.10	750 μm	750 μm
Rule 3.11	750 μm	750 μm
Rule 3.12	375 μm	250 μm

B.4 Resistors

Rules description for Fig. B.7:

- Rule 4.1. Minimum resistor size.
- Rule 4.2. Minimum resistor intrusion inside metal pad.
- Rule 4.3. Minimum extension of metal metal from resistor.
- Rule 4.4. Minimum distance between resistors on the same layer.
- Rule 4.5. Separation of resistor to cavity edge or circuit edge.
- Rule 4.6. Glass cover overlap over surface protected resistor.

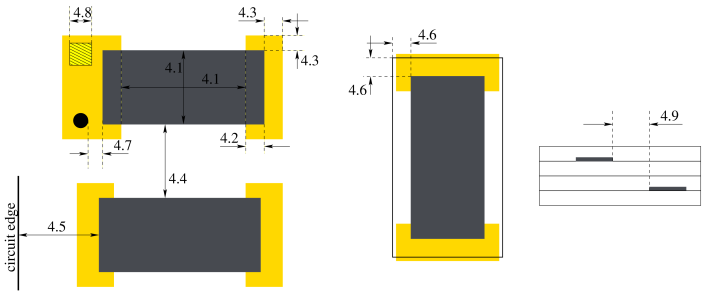

Fig. B.7 Design rules for resistors.

Table B.4 Rules of resistors.

	Standard	Under approval
Rule 4.1	500 μm	250 μm
Rule 4.2	250 μm	125 μm
Rule 4.3	250 μm	125 μm
Rule 4.4	1000 μm	750 μm
Rule 4.5	1000 μm	750 μm
Rule 4.6	250 μm	125 μm
Rule 4.7	1 $\oslash$ via	1 $\oslash$ via
Rule 4.8	375 μm	375 μm
Rule 4.9	750 μm	500 μm
Rule 4.10	15 %	15 %

- Rule 4.7. Minimum distance between via hole in resistor metal pad and resistor layer.
- Rule 4.8. Minimum pad opening for surface trimmed resistors [2].
- Rule 4.9. Minimum distance between resistors on different layers.
- Rule 4.10. Maximum resistor coverage on a single layer.

B.5 High-K capacitors

Rules description for Fig. B.8:

- Rule 5.1. Size range capacitor dielectric.
- Rule 5.2. Overlap of dielectric layer over bottom metal.

[2]Resistor trimming measurement are based on four-probe method. Check company for actual land patterns.

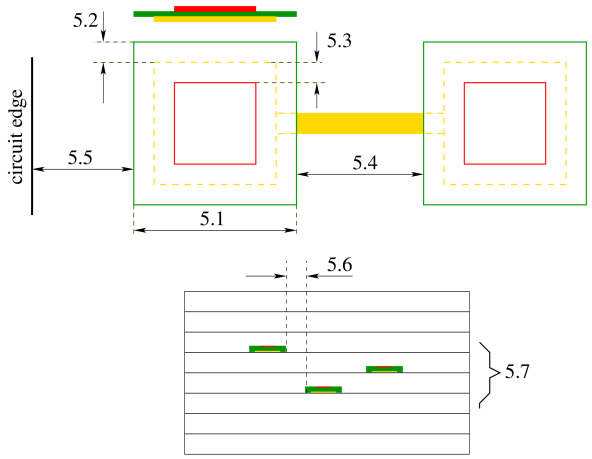

Fig. B.8 Design rules for capacitors.

Table B.5 Rules of capacitors.

	Standard	Under approval
Rule 5.1	600 μm - 20000 μm	$--$
Rule 5.2	200 μm	125 μm
Rule 5.3	200 μm	125 μm
Rule 5.4	1000 μm	750 μm
Rule 5.5	1000 μm	750 μm
Rule 5.6	1000 μm	500 μm
Rule 5.7	± 1 layer from center layer	$--$
Rule 5.8	50 %	50 %

- Rule 5.3. Inclusion of top metal into bottom metal
- Rule 5.4. Minimum distance between capacitors on the same layer.
- Rule 5.5. Separation of capacitor to cavity edge or circuit edge.
- Rule 5.6. Minimum distance between capacitors on the different layers.
- Rule 5.7. Layer location of capacitors.
- Rule 5.8. Maximum dielectric coverage on a single layer.
- Rule 5.9. No vias allowed on top or bottom metal plates.

Appendix C

Hankel's transform

The Hankel transform of order ν of a function $f(r)$ is given by:

$$F_\nu(k) = \int_0^\infty f(r) J_\nu(kr) r dr \tag{C.1}$$

where J_ν is the Bessel function of the first kind of order ν with $\nu \geq -\frac{1}{2}$. The inverse Hankel transform of $F_\nu(k)$ is defined as:

$$f(r) = \int_0^\infty F_\nu(k) J_\nu(kr) k dk\,. \tag{C.2}$$

C.1 Relation to the Fourier transform

The Hankel transform of order zero is essentially the 2-dimensional Fourier transform of a circularly symmetric function. Consider a 2-dimensional function $f(\mathbf{r})$ of the radius vector $\mathbf{r}$. Its Fourier transform is:

$$F(\mathbf{k}) = \int\int f(r) e^{i\mathbf{k}\cdot\mathbf{r}} d\mathbf{r} \tag{C.3}$$

With no loss of generality, we can pick a polar coordinate system (r, θ) such that the $\mathbf{k}$ vector lies on the $\theta = 0$ axis (in K-space). The Fourier transform is now written in these polar coordinates as:

$$F(\mathbf{k}) = \int_{r=0}^\infty \int_{\theta=0}^{2\pi} f(r,\theta) e^{ik\cdot r cos(\theta)} r d\theta dr. \tag{C.4}$$

where θ is the angle between the $\mathbf{k}$ and $\mathbf{r}$ vectors. If the function f happens to be circularly symmetric, it will have no dependence on the angular variable θ and may be written $f(r)$.

The integration over θ may be carried out, and the Fourier transform is now written:

$$F(\mathbf{k}) = F(k) = 2\pi \int_0^\infty f(r) J_0(kr) r dr \tag{C.5}$$

which is just 2π times the zero-order Hankel transform of $f(r)$. For the reverse transform,

$$f(\mathbf{r}) = \frac{1}{(2\pi)^2} \int\int F(\mathbf{k}) e^{i\mathbf{k}\cdot\mathbf{r}} d\mathbf{k} = \frac{1}{2\pi} \int_0^\infty F(k) J_0(kr) k dk \tag{C.6}$$

so $f(r)$ is $\frac{1}{2\pi}$ times the zero-order Hankel transform of $F(k)$.

C.2 Some Hankel transform pairs

Table C.1 lists the Hankel transforms of some particular functions for the important special case $\nu = 0$.

Table C.1 Hankel Transform of Order Zero

$f(r)$	$F_0(k)$
1	$\frac{\delta(k)}{k}$
$\frac{1}{r}$	$\frac{1}{k}$
r	$-\frac{1}{k^3}$
r^3	$\frac{9}{k^5}$
r^m	$\frac{2^{m+1}\Gamma(\frac{m}{2}+1)}{k^{m+2}\Gamma(-\frac{m}{2})}$, $-2 < R(m) < -\frac{1}{2}$
$\frac{1}{\sqrt{r^2+z^2}}$	$\frac{e^{-k\lvert z\rvert}}{k}$
$\frac{1}{z^2+r^2}$	$K_0(kz)$ $\quad z \in C$
$\frac{e^{iar}}{r}$	$\frac{i}{\sqrt{a^2-k^2}}$ $\quad a > 0, k < a.$
	$\frac{1}{\sqrt{k^2-a^2}}$ $\quad a > 0, k < a.$
$e^{-\frac{1}{2}a^2r^2}$	$\frac{1}{a^2} e^{-\frac{k^2}{2a^2}}$
$\frac{1}{r} J_0(lr) e^{-sr}$	$\frac{2}{\pi\sqrt{(k+l)^2+s^2}} K\left(\sqrt{\frac{4kl}{(k+l)^2+s^2}}\right)$
$-r^2 f(r)$	$\frac{d^2F_0}{dk^2} + \frac{1}{k}\frac{dF_0}{dk}$

Appendix D

Skin effect

D.1 Metal strip with ground plane

The skin effect along the thickness (Fig. D.1) is easily introduced using the skin equivalent impedance. Using the definition of the skin depth δ

$$\delta = \sqrt{\frac{2}{\mu W \sigma}}, \tag{D.1}$$

Ohm's law $J = \sigma E$, and the distribution of the electric field inside the conductor $\mathbf{E}(z) = E_0 e^{-\frac{2}{z}(1+j)}$, we can calculate the total power loss as follows:

$$\begin{aligned} P_{loss} &= Real\{\frac{1}{2}\int dz E \cdot \delta^R\} && \text{(D.2)} \\ &= Real\frac{1}{2}\int_0^t dz \cdot E_0 e^{-z(1+j)/\delta} \cdot \sigma E_0 e^{-z(1-j)/\delta} && \text{(D.3)} \\ &= \frac{\sigma E_0^2}{2}\int_0^t dz e^{-2z/\delta} = -\frac{\sigma\delta E_0^2}{4}\left[e^{-2z/\delta}\right]_0^t && \text{(D.4)} \\ &= \frac{\sigma\delta E_0^2}{4}\left(1 - e^{-2t/\delta}\right) && \text{(D.5)} \end{aligned}$$

From a local point of view definition, $P_{loss} = \frac{1}{2}\sigma' E_0^2 t$. Therefore, we can calculate σ' by using Eq. (D.2)

$$\frac{\sigma\delta E_0^2}{4}\left(1 - e^{-2t/\delta}\right) = \frac{1}{2}\sigma' E_0^2 t \Rightarrow \sigma' = \sigma\frac{\delta\left(1 - e^{-2t/\delta}\right)}{2t} \tag{D.6}$$

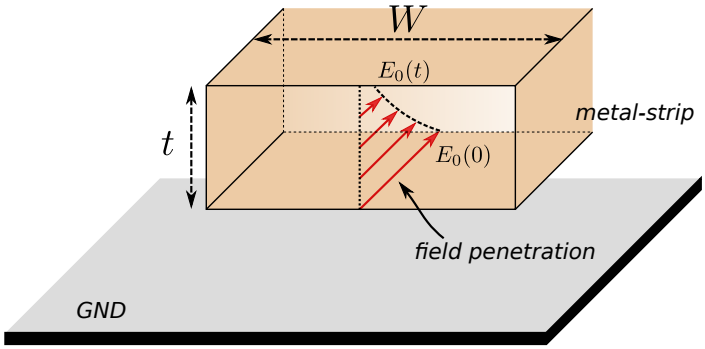

Fig. D.1 Field penetration in metal-strip.

the equivalent resistance is calculated as:

$$R_{RF} = \frac{2t}{\sigma\delta\left(1-e^{-2t/\delta}\right)}\cdot\frac{L}{tW} = \frac{L}{\sigma tW}\cdot\frac{2t}{\delta\left(1-e^{-2t/\delta}\right)} \tag{D.7}$$

$$= R_{DC}\cdot\frac{2t}{\delta\left(1-e^{-2t/\delta}\right)}, \tag{D.8}$$

where $R_{DC} = L/(\sigma tW)$.

D.2 Metal strip without ground plane

In case of strip line without ground plane as show in Fig. D.2, the power loss expression is

$$P_{loss} = 2\cdot Real\{\frac{1}{2}\int_0^{t/2} dz\cdot E_0 e^{-z(1+j)/\delta}\cdot\sigma E_0 e^{-z(1-j)/\delta}\} \tag{D.9}$$

$$= \sigma E_0^2\int_0^{t/2} dz e^{-2z/\delta} = -\frac{\sigma\delta E_0^2}{2}\left[e^{-2z/\delta}\right]_0^{t/2} \tag{D.10}$$

$$= \frac{\sigma\delta E_0^2}{2}\left(1-e^{-t/\delta}\right). \tag{D.11}$$

Now, we determinate σ' by using the above equation

$$\frac{\sigma\delta E_0^2}{2}\left(1-e^{-t/\delta}\right) = \frac{1}{2}\sigma' E_0^2 t \Rightarrow \sigma' = \sigma\frac{\delta\left(1-e^{-t/\delta}\right)}{t}, \tag{D.12}$$

and the equivalent resistance is given by

$$R_{RF} = \frac{t}{\sigma\delta\left(1-e^{-t/\delta}\right)}\cdot\frac{L}{tW} = \frac{L}{\sigma tW}\cdot\frac{t}{\delta\left(1-e^{-t/\delta}\right)} \tag{D.13}$$

$$= R_{DC}\cdot\frac{t}{\delta\left(1-e^{-t/\delta}\right)}, \tag{D.14}$$

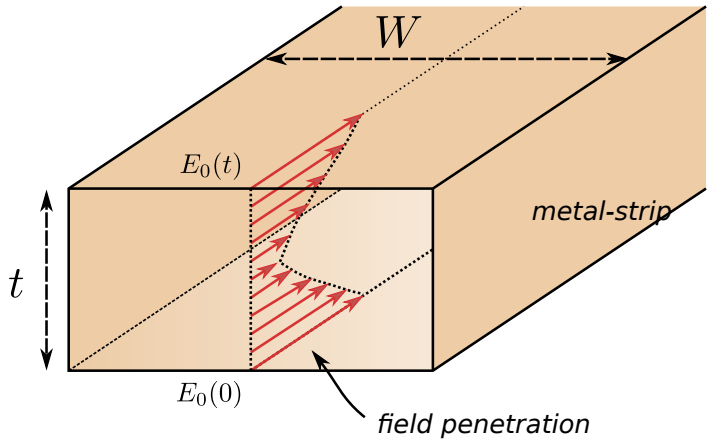

Fig. D.2 Field penetration in metal-strip without ground plane.

where $R_{DC} = L/(\sigma t W)$.

Chapter 7

Resumen

El objetivo de este trabajo es el desarrollo de una metodología de modelado electromagnético de componentes pasivos RF multicapa que permita su análisis rápido sin comprometer la precisión de la solución. En lugar de seguir un enfoque de modelo compacto, frecuentemente utilizado en tecnologías integradas, esta propuesta se basa en el método numérico de los elementos parciales de circuito equivalente (PEEC) con la restricción cuasi-estática de que el mecanismo de radiación no está contemplado. El método ha sido incorporado en un simulador de circuitos de forma transparente para el diseñador. Utilizando este marco de trabajo, la escalabilidad del modelo del componente no es sólo geométrica; también contempla la definición del sustrato, incluyendo sus materiales y sección transversal, la topología y las condiciones de contorno (planos de masa y anillos de guarda).

El desarrollo metodológico se divide en tres partes. En primer lugar, el formalismo del PEEC se adapta convenientemente al tipo de física que describe el comportamiento electromagnético relevante del componente. En esta formulación, se utiliza una perspectiva diferente al desarrollo tradicional introducido por A. Ruehli. En vez de aplicar el método de Galerkin, se demuestra que el PEEC es producto de la aplicación del principio de los trabajos virtuales, utilizado en mecánica analítica, a los sistemas multiconductor. En ese formalismo, ya se establece el papel que juega los elementos parciales cuya evaluación ocupa la segunda parte del desarrollo. Ésta se lleva a cabo utilizando soluciones analíticas de la función de Green (GF) del sustrato en el dominio espacial. Calculados los elementos parciales que constituyen la malla numérica del modelo, se ensamblan como un conjunto de ecuaciones algebraicas que forman la matriz del sistema. El proceso de discretización de la malla juega un papel fundamental para garantizar no sólo la velocidad y exactitud del cálculo, sinó también su estabilidad y convergencia. Por tanto, en la tercera parte del desarrollo, se propone un generador de malla que tiene en cuenta la física del componente aumentando la densidad de malla en las zonas de mayor gradiente de la distribución de la densidad de

corriente. Es muy importante entender que este generador de malla no recalcula la malla de forma iterativa a partir de la solución numérica completa del modelo, tal y como se hace en la técnica de mallado adaptativo en el método de los elementos finitos. Se genera al inicio del cálculo; por tanto, no es un proceso iterativo.

Para validar la metodología, se ha optado por aplicarla en la implementación de una librería de componentes pasivos de RF en sustratos cerámicos multicapa sinterizados a baja temperatura (LTCC). Se ha fabricado, caracterizado y comparado diferentes conjuntos de dispositivos con la predicción del modelo. Además, los resultados obtenidos también se han contrastado utilizando simuladores electromagnéticos comerciales.

Después de introducir el propósito de este trabajo en el **Capítulo 1**, se explica las motivaciones que han llevado a escoger el método de los elementos parciales de circuito equivalente como marco numérico de trabajo y se muestra las prestaciones de la herramienta de análisis desarrollada. Asimismo, se argumenta las razones sobre la elección de la tecnología LTCC para construir la librería de componentes y los parámetros más relevantes de las tecnologías utilizadas a lo largo de la tesis.

En el **Capítulo 2**, se desarrolla el formalismo del método numérico. Se comienza haciendo un repaso de los conceptos de energía eléctrica y magnética en los sistemas multiconductores en régimen estático con el fin de presentar los elementos parciales desde un punto de vista clásico. Siguiendo el símil de la mecánica analítica, se escribe el Lagrangiano del sistema y, aplicando el principio de mínima acción, se llega al primer conjunto de ecuaciones que describe la física del sistema: la ley de voltages de Kirchoff. Para ligar el desarrollo anterior con el método PEEC, se parte de la ecuación integral de los potenciales mixtos (potencial vector $\bar{A}$ y potencial escalar ϕ) adecuándola a la naturaleza de los componentes a estudiar. Para ello, se introduce tres aproximaciones durante la discretización de dicha ecuación que permiten accelerar el tiempo de cálculo: (i) se elimina el potencial retardado; (ii) la densidad de corriente se reduce a su componente axial a lo largo del conductor; (iii) se considera que los conductores en sustratos laminados pueden tratarse como 2D. Para realizar la discretización, se usa el concepto de carga y corriente virtual. Se evalúa el trabajo que realiza el sistema sobre éstas, obteniéndose la ley de voltages al aplicar el principio de d'Alembert de los trabajos virtuales. Como ley de ensamblado de los elementos, se introduce la discretización de la ecuación de continudidad que conduce a la ley de corrientes

de Kirchoff. El conjunto completo de ecuaciones que describen el sistema está dado por

$$V_k^s = R_k I_k + j\omega \sum_{l}^{M} L_{kl} I_l + \phi(r_k^+) - \phi(r_k^-) \tag{7.1}$$

$$I_k^s = j\omega \sum_{l=1}^{N} C_{kl}\, \phi(r_l) + \sum_{m=1}^{N_{OUT_k}} I_m^{OUT_k} - \sum_{m=1}^{N_{IN_k}} I_m^{IN_k}\,. \tag{7.2}$$

que puede escribirse en forma matricial como

$$\begin{bmatrix} \bar{V}^s \\ \bar{I}^s \end{bmatrix} = \begin{bmatrix} \bar{\bar{R}}^s + j\omega \bar{\bar{L}} & D^T \\ D & j\omega \bar{\bar{C}} \end{bmatrix} \begin{bmatrix} \bar{I} \\ \bar{\phi} \end{bmatrix}, \tag{7.3}$$

donde $\bar{I}$ y $\bar{\phi}$ son el vector incógnita de corrientes y voltajes en los elementos, $\bar{\bar{R}}$ es la matriz de resistencias parciales, $\bar{\bar{L}}$ es la matriz de inductancias parciales, $\bar{\bar{C}}$ es la matriz de capacitancias parciales, $\bar{\bar{D}}^T$ es la matriz transpuesta de $\bar{\bar{D}}$ que describe el ensamblado entre los nodos de los diferentes elementos parciales (ramas de circuito), y $\bar{V}^s$ y $\bar{I}^s$ son vectores que representan las fuentes externas de tensión y corriente.

En la parte final de este Capítulo, se indica cómo debe estructurarse la programación del método. Se ha escogido el entorno de diseño Advanced Design System (ADS), de Keysight Technologies, enlazando el algoritmo desarrollado con su simulador de circuitos *hpeesofsim*. De forma esquemática, la Fig. 7.1 los diferentes módulos de programación. En la parte superior, se observa la ventana de entrada de esquemático donde el diseñador combina los componentes de librería para formar un circuito funcional, define la tecnología y el tipo de simulación a realizar. Previa a esta entrada de esquemático, se ha tenido que definir las celdas parametrizadas de los diversos componentes. Cuando el usuario inicia una simulación de circuito, el módulo *hpeesofsim* debe ensamblar y solucionar la matriz de parámetros Y de todo el conjunto. Para determinar los parámetros Y de los componentes de librería desarrollados, el simulador de circuitos transfiere el control al método PEEC. En la fase de PRE_ANALYSIS, se calcula la malla y las matrices $\bar{\bar{R}}$, $\bar{\bar{L}}$, $\bar{\bar{C}}$, $\bar{\bar{D}}^T$ y $\bar{\bar{D}}$. Su combinación como sistema de ecuaciones se realiza en la fase de COMPUTE_Y donde se requiere el conocimiento de la frecuencia angular, dato proporcionado por el simulador *hpeesofsim*. En este punto, se calculan los parámetros Y del componente a través de la solución PEEC y se transfiere el resultado al simulador principal. Finalizado el cálculo del circuito para los puntos de frecuencia deseados, se realiza las operaciones de gestión de memoria y finalización en el módulo de POST_ANALYSIS. En el caso de realizarse una simulación de transitorio, se invoca al módulo de convolución.

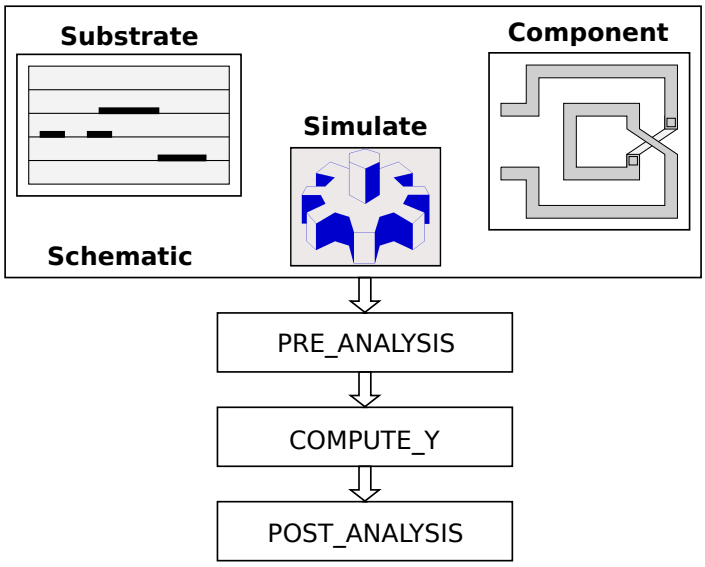

Fig. 7.1 Diagrama de bloques de programación para la implementación del método PEEC en un simulador circuital.

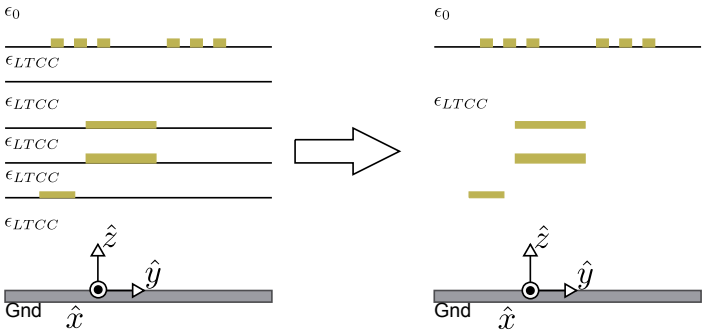

Fig. 7.2 Sección típica de un sistema de cinta multicapa LTCC.

El **Capítulo 3** se centra en el desarrollo y aplicación de una metodología para el cálculo analítico, en el dominio espacial, de la función de Green de un sustrato multicapa. El objetivo que se persigue es computar el valor de los elementos parciales de forma eficiente, garantizando la pasividad de la matriz del sistema de ecuaciones. El punto clave de partida que permite el desarrollo es el hecho que, en la mayoría de las tecnologías multicapa, el material del sustrato es homogéneo, tal y como muestra la Fig. 7.2. Aprovechando esta característica, el problema multicapa original se convierte en el estudio de la función de Green para un substrato homogéneo donde la carga puntual puede estar ubicada en cualquier parte del dieléctrico. Mediante la transformada de Hankel de orden 0, normalmente aplicada en problemas espectrales de simetría cilíndrica, se determina la solución analítica para las configuraciones de carga puntual ilustradas en la Fig. 7.3.

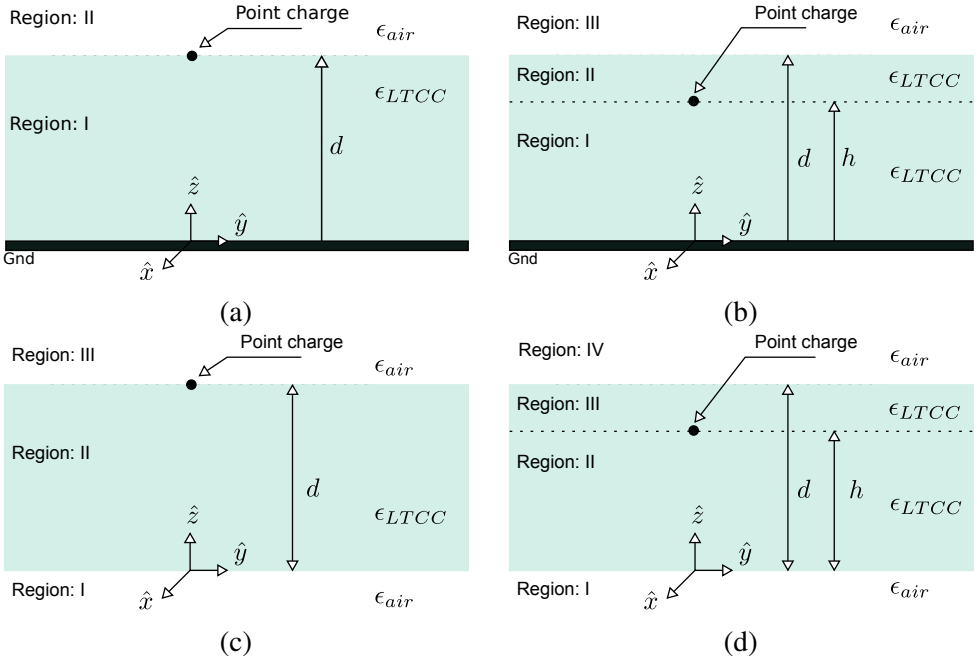

Fig. 7.3 Secciones LTCC: (a) GND con fuente puntual en la interfase dieléctrico-aire; B) GND con fuente puntual dentro del LTCC; (C) límite abierto con una fuente puntual en la interfaz dieléctrico-aire; (D) límite abierto con una fuente puntual dentro del LTCC.

Como ejemplo de cálculo, a continuación se presenta la expresión derivada para la configuración de sustrato de la Fig.7.3a en la cual la carga puntual se ubica en la interficie entre el LTCC y el aire:

$$G_I(\rho,z) = \frac{1}{4\pi\varepsilon_M}\left\{\frac{1}{\sqrt{\rho^2+(d-z)^2}} - \frac{1}{\sqrt{\rho^2+(d+z)^2}} + \right.$$
$$\left. + \sum_{l=1}^{\infty}(-1)^l k^l \left[\frac{1}{\sqrt{\rho^2+(d-z+2d\cdot l)^2}} - \frac{1}{\sqrt{\rho^2+(d+z+2d\cdot l)^2}}\right]\right\} \quad (7.4)$$

donde $\varepsilon_M = (\varepsilon_{LTCC}+\varepsilon_0)/2$, $k = (\varepsilon_{LTCC}-\varepsilon_0)/(\varepsilon_{LTCC}-\varepsilon_0)$, ρ y z son las coordenadas cilíndricas y d es el grosor del substrato. La forma en que se ha ordenado (7.4) sirve para ilustrar de forma clara que el resultado obtenido consiste en una serie infinita de pares de cargas imágenes cuyo plano de antisimetría es GND, un hecho que es bastante complicado de visualizar con técnicas numéricas. Esta situación se ilustra en la Fig. 7.4.

La verificación de las funciones de Green desarrolladas se realiza a través del cómputo de la matriz de capacitancias C_{ij} entre dos parches metálicos cuadrados colocados en una posición concreta dentro del sustrato y se compara con el cálculo obtenido con un simulador comercial basado en el método de los momentos. Los elementos parciales de la matriz de

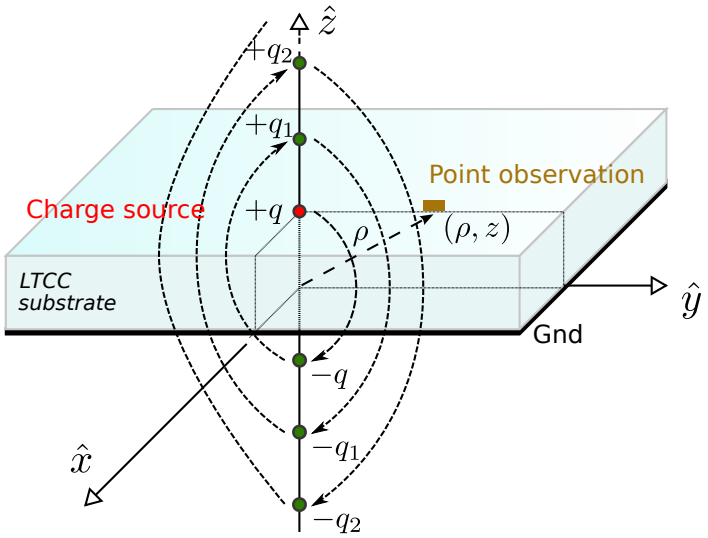

Fig. 7.4 Situación de los pares de carga imagen en el sustrato LTCC con plano de masa.

capacidad se evalúan integrando analíticamente las funciones de Green gracias a las expresiones de Hoer-Love. En la Tabla 7.1 se muestran los resultados obtenidos, observándose pequeñas diferencias entre ambos métodos.

Debido al buen funcionamiento de la metodología, se ha utilizado el mismo procedimiento para la evaluación analítica de un sustrato formado por dos dieléctricos. La resolución de dicho problema es muy interesante pues permitiría utilizar la herramienta PEEC en el análisis de componentes pasivos integrados en silicio. Los diferentes casos calculados se muestran en la Fig. 7.5, donde el sustrato se divide en tres partes: la región I (silicio) tiene un espesor z_1; la región II (óxido) extiende el sustrato hasta d; Y la región III (espacio libre) se extiende indefinidamente. La carga puntual se ubica dentro de la región de óxido, incluyendo las interficies con los otros dos materiales.

La solución encontrada se ha verificado comparándola con un simulador comercial a través del cómputo de la matriz de capacitancia entre dos parches metálicos. Los resultados, presentados en la Tabla 7.2, demuestran pequeñas diferencias entre ambos métodos. Sin

Table 7.1 Comparación de C_{ij} coeficientes de matriz con un simulador comercial.

	Eq. (7.4) [fF]	MoM [fF]	Difference
C_{11}	230.5	231.6	0.475 %
C_{12}	-6.8	-6.839	0.570 %
C_{21}	-6.8	-6.839	0.570 %
C_{22}	230.5	231.6	0.475 %

C_{12} y C_{21} son negativos por definición.

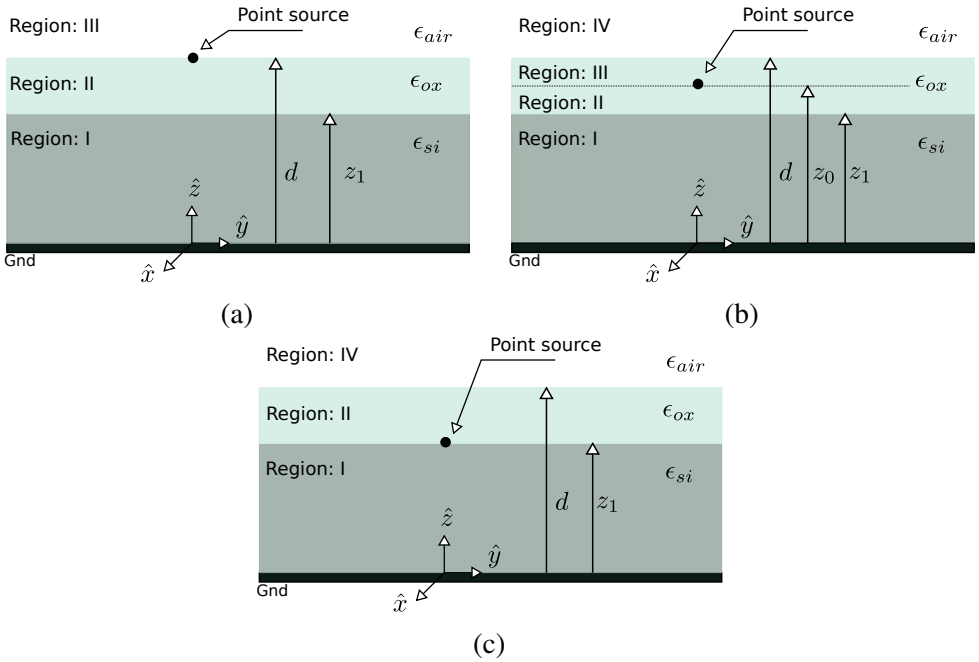

Fig. 7.5 Sección simplificada del substrato de silicio que muestra la ubicación de la fuente de carga: (a) en el límite superior $(\varepsilon_3 - \varepsilon_2)$ interface; (b) dentro del óxido (ε_2); (c) en la interfase de óxido de silicio $(\varepsilon_1 - \varepsilon_2)$.

Table 7.2 Comparación de los coeficientes de la matriz de capacitancia C_{ij}

	GF (eq.3.96) [fF]	MoM [fF]	Difference
C_{11}	345	346.6	0.46 %
C_{12}	-21.4	-21.39	0.047 %
C_{21}	-21.4	-21.39	0.047 %
C_{22}	345	346.6	0.46 %

C_{12} y C_{21} son negativos por definición.

Table 7.3 Resultados de la comparación entre la función analítica y heurística de Green.

	GF analítica [fF]	GF heurística [fF]	Difference
C_{11}	345	344	0.31 %
C_{12}	-21.4	-21.4	0 %
C_{21}	-21.4	-21.4	0 %
C_{22}	345	344	0.31 %

C_{12} y C_{21} son negativos por definición.

embargo, las expresiones resultantes, a diferencia del caso de un dieléctrico, son ineficientes desde el punto de vista computacional. En su lugar, se ha optado por explorar una alternativa

de tipo heurístico. Ésta consiste en dividir el problema original de dos dieléctricos en dos problemas de un sólo dieléctrico: uno con silicio como material; el otro, con óxido. La función de Green resultante es la suma de las soluciones de un único dieléctrico. En la Tabla 7.3 se muestra la validación de esta alternativa con respecto al cálculo analítico para un sustrato de silicio RFCMOS típico.

En el **Capítulo 4**, se presenta un nuevo algoritmo para la generación de mallas que tiene en cuenta, de forma anticipada, la distribución de la densidad de corriente. Este generador de malla es el resultado de la búsqueda de un método eficiente para el análisis de componentes pasivos con factores de calidad altos. La exactitud del cálculo depende principalmente de las condiciones de mallado. Mientras que muchas herramientas comerciales utilizan técnicas de fuerza bruta (por ejemplo, un refinamiento de malla en todas las partes de dispositivo o un método de malla adaptativa iterativa), el camino seguido en este trabajo consiste en dividir la distribución de corriente en dos mecanismos cuasi ortogonales. Por un lado, se tiene en cuenta la dependencia de la distribución de corriente a lo largo de la coordenada de grosor de una pista. Realizando un estudio exhaustivo de las diferentes condiciones geométricas y topológicas de la pista, basta utilizar una expresión modificada de la resistividad cuadro R debida al efecto pelicular en un conductor, i.e.

$$R = R_{DC} \cdot \frac{t}{\delta(1-e^{t/\delta})} \cdot \frac{A(t/H)^2}{1+B(t/H)^2} \tag{7.5}$$

donde t es el grosor de la pista, H el del dieléctrico y δ, el factor pelicular. Los factores A y B deben tabularse para cada una de las frecuencias y sustratos de interés; pero, para la mayoría de tecnologías de laminado, se pueden considerar nulos. Estas pérdidas están ligadas al campo magnético generado por la corriente propia que pasa a través de la pista.

Por otro lado, la dependencia de las pérdidas con la anchura de la pista se calcula generando una malla que es capaz de detectar la influencia del resto de pistas que forman el dispositivo sobre la pista de interés. Para ello, basta realizar un modelo simple de la pista como el que se enseña en la Fig. 7.6 y aplicar los siguientes pasos:

1. Se construye una malla simple del dispositivo que consta de tres celdas por tira.
2. Para cada tira, se calcula los elementos parciales M_l, M_c, $M_{ext_{l_1}}$, $M_{ext_{l_2}}$, M_{ext_c}, L y R:
3. Se resuelve las corrientes del circuito de la Fig.7.6b y se calcula la relación de pérdidas en régimen AC con respecto a DC para cada tira del dispositivo.
4. Gracias a la experiencia acumulada, los criterios mostrados en la Tabla 7.4 se utilizan para asignar las divisiones a lo largo del ancho de la pista.

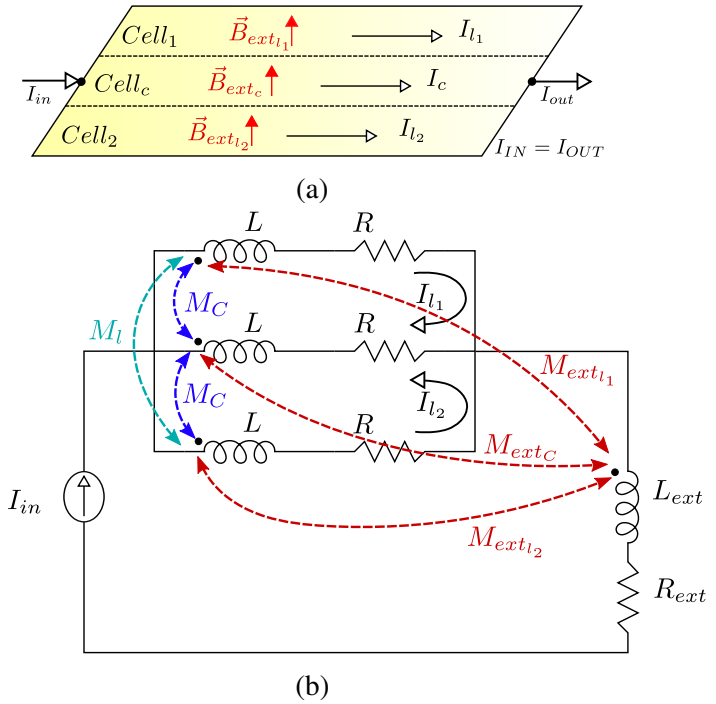

Fig. 7.6 (a) malla simple de una tira de metal; (b) modelo de circuito equivalente.

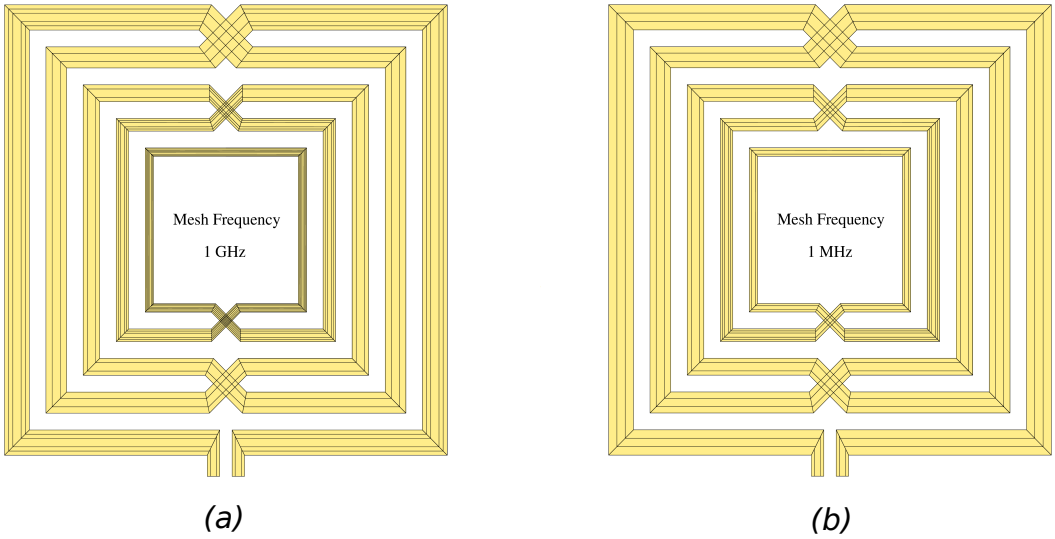

Fig. 7.7 Mallado de inductor cuadrado simétrico, (a) 1Ghz y (b) 1 Mhz.

La Figura 7.7 muestra las mallas típicas obtenidas para un componente inductor. Obsérvese que, mientras el mallado a $1MHz$ es prácticamente uniforme y con tres celdas por pista, el mallado a un $1Ghz$ es más denso en las vueltas interiores. Además, se adapta el tamaño de las celdas seg

Table 7.4 Número de divisiones de celdas de malla a lo largo del ancho de una pista.

$P_{ACloss}/P_{DCloss} = x$	♯ cells
$x < 1.5$	3
$1.5 < x < 2.5$	5
$2.5 < x < 4$	7
$4 < x$	9

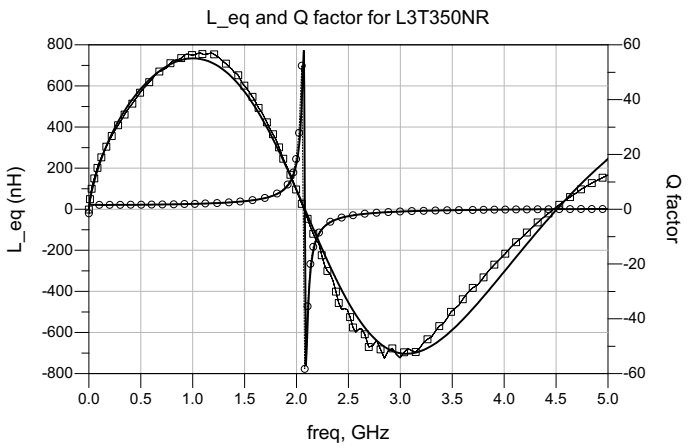

Fig. 7.8 Datos de simulación PEEC vs medidas experimentales para un inductor planar.

En el **Capítulo 5**, todas las técnicas desarrolladas se aplican a la elaboración de un kit de diseño (PDK) que incluye una librería de componentes de RF en LTCC. Gracias a las características de la herramienta de análisis, se permite una escalabilidad mayor de los dispositivos en términos de propiedades de sustrato y condiciones de contorno. Sin ningún cambio adicional, el mismo PDK puede manejar diferentes sistemas de fabricación de LTCC. La librería está formada por resistencias, condensadores de diversos tipos, e inductores simétricos con y sin punto de conexión de modo común. Todos los modelos generados se comparan, al menos, con otras herramientas comerciales de simulación y, cuando es posible, con datos experimentales.

El caso más paradigmático de aplicación de la herramienta es el del inductor planar, gracias a la relación de aspecto ancho / largo / grosor típico de las tiras de metal que conforman el dispositivo. En la Fig. 7.8, se muestra la comparación de los valores de simulación junto con datos experimentales en un rango de frecuencias desde DC hasta la segunda resonancia. Además, se ha comprobado si el mismo modelo es válido para otras tecnologías como la de circuitos impresos (PCB), o la de RFICs. La Tabla 7.5 ofrece los resultados donde se ha utilizado, como parámetros eléctricos del componente, el valor de inductancia a baja frecuencia (L), la resistencia a baja frecuencia (R_{DC}), el factor de calidad

Table 7.5 Medidas vs. simulaciones de inductores en diferentes tecnologías.

		L (nH)	R_{DC} (Ω)	Q_{max}	SRF (Ghz)	t_{comp} (51 points)
L1	PEEC	23.3	0.86	32	1.95	5.25s
	MoM	22.8	0.52	103	2.27	13min55s
	Sonnet	22.2	0.49	53	2.32	14min
	CST	20.4	0.10	124	2.24	6min17s
	Meas	23.8	1.01	46	2.03	**
L2	PEEC	141.0	0.138	80.9	333	1.89s
	MoM	143.2	0.19	66.9	334	1min27s
	Sonnet	144.8	0.17	84.1	335	2min3s
	CST	139.0	0.02	142.0	332	2min51s
	Meas	141.8	0.22	82.2	329	**
L3	PEEC	2.09	1.23	21.3	16.80	1.9s
	MoM	2.19	1.42	17.3	17.49	2min16s
	Sonnet	2.17	1.57	14.09	16.19	5min48s
	CST	2.27	0.06	38.7	16.41	3min48s
	Meas	2.00	1.11	29.8	18.75	**

máximo (Q_{max}) y la frecuencia de resonancia (SRF). Además, también se da el tiempo necesario para calcular la solución. Hay que destacar que el algoritmo PEEC implementado es 30 veces más rápido para un sustrato de una capa (casos L2 y L3) y hasta 160 veces más rápido para un sustrato de diez capas (caso L1), conservando la precisión de la solución.

Para resistencias, se ha verificado el modelo usando simuladores comerciales. Se ha obtenido un rendimiento parecido al caso de los inductores. De hecho, desde el punto de vista de la simulación, la única diferencia entre resistencias e inductores es el valor de conductividad de las regiones conductoras. La Figura 7.9 muestra la comparación de PEEC con un software basado en el método de los momentos. Para el caso de los condensadores, se ha desarrollado diferentes tipos de componentes: de película, de apilamiento e interdigitados. La velocidad de cálculo es dos a cuatro veces más rápida que con otros simuladores. Comparado al caso de los inductores, este decremento se debe a la necesidad de modelar la distribución de corriente como un vector de dos componentes. El hecho que el simulador siga siendo más rápido que los simuladores comerciales se debe a que se ha conseguido generar una malla que permite combinar elementos de corriente 1D con elementos 2D. En la Fig. 7.10, se muestran ejemplos de los tres tipos de condensadores simulados en un rango de frecuencias

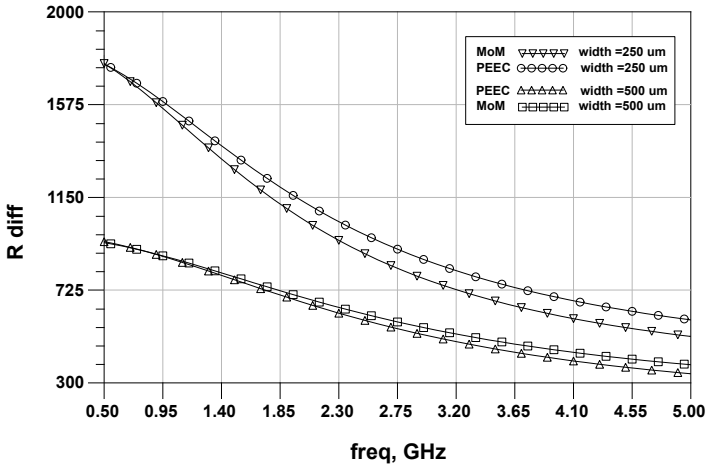

Fig. 7.9 Comparación de los datos de simulación PEEC vs MoM para una resistencia.

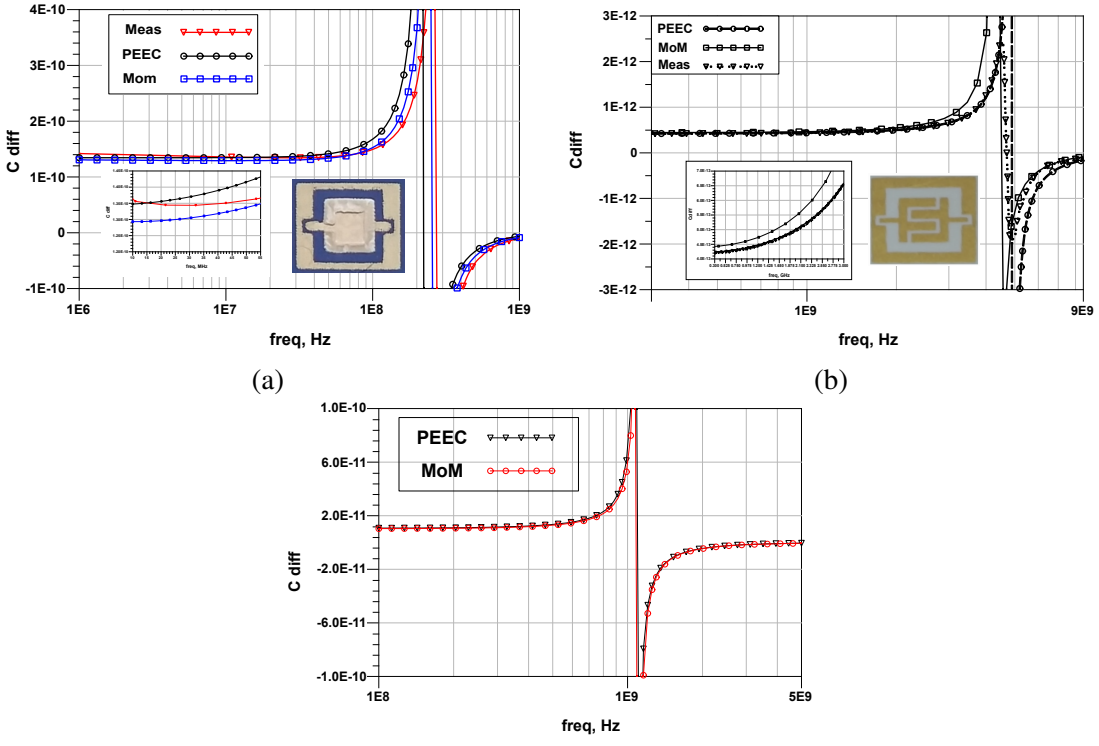

Fig. 7.10 Verificación de condensadores: Datos medidos vs simulados de (a) un condensador de película, (b) un condensador de dedo, y (c) comparación de datos de simulación de un condensador apilado (4 capas).

amplio, siendo muy satisfactorios los resultados obtenidos. En el caso del condensador de apilamiento, no se ha podido contrastar con valores experimentales.

La disertación finaliza, en el **Capítulo 6**, con las conclusiones de esta tesis doctoral:

- Se ha demostrado que el método PEEC puede derivarse de la aplicación del principio de d'Alembert de los trabajos virtuales aplicado a un sistema multiconductor.

- Para reducir la complejidad del modelo, se ha formulado y aplicado correctamente un criterio heurístico basado en la distribución de la densidad de corriente evaluada en DC y se ha aplicado al modelado de resistencias, condensadores e inductores en el rango de frecuencias RF.

- La robustez del método, en términos de estabilidad y convergencia, se garantiza gracias al desarrollo de un procedimiento analítico para el cálculo de la función de Green del sustrato en el dominio espacial.

- Para sustratos de un único dieléctrico, la función de Green desarrollada es computacionalmente eficiente. Además, puede tener en cuenta cualquier valor de permitividad, cualquier número de capas y condiciones de frontera diferentes (plano GND o espacio abierto).

- También se ha desarrollado de forma analítica la función de Green para sustratos de dos dieléctricos. Sin embargo, es computacionalmente ineficiente. Para paliar esta situación, se ha orientado el cálculo a un enfoque heurístico que consiste en descomponenr la función de Green en dos términos, asociados a dos problemas homogéneos de un dieléctrico. Se ha demostrado un buen acuerdo en comparación con otros simuladores.

- Se ha desarrollado un generador de malla adaptativo ab initio que ha sido aplicado al cálculo de inductores de alta Q.

- También se ha desarrollado una técnica de malla híbrida 1D / 2D para combinar regiones de distribución de corriente 2D con otras de naturaleza 1D dentro del mismo dispositivo. Además, esta técnica ha permitido la implementación de mallas no estructuradas.

- Con el solver EM propuesto, se ha implementado un PDK capaz de manejar cualquier sistema de fabriación LTCC comercial, de dieléctrico homogéneo. Las resistencias y los inductores se simulan al menos 30 veces más rápido que los simuladores comerciales, manteniendo el mismo grado de precisión. Para los condensadores, la velocidad es 4 veces más rápida.